

The Structure of Charm Jets and the Dead Cone Effect in Deep-Inelastic Scattering at HERA

Dissertation

zur Erlangung des Doktorgrades
des Fachbereichs Physik
der Universität Hamburg

vorgelegt von
ADRIAN PERIEANU
aus Tîrgovişte

Hamburg
2006

Gutachter der Dissertation : Prof. Dr. G. Heinzelmann
Prof. Dr. B. Naroska

Gutachter der Disputation : Prof. Dr. P. Schleper
: Dr. H. Jung

Datum der Disputation : 23.01.2006

Vorsitzender des Prüfungsausschusses : Dr. H. D. Rüter

Vorsitzender des Promotionsausschusses : Prof. Dr. G. Huber

Dekan des Fachbereichs Physik : Prof. Dr. G. Huber

Abstract

The structure of charm jets in deep-inelastic scattering is studied with the H1 detector at HERA using an integrated luminosity of 50 pb^{-1} . The analysis is performed in the phase space region $2 \leq Q^2 \leq 100 \text{ GeV}^2$ and $0.05 \leq y \leq 0.7$. Charm events are tagged by a D^* -meson required to have a transverse momentum $p_{T,D^*} > 1.5 \text{ GeV}$ and a pseudorapidity $|\eta_{D^*}| < 1.5$. Furthermore, the events are required to have at least one jet containing the D^* -meson (D^* Jet). If there is a second jet ($OtherJet$) in the event, it must have, like the D^* Jet, $p_{T,Jet} > 1.5 \text{ GeV}$ and $|\eta_{Jet}| < 1.5$. The structure of the D^* Jet and the $OtherJet$ is investigated by measuring jet shape variables and subjet multiplicities. In addition the angle of subjets with respect to the jet axis of the D^* Jet and the $OtherJet$ is used to study gluon radiation at the parton level.

Study of the latter distribution as well as the derived one of a characteristic angle $\alpha_0 E_{Jet}$ as a function of E_{Jet} is motivated by the expected suppression of soft gluon radiation from heavy quarks, the so-called "Dead Cone" effect, predicted by QCD. In all distributions differences between the D^* Jet and the $OtherJet$ are observed. The data are found to be well described by the QCD model for charm production, which includes the suppression of soft gluon radiation, as implemented in RAPGAP 2.8 and JETSET 7.4. Various checks and a further analysis using higher statistics are presented in order to get a better understanding of the contribution from the "Dead Cone" effect to the $\alpha_0 E_{Jet}$ vs. E_{Jet} distribution.

Kurzfassung

In dieser Arbeit wird die Struktur von Charm-Jets in der tief-inelastischen Streuung (DIS) mit dem H1 Detektor am HERA Speicherring untersucht. Die verwendeten Daten entsprechen einer Luminosität von 50 pb^{-1} . Die Analyse wird in dem kinematischen Bereich $2 < Q^2 \leq 100 \text{ GeV}^{-2}$ und $0.5 \leq y \leq 0.7$ durchgeführt. Die Charm-Quarks werden durch die Rekonstruktion von D^* -Mesonen mit einem Transversalimpuls von $p_T > 1.5 \text{ GeV}$ und einer Pseudorapidität $|\eta_{D^*}| < 1.5$ nachgewiesen. Außerdem muss es mindestens einen Jet in dem Ereignis geben, der das D^* -Meson enthält. Falls das Ereignis einen weiteren Jet aufweist, muss dieser Jet ($OtherJet$), ähnlich dem D^* -Jet, einen Transversalimpuls $p_{T,Jet} > 1.5 \text{ GeV}$ und eine Pseudorapidität $|\eta_{Jet}| < 1.5$ haben. Die Struktur von beiden Jets wird mit Hilfe verschiedener Ereignisform-Variablen und der Subjet-Multiplizität, sowie der Winkelverteilung von Subjets relativ zur Jetachse untersucht. Jets und Subjets sind so definiert, dass sie mit dem entsprechenden Quark bzw. dem abgestrahlten Gluon auf Partonniveau möglichst gut korreliert sind.

Die Winkelverteilung der Subjets und die Verteilung des charakteristischen Winkels $\alpha_0 E_{Jet}$ als Funktion von E_{Jet} wurden gewählt, weil die QCD eine Unterdrückung der Abstrahlung von 'weichen' Gluonen von schweren Quarks bei kleinen Winkeln vorher-sagt. Diese Unterdrückung wird als "Dead Cone Effect" bezeichnet. Die Daten werden von dem QCD Modell für Charm Produktion, wie es in RAPGAP 2.8 und JETSET 7.4 implementiert ist, gut beschrieben. Um die $\alpha_0 E_{Jet}$ versus E_{Jet} Verteilung besser zu verstehen werden verschiedene Tests und eine erweiterte Analyse mit erhöhter Statistik präsentiert.

Резюме

La structure des jets issus de la fragmentation des quarks charmés produits dans les collisions electron–proton à HERA est étudiée en utilisant les données enregistrées par le détecteur H1, correspondant à une luminosité intégrée de 50 pb^{-1} . L’espace de phase de l’analyse est défini par une virtualité du photon dans le domaine $2 < Q^2 \leq 100 \text{ GeV}^2$ et une inélasticité $0.5 \leq y \leq 0.7$. Les événements contenant des particules charmées sont étiquetées en identifiant un meson D^* avec une impulsion transverse supérieure à 1.5 GeV dans le domaine de pseudorapidité $|\eta_{D^*}| < 1.5$, contenu dans un jet (le D^* -Jet) dans le même domaine cinématique. La structure du jet contenant le meson D^* est étudiée en mesurant les paramètres de forme et la multiplicité des "sous-jets", et comparée à celle des autres jets dans l’événement.

En particulier, la distribution angulaire relative des sous-jets, caractérisée par un angle α_0 , est révélatrice de la radiation gluonique du quark initial dans le processus de fragmentation. D’après Chromodynamique Quantique (CDQ), cette radiation gluonique est moins intense dans le cas du quark charmé en comparaison avec les quark légers. Cette suppression pourrait être mise en évidence en étudiant la variation de l’angle α_0 en fonction de l’énergie du jet. La simulation Monte Carlo basée sur les programmes RAPGAP et JETSET est en bon accord avec les données.

Des différences sont observées entre la structure du D^* Jet et celle du *OtherJet*, le deuxième jet dans l’événement. Afin d’investiguer si la distribution observée de l’angle α_0 pour le D^* Jet est révélatrice de la suppression attendue, cette distribution est également étudiée sur des échantillons de contrôle.

Краткий обзор

Представлены результаты изучения адронных струй порождённых очарованным кварком в глубоко неупругом рассеянии в данных, набранных на установке H1 с суммарной светимостью 50 pb^{-1} .

Анализ представлен в области фазового пространства $2 \leq Q^2 \leq 100 \text{ ГэВ}^2$ и $0.05 \leq y \leq 0.7$. События, содержащие очарованный кварк выделялись с помощью реконструкции D^* -мезона с поперечным импульсом и псевдобыстротой удовлетворяющими условию $p_{T,D^*} > 1.5 \text{ ГэВ}$, $|\eta_{D^*}| < 1.5$. Дополнительно требовалось, чтобы события содержали не менее одной струи с D^* -мезоном, D^* Jet. При наличии второй струи (*OtherJet*) в событии её поперечный импульс также должен удовлетворять условию, $p_{T,\text{Jet}} > 1.5 \text{ ГэВ}$, аналогично D^* Jet. Структура D^* Jet и *OtherJet* исследована с помощью переменных связанных с формой струй и множественностью министруй в струе, а также углового распределения министруй в D^* Jet и *OtherJet*, дающего информацию о корреляции с соответствующим глюоном на партонном уровне. Кроме этого, получено распределение по характерному углу $\alpha_0 E_{\text{Jet}}$ как функции энергии струи E_{Jet} . Два последних распределения мотивированы эффектом подавления излучения мягких глюонов тяжелым кварком, предсказанным в КХД.

Во всех представленных распределениях обнаружена разница между характеристиками D^* Jet и *OtherJet*. Показано, что экспериментальные данные хорошо описываются КХД моделью рождения очарованных кварков в виде, реализованном в Монте Карло программах RAPGAP 2.8 и JETSET 7.4 .

Для лучшего понимания зависимости $\alpha_0 E_{\text{Jet}}$ от E_{Jet} проведены дополнительные проверки, а также анализ данных большей статистики.

摘 要

本文利用H1探测器采集的积分亮度为 50pb^{-1} 的数据样本, 讨论深度非弹性碰撞过程中粲喷注的结构, 其中相空间范围为 $2 \leq Q^2 \leq 100 \text{ GeV}^2$ 和 $0.05 \leq y \leq 0.7$ 。本文选择的事例中存在一个包含 D^* 介子的喷注 (此喷注被称为 $D^*\text{Jet}$), 其中 D^* 介子和喷注的选择条件为横动量大于 1.5 GeV 和赝快度的绝对值小于 1.5 。如果事例中含有第二个喷注, 此喷注被称为 OtherJet , 文中通过测量喷注形状变量和子喷注多重数研究 $D^*\text{Jet}$ 和 OtherJet 的特性。同时测量 $D^*\text{Jet}$ 和 OtherJet 的角分布来讨论部分子层次的胶子行为。

由子喷注的角分布可以提取变量 $\alpha_0 E_{\text{Jet}}$, 文中通过研究 $\alpha_0 E_{\text{Jet}}$ 对 E_{Jet} 的依赖关系, 讨论QCD预言的重夸克的软胶子辐射的压低现象。根据 $D^*\text{Jet}$ 和 OtherJet 所得到的各种分布是有差别的。实验结果能被基于粲夸克产生的QCD模型 (RAPGAP 2.8 和 JETSET 7.4) 很好的描述。为了更好的理解 $\alpha_0 E_{\text{Jet}}$ 对 E_{Jet} 的依赖关系, 本文也做了多重检查和高统计量数据的探索。

Contents

Preface	ix
1 Theoretical Basis	1
1.1 General View of the Standard Model	1
1.2 Charm Production in ep Collisions at HERA	4
1.2.1 The ep Collisions at HERA	4
1.2.2 Charm Production at HERA	7
1.3 Jet Finders and Jet Shape Variables	12
1.3.1 Jet Finders	12
1.3.2 Jet Shape Variables	14
1.4 Gluon Emission from Heavy Quarks	16
1.5 The <i>Dead Cone</i> Effect: from ED to QCD	17
1.6 The Monte Carlo Models	19
2 The H1 Detector at the HERA Collider	23
2.1 The HERA Collider	23
2.2 The H1 Detector	24
2.3 The Central Jet Chambers	29
2.4 The Liquid Argon Calorimeter	30
2.5 The Spaghetti Calorimeter - SpaCal	32
2.6 The H1 Trigger System	33
3 Event Selection	37
3.1 Charm Events Tagged with a D^* -meson	37
3.2 The Online Selection	39
3.2.1 The General Event Selection	39
3.2.2 The Subtrigger Description	40
3.2.3 The ST61 Efficiency	43
3.2.4 The D^* -meson Online Selection	47
3.3 The Offline Selection	48
3.3.1 The DIS Selection	48
3.3.2 The Scattered Electron Selection	52
3.3.3 The D^* -meson Offline Selection	56
3.3.4 Track Quality Cuts	58
3.3.5 The Δm Reconstruction	61

4	Measurements of the Jet Shape Variables	65
4.1	Hadronic Final State Objects	65
4.2	Jet Selection	69
4.3	Background Subtraction	70
4.4	Error Calculation	72
4.4.1	Systematic Errors	73
4.5	Results at the Detector Level	78
4.6	Correction of the Data to the Hadron Level	80
4.7	Results at the Hadron Level	83
4.8	Investigation of the Difference between the D^* Jet and $OtherJet$	84
4.8.1	Different D^* Jet Definitions	85
4.8.2	Alternative Radius Definition	86
4.8.3	Dependence of Jet Shape Variables on Jet Kinematics	87
5	The <i>Dead Cone</i> Effect	91
5.1	Two Approaches to Study the Dead Cone Effect	92
5.1.1	The Mass Variation Approach	92
5.1.2	The Energy Variation Approach	93
5.2	The Experimental Method	95
5.2.1	The Gluon Subjet of the D^* Jet	96
5.2.2	The Gluon Subjet of the $OtherJet$	97
5.3	Results	98
5.3.1	The α_0 Determination	99
5.3.2	The Systematic Errors	100
5.3.3	The Distribution of $\alpha_0 E_{Jet}$ vs. E_{Jet}	101
5.3.4	Checks of the Experimental Method	103
5.3.5	Monte Carlo Study of b -jets vs. c -jets	107
5.3.6	A Comparison of Charm Jets with Jets from a $2Jet$ Sample	109
5.3.7	Higher Statistics '96-'04	113
6	Conclusions	115
A	QCD Environment	117
B	Mandelstam Variables	123
C	The Track Reconstruction	125
D	The ST61 Efficiency	131
E	The Sigma Method	137
F	The $c \Leftrightarrow$ Jets Correlations	139
G	HFS and Jet Control Distributions	145
H	The Systematic Error Contributions	151

Preface

In everyday life our existence is governed by two questions: *why?* and *how?*. For the first question we never understood exactly where is it coming from, but the second one appears when the people around us cannot any longer give answers to the first one at the level of our expectation. This is *why* the people go to the next stage and ask themselves *how?*. Up to some moment in time the *why?* question has hidden in the shadow of the *how?* question.

If one asks *why* the Earth is moving around the Sun, for some of us, the answer that this is due to an abstract entity called gravity is just not enough, we are eager to know *how* the abstract gravity looks like. Not that we completely understand it afterwards, but the more often the *how?* question is asked, the higher the probability is to get a new idea of explaining *how* gravity works – not only for the Earth and the Sun, but also for a quark and an antiquark.

Until now we figured out that there are four types of interactions: the electromagnetic, the weak, the strong and the gravitational force, as it is presented in the first chapter. Although for some of them we have already solved most of the *how?* questions, the strong and the gravitational interaction still have plenty of questions which are not yet solved or not even thought of. For the questions *why* and *how* the quarks are produced we do have a theory, but for the question *how* the quarks look like we do not have yet the final answer.

In Chapter 1 it is explained *why* the quarks cannot be seen as all the other particles. But the fact that the quarks have no freedom makes people ask themselves: if one cannot see the quarks in a direct way, *how* one can do this indirectly? Feynman pointed out that the momenta of the quark system have to be conserved and he introduced the quark - jet analogy. The particles which are produced in an interaction can be grouped together, e.g. in space, in objects called *jets* which should have, within some approximation, the same momentum and direction as the initial quarks. *How* one distinguishes between the different quark flavour jets is presented also in the first chapter. This is done using so-called jet shape variables. Once the second type of partons was predicted, the gluons, one could observe that hard gluons with high enough energy can also produce hadronic jets. For these hard gluon jets, the same jet shape variables can be used.

A natural question is *how* the quark mass does influence the quark evolution and its hadronic jets. For this, the theory uses a model in analogy to electrodynamics: the emission of quanta by a moving charged particle. If in electrodynamics the quantum was the photon, in chromodynamics (QCD) the quantum is the gluon. In the heavy quark case the prediction from QCD suppresses the emission of soft gluons close to the quark direction. This effect is called the *dead cone effect*. In the second part of the first chapter the jet shape variables and the theory of the *dead cone effect* are presented.

The study of the soft gluon emission by heavy quarks can be also viewed as a next generation of variables that can discriminate in a statistical way between parton jets of different type. This way, another piece of the puzzle *how* the quarks look like can be understood.

The data used in this analysis were acquired at the HERA collider with the H1 experiment, therefore in the second chapter an overview of the H1 detector is presented.

The third chapter is dedicated to the event selection. Here it is explained in detail *how* the events were triggered and selected in order to make sure that the charm event sample used for this analysis has the smallest possible background.

A traditional method to study charm jets is to use jets shape variables. In the fourth chapter the jet shape study of the charm jets is presented. The jets that reconstruct the two charm quarks in an event are compared. The differences between them are studied using different jet definitions for the jet that contains the D^* -meson, the so-called D^* Jet which is used to reconstruct the charm quark. A new definition of the jet radius and its influences on the jet shape variables are presented too. In the last part of the chapter the dependencies of the jet shape variables with respect to the transverse energy, the pseudorapidity and the jet energy are shown. The correlation between the charm quark and the corresponding jet is shown in Appendix F. Based on them, the definition of the D^* Jet is chosen.

In the fifth chapter an innovative approach of *how* to study charm jets, namely using the angle between the charm jet direction and one of its subjets, which is considered as coming from a soft gluon radiated by the charm quark, is presented. This technique allows the direct measurement of the *dead cone effect*. The specific angle of the *dead cone*, α_0 , is determined using a fit function inspired from QCD theory. The similarities obtained for the $\alpha_0 E_{\text{Jet}}$ vs. E_{Jet} distribution in the data and in the MC model, which has this effect implemented, are astonishing. In order to clarify various influences from different related effects on the $\alpha_0 E_{\text{Jet}}$ variable a long list of checks are performed. The most conclusive check is the comparison between the charm event sample and a reference di-jet sample, which is dominated by $\sim 85\%$ of light quarks, as presented at the end of this chapter. The difference observed in the $\alpha_0 E_{\text{Jet}}$ vs. E_{Jet} distribution between the charm jet and the light quark jets becomes clearer when one includes all the statistics available until now, from 1996 to 2004. This way the puzzle *how* the quarks look like reveals a new side of its own, hidden until now.

In order to make a fluent reading of the thesis possible, some chapters are linked to appendices. In these appendices general information about QCD, the track reconstruction, the subtrigger efficiencies, the correlations between the charm quark and the corresponding jets as well as a detailed overview of the systematic errors are presented.

With this overview and the eagerness of knowing *how* a new piece of QCD can be understood and probed, the author wishes every reader a pleasant time during reading of this thesis.

Chapter 1

Theoretical Basis

1.1 General View of the Standard Model

The Standard Model of particle physics (SM) is a theoretical framework [1] where the particle physics phenomena which have been observed are described within the often small experimental errors, with the exception of neutrino oscillations and the existence of dark matter. Behind these experimental errors, everyone hopes for a new theory which will take over at some moment of time.

The SM describes the interactions of *elementary particles*. The *elementary particles* are defined as being the matter constituents¹ with no known² substructure down to the present limit of 10^{-3} fm, about 1/1000 of the diameter of a proton.

The units used in particle physics are not the standard S.I. units: m (length), kg (mass) and s (time). It was found more convenient to use relative units. The length is expressed using the *femtometer* or *fermi* ($1 \text{ fm} = 10^{-15} \text{ m}$), the mass is measured in MeV/c^2 and has usually the meaning of rest-energy. The energy unit is the electron volt ($1\text{eV} = 1.6 \cdot 10^{-19} \text{ J}$). In order to make calculations easier, a system of units with $\hbar = c = 1$ was adopted on the basis of a standard mass³ of 1 GeV.

The elementary particles can be divided into *matter particles* and *intermediate interaction particles*. The first category can be split into *leptons* and *quarks*, which are fermions with spin $s = 1/2$. The leptons which are known until now are the electron (e^-), the muon (μ^-) and the tau (τ^-) having the electric charge⁴ -1 and the neutrinos ν_e, ν_μ, ν_τ with no charge. The quarks come in six flavours: up (u), down (d), strange (s), charm (c), beauty (b) and top (t). They have a fractional charge of $2/3, -1/3, -1/3, 2/3, -1/3$ and $2/3$ respectively.

The quarks have one more quantum number: *colour*. The colour of a quark can be *red, green* or *blue*. The concept of quark colour has been introduced as an explanation for the fact that the quarks have not yet been observed as 'free' entities. Thus they have to be confined in experimentally observed *colourless* particles, the *hadrons*. The observed hadrons can be classified as *baryons* and *mesons*. The baryons are fermions which contain three quarks as for example the *proton* (uud) or the *neutron* (ddu). The mesons are bosons formed by a quark and an antiquark like for example the π^- ($d\bar{u}$) or the D^{*+} ($c\bar{d}$).

¹The elementary particles are also called 'point-like' objects.

²No substructure have been observed for quarks and leptons yet.

³The mass of 1 GeV was used as an approximation of the proton mass $m_p = 938.28 \text{ MeV}$

⁴All the charges are expressed in units of the elementary charge e .

The intermediate interaction particles, relevant in particle physics phenomena, are bosons with spin $s = 1$. There are four types of interactions: *electromagnetic*, *weak*, *strong* and *gravitational*⁵.

The electromagnetic interaction has the *photon*, γ , as exchange particle. The range of interaction is infinite. The photon is massless, charge-less and non-self-interacting. The weak interaction has a short range of about 10^{-3} fm, corresponding to the exchange of a massive gauge particle with a mass of $M_{weak} \sim 100$ GeV. The intermediate interaction particles are the weak bosons W^\pm , with ± 1 charge, and Z^0 , which is neutral. They are massive⁶ and self-interacting. The strong interaction has a finite range due to physical confinement property. The range is of about 1 fm, corresponding to the typical size of the lightest hadron. Eight gluons g_i , $i = \overline{1,8}$, are mediating the strong interaction. They have colour and interact with quarks and with themselves.

The strength of the electromagnetic interaction is governed by the size of the electromagnetic *coupling* e , which can be also written as $\alpha_{em} = e^2/4\pi$. At low energies the coupling strength is given by the fine structure constant $\alpha(Q = m_e) = 1/137$. As the energy increase so does the electromagnetic coupling. The weak interaction has the strength given by the *Fermi* constant $G_F = 1.167 \cdot 10^{-5} \text{ GeV}^{-2}$ for energies much lower than the mass of the exchanged boson mass. The strong interaction has a strength given by the size of the strong coupling g_s , $\alpha_s = g_s^2/4\pi$. It is called *strong* because it is stronger than any of the other interactions. One should note that α_s decreases with increasing of the energy [2], as shown in Fig. 1.1. This behaviour is referred to as *asymptotic freedom*.

The name asymptotic freedom is inspired by the fact that at infinitely large energy or the equivalently infinitely short distance, the quarks behave as free particles. The Nobel Prize in Physics was awarded in 2004 to D. Gross, D. Politzer and F. Wilczek for the discovery of the asymptotic freedom in non-abelian field theory.

The SM is a quantum field theory based on the $SU(3)_C \otimes SU(2)_L \otimes U(1)_Y$ *gauge symmetry group*⁷. The $SU(3)_C$ is the symmetry group of the strong interactions. The electroweak interaction is described by the symmetry group $SU(2)_L \otimes U(1)_Y$. The weak and electromagnetic interactions are unified in the sense that $U(1)_{em}$, the group of the electromagnetic interactions, appears as subgroup of $SU(2)_L \otimes U(1)_Y$ in the SM.

The eight gluons which are the gauge bosons of $SU(3)_C$ and γ , W^\pm and Z , the particles which make up the four gauge bosons of $SU(2)_L \otimes U(1)_Y$, form the so-called *gauge sector*.

The *fermionic* sector is composed of quarks and leptons which are grouped into

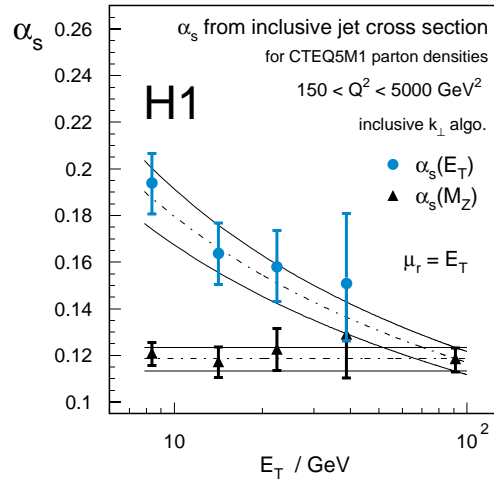


Figure 1.1: Determination of α_s from the inclusive jet cross section.

⁵The gravitational interaction, mediated by the graviton, is the weakest and is neglected in high energy physics. The graviton, if exists, is expected to have spin 2.

⁶ $M_W = 80.423 \pm 0.039 \text{ GeV}$; $M_Z = 91.1876 \pm 0.0021 \text{ GeV}$;

⁷The indices refer to: C - colour, L - lepton number and Y - hypercharge.

three families with identical properties, exceptions being the mass, the flavour and the lepton number. The particle content of each family is:

$$1^{st} \text{ family: } \begin{pmatrix} \nu_e \\ e^- \end{pmatrix}_L, e_R^-, \begin{pmatrix} u \\ d \end{pmatrix}_L, u_R, d_R$$

$$2^{nd} \text{ family: } \begin{pmatrix} \nu_\mu \\ \mu^- \end{pmatrix}_L, \mu_R^-, \begin{pmatrix} c \\ s \end{pmatrix}_L, c_R, s_R$$

$$3^{rd} \text{ family: } \begin{pmatrix} \nu_\tau \\ \tau^- \end{pmatrix}_L, \tau_R^-, \begin{pmatrix} t \\ b \end{pmatrix}_L, t_R, b_R$$

and similarly the corresponding antiparticles. The left-handed and the right-handed fields, respectively, are given by the chirality operator γ_5 :

$$e_L^- = \frac{1}{2}(1 - \gamma_5)e^-; \quad e_R^- = \frac{1}{2}(1 + \gamma_5)e^-.$$

The *scalar* sector is the part of the SM which is not yet confirmed experimentally. The weak gauge bosons are massive particles. This indicates that $SU(2)_L \otimes U(1)_Y$ is not a vacuum symmetry. The fact that the photon is massless shows that $U(1)_{em}$ is a vacuum symmetry. Therefore the *spontaneous symmetry breaking* in SM must be: $SU(3)_C \otimes SU(2)_L \otimes U(1)_Y \rightarrow SU(3)_C \otimes U(1)_{em}$. This is implemented in SM by the *Higgs* mechanism which provides the proper mass to W^\pm , Z gauge bosons and to the fermions. The mechanism is based on a scalar, neutral and yet undiscovered, Higgs boson particle. In the next section the 'place' of the c quark in SM is presented.

The *Gell-Mann-Nishijima* law [3] relates the *electrical charge* Q with the *hypercharge* Y and the third component of the *isospin* I_3 of a particle.

$$Q = I_3 + \frac{Y}{2}$$

The hypercharge is defined as the sum of the *baryon number* B and the *flavour charges*: *strangeness* S , *charm* C , *bottomness* \mathbf{B} and *topness* T .

$$Y = B + S + C + \mathbf{B} + T$$

All mesons and baryons, until the J/Ψ discovery, with the same spin and parity could be grouped into irreducible representations of the *flavour* symmetry group, $SU(3)_F$. Every particle can be labeled with its quantum numbers (I_3, Y) and can be grouped within the elements of these representations: *triplets*, *octets*, *nonets*, *decuplets*.

The group representations are built for a fixed *spin* and *parity* value, noted J^P .

In $SU(3)_F$, the lowest dimensional representation which is irreducible [4] is the triplet with dimension equal to three. This triplet was not occupied by any known hadron, in 1964.

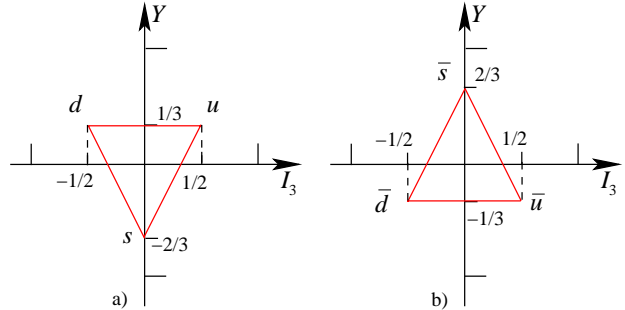


Figure 1.2: $SU(3)_F$ group: u , d and s quarks.

The high Q^2 events were seen as one of the main goals in the ep collisions. The reason for this was to achieve a high resolution to investigate the proton structure. This resolution depends linearly on the de Broglie wave length $\lambda = h/|q_t|$ where the q_t is just the transverse momentum of the

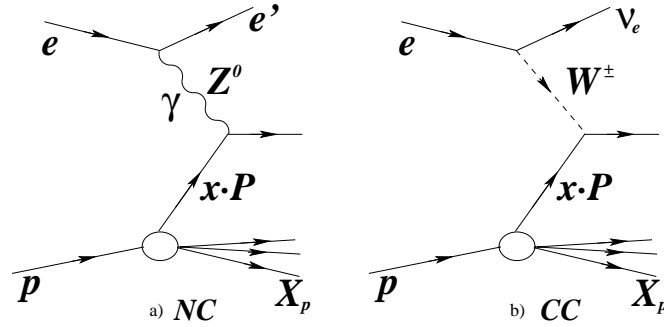


Figure 1.5: The Feynman diagrams of the ep scattering: a) neutral current (NC), b) charged current (CC).

exchanged boson $\sqrt{Q^2}$. In the end, many interesting physics phenomena proved to be at *low* Q^2 . The physics at *low* Q^2 can be split in two parts.

The regime where $Q^2 \rightarrow 0$ GeV² is called *photoproduction* because a quasi-real photon is produced.

For the $Q^2 > 1$ GeV², the regime is called *deep* ($Q^2 > m_p^2$) *inelastic* ($W^2 > m_p^2$) *scattering* (DIS). The analysis presented in this thesis is focused on DIS events with $2 < Q^2 < 100$ GeV². Details of the kinematic cuts applied in this analysis can be found in Chapter 3.

The cross-sections of the NC and CC are given by:

$$\frac{d^2\sigma_{NC}^{e\pm p}}{dx dQ^2} = \frac{2\pi\alpha^2}{x} \left[\frac{1}{Q^2} \right]^2 \phi_{NC}^{\pm}(x, Q^2); \quad (1.4)$$

$$\frac{d^2\sigma_{CC}^{e\pm p}}{dx dQ^2} = \frac{G_F^2}{4\pi x} \left[\frac{M_W^2}{Q^2 + M_W^2} \right]^2 \phi_{CC}^{\pm}(x, Q^2), \quad (1.5)$$

having the *structure function terms* [8]:

$$\phi_{NC}^{\pm}(x, Q^2) = Y_+ \tilde{F}_2(x, Q^2) - y^2 \tilde{F}_L(x, Q^2) \mp Y_- x \tilde{F}_3(x, Q^2); \quad (1.6)$$

$$\phi_{CC}^{\pm}(x, Q^2) = Y_+ \tilde{W}_2(x, Q^2) - y^2 \tilde{W}_L(x, Q^2) \mp Y_- x \tilde{W}_3(x, Q^2), \quad (1.7)$$

where the inelasticity dependence is contained in $Y_{\pm} = 1 \pm (1 - y)^2$. The *generalised* structure functions are \tilde{F}_2 , \tilde{F}_L , $x\tilde{F}_3$ for NC and \tilde{W}_2 , \tilde{W}_L , $x\tilde{W}_3$ for CC . One can see from the Q^2 dependence of the two cross-sections that for low Q^2 the CC process is strongly suppressed due to the $M_W^2/(Q^2 + M_W^2)$ term. The longitudinal structure function \tilde{F}_L contributes significantly at high y .

The \tilde{F}_2 and $x\tilde{F}_3$ can be written also as:

$$\tilde{F}_2 = F_2 - v_e \left[\frac{\kappa_w Q^2}{(Q^2 + M_Z^2)} \right] F_2^{\gamma Z} + (v_e^2 + a_e^2) \left[\frac{\kappa_w Q^2}{(Q^2 + M_Z^2)} \right]^2 F_2^Z; \quad (1.8)$$

$$x\tilde{F}_3 = -a_e \left[\frac{\kappa_w Q^2}{(Q^2 + M_Z^2)} \right] xF_3^{\gamma Z} + (2v_e a_e) \left[\frac{\kappa_w Q^2}{(Q^2 + M_Z^2)} \right]^2 xF_3^Z, \quad (1.9)$$

were:

$$\begin{aligned} a_e &= T_{3e}; & v_e &= T_{3e} - 2e_e \sin^2 \theta_w; \\ a_q &= T_{3q}; & v_q &= T_{3q} - 2e_q \sin^2 \theta_w; & \kappa_w &= 1/(4 \sin^2 \theta_w \cos^2 \theta_w) \end{aligned}$$

with the weak isospin $T_3 = \pm 1/2$ and θ_w - the Weinberg angle. M_Z is the mass of the Z boson.

The NC generalised structure functions are composed of five *structure functions* which describe the Z^0 exchange, the γ exchange and the γZ^0 interference. The NC cross-sections can be written using the dominant contributions as:

$$\begin{aligned} \frac{d^2\sigma_{NC}^{e\pm p}}{dx dQ^2} \simeq \frac{2\pi\alpha^2}{x} \left\{ \frac{1}{Q^4} Y_+ F_2 + a_e^2 \kappa_w^2 \left[\frac{1}{Q^2 + M_Z^2} \right]^2 Y_+ F_2^Z \right. \\ \left. \mp 2a_e \kappa_w \left[\frac{1}{Q^2(Q^2 + M_Z^2)} \right] Y_- x F_3^{\gamma Z} \right\}. \end{aligned} \quad (1.10)$$

In the quark parton model (QPM), the F_2 and F_2^Z structure functions are related to the sum of the quark and antiquark densities as:

$$F_2(x, Q^2) = x \sum_q e_q^2 \cdot (f_{q/p}(x, Q^2) + f_{\bar{q}/p}(x, Q^2)) \quad (1.11)$$

$$F_2^Z(x, Q^2) = x \sum_q (v_q^2 + a_q^2) \cdot (f_{q/p}(x, Q^2) + f_{\bar{q}/p}(x, Q^2)) \quad (1.12)$$

and the $x F_3^{\gamma Z}$ structure function is sensitive to the difference between the quark and antiquark densities as:

$$x F_3^{\gamma Z}(x, Q^2) = x \sum_q 2e_q a_q \cdot (f_{q/p}(x, Q^2) - f_{\bar{q}/p}(x, Q^2)), \quad (1.13)$$

where v_q and a_q are the vector and the axial-vector couplings of the quarks, respectively, and e_q is the quark charge. The sum is over all quark flavours q in the proton. The quark density $f_{q/p}(x, Q^2)$ is giving the probability to find a quark with the flavour q and the momentum x at a scale Q^2 in the proton. The analogous statement for the antiquark density also applies.

1.2.2 Charm Production at HERA

For $Q^2 < 100 \text{ GeV}^2$, due to large mass of the Z^0 exchange boson, the contribution of F_2^Z and $x F_3^{\gamma Z}$ related terms in the cross-section is strongly suppressed. Taking this approximation into account and that the F_L contribution is predicted to be negligible for y not too large, the NC cross-section can be written as:

$$\frac{d^2\sigma_{NC}^{e\pm p}}{dx dQ^2} \simeq \frac{2\pi\alpha^2}{xQ^4} \cdot (1 + (1 - y)^2) \cdot F_2(x, Q^2). \quad (1.14)$$

The charm cross-section in ep collisions in DIS is related to the charm contribution F_2^c of the inclusive structure function F_2 as follows:

$$\frac{d^2\sigma^{ep \rightarrow e'cX}}{dx dQ^2} \simeq \frac{2\pi\alpha^2}{xQ^4} \cdot (1 + (1 - y)^2) \cdot F_2^c(x, Q^2, m_c^2). \quad (1.15)$$

The structure function $F_2^c(x, Q^2, m_c^2)$ contains the convolution of the *partonic hard* cross-section $\hat{\sigma}_{\gamma^*i}$ and the *parton distribution* of the *proton* $f_{i/p}$ at a scale:

$$\mu_F^2 = Q^2 + m_c^2,$$

where the proton is probed. The type of the parton out of the proton, most of the time a gluon, is indicated with the index i . The structure function F_2^c can be expressed as:

$$F_2^c(x, Q^2) = \sum_i \int_{z_{min}}^{z_{max}} \frac{dz}{z} e_q f_{i/p} \left(\frac{x}{z}, Q^2, \mu_F \right) \hat{F}_i(z, Q^2, \mu_F) \quad (1.16)$$

with z being the momentum fraction of a gluon after emitting another parton, having the upper limit at $z_{max} = Q^2/(\hat{s} + Q^2)$ and the lower limit $z_{min} = (Q^2 + 4m_c^2)/Q^2$, and where:

$$\hat{F}_i(z, Q^2, \mu_F) = \frac{Q^2}{4\pi^2\alpha} (\hat{\sigma}_{\gamma^*i}^T(\hat{s}, Q^2, \mu_F) + \hat{\sigma}_{\gamma^*i}^L(\hat{s}, Q^2, \mu_F)). \quad (1.17)$$

Here \hat{s} is one of the Mandelstam variables. The $\hat{\sigma}_{\gamma^*i}$ are the hard parton cross-section for transversely and longitudinally polarised photons¹⁰.

At HERA charm production covers mainly the $\mu \approx m_c$ regime. The extremes like small x or high energies can be also reached. In the dominant HERA regime where the partonic collision energy is close to threshold and x is moderate, the charm quarks are treated as heavy objects (the mass is taken into account) which do not occur inside the proton. For this regime the dominant production mechanism is the *flavour creation* usually called the *boson gluon fusion* process (BGF) and is depicted in leading order (LO) in Fig. 1.6.

In the regime where the initial colliding particles have a high center of mass energy (high energy scale $\mu^2 \gg m_c^2$) and a moderate x , the mass of the charm quark can be neglected in comparison to μ and the charm quark is part of the proton and can be described in a similar way as the light quarks. In this regime the dominant production mechanism is the so-called *flavour excitation*, where the charm quark is an active flavour in the proton.

In the small x regime, the terms $\ln(1/x)$ are becoming large and *small x resummation* is needed. This resummation is performed in the BFKL [9] and CCFM [10] evolution models¹¹ but not in the DGLAP [11] one. The charm quark treatment is similar to the one for $\mu \approx m_c$ and the moderate x regime.

The incoming *lepton* interacts with a *gluon* from the proton via the virtual *photon* γ^* and a $c\bar{c}$ pair is produced. The charm quark is treated as a particle with mass and the cross-section calculation is done in the massive scheme.

Another charm production mechanism is pair production via *gluon splitting* $g \rightarrow c\bar{c}$. At HERA the contribution from this mechanism is suppressed, because it is a higher order process in α_s . At the $p\bar{p}$ collider TEVATRON,

the process $gg \rightarrow gQ\bar{Q}$ gives a sizeable contribution to the $gg \rightarrow Q\bar{Q}$ (here Q denotes a heavy quark).

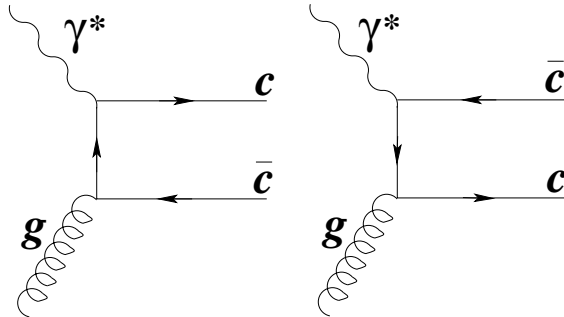


Figure 1.6: The BGF LO Feynman diagrams.

¹⁰More detailed explanations about parton distributions, scale, factorisation and evolution models can be found in the Appendix A, and about Mandelstam variables in Appendix B.

¹¹BFKL - Balitsky, Fadin, Kuraev, Lipatov; CCFM - Catani, Ciafaloni, Fiorani, Marchesini; DGLAP - Dokshitzer, Gribov, Lipatov, Altarelli, Parisi. The different evolution models are presented in the Appendix A.

In LO the total cross-section for charm production in DIS at HERA has two components [12]. One component is due to transversely polarised photons and can be written as:

$$\sigma_{\gamma^*g \rightarrow c\bar{c}}^T = \frac{2\pi \alpha e_c^2 \alpha_s(\mu^2)}{\hat{s} + Q^2} \left[- \left(\frac{\hat{s}^2 - Q^4 + 4\hat{s}m_c^2 - 8m_c^4}{(\hat{s} + Q^2)^2} \right) \ln \left(\frac{1 + \beta}{1 - \beta} \right) - \left(\frac{(\hat{s} - Q^2)^2 + 4\hat{s}m_c^2}{(\hat{s} + Q^2)^2} \right) \beta \right] \quad (1.18)$$

and the second component is due to longitudinally polarised photons:

$$\sigma_{\gamma^*g \rightarrow c\bar{c}}^L = 8\pi \alpha e_c^2 \alpha_s(\mu^2) \cdot \frac{Q^2 \hat{s}}{(\hat{s} + Q^2)^3} \left[\beta - \frac{2m_c^2}{\hat{s}} \ln \left(\frac{1 + \beta}{1 - \beta} \right) \right] \quad (1.19)$$

where:

$$\beta = \sqrt{1 - \frac{4m_c^2}{\hat{s}}}.$$

In order to calculate the hadronic cross-sections, one has to convolute the LO partonic cross-sections with the corresponding LO parton densities.

The scale μ^2 contributes mainly in the lowest order α_s and there is no physical criteria to choose a certain scale. As a consequence, large variations of the cross-section are obtained for different μ^2 values. This strong dependence of the cross-section on the scale can be reduced using the *next to leading order* calculation (NLO). One can see this effect especially for charm quark production, which (at the threshold and for low Q^2) provides a small scale, and α_s is relatively large. The NLO calculations [13] make use of the virtual corrections shown in Fig. 1.7 and the gluon radiation as in Fig. 1.8. Including these new elements in the calculation, one has to take into account also the *ultraviolet*, the *infrared* and the *collinear* divergencies. To remove the *ultraviolet* divergencies the renormalisation prescription is used, loop contributions cancel the *infrared* ones and the *collinear* divergencies are absorbed in the definition of the parton densities.

In the small x regime, a resummation of the $\ln(1/x)$ terms is performed using the BFKL and CCFM evolution models. In these models, the so-called k_T -factorisation is used. The cross-section of the hard interaction is calculated *off-shell*. The off-shell calculation implies that the gluon out of the proton, which is part of the hard interaction, does not lose its virtuality. Here the gluon density is *unintegrated* and depends on k_T . A comparison between the k_T -factorisation model and the collinear factorisation is shown in Fig. 1.9, where the dashed box illustrates the diagram part which is calculated. In the k_T -factorisation some terms of NLO, NNLO are also incorporated.

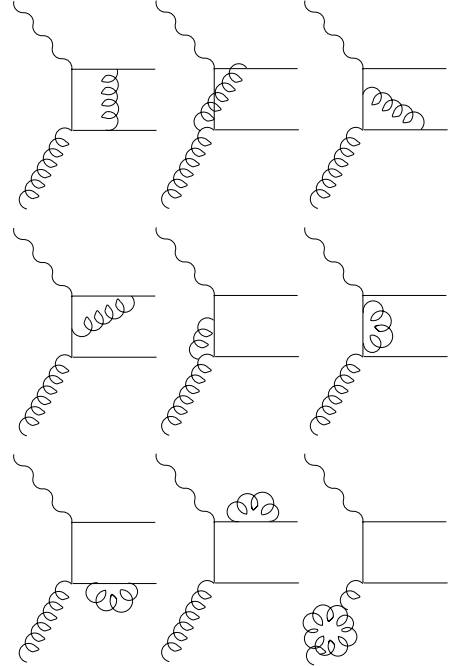


Figure 1.7: Feynman diagrams of the virtual corrections in NLO.

The transition of the *coloured* charm quarks into *colourless* hadrons is called fragmentation. The coupling constant rises strongly at large distances, reducing the applicability of perturbative calculations. Thus for the study of fragmentation, only phenomenological models are used until now.

The inclusive cross-section for heavy hadrons production is:

$$d\sigma_h(p) = \sum_{i \in \text{partons}} \int_0^1 \frac{dz}{z} d\hat{\sigma}_i\left(\frac{p}{z}, \mu_F\right) D_i^h(z, \mu_F) \quad (1.20)$$

where p is the momentum of the parton and $\hat{\sigma}_i$ is the hard ep cross-section at the factorisation scale μ_F .

The $D_i^h(z, \mu_F)$ is the *fragmentation function* and gives the probability for an initial parton i to produce a hadron h having the momentum fraction z at the factorisation scale μ_F . For a certain hadron h , the function D_i^h is assumed to be independent of the hard scattering process, the so-called universality of the fragmentation process.

This assumption is partially sustained by the reasonable agreement between different experimental results from ep and e^+e^- collisions.

The fragmentation function part can be split into a perturbative part, D_i , and a non-perturbative one, D^H , as follows:

$$D_i^h(z, \mu_F) = \int_z^1 \frac{dx}{x} D_i(x, \mu_F) D^H\left(\frac{z}{x}\right). \quad (1.21)$$

The D_i includes the transition from the quarks produced at the scale μ_F to the quarks on their mass shell via gluon radiation. In Monte-Carlo generators D_i is described perturbatively via parton showers.

The D^H function describes the non-perturbative transition from the quarks on mass shell to the hadrons.

For this, non-perturbative functions as the *Peterson* fragmentation function [15] or the *Kartvelishvili* function [16] are used to describe the HERA physics. These functions can be used in

independent fragmentation as well as in the Lund string model.

The independent fragmentation model assumes that a bound meson $Q\bar{q}$ is created when a $q\bar{q}$ pair from the vacuum is formed as illustrated in Fig. 1.10 a) for a light u quark. The quark with energy E_q fragments into a hadron with energy zE_q according to a distribution function $f(z)$. The process is iterated until no energy to produce a hadron is left. The baryons are obtained within this model from vacuum fluctuations $qq\bar{q}\bar{q}$. While the independent fragmentation model provides a very rough description

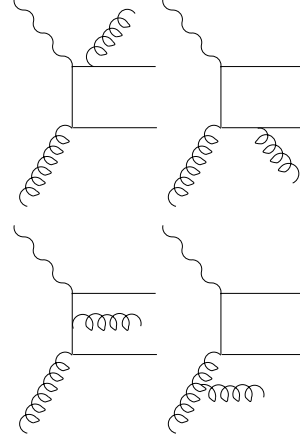


Figure 1.8: Feynman diagrams of the gluon radiation corrections in NLO.

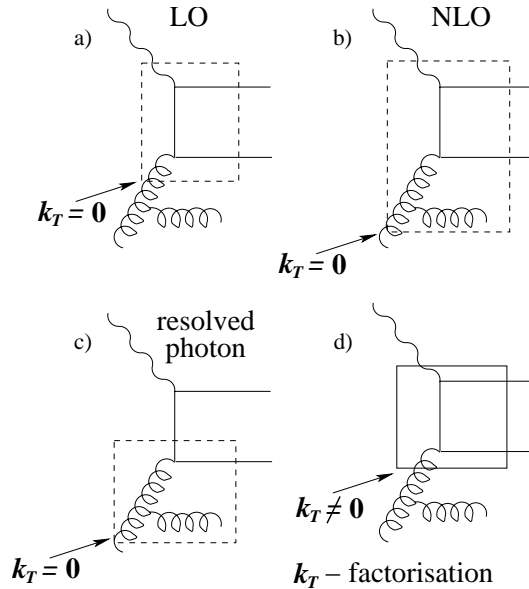


Figure 1.9: The collinear factorisation ($k_T = 0$) vs. the k_T -factorisation ($k_T \neq 0$).

of data, it has several limitations: needs an ad hoc neutralisation of the colour and flavour with the last quark, is not Lorentz invariant and has limitations for small z .

The D^H fragmentation function is expressed in the Peterson model by the transition amplitude $P(Q \rightarrow h)$ and the longitudinal phase space factor $1/z$, where $z = E_h/E_Q$. The amplitude $P(Q \rightarrow h)$ can be written as $P \sim 1/(\Delta E)^2$, where ΔE is the energy difference between the initial and the final state:

$$\Delta E = E_Q - E_h - E_q \approx \frac{m_Q^2}{2p_Q} \left(-\frac{1}{z} - \frac{\epsilon_Q}{1-z} + 1 \right). \quad (1.22)$$

The parameter $\epsilon_Q = m_q^2/m_Q^2$ is usually called the *Peterson parameter* and is adjusted to describe the data.

The Peterson fragmentation function is written as:

$$D_Q^H = \frac{N_A}{z} \frac{1}{\left[1 - \frac{1}{z} - \frac{\epsilon_Q}{1-z} \right]^2}. \quad (1.23)$$

Another fragmentation function is the Kartvelishvili function:

$$D_Q^H = N_A z^\alpha (1-z) \quad (1.24)$$

with N_A the normalization of the total probability for hadron formation to unity and α a free parameter. The fragmentation parameters for charm, obtained from different data and under various assumptions, have a large spread of values.

The Lund string model illustrated in Fig. 1.10 b) considers the colour field between a $q\bar{q}$ pair as one dimensional colour flux tube which is called a *string*. The energy of the string is given by:

$$E_{string} = \kappa \cdot r \quad (1.25)$$

where $\kappa \sim 1$ GeV/fm is the string tension constant or the energy density in the string and r is the distance between the coloured quark q and antiquark \bar{q} .

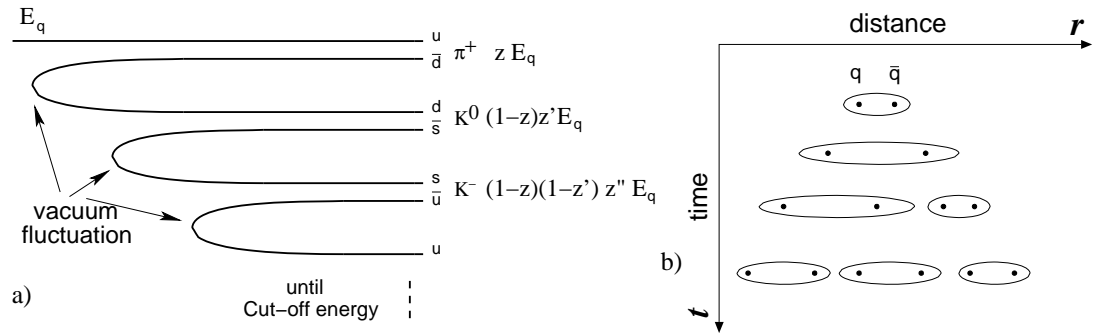


Figure 1.10: The independent fragmentation model of Feymann and Field, a), and the Lund string fragmentation model b).

When the string energy is large enough to produce a $q\bar{q}$ pair, the string breaks up the colourless $q\bar{q}$ pair. The process is iterated with the new string until all available energy is used to form hadrons. In this model the gluon, carrying two colour charges, is always the end point of two strings. In a $q\bar{q}g$ configuration the gluon appears as a kink in the colour connection between $q\bar{q}$ pair. The string model does not suffer from the defects of the independent fragmentation model mentioned above.

Both models assume that in the fragmentation process only limited transverse momenta are produced, usually parametrised with a falling exponential distribution in p_T^2 with $\langle p_T^2 \rangle \approx 440 \text{ MeV}^2$.

1.3 Jet Finders and Jet Shape Variables

1.3.1 Jet Finders

The observation of quarks as free particles is not possible due to their colour. The quarks produced in the hard interaction, e.g. the BGF process, are fragmenting into hadrons. Due to the limited transverse momenta they produce the so-called jets of particles. These jets keep some of the kinematical characteristics of the corresponding quark or gluon, even if they are relatively smeared. The reconstruction of these jets of hadrons is done using *jet algorithms*. The resulting jets have to be well correlated in momentum and angle with the quarks or gluons that produced them.

In 1975 was reported the first evidence [18] of a jet structure in the final state hadrons in e^+e^- collisions. In this report the jet definition was very intuitive and qualitative, namely the jet was considered to be a "large amount of hadronic energy in a small angular region".

The e^+e^- collisions are characterised by a pure electromagnetic *initial state* which creates a $q\bar{q}$ pair via the γ or Z^0 .

In an ep collision the *initial state* contains soft radiation of the incoming parton in the hard process. This is an additional contribution to the *final state* hadrons. Only a fraction of the final hadrons can be associated with the hard scattering process.

A jet definition should fulfill some general rules such as to be collinear and infrared safe, to be measurable in the experimental analysis using the hadronic final state as input, and to be calculable order by order in perturbation theory, to be as little as possible sensitive to the effects of hadronisation, to be insensitive to the beam remnant, and to provide a good correlation between the jet and the corresponding quark in energy and in angle.

The collinear divergency in pQCD is due to the situation when two massless partons

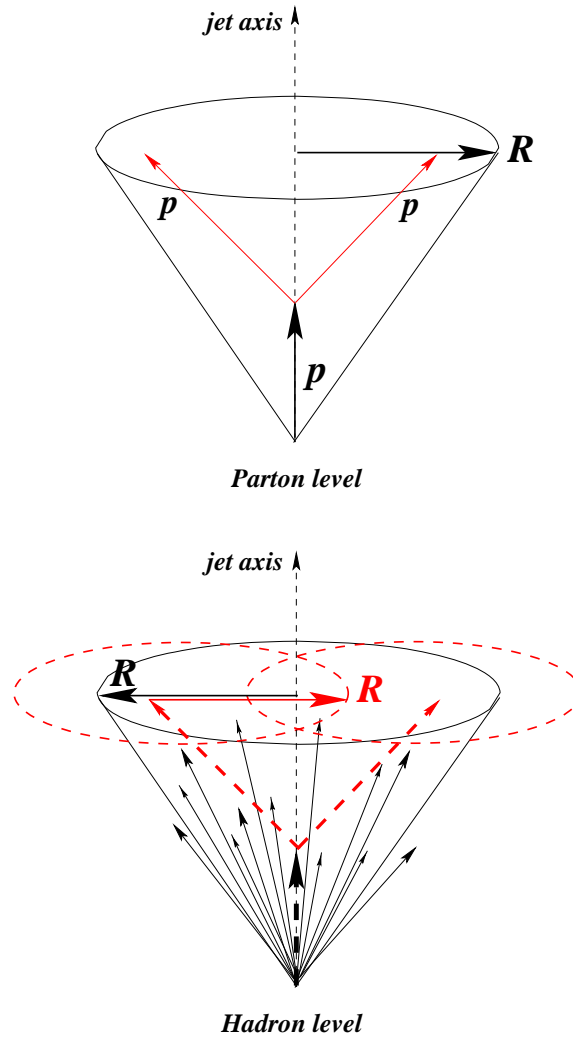


Figure 1.11: The cone type algorithm problem.

are emitted collinear. The infrared divergencies come from the partons which have a very low energy. In a jet finder algorithm it is very important that the contribution of these partons do not affect the jet observables.

The many jet algorithms which are existing can be classified into two large categories. One of them contains the *cone-type algorithms* which are based on the ideas of Sterman and Weinberg [19]. The second category includes the *cluster-type algorithms*, the first of which was introduced by the JADE collaboration [20].

The *cone-type algorithm* is based on finding a jet direction, a *jet axis*, for which the amount of energy inside a *cone* with fixed radius R has a maximum. The *cone axis* coincides with the jet one. The radius R is defined in a plane given by the pseudorapidity η , which is invariant with respect to longitudinal boosts in the γ^*p -frame:

$$\eta = -\ln \left[\tan \left(\frac{\theta}{2} \right) \right] \quad (1.26)$$

and the azimuthal angle ϕ . The definition of the radius R is:

$$R = \sqrt{\Delta\eta^2 + \Delta\phi^2}. \quad (1.27)$$

A known problem of the cone algorithm is the overlapping of two jets when the distance between the *jet axes* less than $2R(\eta, \phi)$. The jet finder should give a good correlation between a hard parton and the corresponding jet on hadron level. In Fig. 1.11, the case of a hard parton splitting into another two partons is presented. At the hadron level two jets may be found, but at the parton level only one. This result brings ambiguity in getting the kinematical properties of the hard parton. The problem can be seen also the other way around, when at the parton level are indeed two hard partons as the two partonic jets suggest, but the jet algorithm finds only one at the hadron level.

The *cluster-type algorithm* is defined by: a *separation variable* d_{ij} , which decides whether the parton or particle i and j are combined or not, using the relative transverse momentum, and a *recombination procedure*. The *recombination procedure* defines how partons or particles are to be combined and thereby how the jet variables are calculated.

The jet finder algorithm used in this analysis is the *longitudinally invariant k_{\perp} cluster algorithm* [21]. As in any jet finder, the input used is a list of partons, hadrons or particle candidates at the detector level. These particles are described by their transverse energy $E_{T,i} = |\vec{p}_{T,i}|$, pseudorapidity η_i and azimuthal angle ϕ_i .

The jets are found by the iterative k_{\perp} algorithm in the following steps:

1. a *separation variable* d_{ij} is defined for every pair of particles:

$$d_{ij} = \min(E_{T,i}; E_{T,j})^2 \cdot R_{ij}^2 \quad (1.28)$$

with $R_{ij}^2 = (\eta_i - \eta_j)^2 + (\phi_i - \phi_j)^2$; for small opening angles $R_{ij}^2 \ll 1$ and:

$$\min(E_{T,i}; E_{T,j})^2 \cdot R_{ij}^2 \sim \min(E_i; E_j)^2 \cdot \theta_{ij}^2 \sim k_{\perp,ij}^2, \quad (1.29)$$

where θ_{ij} is the opening angle between the two particles and $k_{\perp,ij}$ is the transverse momentum of the particle i with respect to particle j ;

2. a similar quantity as the separation variable is defined for every particle with respect to the beam:

$$d_i = E_{T,i}^2 \cdot R_0^2, \quad (1.30)$$

where R_0 is a parameter of the k_\perp algorithm which can be steered; the meaning of R_0 is similar to the jet radius $R(\eta, \phi)$ of the cone-type algorithm; the R_0 value taken in this analysis is 1. Choosing $R_0 = 1$, the initial and final state radiation are treated on the same footing;

3. find the minimum between d_{ij} and d_i :

$$d_{min} = \min(d_{ij}, d_i);$$

4. if $d_{min} = d_{ij}$, the two particles i and j are merged together into a pseudoparticle κ , which via the massless *recombination procedure* is described by the following variables:

$$E_{T, \kappa} = E_{T, i} + E_{T, j} \quad (1.31)$$

and:

$$\eta_\kappa = \frac{E_{T, i} \cdot \eta_i + E_{T, j} \cdot \eta_j}{E_{T, \kappa}}; \quad (1.32)$$

$$\phi_\kappa = \frac{E_{T, i} \cdot \phi_i + E_{T, j} \cdot \phi_j}{E_{T, \kappa}}; \quad (1.33)$$

5. if $d_{min} = d_i$, the particle i is considered a complete *protojet*; particle i is added to the output list and removed from the list of particles to be considered further.

Then the k_\perp algorithm returns to the first step considering now the already formed pseudoparticles and the remaining particles. The iteration of the five steps stops when only protojets are left. The protojets are ordered according to decreasing E_T in the output list. As *jets* are defined those *protojets* with an $E_{T, protojet}$ larger than a certain threshold value:

$$E_{T, jet} \geq E_T^{min}. \quad (1.34)$$

The invariant k_\perp algorithm is less affected by soft particles than the cone-type algorithms. As a consequence the hadronisation and detector corrections are smaller.

The purpose of this analysis is to study the structure of charm jets and to identify soft gluon radiation of the hard charm quark. A useful tool in this study is the *k_\perp subjet finder algorithm*.

The *k_\perp subjet finder* consists in re-running the usual k_\perp algorithm over the hadrons belonging to a found jet with transverse energy E_T using a resolution parameter y_{cut} . In contrast to the usual k_\perp algorithm, the *subjet finder* is stopped when all values of d_{ij} obey the condition:

$$d_{ij} > y_{cut} \cdot E_T^2. \quad (1.35)$$

The protojets of this output list are called *subjets*.

1.3.2 Jet Shape Variables

The internal structure of quark jets is different from the one of gluon jets. The gluon jets are found to be broader than the quark jets [22]. Furthermore the structure of quark jets depends on the mass of the quarks and on their energy. A charm jet is much broader than a light quark jet at the same $E_{T, jet}$. Charm jets are broader at lower energies than at higher energies. For the charm quark, the fragmentation into a charm meson that can be experimentally reconstructed plays an important role.

In order to be able to characterize the internal structure of jets, the following observables are proposed: the *jet shape variables* and the *subjet multiplicity*. The *jet shape variables* are of two types: the integrated and the differential jet shape.

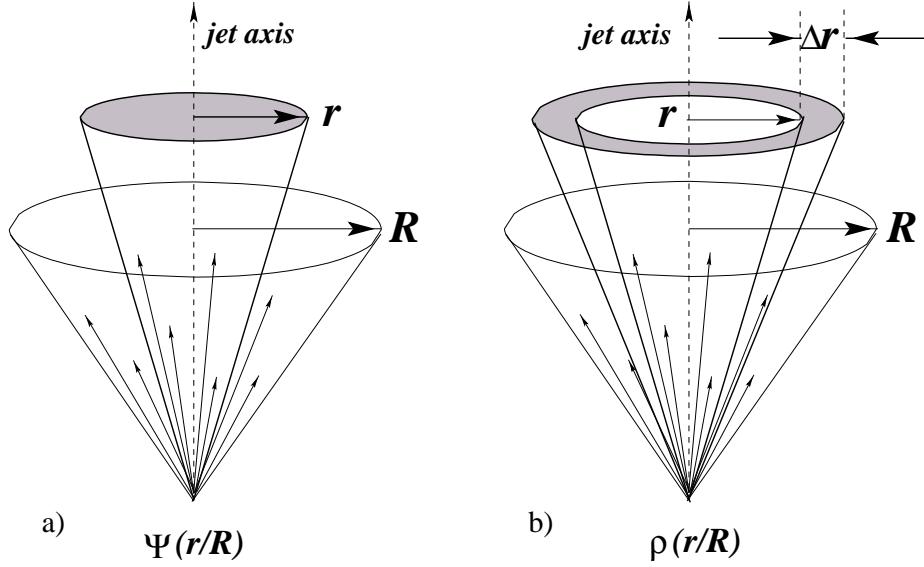


Figure 1.12: The integrated jet shape variable a); the differential jet shape variable b).

The *integrated jet shape variable* $\langle \Psi(r, R) \rangle$ is defined as the average fraction of the jet transverse energy inside an inner cone with radius r in (η, ϕ) space, concentric with the jet axis as shown in Fig. 1.12 a):

$$\langle \Psi(r, R) \rangle = \frac{1}{N_{\text{jets}}} \sum_{\text{jets}} \frac{E_{\text{T}}^{\text{jet}}(r)}{E_{\text{T}}^{\text{jet}}(r = R)}, \quad (1.36)$$

where $E_{\text{T}}^{\text{jet}}(r)$ is the transverse energy within the cone with radius r . N_{jets} represents the total number of jets in the sample. R is the "jet radius" for the k_{\perp} cluster algorithm with the usual value of $R=1$. From the definition: $\langle \Psi(r, R) \rangle = 1$. Narrow jets have larger values of $\langle \Psi(r, R) \rangle$ for $r < R$ compared to broad jets. For low r , the quantity is sensitive to soft gluon emission and for large r to harder gluon emission.

The *differential jet shape variable* $\langle \rho(r, R) \rangle$ is defined as the average fraction of the jet transverse energy between two concentric cones with the jet axis, having the radius r and $r + \Delta r$ respectively, as in Fig. 1.12 b):

$$\langle \rho(r, R) \rangle \equiv \left\langle \frac{d\Psi}{dr} \right\rangle = \frac{1}{N_{\text{jets}}} \sum_{\text{jets}} \frac{E_{\text{T}}^{\text{jet}}(r, r + \Delta r)}{E_{\text{T}}^{\text{jet}}(r = R)}, \quad (1.37)$$

with $E_{\text{T}}^{\text{jet}}(r, r + \Delta r)$ being the transverse energy between the two cones. Narrow jets compared to broad ones are characterised by large values of $\langle \rho(r, R) \rangle$ at small radius r .

The *subject multiplicity* n_{sbj} is defined as the number of subjets obtained after the k_{\perp} subjet finder is re-run over the hadrons of a certain jet for a specific resolution parameter y_{cut} . For a resolution scale $y_{\text{cut}} \sim 1$, the jet contains only one subjet, the jet itself, $n_{\text{sbj}} \rightarrow 1$. If $y_{\text{cut}} \rightarrow 0$, every hadron from the N_{hadrons} within the jet is considered a subjet and $n_{\text{sbj}} \rightarrow N_{\text{hadrons}}$.

The *mean subjet multiplicity* is defined as:

$$\langle n_{\text{sbj}}(y_{\text{cut}}) \rangle = \frac{1}{N_{\text{jets}}} \sum_{i=1}^{N_{\text{jets}}} n_{\text{sbj}}^i(y_{\text{cut}}). \quad (1.38)$$

1.4 Gluon Emission from Heavy Quarks

For light quarks, the cross-section [23] of the $e^+e^- \rightarrow q\bar{q}g$ process can be written as:

$$\frac{1}{\sigma} \frac{d^2\sigma}{dx_1 dx_2} = C_F \frac{\alpha_s}{2\pi} \frac{x_1^2 + x_2^2}{(1-x_1)(1-x_2)} \quad (1.39)$$

where $x_1 = 2E_q/\sqrt{s}$ and $x_2 = 2E_{\bar{q}}/\sqrt{s}$ are the energy fraction of the final state quark and antiquark, respectively.

For heavy quarks and s -channel vector exchange the cross-section for $e^+e^- \rightarrow Q\bar{Q}g$ can be written as function of the mass m of the quark:

$$\begin{aligned} \frac{1}{\sigma} \frac{d^2\sigma}{dx_1 dx_2} = & \frac{1}{\beta} C_F \frac{\alpha_s}{2\pi} \left[\frac{2(x_1 + x_2 - 1 - 2\gamma)}{(1-x_1)(1-x_2)} - 2\gamma \left\{ \frac{1}{(1-x_1)^2} + \frac{1}{(1-x_2)^2} \right\} \right. \\ & \left. + \frac{1}{1+2\gamma} \frac{(1-x_1)^2 + (1-x_2)^2}{(1-x_1)(1-x_2)} \right], \end{aligned} \quad (1.40)$$

where

$$\beta = \sqrt{1-4\gamma}, \quad \gamma = \frac{m^2}{s} \leq \frac{1}{4}. \quad (1.41)$$

The phase space available for gluon emission is reduced due to the mass of the heavy quarks. An intuitive illustration for the phase space boundary given by the Eq. 1.40 can be seen in Fig. 1.13. The phase space boundaries are shown for different quark flavours and energies in various collider types. If one approximates the cross-section for ep collision, at HERA energies, $E_c = 3$ GeV and $E_b = 9$ GeV, where the heavy quarks are produced close to threshold, a clear phase space suppression for gluon emission can be seen. At LEP energies, $E_b = 45$ GeV, the heavy quarks behave as the light quarks, and no suppression can be observed. For a 300 GeV t quark at LHC the phase space suppression is clearly seen, but for a 1.8 TeV energy the t quark behaves also like a light one. When $\gamma \rightarrow 0$, the boundary becomes the massless quark triangle with $x_1 = 1$, $x_2 = 1$ and $x_1 + x_2 = 1$. For $\gamma \rightarrow 1/4$, the threshold of the heavy quarks, the phase space is reduced to the point $x_1 = x_2 = 1$. The collinear divergencies in the cross-section are regularised by the non zero mass of the quark. In Fig. 1.13 one can see that the lines $x_1 = 1$ and $x_2 = 1$ are outside the phase space. There is an infrared divergence for the case when the gluon momentum goes to zero, i.e. for $x_1 = x_2 = 1$.

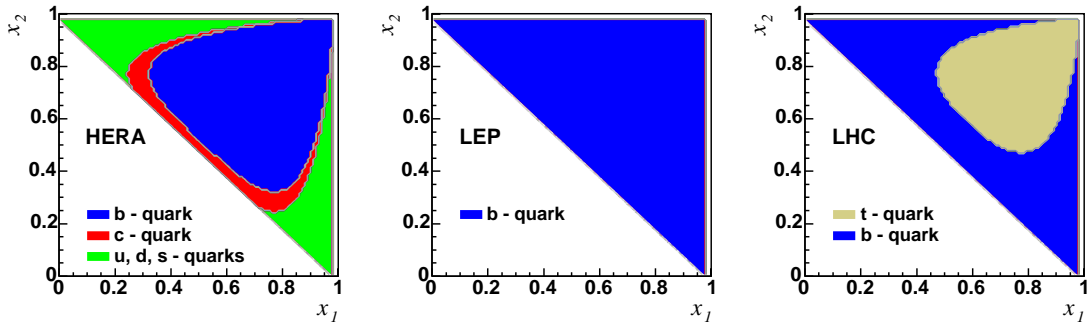


Figure 1.13: The phase space for different quark flavours in case of the radiation of a gluon. The corresponding energies are presented in the text.

The cross-section is suppressed near the phase space boundary, the region where the soft gluons are approximately collinear with the heavy quarks. The suppression of soft gluon emission is called the *dead cone effect*. This can be interpreted as a consequence of the fact that the angular momentum conservation suppresses the emission, via a helicity conserving interaction, of a gluon with spin 1 in the same direction as a quark with spin 1/2.

For soft gluons, $z = 1 - x_1 + 1 - x_2 \ll 1$ and close in angle α to the direction of the heavy quark with $\gamma \ll 1$, the differential cross-section from Eq. 1.40 can be approximated with:

$$\frac{1}{\sigma} \frac{d^2\sigma}{dzd\alpha^2} \approx C_F \frac{\alpha_s}{\pi} \frac{1}{z} \frac{\alpha^2}{(\alpha^2 + 4\gamma)^2}. \quad (1.42)$$

The gluon radiation is suppressed in a cone with the angle:

$$\alpha_0 \sim 2\sqrt{\gamma} = \frac{2m}{\sqrt{s}} = \frac{m}{E} \quad (1.43)$$

with E the energy of the heavy quark. The direct dependence of the angle α on the mass shows that the *dead cone* is broader when the mass of the heavy quark is higher.

1.5 The Dead Cone Effect: from ED to QCD

The theory of the *dead cone effect* in QCD is built on the analogy with electrodynamics (ED).

In ED the role of the quark is taken by a charged particle in motion. The γ radiation of the moving charged particle has the role of the gluon in QCD.

A charged particle in motion can be described using the four-vector potential $A^{4v}(x)$, the velocity $V^{4v}(\tau)$ and the position $r^{4v}(\tau)$. Here τ represents the proper time.

The world line of the particle $r(\tau)$ crosses the *light cone* in only two points, one before x_0 and one after, as shown in the Fig. 1.14.

The time τ_0 is defined by the *light cone* condition:

$$[x - r(\tau_0)]^2 = 0 \quad (1.44)$$

and the retardation requirement $x_0 > r_0(\tau_0)$.

The four-vector potential can be written as:

$$A^{4v}(x) = \left. \frac{eV^{4v}(\tau)}{V \cdot [x - r(\tau)]} \right|_{\tau=\tau_0}. \quad (1.45)$$

The potentials from Eq. 1.45 are known as the *Liénard - Wiechert potentials* [24]. The *light cone* condition implies: $x_0 - r_0(\tau_0) = |\vec{x} - \vec{r}(\tau_0)| \equiv R$.

One can write the denominator of the Eq. 1.45 as:

$$V \cdot (x - r) = V_0[x_0 - r_0(\tau_0)] - \vec{V} \cdot [\vec{x} - \vec{r}(\tau_0)] = \gamma cR(1 - \vec{\beta} \cdot \vec{n}), \quad (1.46)$$

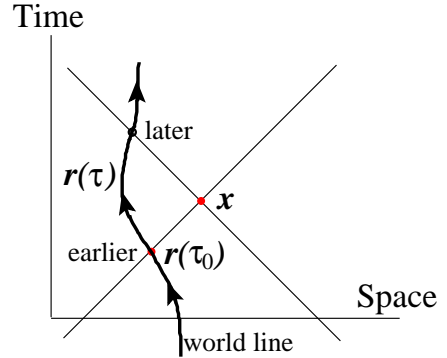


Figure 1.14: The world line of the particle $r(\tau)$.

where $\vec{n} = (\vec{x} - \vec{r}(\tau))/|\vec{x} - \vec{r}(\tau)|$, $\vec{\beta} = \vec{v}(\tau)/c$ and c the light velocity.

The noncovariant form of the potentials from Eq. 1.45 is:

$$\Phi(\vec{x}, t) = \left[\frac{e}{(1 - \vec{\beta} \cdot \vec{n})R} \right]_{ret} ; \vec{A}(\vec{x}, t) = \left[\frac{e\vec{\beta}}{(1 - \vec{\beta} \cdot \vec{n})R} \right]_{ret} ; \quad (1.47)$$

where the notation *ret* means that the potential is to be evaluated at the retarded time τ_0 given by $r_0(\tau_0) = x_0 - R$.

The moving charged particle fields that can be derived from the potentials are:

$$\vec{B} = [\vec{n} \times \vec{E}]_{ret} \quad (1.48)$$

$$\vec{E}(\vec{x}, t) = e \left[\frac{\vec{n} - \vec{\beta}}{\gamma^2(1 - \vec{\beta} \cdot \vec{n})^3 R^2} \right]_{ret} + \frac{e}{c} \left[\frac{\vec{n} \times ((\vec{n} - \vec{\beta}) \times \dot{\vec{\beta}})}{(1 - \vec{\beta} \cdot \vec{n})^3 R} \right]_{ret} \quad (1.49)$$

The two fields can be split into *velocity fields*, not depending on acceleration, and *acceleration fields*, which depend linearly on $\dot{\vec{\beta}}$.

The energy emitted per solid angle unit and per time unit can be defined as:

$$\frac{dP(t')}{d\Omega} = R^2 (\vec{S} \cdot \vec{n}) \frac{dt}{dt'} \quad (1.50)$$

with the *Poynting vector* \vec{S} :

$$\vec{S} = \frac{c}{4\pi} (\vec{E} \times \vec{B}) = \frac{c}{4\pi} |E_{acc}|^2 \vec{n}. \quad (1.51)$$

The Eq. 1.50 can be re-written taking into account that E_{acc} is the acceleration component of the \vec{E} field:

$$\frac{dP(t')}{d\Omega} = \frac{e^2}{4\pi c} \frac{|\vec{n} \times ((\vec{n} - \vec{\beta}) \times \dot{\vec{\beta}})|^2}{(1 - \vec{\beta} \cdot \vec{n})^5}. \quad (1.52)$$

In the simplest case when the vectors $\vec{\beta}$ and $\dot{\vec{\beta}}$ are parallel, as illustrated in Fig. 1.15, the observed energy at an α angle from the common direction of velocity and acceleration vectors is:

$$\frac{dP(t')}{d\Omega} = \frac{e^2 v^2}{4\pi c^3} \frac{\sin^2 \alpha}{(1 - \beta \cos \alpha)^5}. \quad (1.53)$$

For small angles, $\sin \alpha \rightarrow \alpha$, and in the relativistic limit the angular distribution can be approximated by:

$$\frac{dP(t')}{d\Omega} \simeq \frac{8 e^2 v^2}{\pi c^3} \frac{\alpha^2}{(\alpha^2 + \gamma^{-2})^5} \quad (1.54)$$

with:

$$\gamma^{-1} = \alpha_0 = \frac{m_e}{E_e}, \quad (1.55)$$

where E_e is the energy of the moving charged particle.

The suppression of the photon emission within a cone with angle α_0 around the moving direction of a charged particle is called the *dead cone effect*.

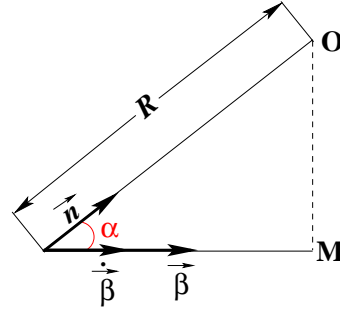


Figure 1.15: The case of $\vec{\beta}$ and $\dot{\vec{\beta}}$ being parallel.

In analogy with ED, the *dead cone effect* can be derived in QCD. The $Q \rightarrow Q + g$ cross-section [25] can be written as:

$$d\sigma_{Q \rightarrow Q+g} = \frac{\alpha_s}{\pi} C_F \frac{(2 \sin \alpha/2)^2 d(2 \sin \alpha/2)^2 d\omega}{[(2 \sin \alpha/2)^2 + \alpha_0^2]^2 \omega} \cdot [1 + O(\alpha_0, \omega)], \quad (1.56)$$

where ω is the energy of the emitted gluon, and the heavy quark is treated relativistically: $E_Q \gg m_Q$ and $\alpha_0 \equiv m_Q/E_Q \ll 1$.

For the small angle approximation, the cross-section from Eq. 1.56 becomes:

$$\frac{d\sigma_{Q \rightarrow Q+g}}{d\alpha} = \frac{\alpha_s}{\pi} C_F \frac{d\omega}{\omega} \frac{\alpha^3}{(\alpha^2 + \alpha_0^2)^2} \quad (1.57)$$

with:

$$\alpha_0 = \gamma^{-1} = \frac{m_Q}{E_Q}. \quad (1.58)$$

In Fig. 1.16, the angular dependence α_{Q-g} on m_Q , as described by Eq. 1.57, is shown. The angle α_{Q-g} is the α angle in Eq. 1.57.

One can observe that for a quark mass of 1.4 GeV the gluons are not any-longer radiated close to the direction of the moving quark. A clear depletion of the emitted gluons with respect to the quark can be identified, the *dead cone effect*.

This cross-section is calculated for the case $E_Q \gg m_Q$. However at HERA, the charm quarks are produced close to threshold and $E_Q \gtrsim m_Q$. The $Q \rightarrow Q + g$ cross-section in this case is calculated using different Monte Carlo models.

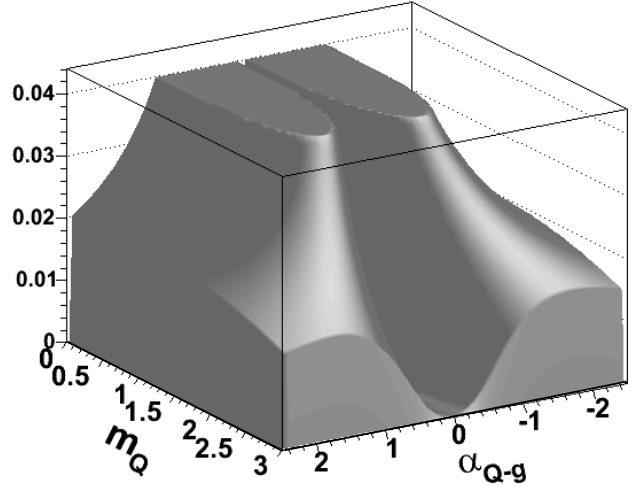


Figure 1.16: Representation of the gluon emission as described by Eq. 1.57.

1.6 The Monte Carlo Models

Monte Carlo (MC) generators are used to simulate the different physics processes and also to determine the detector response.

The MC packages used in this analysis are RAPGAP [26], JETSET [27], HERWIG [28] and DJANGO [29]. Besides incorporating leading order (LO) matrix elements, these MC models include parton showers in a coherent leading logarithms approximation (LLA) as in HERWIG and RAPGAP, or based on the colour dipole model, cascade parton shower, which are also available in RAPGAP. The fragmentation is performed with the cluster fragmentation model in HERWIG and with the Lund string model in RAPGAP. The Peterson parametrisation is used for charm quark fragmentation in charm mesons. In the next lines, HERWIG and RAPGAP models, which are used in charm jets studies of this analysis, are presented.

HERWIG

The HERWIG¹² generator is a general purpose MC program for hadronic processes at high energy. The pQCD processes are calculated using LO matrix elements. The heavy quarks are produced in ep collisions via the BGF mechanism. Colour coherence effect between the initial and the final partons are taken into account.

In HERWIG a branching formalism based on an extension of the coherent LLA is used to generate the parton showers. For parton showers a resummation of pQCD, including all leading logarithmic terms and the dominant part of the sub-leading soft and collinear gluon contribution, is performed. The main parameters in the parton shower are Λ_{QCD} and the shower *cut-off* Q_i for the parton i : $Q_i = m_i + Q_0$ where m_i is the mass of the parton i . Q_0 is the *virtuality cut-off*. After the parton shower, the gluons are split non-perturbatively into $q\bar{q}$ pair.

The hadronisation is calculated in a cluster fragmentation model. The colour of a quark is balanced by the colour of an antiquark close in phase space. This is the mechanism to construct low mass colour neutral clusters. The hadrons are produced in a two body cluster decay corresponding to phase space and spin constraints. The transverse momentum of a hadron is a consequence of the cluster mass spectrum. The coherence effects are also taken into account in the heavy hadron production.

RAPGAP

The MC generator RAPGAP was initially designed to generate diffractive events. The diffractive events are characterised by a large rapidity gap, the name is coming from *rapidity-gap*, which contains no final state hadrons. The developments of RAPGAP ended up in a general purpose MC program for ep collisions.

The photon emission of the incoming and scattered electron are called QED radiative effects. These effects are simulated with the HERACLES [32] event generator which is interfaced with RAPGAP.

The inclusive cross-section for ep in DIS is calculated as in Eq. 1.14 using the structure function F_2 given in terms of parton distribution functions in Eq. 1.11. Different parametrisations of the parton densities in the proton used in F_2 can be selected. The CTEQ5L [31] proton structure function as implemented in the PDFLIB [31] is used in this analysis.

For this analysis an important part of the RAPGAP MC is the parton shower which, as in HERWIG, contains an implementation of the *dead cone effect*. The BGF process generated uses the exact LO matrix elements for heavy quarks.

In the light quarks case, a *pseudo dead cone effect* appears at an invariant mass of ~ 1 GeV. This is due to the fact that in the parton shower evolution an invariant mass *cut-off* is applied with the default value of 1 GeV. Below this mass *cut-off*, the partons are not assumed to radiate. This mass *cut-off* was tuned using e^+e^+ data. This is the reason why in the RAPGAP MC, as well as in the experimental data, a *pseudo-mass* level of ~ 1 GeV is observed as shown in detail in Chapter 5. The *pseudo-mass* level decreases for the light quarks in the same way as the mass *cut-off*. This behaviour is not seen for the heavy quark case.

The fragmentation is done in RAPGAP using the Lund string model as implemented in the JETSET package.

¹²HERWIG - **H**adron **E**mission **R**eaction **W**ith **I**nterfering **G**luons.

After the charm events are generated, the detector response needs to be simulated. This simulation is done using the H1SIM package which is based on the GEANT [33] program. The parameters used for the detector response are determined in test beam measurements and are further tuned with ep data. The default simulation of the energy response of the calorimeters is performed in H1FAST which uses a fast parametrisation of the development of electromagnetic and hadronic showers.

The simulated events are passed to the reconstruction program H1REC which is used also for the experimental data. H1SIM, H1FAST and H1REC are internal H1 program packages.

Chapter 2

The H1 Detector at the HERA Collider

The analysis presented here makes use of the experimental data taken with the H1 detector at the HERA collider. The HERA (**H**adron-**E**lektron **R**ing **A**nlage) machine is the first lepton-nucleon collider. There are four experiments at HERA, two of them are colliding beam experiments, H1 and ZEUS, and the other two are fixed target experiments, HERMES and HERA-B. The HERA-B experiment was closed in 2003.

2.1 The HERA Collider

The HERA ep collider is located at the DESY laboratory in Hamburg, Germany. The HERA collider consists of two separate storage rings, one for leptons (electrons or positrons), and one for protons, each of which has a circumference of 6.4 km. The geometry of the collider and the pre-accelerators is shown in Fig. 2.1.

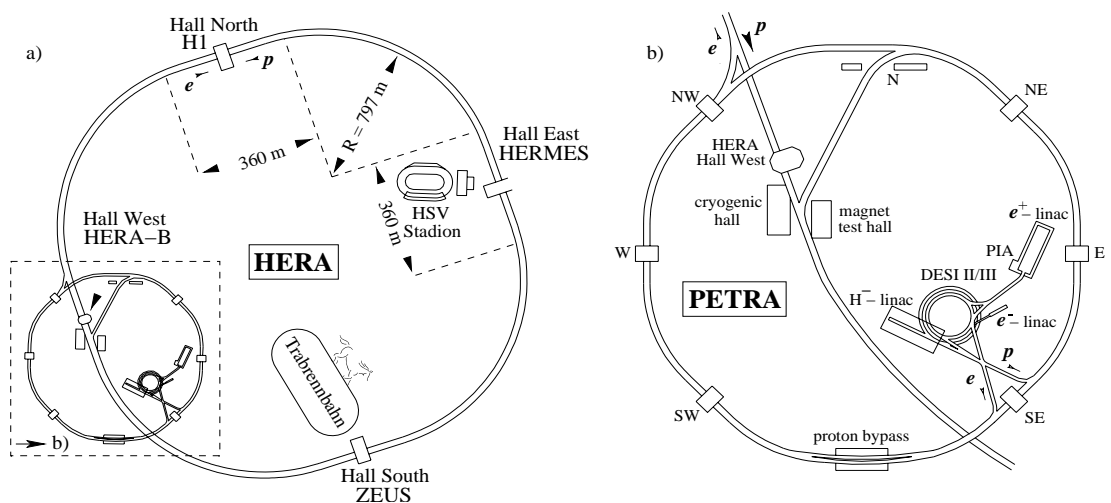


Figure 2.1: The geometry of the HERA collider a) and its pre-accelerators b).

At HERA there are two 4π detectors H1 and ZEUS situated in the North Hall and the South Hall, respectively. These two experiments are colliding beam experiments with the interaction region inside the detectors. The results from H1 and ZEUS, when

covering the same type of physics, can cross check one each other and, eventually, they can be combined to obtain the best possible precision. The other two experiments are using only one of the beams due to their fixed target design.

The HERA-B experiment made use of the proton beam halo from HERA. As fixed target, wires made of C , Ti or W were used to produce B -mesons. This experiment was designed to observe and to measure CP -violation in the decays of B -mesons, like $B \rightarrow J/\Psi + K^0$. The complex design delayed the experiment with respect to the B -factories. Very good data were taken just at the end of the running period.

The HERMES experiment, still running at this time, has the study of the spin structure of the nucleons as its special challenge. The beam used by HERMES is an unpolarised or a longitudinally polarised electron beam and as target different gases, polarised ones (H , D) or unpolarised ones (H , D , Ne , Kr , Xe) are used. To obtain longitudinally polarised electrons spin rotators are needed, which rotate the naturally transversally polarised electrons. The success of the spin rotators for HERMES insured their installation also for collider experiments during the luminosity upgrade of HERA.

The electrons or positrons and the protons are starting to be accelerated in the so-called pre-accelerators DESY II/III and PETRA before they are injected into the HERA storage ring. The two beams are further accelerated in the HERA ring until they reach their nominal values. The lepton beam at HERA has an energy value of 27.5 GeV. The energy of the proton beam was 820 GeV yielding a centre of mass energy of $\sqrt{s} \simeq 300$ GeV. The first luminosity was delivered in summer of 1992 using *electrons*. In August 1994 the electron beam was replaced by a positron beam. The switchback to electrons was done in 1998 until mid 1999. The energy of the proton beam was increased to 920 GeV in 1998 raising the centre of mass energy to $\sqrt{s} \simeq 318$ GeV. After new experience with electrons, positrons were used for the rest of 1999 and 2000 being a real success in delivered luminosity and data taking. After 2000 an ambitious upgrade of the collider and the experiments was undertaken to increase the delivered luminosity by a factor of three to four. After a difficult restart in 2002 with positrons, HERA returned to good running conditions at the end of 2003 and in 2004. From the fall of 2004 the electron beam was favoured and used also in 2005.

The design of the beams is to deliver up to 220 bunches with a bunch crossing interval of 96 ns, corresponding to a 10,4 MHz rate, the so-called HERA-*clock*. The bunches consist of about $10^{10} - 10^{11}$ particles. For background studies so-called pilot bunches, which are non-colliding bunches, are used. The life time of the electrons is about 6 hours and of the positrons 10 hours. The proton beam has a life time of at least one or two orders of magnitude larger.

The life of HERA consists of two parts, before and after the luminosity upgrade, with HERA I until the end of 2000 and HERA II starting from 2002.

2.2 The H1 Detector

The H1 detector is a 4π multi-purpose detector which was designed to measure the momenta of charged particles and energy in ep collisions. In order to have the best coverage in particle reconstruction of an ep event, the detector acceptance goes down close to the beam pipes. Since the energy of the electron and of the proton beam are substantially different, the design of the collider detectors is asymmetric as shown in Fig. 2.2. The centre of mass system is shifted in the proton direction due to the higher energy of the proton beam. The Liquid Argon (LAr) detector has therefore a higher

granularity in the proton beam direction than in the central region or in the electron beam direction.

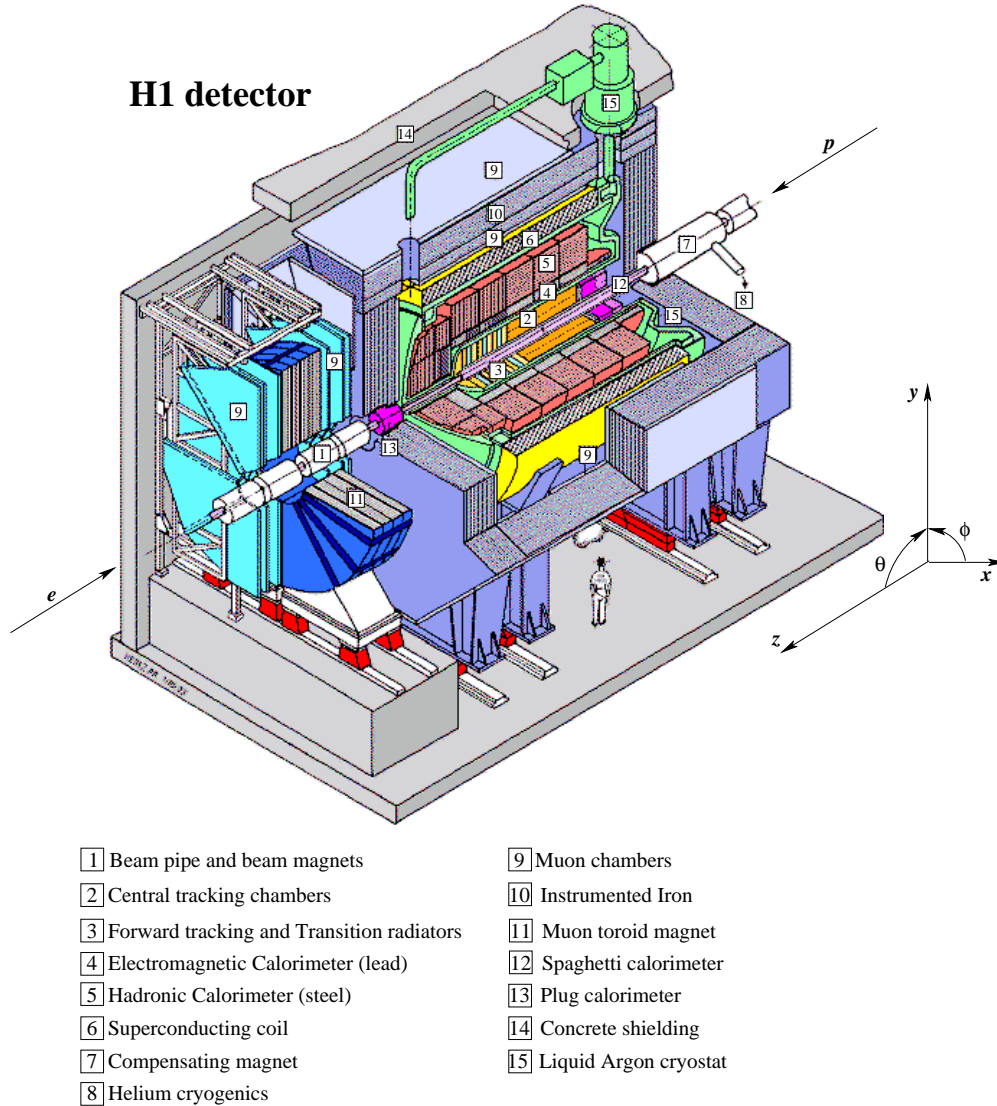


Figure 2.2: The H1 detector architecture.

The right-handed coordinate system of the H1 detector is oriented such that the proton direction corresponds to the z -axis and the y -axis is normal to the plane of the colliding beams as shown in the Fig 2.2. The origin of the H1 coordinate system is at the nominal interaction point. The region with $z > 0$ is called the *forward* region. The x -axis is oriented towards the centre of the HERA ring. The azimuthal angle ϕ is defined with respect to the x -axis in the xy -plane. The polar angle θ is the angle with respect to the z -axis. The *forward* region is defined also by $\theta \rightarrow 0^\circ$ and the *backward* one by $\theta \rightarrow 180^\circ$.

The H1 detector components are mounted around the beam axis. A super-conducting coil is used to produce the magnetic field needed for the momentum measurement. The tracking system and the LAr calorimeter are centred around the beam axis and inside

the super-conducting coil. The amount of dead material was minimised in order to have a proper calorimetric energy measurement.

A brief description of the H1 detector components follows starting from the inside.

The Silicon Tracker Detectors

The silicon tracker detectors are installed in the immediate vicinity of the beam pipe. The central silicon tracker (CST) [34] was implemented partially in 1996 and completed in 1997. The CST consists of two cylindrical layers of silicon sensors. The inner radius is 5.57 cm and the outer radius 9.7 cm and the total length of 44.2 cm. The CST covers the θ range $30^\circ \leq \theta \leq 150^\circ$. The inner layer is made out of 12 ladders arranged around the z axis. Each ladder consists of 6 silicon sensors in the z -direction with read-out electronics at both ends. The outer layer has 20 ladders.

A charged particle passing through the CST produces *electron – hole* pairs in the *pn* junction of the silicon detector. The electrons and the holes are drifted to the inner or outer side of the sensors due to the voltage applied between the two surfaces. On the surface of the sensors strips are mounted which are used to read-out the deposited charge. The strips are perpendicular to each other making possible the measurement of the $r\phi$ -coordinate as well as the z -coordinate. The resolution achieved in $r\phi$ is $\sigma_{r\phi} = 12 \mu\text{m}$. The z -resolution depends on the θ angle and reaches up to $\sigma_z = 22 \mu\text{m}$. A hit is determined taking into account the sensor position and the two measured coordinates. The CST hits are assigned to tracks and used to improve the track measurements in the central jet chamber. The CST is used also for the determination of the B -mesons secondary vertices. The background of the D^* -meson given by the secondary vertices tracks, which are classified on the base of the CST information, is reduced.

The choice of silicon strip detection was governed by the occurrence of deep inelastic events at low and high *Bjorken x*, which leave only the electron for detection as the hadronic flow is occurring either extremely forward or backward, respectively. In these events, contrary to the usual situation, the electron track alone determines the vertex position.

The backward silicon tracker (BST) [35] is measuring the tracks in the angular range of $162^\circ \leq \theta \leq 176^\circ$. The BST consists of eight planes of silicon detector discs with 16 wedge shaped four inch wafers per disc. Due to its coverage an approximate Q^2 range between 2 and 100 GeV^2 for the nominal vertex position can be measured. The BST has a strip detector part, with circular strips of 48 μm , and a pad detector part, with pads of about 1 cm^2 size. The strip detector measures the θ angle of the backward scattered particles.

The Tracking Detectors

The central tracking detector consist of two *central jet chambers* (CJC1 and CJC2), two central z *drift chambers*, the inner (CIZ) and the outer one (COZ), and two *proportional chambers*, an inner one (CIP) and an outer one (COP).

The jet chambers are measuring the momentum and the direction of the charged particles using the ionisation process in a certain gas mixture. The resolutions achieved are not as good as the ones from the silicon tracker detectors. The $r\phi$ -measurement resolution is $\sigma_{r\phi} = 170 \mu\text{m}$. The z -resolution is $\sigma_z = 22 \text{mm}$. The z -coordinate measurement is improved using the z -chamber information. A resolution of $\sigma_z = 260 \mu\text{m}$ is obtained for the CIZ and of $\sigma_z = 200 \mu\text{m}$ for the COZ. A more detailed description of the CJC and the complementary tracking chambers CIZ, COZ, CIP and

COP can be found in the Sec. 2.3.

For the measurement of tracks in the forward region, the forward tracking detector (FTD) is used. The FTD is made out of three so-called *super modules*. The modules are almost identical and consist of three *planar drift* chambers, a *forward multi-wire proportional* chamber (FWPC), a *transition radiator* and a *radial* chamber. The design of the FTD makes possible a coverage in θ of $7^\circ \leq \theta \leq 25^\circ$, with an $r\phi$ resolution of $\sigma_{r\phi} = 170 \mu\text{m}$. The goal of the FTD is to have a momentum resolution of $\sigma_p/p < 0.003$ and an angular track resolution of $\sigma_{\theta, \phi} < 1 \text{ mrad}$.

For this analysis, the FWPC component of the FTD is used. It consists of three layers of concentric cathodes separated by two layers of dense parallel wires and which are perpendicular to the beam line having an y orientation. The proportional chambers provide signals within less than $\sim 20 \text{ ns}$ making the FWPC a useful forward trigger device.

The backward drift chamber (BDC) is mounted in front of the "spaghetti" calorimeter (SpaCal). The BDC consists of eight octants, each octant having four double layers of drift chambers along the negative z -direction. The wires of the chambers are oriented perpendicular to the beam pipe such that the drift direction is almost radial. The double layers are rotated by 11.5° with respect to each other, making possible the measurement of the azimuthal angle ϕ . The purpose of the BDC detector is to provide an accurate θ and ϕ angles measurement of the scattered electron, as well as to discriminate between energy clusters in the electromagnetic part of the SpaCal due to electrons and photons. The angular coverage in θ is $155^\circ \leq \theta \leq 175^\circ$. The resolution of the BDC in the xy plane is $\sigma_{x,y} = 1 \text{ mm}$.

The Calorimeters

A liquid argon calorimeter (LAr) is surrounding the central and the forward tracking detectors. It is used to identify electrons, photons and muons, and to measure the energy depositions. The calorimeter consists of an inner electromagnetic part (EMC) and an outer hadronic part (HAC). The HAC covers the angular range $4^\circ \leq \theta \leq 135^\circ$ while EMC has an extended coverage in the backward direction up to $\theta \leq 153^\circ$. A detailed presentation of the LAr can be found in Sec. 2.4.

The plug calorimeter (PLUG) was designed to cover the gap of acceptance for the energy flow measurements between the forward part of the LAr and the beam pipe. The angular opening of the PLUG is $0.6^\circ \leq \theta \leq 4^\circ$. The PLUG information can be used to minimise the missing part of the total transverse momentum due to the hadrons emitted close to the beam pipe. The PLUG calorimeter consists of 9 copper absorber plates interleaved with 8 sensitive layers of detectors [37]. The PLUG is used for diffractive physics in order to veto events which have no rapidity gap.

The SpaCal consists of an electromagnetic and a hadronic section. The SpaCal covers the backward region, having a range in polar angle of $153^\circ \leq \theta \leq 177.5^\circ$. The main purpose of this calorimeter is to measure the energy and the angle of the scattered electron or positron. The SpaCal is discussed in more detail in Sec. 2.5.

The Solenoid

The superconducting solenoid produces an uniform and longitudinal magnetic field of 1.15 T in the H1 detector. It encapsulates the LAr and the tracker detectors.

The Muon System

The muon system is made of two subdetectors covering the central region (CMD) and the forward region (FMD). The CMD consists of limited streamer tubes (LST), which are installed in the slits of the iron return yoke of the solenoid. The goal of the CMD is to measure the penetrating tracks of the muons. The same technology is used by the tail catcher (TC) to measure hadronic energy leaking from the LAr and SpaCal. The CMD is divided into four regions: the forward and the backward barrel covering the range $33^\circ \leq \theta \leq 137^\circ$, and the forward and the backward end-cap with the angular acceptance of $6^\circ \leq \theta \leq 33^\circ$ and $137^\circ \leq \theta \leq 172^\circ$, respectively. Each of these parts of CMD is made of 16 modules. Each module consists of 10 iron plates with a thickness of 7.5 cm in the radial direction for the central barrel and in the z -direction for the end-cap region. In every slit of the iron, one layer of LST is located. Between the fourth and the fifth iron layer two LST layers are located. In front and behind the instrumented iron are installed muon boxes, each of them with 3 LST layers. These muon boxes are used to improve the muon track measurement.

The muon chambers are filled with a gas mixture of Ar/CO₂/CH₄ in proportion of 92.5/5/2.5. The momentum and the direction of the penetrating muons are measured via gas ionisation. The resolution of the position measurement given by the wires is up to $\sigma_{wire} = 3 - 4$ mm. The resolution for the strips hits is about $\sigma_{strip} = 10 - 15$ mm. The barrel polar angular resolution is $\sigma_\theta = 15$ mrad and for ϕ is $\sigma_\phi = 10$ mrad. The track segments found are fitted using a straight line, and the curvature is obtained connecting several track segments. The track reconstruction is completed including the strip information and taking into account energy losses of at least 80 MeV, and the fact that the magnetic field can vary.

The FMD is a spectrometer consisting of a toroid magnet between double layers of drift chambers at both sides. It covers an angular range of $3^\circ \leq \theta \leq 17^\circ$. For a 5 GeV momentum muon, the momentum resolution is about 24%, deteriorating to 36% for a 200 GeV muon.

The Time of Flight and the Veto System

The time of flight system (ToF) consists of scintillators located at both ends of the detector down to the beam pipe. These scintillators are used to reject the beam induced background in the H1 detector. There are several ToF counters. The forward ToF (FToF) is located at $z \approx 7$ m. The plug ToF (PToF) is installed in the PLUG region at $z \approx 5.3$ m. The backward ToF (BToF) is situated at $z \approx -3.3$ m.

The H1 detector has also a *veto-wall* system, the outer and the inner veto wall. The outer veto wall is installed at $z = -6.5$ m. The inner veto wall is located at $z = -8.1$ m. The area covered by the inner veto wall is the near beam area 110×90 cm² down to a radius of 11 cm. A background event is rejected if the event arrives out of time with respect to the bunch crossing or if the determined z -position of the ep interaction point is not in the allowed region.

The Luminosity System

The luminosity system is designed to measure the luminosity via the *Bethe-Heitler* process $ep \rightarrow ep\gamma$. The *Bethe-Heitler* process has a large and accurately calculable cross-section. The luminosity determined online is needed by the HERA machine group to steer the electron beam.

The luminosity system consists of the photon detector (PD) at $z = -103$ m and the electron tagger at $z = -33$ m (ET33). The ET33 measure the energy of the scattered electrons with $\theta \simeq 180^\circ$.

The instantaneous luminosity can be defined as:

$$L = \frac{R_{tot} - (I_{tot}/I_0)R_0}{\sigma_{vis, BH}}, \quad (2.1)$$

where R_{tot} is the total rate of bremsstrahlung events, and R_0 is the rate of bremsstrahlung events coming from the electron pilot bunches. The corresponding electron currents are I_{tot} and I_0 . The *Bethe-Heitler* cross-section, $\sigma_{vis, BH}$, is corrected with respect to acceptance and trigger efficiency.

The main source of background for the *Bethe-Heitler* process is the electron interaction with the residual gas in the beam pipe $eA \rightarrow eA\gamma$. An estimation of this background contribution can be obtained using the event rate from the electron pilot bunches. More about the luminosity measurement can be found in [38].

In the next section the H1 detector components which are primarily used in this analysis are presented. A more detailed description of the H1 detector can be found in [39] and of some of its components in [37].

2.3 The Central Jet Chambers

The central jet chambers are two coaxial cylinders situated along the beam axis and covering in the z -direction the range $-1.1 \text{ m} \leq z \leq 1.1 \text{ m}$. The chamber closest to the beam pipe is the CJC1, with an inner radius of 20.3 cm and an outer one of 45.1 cm. With these geometrical dimensions the CJC1 covers the θ range $11^\circ \leq \theta \leq 169^\circ$. The angular coverage of the outer chambers CJC2 is $26^\circ \leq \theta \leq 154^\circ$ due to its inner radius of 53.0 cm. The outer radius of the CJC2 is 84.4 cm. The CJC1 is filled with the gas mixture Ar/CO₂/CH₄ in proportion of 89.5/9.5/1. The CJC2 gas mixture is Ar/C₂H₆ in 50/50 proportion.

The structure of the CJC1 consists of 30 cells, each of them containing 24 sense wires. The CJC2 is made out of 60 cells with 32 sense wires each. The wires are parallel to the z direction and displaced in 24 radial layers in ϕ , as can be seen in Fig. 2.3. The drift field is formed using cathode wires which separate the sense wires in ϕ . The jet chambers have the wires arrangement such that the drift field and the gas amplification can be adjusted

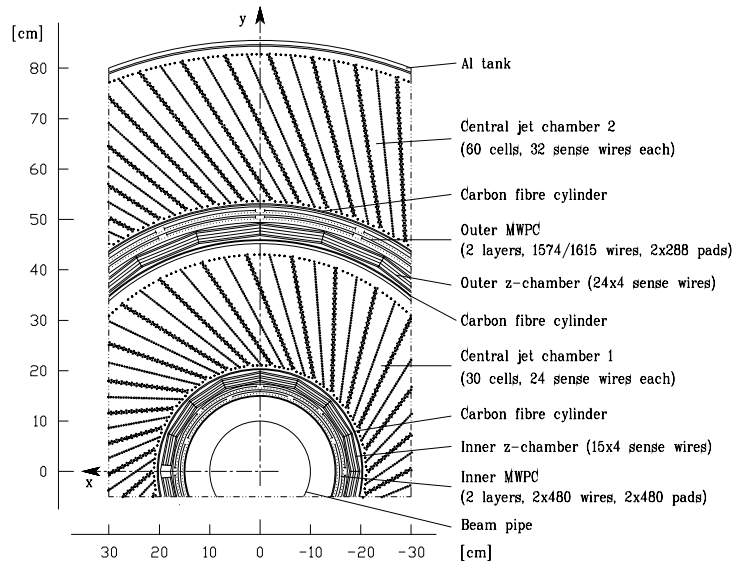


Figure 2.3: The (x, y) plane wire structure of the CJC .

almost independently. The cells of the jet chambers are tilted by 30° with respect to the radial direction. This tilt of the cells allows the charged particles passing through the CJC to cross a large amount of sensitive wires. In this way a large number of cells are hit and their information can be used for the track reconstruction. The more cells are used, the better the reconstruction is. Furthermore, one can avoid this way the drift chambers ambiguities, the so-called *mirror* tracks made out of mirror hits which connect wrongly track segments. Another advantage of the tilt is an almost full compensation of the angle between the electrical field and the electron drift direction given by the magnetic field, the so-called Lorentz angle.

The charged particles traversing the chamber ionise the gas molecules. The field between the cathode wires and the sense ones is almost uniform. The electrons drift velocity is approximately constant. Close to the anode wires the electric field is proportional to $1/r$, the electron at the distance r from the sense wire gains energy which is sufficient to produce secondary ionisations. The avalanche caused by the charged particle deposit the charge on the sense wires from where is measured and read out.

Every hit of such charged particle is determined using the drift distance and the z coordinate. The hits are assigned to tracks and a helix trajectory is fitted for each track, as it is described in Appendix C.

The drift chamber information about the energy loss per distance dE/dx can be determined from the total collected charge on a sense wire. The particle type can be found in terms of probability using the *Bethe-Bloch* formula [40] which gives the dependence of the velocity β with respect to the energy loss.

In order to improve the resolution in the z direction, two additional chambers are used. The inner (CIZ) and the outer (COZ) z chambers have their wire perpendicular to the z direction. The track momentum measurement is improved including the CIZ and COZ informations. An additional fit of the track is performed when the track elements of the z chambers are established.

Another two chambers are complementary to the main tracking system but do not influence the final track measurement. The inner (CIP) and the outer (COP) proportional chambers are used in combination with FWPC to provide a fast information about the z vertex position which is used in the level 1 of the trigger system. The wires of these chambers are parallel to the z axis. The two detectors consists of two pads layers delimited by three concentric cylinders. The two CIP chambers are tilted by $\pi/8$ in ϕ with respect to the COP ones, together giving a 16 segments ϕ structure.

2.4 The Liquid Argon Calorimeter

The main calorimeter of the H1 detector is the liquid argon calorimeter (LAr) [37]. By design the LAr was supposed to measure the scattered electrons in events with high Q^2 and to measure also the energy of jets in the final state. The LAr is one of the most stable components of the H1 detector which reached and maintained its designed performances. The coverage in the θ angle is of $4^\circ \leq \theta \leq 154^\circ$, which corresponds to an η range of $3.35 \geq \eta \geq -1.43$. In azimuthal angle the LAr is fully hermetic. The LAr consists of two parts: the electromagnetic calorimeter (EMC) and the hadronic calorimeter (HAC), which are contained within a single cryostat.

A longitudinal section of LAr can be seen in the Fig. 2.4 a). The LAr is located within the solenoid in order to reduce the amount of dead material that a particle has to pass through before it reaches the calorimeter. The LAr is made of 8 wheels in η ,

and each of them is divided in octants in ϕ , as one can see in Fig. 2.4 b). The most backward wheel has only an EMC.

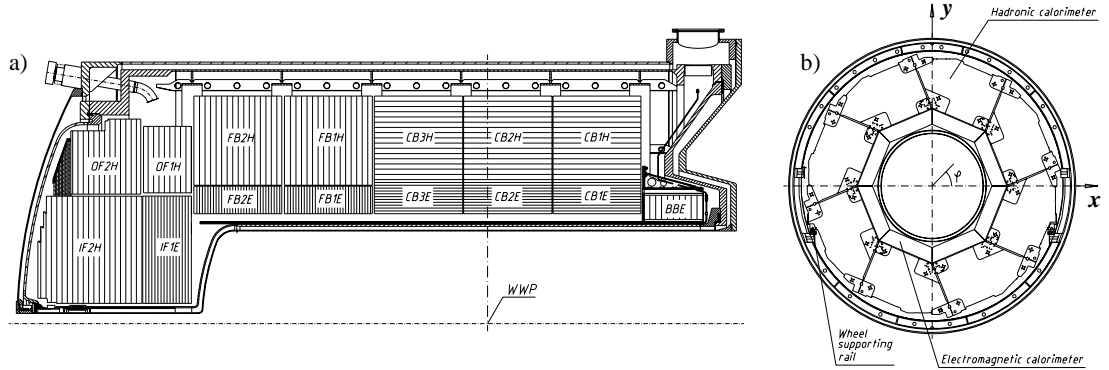


Figure 2.4: The Liquid Argon calorimeter; a) longitudinal and b) transversal section in the central region.

The LAr is a sampling calorimeter constructed from plates of absorber material separated by gaps filled by the sampling material, the liquid argon. A high voltage is applied across the gaps and the readout pads are grounded. A particle which passes through the calorimeter is producing a particle shower. The electromagnetic particles, electrons or photons, interact via the bremsstrahlung and pair production processes. Hadronic particles interact via elastic and inelastic scatterings with the nuclei of the material. The secondary particles which are produced are also interacting further, thus leading to a cascade process resulting in a shower of particles. The energy of the shower is sampled by the liquid argon. The argon atoms are ionised by the charged particles of the shower. The number of ions is proportional to the shower energy. The produced charge is collected at the electrodes and readout. The EMC is made from 2.4 mm thin lead plates with gaps between them of 2.35 mm thickness. The HAC has steel plates of 19 mm with gaps of 4.8 mm in between. The electrons and the photons lose almost all their energy in the layers of EMC, while the hadrons are absorbed in the thicker plates of the HAC.

The EMC has a total thickness which varies from 30 radiation lengths in the forward direction to 20 radiation lengths in the backward direction. The readout of the EMC includes 30784 channels and the HAC readout involves 13568 channels. The HAC has a total thickness of 8 interaction lengths in the forward direction and 5 interaction lengths in the central barrel. A very important achievement in the maintenance of the LAr is to keep the number of the noisy (dead) channels around the per mill level, 40-50 channels. The channels of the LAr are combined into 256 trigger towers. The summed energy of each tower is used by the LAr triggers. The LAr granularity is optimised to have an almost uniform segmentation in η and ϕ . This type of segmentation makes an easier noise reduction possible. The fine granularity is also used to distinguish between electrons and hadrons, i.e. based on their different shower shapes.

The LAr is non-compensating, the response to electromagnetic and hadronic particles is different. At the same particle energy, the deposited energy in the liquid argon is on average $\sim 30\%$ less from hadrons than from electrons. This energy of hadronic particles is lost due to nuclear excitations or break-up in the absorber. In order to compensate for this loss, the energy of the hadronic clusters is corrected during the reconstruction.

Beam tests at CERN and DESY [41] were done in order to measure the energy

collected at the cell end and readout by a single photomultiplier. The readout is done after the scintillation light is mixed using an acrylic light mixer. Eight 2 cell modules are grouped together to a 16 cell module as can be seen in Fig. 2.5 b). The orientation of the 2 cell modules within the 16 cell one is done such that the channeling effect is minimised. The channeling effect shows the degradation of the energy resolution, which occurs when the fibers or the lead sheets are aligned with the particle trajectory.

The HAD part of the SpaCal has cells of the size $119.3 \times 119.3 \text{ mm}^2$. They are made of 65 lead plates, each with 54 fibers. The EM and the HAD parts have an active length of 25 cm each. This active length corresponds to 27.8 radiation lengths for the EM and 29.4 for the HAD part of the calorimeter.

Test beam measurements performed at CERN and at DESY [43] concluded that the energy resolution of the EM section of the SpaCal is for electrons:

$$\frac{\sigma_E}{E} = \frac{(7.1 \pm 0.2)\%}{\sqrt{E/\text{GeV}}} \oplus (1.0 \pm 0.1)\%. \quad (2.4)$$

From the SpaCal operation in the H1 detector studies of the energy spectrum of the scattered electron showed at the kinematic peak (27.5 GeV electrons) an energy resolution of 1% and for scattered electrons of 7 GeV a resolution of 2.5%.

For the HAD part of the SpaCal the hadronic energy resolution is:

$$\frac{\sigma_E}{E} = \frac{(56.0 \pm 3.0)\%}{\sqrt{E/\text{GeV}}} \oplus 7\%. \quad (2.5)$$

The good resolutions in energy and polar angle of the scattered lepton are fundamental for a precise measurement of Q^2 and y using the electron method described in Chapter 3. The fine granularity of the EM section gives a polar angle resolution of $\sigma_\theta = 2 \text{ mrad}$.

2.6 The H1 Trigger System

The electron and proton bunches are colliding every 96 ns at HERA which corresponds to a frequency of 10.4 MHz. From the crossing bunches only a small amount out of $\sim 100 \text{ kHz}$ gives an ep reaction. One frequent problem in a collider experiment is that the background processes have a rate several orders of magnitude higher than the ep events of interest. One can identify as a main source of background the collisions of the beam protons with the rest gas atoms within the beam pipe, the so-called *beam-gas background*. Another source of background is coming from the off-orbit protons that hit the accelerator or the detector components producing *beam-wall background* events. In addition to these major contributions, cosmic muons and synchrotron radiation make the background rate higher.

The short time interval of only 96 ns between two bunch crossings makes the readout of the whole detector information for each bunch crossing not possible. It would make the dead time too high. In order to minimise the dead time, a trigger system is used. The trigger system needs to take a decision whether an event is of interest to be readout in the shortest possible time. The trigger system needs to be highly efficient in discriminating interesting ep events from background or to be able to reduce the rate of the events which have a too high rate.

The H1 trigger system has a four level structure as can be seen in Fig. 2.6. The input rate is about 100 kHz at the first level (L1) and is reduced to 50 Hz at the fourth

level (L4). The amount of time available for a decision to be taken increases from 2.4 μs on L1 to 100 ms on L4.

Level One Trigger - L1

The detector information of every bunch crossing is stored in buffers, the so-called pipeline, due to the time needed to have trigger information available from all detector components. The storage of the detector information in the pipeline avoids dead time until L1 decision is made.

The length of the pipeline is 2.4 μs (25 bunch crossings), thus giving the time limit for a L1 decision. In case of a decision to keep the event, the pipeline is stopped and the dead time starts. The L1 decision is mainly given by certain trigger signals of the detector components, the so-called trigger elements (TE). There are 208 TE used out of 256 available possibilities. The TE are logically combined into 128 subtriggers (ST). If at least one of the ST accepts an event, then the trigger decision is positive. Depending on the background conditions, a ST can be *prescaled* in order to get an acceptable rate. A *prescale* factor n would mean that only every n^{th} event that gives a positive trigger decision is accepted by L1. The first trigger level reduces the rate from 100 kHz to 1 kHz, the input rate for the next trigger level.

Level Two Trigger - L2

If the L1 decision is positive, the event passes to the second level of the trigger system (L2). L2 makes use of two systems, the neural networks (L2NN) and the topological triggers (L2TT), in order to reduce the rate. The time for a L2 decision is 20 μs . If L2 gives a negative decision, the readout is stopped and the L1 pipelines are cleared and can again store detector signals. If a L2 positive decision is taken, the detector read out starts. From the 1 kHz input rate L2 reduces the rate to 50 Hz. The third trigger level (L3), where more detector information can be used to perform a decision, was not implemented.

Level Four Trigger - L4

At L4 a computer farm is used to perform a full event reconstruction. The purpose of L4 is to verify if the events are of interest for physics or not, to provide monitoring of ST's and to perform calibrations of the detector components. Until 1997, this veri-

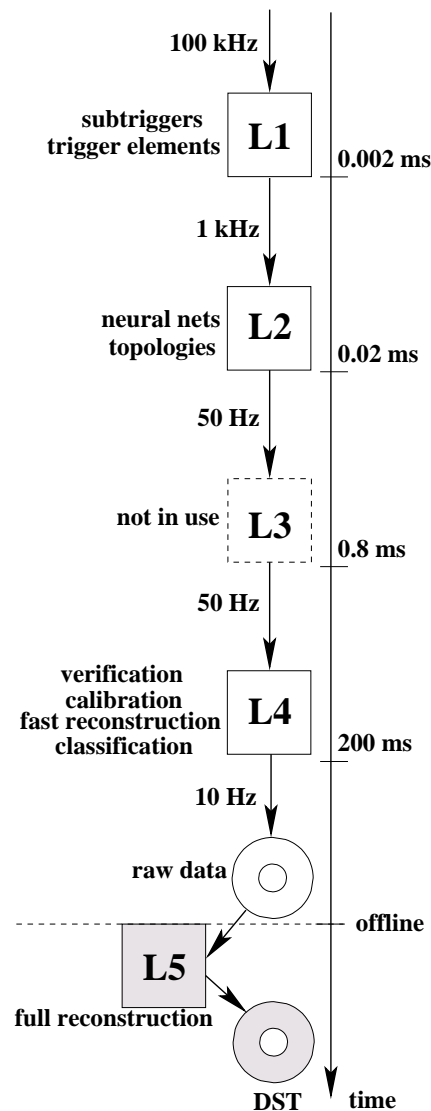


Figure 2.6: The H1 Trigger System.

fication was similar to the L1 subtriggers conditions. From 1997, L4 has implemented finder algorithms to trigger on specific physics processes of interest. There are also events which are recorded without L4 verification, e.g. events with a high transverse momentum track or a high energy cluster in LAr. The largest amount of events are verified. The so-called *open heavy flavour* finder reconstructs D -mesons and so called wrong charged background events. In 1998 the finder conditions were made harder, and the events had to be attributed to a class. If an event on L4 is assigned to a physics class, like class 15 for D -mesons, then it is accepted by L4 without a prescale. In case of a prescale, an L4 weight is attributed to the event.

The Offline Reconstruction

The last level (L5) is used to perform a complete offline reconstruction on the accepted L4 events using the H1REC package and the final calibration. This level was classifying the events in classes until 1998. The events with a D^* -mesons candidate were assigned to the class 16. The events were stored on tape, the physics output tape (POT), only if they were belonging to at least one class. This reduced the rate by a factor of 2. The data used in this analysis are stored in a compressed way on disk, the data summary tape (DST). From 1998, the classification was already done on L4 and no event was rejected any longer on L5.

Chapter 3

Event Selection

The analysis presented here follows two directions in the study of the charm jets. A charm jet is defined here as the jet found in an event which has a reconstructed D^* -meson within its particle content. This is called the D^* Jet. If additional jets are reconstructed in an event, the one with highest E_T is called the *OtherJet*¹. It has a high probability to contain the "second" charm quark.

One of the study's directions is more traditional. It makes use of the well known jet shape observables. Nevertheless, new definitions of the D^* Jet and of the concentric jet energy fraction, as described in the Chapter 4, are also introduced.

The second direction of the analysis is more innovative. Here the jet structure is investigated using the angle between the jet direction, which approximates the heavy quark direction, and the direction of a subjet found within this jet, which approximates the direction of a soft gluon radiated by the heavy quark. The distribution of this angle, called the *soft gluon angle*, in bins of the jet energy, is fitted. From the fit parameters another characteristic angle, called the *dead cone angle* α_0 , is obtained. The angle α_0 multiplied by the energy of the quark jet is a measure of the quark mass as predicted by the theory, see Sec. 5.3.1.

The experimental data used in the study of the jet shape observables were taken with the H1 detector at the HERA collider during the HERA I periods: 1999 (e^+) and 2000 (e^+), with an integrated luminosity of 50 pb^{-1} . For the study of the *dead cone effect*, the data taken in 1996 (e^+), 1997 (e^+), 1999 (e^-) of HERA I and 2003 and 2004 (e^+) of HERA II are also used in order to reduce the statistical errors.

The event selection used for the 1999 (e^+) and 2000 (e^+) data sample is presented in this chapter. The differences in selection for the other years are presented in Sec. 5.3.7. The selection is based on requirements for the DIS regime and for the reconstructed D^* -mesons. Charm events are defined by containing a reconstructed D^* -mesons candidate. For different checks used in the *dead cone effect* study also a *2Jet* sample, with charm content suppressed, is obtained, which is regarded as a light flavour event sample due to its content of light quarks of 70 – 80% according to MC simulation. The selection principles and the cuts are described in Sec. 5.3.6.

3.1 Charm Events Tagged with a D^* -meson

The principle of charm quark tagging using a D^* -meson is presented in Fig. 3.1. The second charm can be tagged using the *OtherJet* but with a lower efficiency. The

¹The jets used in this analysis are massless, thus $E_{T, \text{Jet}} = p_{T, \text{Jet}}$.

probability to have a gluon which forms the *OtherJet* (at the hadron level) increases with the η of the *OtherJet*.

For the D^* -meson² reconstruction the following decay channel is used:

$$D^{*+} \rightarrow D^0 \pi^+ \rightarrow K^- \pi^+ \pi_s^+ \quad (3.1)$$

The MC studies presented in Sec. 4.2 show that the charm quarks which are tagged by these D^* -mesons are very well approximated in energy and in the (η, ϕ) plane by the D^* Jet. Even though the branching ratio of this decay channel is very small, the small combinatorial background of the D^* -meson reconstruction, using the good mass resolution obtained with the Δm - technique (see Sec. 3.3.5), is favouring this choice.

The D^* -meson has a mass of

$$m_{D^*} = 2010.0 \pm 0.5 \text{ MeV} \quad [46] \quad (3.2)$$

and is made out of a charm quark and a down antiquark in the positive charged state D^{*+} , or of a charm antiquark and a down quark in the negative charged state D^{*-} .

The probability that a charm quark fragments into a D^* -meson is [47]:

$$P(c \rightarrow D^* X) = 0.235 \pm 0.007 \pm 0.007. \quad (3.3)$$

In the decay channel used in this analysis, see Fig. 3.2, the D^* -meson decays via the strong interaction into a D^0 -meson and a charged pion with a branching ratio of [46]:

$$BR(D^{*+} \rightarrow D^0 \pi^+) = 67.7 \pm 0.5 \%. \quad (3.4)$$

The life time of the D^* -mesons is of the order of $10^{-23} - 10^{-24}$ s due to the decay via the strong interaction decay. Within the H1 detector, these decay vertices cannot be separated.

The D^0 -meson mass is

$$m_{D^0} = 1864.6 \pm 0.5 \text{ MeV}. \quad (3.5)$$

The decay of a D^* -meson into a D^0 -meson offers a big advantage in achieving a good signal to background ratio due to the small mass difference between the D^* and D^0 -meson:

$$\Delta M = m_{D^*} - m_{D^0} = 145.42 \pm 0.01 \text{ MeV}, \quad (3.6)$$

² D^* refers to both D^{*+} and D^{*-} states. For the D^{*-} -meson the conjugate decay channel is used.

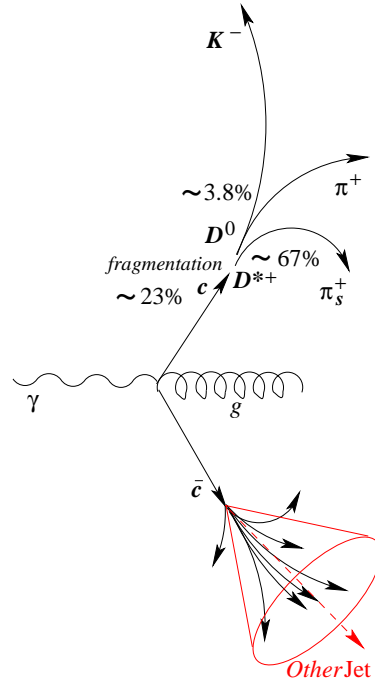


Figure 3.1: The charm quark tagging with a D^* -meson.

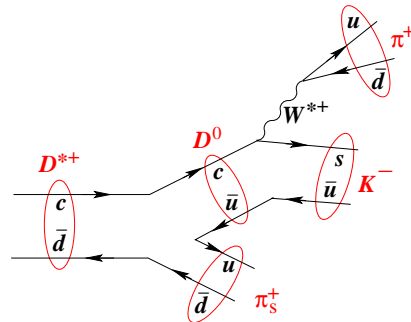


Figure 3.2: The D^* -meson decay channel used in this analysis.

which is only slightly larger than the pion mass $m_\pi = 139.57 \pm 0.00$ MeV, restricting this way the phase space for the decay into D^0 -mesons. A better reconstruction of the mass difference ΔM in comparison with the individual masses of the D^* and D^0 -meson is achieved [48]. The charged pion of the $D^* \rightarrow D^0\pi_s$ decay is named *slow pion*, π_s , due to its small kinetic energy.

The D^0 -meson decays via the weak interaction into a kaon and additional particles. The charm quark transforms into a strange quark via the radiation of a charged W boson. Since the smallest combinatorial background is given by the minimum number of decay products, in this analysis the decay $D^0 \rightarrow K^-\pi^+$ is used. This decay channel has a branching ratio of:

$$BR(D^0 \rightarrow K^-\pi^+) = 3.83 \pm 0.09 \%. \quad (3.7)$$

The overall branching ratio of the decay channel $D^{*+} \rightarrow K^-\pi^+\pi_s$ is:

$$BR(D^* \rightarrow K^-\pi^+\pi_s^+) = BR(D^* \rightarrow D^0\pi_s) \cdot BR(D^0 \rightarrow K^-\pi^+) = 2.59 \pm 0.06 \%. \quad (3.8)$$

As it can be seen in Fig. 3.1, one charm can be tagged using the D^* -meson and the second by the *OtherJet*. The reconstruction of the second charm using the *OtherJet* is not so efficient as the one with the D^* -meson.

3.2 The Online Selection

This analysis has two selection levels: an *online selection*, where efficient H1 detector components, triggers and stable beam conditions are needed, and an *offline selection*, where the track reconstruction and background reduction is performed in more detail.

3.2.1 The General Event Selection

The event selection is based on a good *run* selection. A *run* is defined as the collection of a sequence of events over a time period with relatively stable beam, detector and trigger conditions. The run selection performed in this analysis takes into account the following factors which lead to data sample with very good quality.

The first requirement of a good run is that the beam and the magnet parameters are stable and in the appropriate range. The energy of the electron beam should fulfill the condition $E_e = 27.5 \pm 0.5$ GeV, the proton beam energy $E_p = 920 \pm 5$ GeV and the magnetic field $B = 1.15 \pm 0.05$ T.

The second factor of importance is the *trigger phase*, which has to be larger than 1 and less than 5. Values in this range denote good background conditions, which allow to have the CJC1 and the CJC2 High Voltage (HV) turned on, and the H1 detector status, the trigger system and the beam conditions are optimal for data taking. Larger values of the trigger phase are used for dedicated studies of the detector, e.g. phase 12 means that the trigger settings are tuned for cosmic runs.

The next condition is that the events are produced by the *colliding* bunches and not by the *satellite* ones.

A *quality* factor is attributed to every run. The levels of the *run quality* are poor, medium, good and unknown. Only runs with medium and good quality are accepted. The quality is determined mainly online taking into account the type and the number of operational detector components during the run time.

This analysis makes use of the following detector components: the jet chambers CJC1 and CJC2, the proportional chambers CIP and COP, the z -chambers CIZ and COZ, the silicon tracker CST, the calorimeters LAr, SpaCal, the drift chamber BDC, and the ToF and the Veto systems. They have to be operational and included in the readout. In addition, it is required also for the FWPC and the luminosity system (Lumi) to be operational.

Another important factor is the position of the *primary vertex*, the ep collision point in the z -direction, the so-called z -vertex. Due to the satellite bunches from the electron and proton beam, an important source of background is the overlap with the ep events. In order to suppress background events from interactions of nominal with satellite bunches, the z -vertex position has to be less than 35 cm away from the nominal interaction point in both directions.

From the events passed so far, only the ones triggered by subtrigger 61 (ST61) on L1 and L4 of the trigger system are selected. If the ST61 conditions are fulfilled, the event is stored.

The luminosity of the event sample used in this analysis is about 50 pb^{-1} .

3.2.2 The Subtrigger Description

The L1 dedicated subtrigger for the D^* -meson analysis in the DIS regime is the ST61. The ST61 decision is based on the information delivered by several essential detector components in form of trigger elements (TE). The logical structure of ST61 on L1 in terms of TEs for the 1999 and 2000 (e^+) data taking periods was the following³:

```
(DCRPh_THig && zVtx_sig && (SPCLe_IET > 2 || SPCLe_IET_Cen_3))
&& (! SPCLh_AToF_E_1 && ! SPCLh_ToF_E_2 && ! VETO_inner_BG &&
VETO_Outer_BG && ! VLQToF_BG)
&& (! (DCRPh_NL_many && DCRPh_NH_many && DCRPh_PL_many &&
DCRPh_PH_many))
&& ((FToF_IA || FIT_IA) || (! FToF_BG && ! FIT_BG))
```

The ST61 can be split into two main parts. The first part:

```
(DCRPh_THig && zVtx_sig && (SPCLe_IET > 2 || SPCLe_IET_Cen_3))
```

is the one which selects events with high momentum tracks – **DCRPh_THig**, a good z -vertex position – **zVtx_sig**, and a scattered electron candidate above a certain energy threshold, selected with **SPCLe_IET**. The second part contains veto conditions which reduce the number of background events that might fake the events with a D^* -meson in DIS.

The **DCRPh** trigger makes use of the CJC information. Out of the 56 wire layers in total, the signals from 10 layers, 7 from CJC1 and 3 from CJC2, are digitised and used by the trigger. The drift time information from them is compared with predefined masks in the (r, ϕ) plane. Tracks are classified according to two momentum ranges, a low p_T range $400 < p_T < 800 \text{ MeV}$ and a high p_T one with $p_T > 800 \text{ MeV}$. Information about the track charge is also obtained and used by the trigger. The **DCRPh** trigger elements are shown in Table. 3.1.

³The signs "&&", "||" and "!" are logical operators in C++.

ST61 requires at least one high momentum track using the **DCRPh_THig** TE. In addition, a veto condition is obtained by combining the following TEs:

(! (**DCRPh_NL_many** && **DCRPh_NH_many** && **DCRPh_PL_many** && **DCRPh_PH_many**)).

This veto condition makes sure that events with a too high multiplicity of positive (P), negative (N) tracks of low (L) and of high momentum (H), which are coming from non *ep* events are rejected.

DCRPh TE	DCRPh trigger condition
DCRPh_T0	at least one validated t0 mask fired
DCRPh-Ta	at least one mask fired
DCRPh-Tb	at least b (=2) masks fired (b programmable)
DCRPh-Tc	at least c (=3) masks fired (c programmable)
DCRPh_TPos	at least x (=1) positive masks
DCRPh_TNeg	at least x (=1) negative masks
DCRPh_THig	at least x (=1) $p_T > 800$ MeV masks
DCRPh_TLow	at least x (=1) $400 < p_T < 800$ MeV
DCRPh_NL_many	at least 20 negative low momentum track candidates
DCRPh_NH_many	at least 20 negative high momentum track candidates
DCRPh_PL_many	at least 20 positive low momentum track candidates
DCRPh_PH_many	at least 20 positive high momentum track candidates

Table 3.1: The **DCRPh** trigger elements and their conditions.

The TE **zVtx_sig** information is provided by the **zVtx** trigger subsystem, see Table. 3.2.

zVtx TE	zVtx trigger condition
zVtx_T0	At least one ray (<i>track</i>)
zVtx_T0_nextbc	At least one ray in the next Bunch Crossing
zVtx_mul	coding number of entries in the <i>z</i> vertex histogram
zVtx_Cls	all histogram entries within 4 neighbouring bins
zVtx_sig	histogram peak significance: = 0 : no significant peak > 0 : significant peak in the <i>z</i> -vertex histogram found

Table 3.2: The **zVtx** trigger elements and their conditions.

The **zVtx** trigger combines information from the CIP, COP and the first two layers of the FWPC. The time resolution of these proportional chambers ($\simeq 20$ ns) allows identification of the bunch crossing to which an event belongs to. All possible *tracks* from the combination of 2×2 signals are reconstructed by the **zVtx** trigger. In addition, these tracks need to have $p_T > 150$ MeV in order to cross the CIP and COP or the CIP and FWPC. The intersections of these reconstructed *tracks* with the *z*-axis are filled into a histogram as indicated in Fig. 3.3. Real tracks will all intersect the *z*-axis around a common vertex position. The wrong combinations will lead to randomly distributed entries in the histogram. The **zVtx_sig** value will be larger than 0, if a bin within the indicated range values contains significantly more entries than

the average of the other bins. The event then fulfills the TE condition. With this TE proton induced background (beam halo) can be reduced.

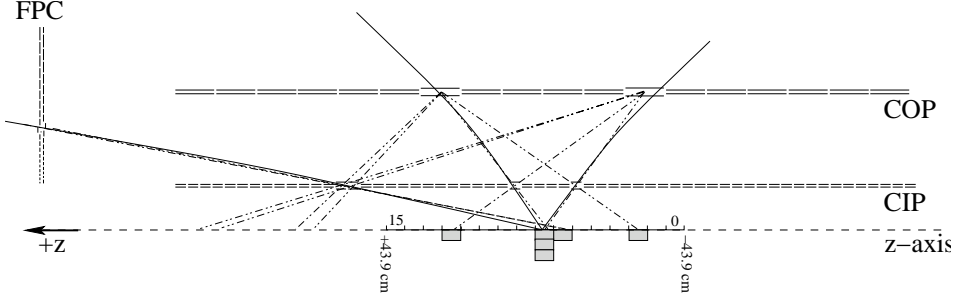


Figure 3.3: Sketch of the online determination of the $zVtx_sig$ trigger element.

The first step in having a scattered electron in the event makes use of the SpaCal inclusive electron trigger system (IET). The IET starts by finding all energy cluster. Energies deposited in 4×4 electromagnetic cells, which are combined to trigger tower (TT), are summed. The energy of a TT is compared with three different thresholds, which can be set by the trigger software, and the result of this comparison is stored in three cluster bits of each TT. The 320 TTs are overlapping in size in the x and the y -direction to avoid trigger inefficiencies due to TT edge effects concerning the impact point of the scattered electron. TE are formed for the inner (IET_Cen, $R < 16$ cm) and the outer (IET, $R > 16$ cm) region of the SpaCal. The definitions of the SpaCal TEs important for this analysis are given in Table. 3.3.

SPCL(IET) TE	SPCL(IET) trigger condition
SPCLe_IET_Cen_1	cluster in central region of the SpaCal with $E > 0.5$ GeV
SPCLe_IET_Cen_2	cluster in central region of the SpaCal with $E > 2$ GeV
SPCLe_IET_Cen_3	cluster in central region of the SpaCal with $E > 6$ GeV
SPCLe_IET	> 0: cluster SpaCal with $E > 0.5$ GeV > 1: cluster in SpaCal with $E > 2$ GeV > 2: cluster in SpaCal with $E > 6$ GeV
SPCLh_AToF_E_1	energy cluster in hadronic Spacal
SPCLh_ToF_E_2	sum of the energy in hadronic Spacal

Table 3.3: The **SPCL(IET)** trigger elements and their conditions.

ST61 uses the following TEs combination: (**SPCLe_IET > 2 || SPCLe_IET_Cen_3**), which requires the scattered electron candidate to have an energy of at least 6 GeV in the outer or the inner region of the SpaCal.

The energy deposition in the SpaCal HAD is used as a veto condition with the TEs:

$$(! \text{ SPCLh_AToF_E_1} \ \&\& \ ! \ \text{SPCLh_ToF_E_2}),$$

where the hadronic energy of the electron candidate cluster (AToF) is more than 0.6 GeV and the sum of all energies in HAD is above 12 GeV. This condition makes sure that the scattered electron is not faked by a hadron.

Informations from the **ToF** and **VETO** systems are also used as veto conditions. The TEs of these systems needed for ST61 are listed in Table. 3.4 and Table. 3.5.

VETO TE	VETO trigger condition
VETO_inner_BG	Inner Veto Wall, p related background timing
VETO_Outer_BG	Outer Veto Wall, p related background timing

Table 3.4: The **VETO** trigger elements and their conditions.

ToF TE	ToF trigger condition
FIT_IA	Forward Interaction Timing hit in proton time window (p)
FIT_BG	F.I.T. hit background or late p-satellite time window ($!p$ & $!e$)
FToF_IA	Forward ToF hit in main proton time window (p)
FToF_BG	Forward ToF hit in late satellite time window ($!p$ & $!e$)
VLQToF_BG	VLQ ToF hit proton time window (p)

Table 3.5: The **ToF** trigger elements and their conditions.

The TEs indicated with ”_BG” are set when a subdetector answer is arriving outside the ep interaction time window. The ones with ”_IA” termination are indicating that the answers of the subdetectors are within the interaction time window.

3.2.3 The ST61 Efficiency

It is important for this analysis that ST61 has a high efficiency and that it is well described by the MC simulation. The physics model used for the MC simulation was RAPGAP. The efficiency of a ST is checked using a second ST as monitor which is independent of the one used in the analysis. Generic, the efficiency can be written as:

$$\epsilon_{ST} = \frac{N_{Trigger}}{N_{Analysed}} = \frac{N_{Trigger}}{N_{Trigger} + N_{!Trigger}}. \quad (3.9)$$

$N_{Analysed}$ is the number of events selected by the analysis chain when instead of ST61 a monitor ST is used. From these, the number of events triggered by the ST61 is given by $N_{Trigger}$. The error of the efficiency determination is calculated using the formula [49]:

$$\left(\frac{\sigma(\epsilon)}{\epsilon}\right)^2 = \left(\frac{\sigma(N_{Analysed})}{N_{Analysed}}\right)^2 + (1 - 2\epsilon) \left(\frac{\sigma(N_{Trigger})}{N_{Trigger}}\right)^2, \quad (3.10)$$

which includes the correlations between $N_{Analysed}$ and $N_{Trigger}$.

As it can be seen in Sec. 3.2.2, ST61 consists of various TEs. In order to find a ST monitor independent of ST61, one has to make sure that the TEs used by the two STs are also independent. Unfortunately, there is no ST completely independent of the TEs from the ST61. Due to this the TE efficiency is calculated. For a TE one can easily find a ST which is independent of it.

The algorithm used in the TE efficiency calculation is the following: in data, for every TE an independent ST monitor is chosen. The analysis is performed once more, but this time triggering the events with the chosen monitor ST. The $N_{Analysed}$ is as before the number of the events that pass the analysis chain and are triggered by the monitor ST. From these events, the $N_{Trigger}$ would be the number of events in which

the TE was on – its condition was fulfilled. The ratio of these two numbers will give the TE efficiency.

In the next paragraphs the efficiency of ST61 TEs is presented. The bins used in the $E_{D^* \text{Jet}}$ distribution are used afterwards in the analysis.

The SPCLe_IET Efficiency

The TEs from ST61 given by the SPCLe_IET are used in the combination:

$$(\text{SPCLe_IET} > 2 \parallel \text{SPCLe_IET_Cen_3}).$$

A ST that is independent is ST9 which uses the TE combination:

$$(\text{SPCLe_IET} > 1) \ \&\& \ (\text{!SPCLh_AToF_E_1} \ \&\& \ \text{!SPCLh_ToF_E_2} \ \dots)$$

and continues with other VETO and zVtx TEs. The SPCLe_IET > 1 condition is requiring that the energy deposition in SpaCal is larger than 2 GeV.

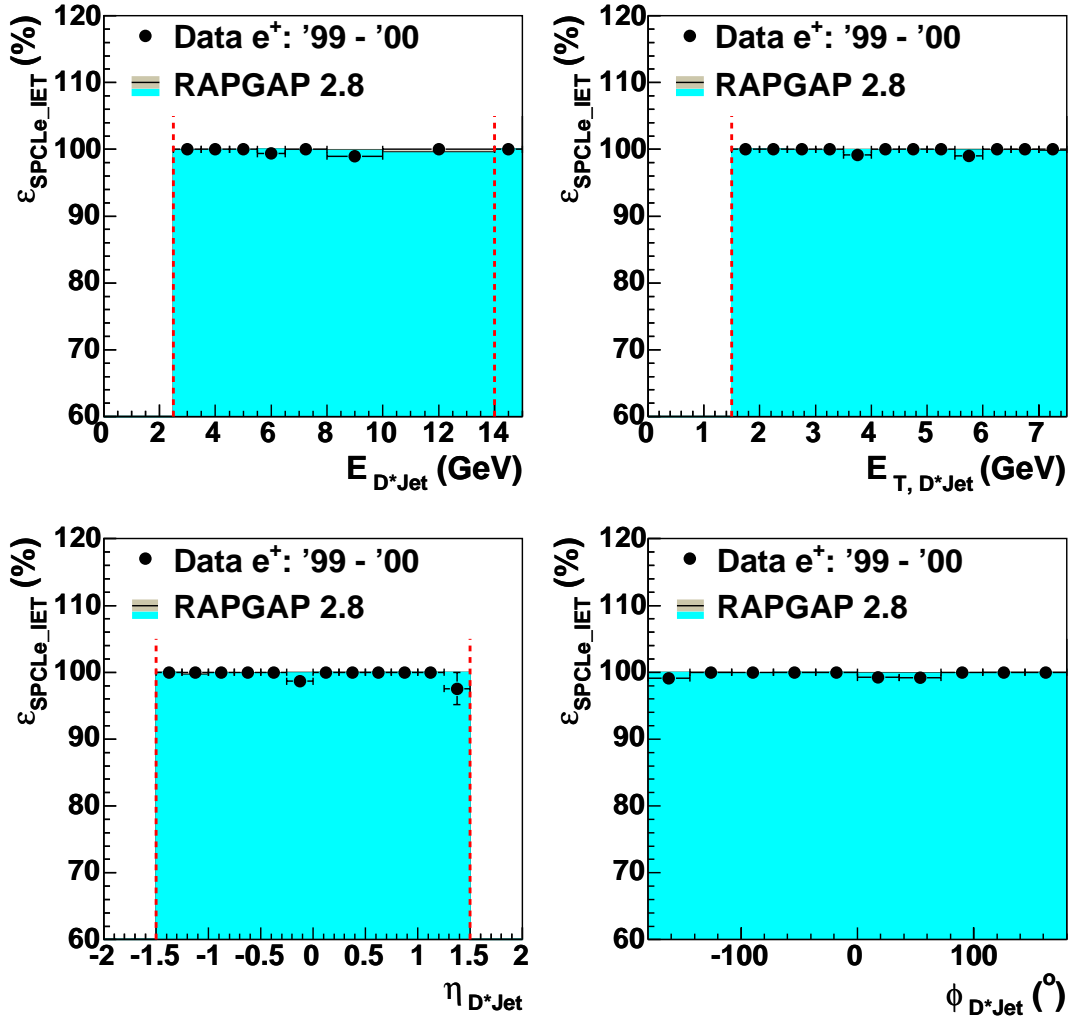


Figure 3.4: The SPCLe_IET efficiency for the $D^* \text{Jet}$ measurements. The errors are the statistical ones.

This TE can be considered independent, in a first approximation, of the combination used in ST61, which accepts only energy depositions above 6 GeV. The efficiency of the SPCLe trigger elements from ST61, relevant for this analysis, is shown in Fig. 3.4 for the $E_{D^* \text{Jet}}$, E_T , $D^* \text{Jet}$, $\eta_{D^* \text{Jet}}$ and $\phi_{D^* \text{Jet}}$. Good agreement with the MC model can be observed.

The efficiencies for the control variables such as Q_e^2 , y_e , E'_e , θ_e , p_T , D^* and η_{D^*} can be found in the Appendix D.

The DCRPh_THig Efficiency

The ST monitor independent of **DCRPh_THig** is ST0. The ST0 composition as the follows:

$$\begin{aligned}
 & (\text{SPCLe_IET} > 2) \ \&\& \ (\ !\text{VETO_inner_BG} \ \&\& \ !\text{VETO_Outer_BG} \ \&\& \ !\text{VLQToF_BG}) \\
 & \&\& \ (((\text{FToF_IA} \ || \ \text{FIT_IA}) \ || \ (\! \text{FToF_BG} \ \&\& \ !\text{FIT_BG})) \ \&\& \ (\text{PToF_IA} \ || \ !\text{PToF_IA})).
 \end{aligned}$$

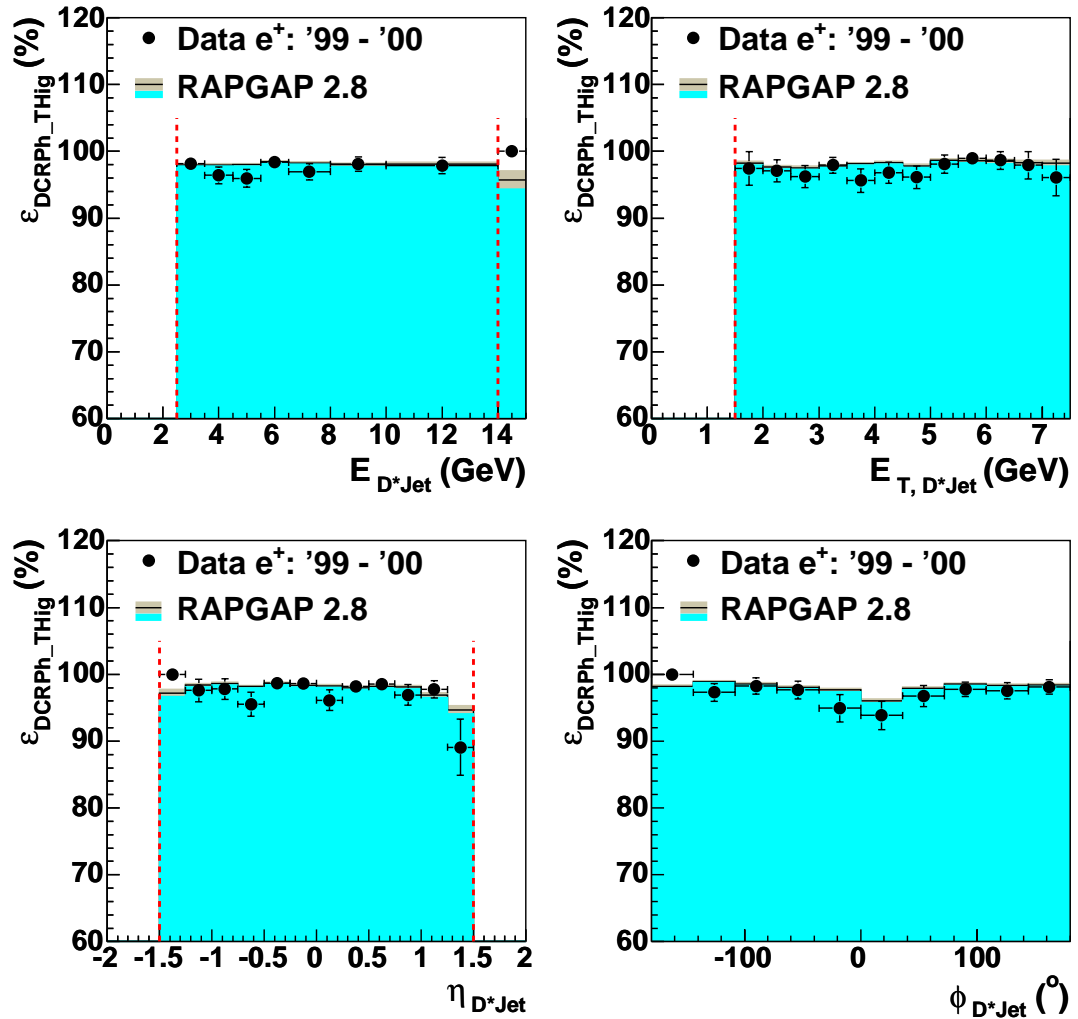


Figure 3.5: The **DCRPh_THig** efficiency for the $D^* \text{Jet}$ measurements. The errors are the statistical ones.

One can observe that no TE of the **DCRPh** trigger subsystem is used. The efficiency of the **DCRPh_THig** is presented in Fig. 3.5, for the control observables see Appendix D.

The $zVtx_sig$ Efficiency

As it can be seen from the previous discussion of the **DCRPhi_THig**, ST0 is also independent of $zVtx_sig$. Therefore, ST0 can again be used as monitor trigger. The efficiency of $zVtx_sig$ is shown in Fig. 3.6. The ϕ_{D^*Jet} distribution shows a systematic shift from -180° to 40° of $\sim 4\%$ between the MC model and the data. The same shift can be observed for the ϕ_{D^*} distribution. In Appendix D the efficiency plots in bins of the control observables as well as of ϕ_{D^*} can be found. This systematic shift as well as the loss in efficiency observed for η_{D^*Jet} in the lower and the upper bins are included in the systematic error calculation.

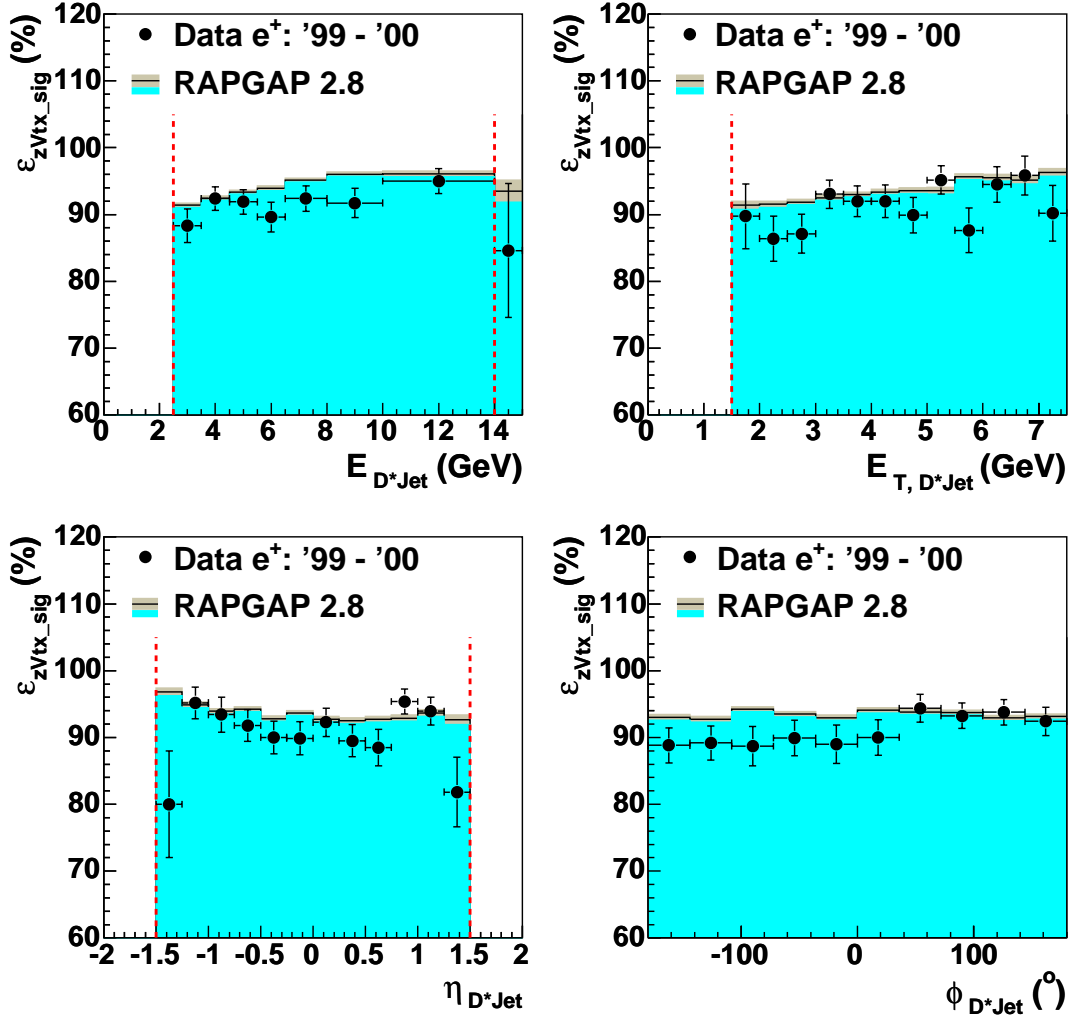


Figure 3.6: The $zVtx_sig$ efficiency for the D^*Jet measurements. The errors are the statistical ones.

The efficiencies of the **ToF** trigger elements are discussed in [50], where an efficiency

of $99.2 \pm 0.4\%$ has been determined for them.

Under the assumption that all TEs of ST61 are independent, the ST61 efficiency can be determined by multiplying the efficiencies of the TEs for the measured physical quantities, as shown in Fig. 3.7. In MC, the trigger efficiency is calculated taking into account all events which pass the analysis selection, without requiring an ST61 condition, yielding $N_{Analysed}$. From these events the fraction triggered by ST61 yields $N_{Trigger}$. ST61 is not simulated in MC, but rather its TEs, therefore it has to be reconstructed from them.

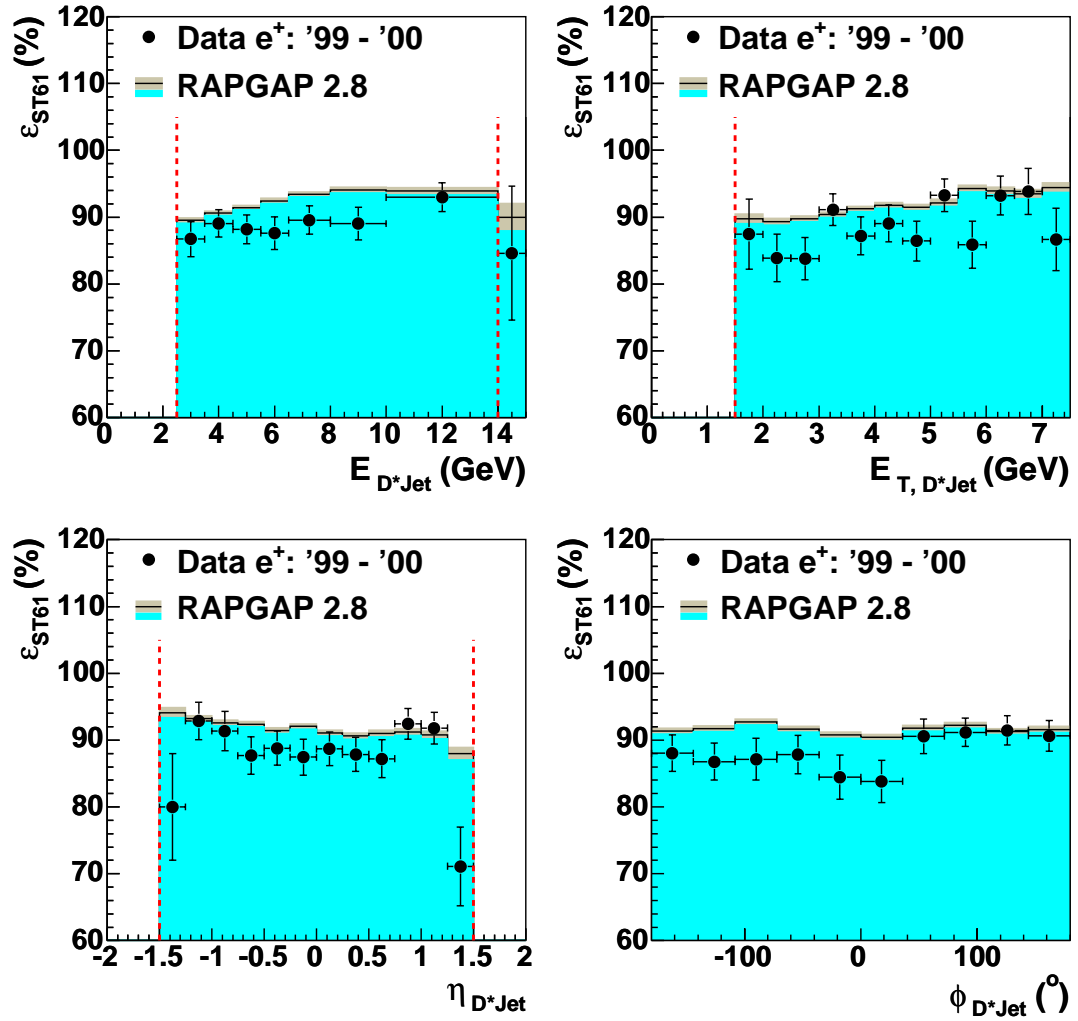


Figure 3.7: The ST61 efficiency for the D^*Jet measurements. The errors are the statistical ones.

3.2.4 The D^* -meson Online Selection

The open charm finder implemented at L4 is called HQSEL (Heavy Quark SELECTION). The HQSEL global requirements imply the selection of events with a well defined z -vertex position, a minimal energy for the SpaCal cluster of the scattered electron and a maximal radius of its cluster.

Since 1999, the D^* -meson finder requires that the kaon and the pion tracks fulfill

the *nominal track quality* requirement and the slow pion at least the *minimal track quality* requirement. Based on the decay channel from Eq. 3.1, the D^* -meson finder uses additional selection cuts applied on the p_T of the daughters and on the ΔM of the reconstructed mass of the D^0 and D^* -mesons. The conditions of the L4 D^* -meson finder are summarised in the Table. 3.6.

Global condition	Threshold
z position of the event vertex	$ z < 40$ cm
Energy of the scattered electron	> 5.5 GeV
Radius of the scattered electron cluster in the Spacal	< 4 cm
Nominal track quality	
z chamber flag	1 (use)
d'_{ca} of the track	< 4 cm
track length	> 15 cm
p_T of the track	> 0.15 GeV
Minimal track quality	
track length	> 10 cm
p_T of the track	> 0.10 GeV
Additional conditions	
$m_{K\pi}$ lower limit	> 1.464 GeV
$m_{K\pi}$ upper limit	< 2.264 GeV
$p_T(K\pi\pi_s)$	> 1.4 GeV
$p_T(K\pi\pi_s)$ for $ m_{K\pi} - M_{D^0} < 0.100$ GeV	> 1.0 GeV
$\Delta m = m_{K\pi\pi_s} - m_{K\pi}$	< 0.180 GeV

Table 3.6: The L4 D^* -meson finder requirements.

3.3 The Offline Selection

Events on DST are used as input in this analysis. Not all of these events are DIS events and have a "real" D^* -meson candidate.

In order to reduce the background contributions, e.g. photoproduction events with $Q^2 < 1$ GeV² and where a hadron has been misidentified as the scattered electron, an *offline selection* is applied. The DIS selection cuts use the kinematic variables Q_e^2 and y_e , where the index "e" means that Q^2 and y are calculated using the electron method. In order to select a clean DIS event sample, one should make sure that misidentified electron candidates are removed. Moreover, not all D^* -meson candidates reconstructed at L4 are "real". One has to apply quality cuts on the daughter particle tracks in order to minimise the contributions of misidentified D^* -mesons.

3.3.1 The DIS Selection

The DIS selection rejects two important sources of background. The background from non- ep events due to beam wall background interactions, is rejected by applying a cut on the z -position of the event vertex. The second major source of background are the photoproduction events. They are rejected by requiring an identified scattered electron and a cut on the quantity $E - p_z$. The *low* Q^2 DIS regime, used in this analysis, is

selected by cutting on the kinematic variables Q_e^2 and y_e . They are calculated using the electron method as will be explained later in this section. The energy calibration of the SpaCal is checked using the *double angle* method. A third method, which can be used to calculate the kinematic variables, is the *sigma* method. The sigma method takes into account possible QED radiation emitted by the incoming electron. Due to the scattered electron selection cuts, the effect of the QED radiation is minimised. The sigma method is presented in Appendix E for completeness.

The z -Vertex Position

The design-orbit of the proton and electron beam bunches ensures that the collision point of the two beam bunches is well defined inside the H1 detector. The approximative Gaussian profile of the proton bunches in the longitudinal direction gives a distribution of the collision points around the nominal interaction point.

In contrast, events coming from beam gas and wall interactions are equally distributed along the z -axis. Also events given by the interaction of the electron bunches with the proton satellite bunches have a large absolute value of the z -vertex position. In order to reject these non- ep events, the following limit is chosen:

$$|z_{vtx}| < 35 \text{ cm.} \quad (3.11)$$

A comparison of the z_{vtx} distribution of data with MC simulation is shown in Fig. 3.8. The MC events had to be reweighted to the z -vertex distribution of the data, in order to remove a systematic shift between data and MC. All other MC distributions shown are reweighted with a z_{vtx} -weight that is calculated from the ratio of the Gaussian fit applied independently to data and MC.

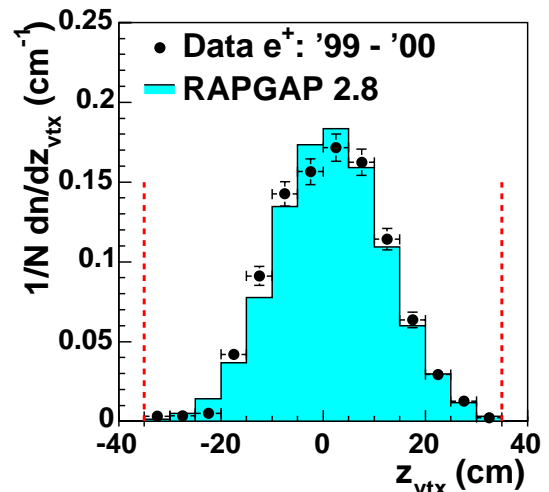


Figure 3.8: The z_{vtx} distribution.

Rejection of Photoproduction Events

In the HERA frame of reference for DIS events the following relation can be established between the energies and the longitudinal momenta of the incoming beams:

$$E - p_z = (E_e + E_p) - (p_{z,e} + p_{z,p}) = 2E_e = 55 \text{ GeV.} \quad (3.12)$$

Due to energy and momentum conservation and because particles which escape through the beam pipe in the forward direction do not contribute, the same quantity can be determined from the final state hadrons and the scattered electron:

$$E - p_z = (E'_e + \sum_{hads} E) - (p'_{z,e} + \sum_{hads} p_z) = 55 \text{ GeV.} \quad (3.13)$$

In Eq. 3.13 all particles measured in the LAr, SpaCal and CJC contribute. The photoproduction, γp , events are characterised by the fact that the scattered electron

escapes in the beam pipe in the backward direction. Due to the missing contribution of the scattered electron in γp events, the quantity $E - p_z$ will strongly deviate from the expected value of 55 GeV. The distributions from γp and DIS events can be seen in Fig. 3.9.

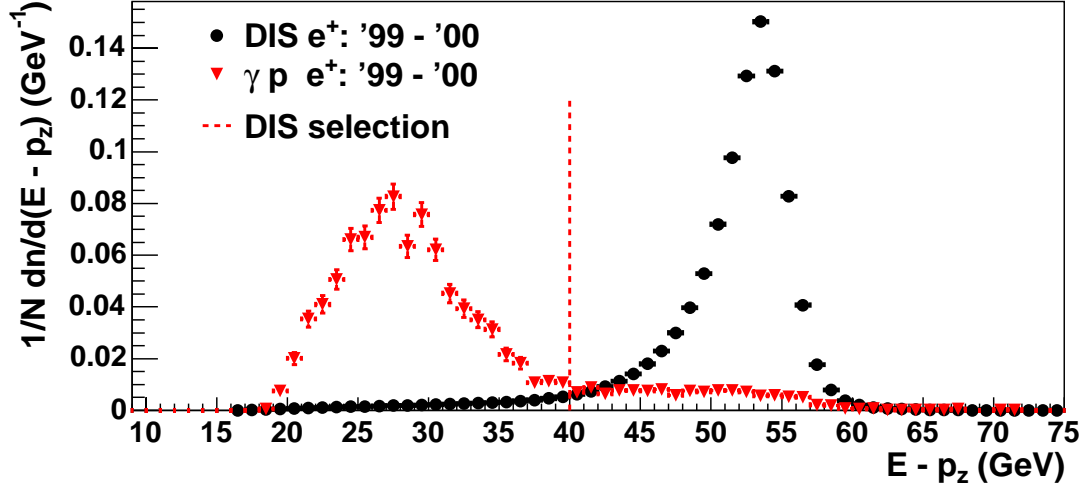


Figure 3.9: The comparison of $E - p_z$ from γp and DIS events. The dashed line shows the minimum cut applied on $E - p_z$ to select DIS events.

The γp events are selected using ST83 and the DIS events using ST61. For the DIS events no D^* -meson is required yet.

The γp events can be suppressed applying the following cut:

$$E - p_z > 40 \text{ GeV.} \quad (3.14)$$

The $E - p_z$ spectrum of the events selected for this analysis is shown in Fig. 3.10. Here the D^* -meson selection is applied and the background from misidentified D^* -meson candidates is subtracted as presented in Sec. 3.3.5.

In addition, the $E - p_z$ cut suppresses also events with QED radiation from the incoming electron, when the emitted energetic photon leaves the H1 detector through the beam pipe.

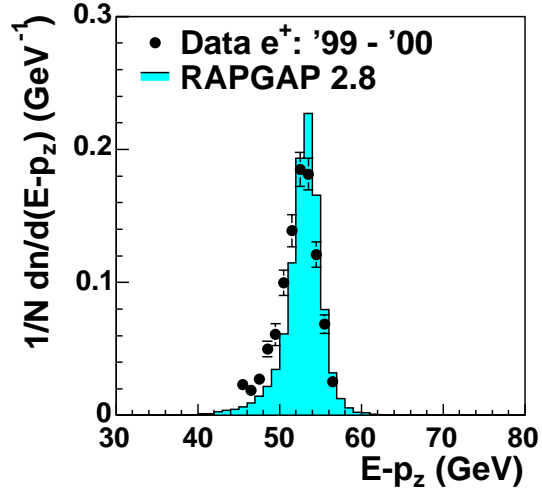


Figure 3.10: The $E - p_z$ spectrum.

The Electron Method

Knowledge of the energy of the scattered electron, E'_e , its angle θ'_e , and the electron beam energy E_e allows the determination of the full event kinematics. At HERA beam energies the mass of the proton and electron can be neglected. The kinematic variables are given by:

$$Q_e^2 = 4E_e E'_e \cos^2 \left(\frac{\theta'_e}{2} \right); \quad y_e = 1 - \frac{E'_e}{E_e} \sin^2 \left(\frac{\theta'_e}{2} \right); \quad x_e = \frac{Q_e^2}{s \cdot y_e}. \quad (3.15)$$

The advantages of the electron method are its simplicity, the best resolution for y not too small and the independence of hadron final state measurement. In order to have an accurate determination of the kinematic variables, one needs a good resolution of the scattered electron energy and its θ angle.

The Q_e^2 and y_e kinematic variables, as well as the electron variables E'_e and θ'_e , are shown in Fig. 3.11. The MC model describes the data reasonably well without applying any other reweighting except for the z_{vtx} .

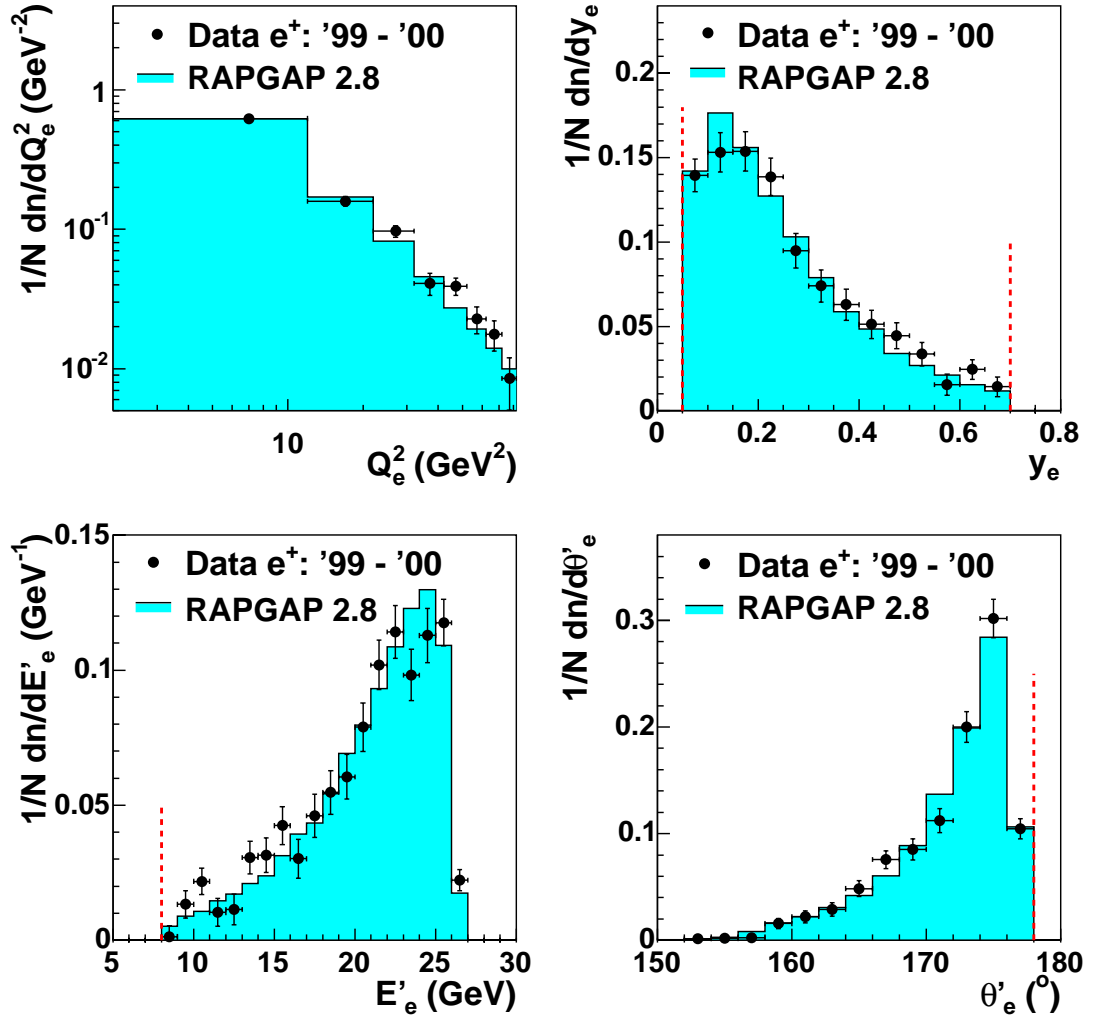


Figure 3.11: The event kinematics and the electron variables. The dashed line illustrates the cut applied in the analysis.

The Double Angle Method

The double angle method makes use just of angle measurements of the hadrons and of the scattered electron to determine the energy of the scattered electron and the event kinematics.

With this method the calibration of the scattered electron energy can be checked due to fact that it is independent, in first order, of the hadron energy resolution.

The angle γ of the hadronic final state is given by:

$$\cos \gamma = \frac{\left(\sum_{hads} p_x\right)^2 + \left(\sum_{hads} p_y\right)^2 - \left(\sum_{hads} (E - p_z)\right)^2}{\left(\sum_{hads} p_x\right)^2 + \left(\sum_{hads} p_y\right)^2 + \left(\sum_{hads} (E - p_z)\right)^2}. \quad (3.16)$$

The kinematic variables in terms of γ and θ_e are given by:

$$\begin{aligned} Q_{DA}^2 &= \frac{4E_e^2 \sin \gamma \cdot (1 + \cos \theta'_e)}{\sin \gamma + \sin \theta'_e - \sin(\gamma + \theta'_e)}; \\ y_{DA} &= \frac{\sin \theta'_e \cdot (1 - \cos \gamma)}{\sin \gamma + \sin \theta'_e - \sin(\gamma + \theta'_e)}; \\ x_{DA} &= \frac{Q_{DA}^2}{s \cdot y_{DA}} \end{aligned} \quad (3.17)$$

The energy calibration can be checked using E'_{DA} :

$$E'_{DA} = \frac{E_e(1 - y_{DA})}{\sin^2(\theta'_e/2)} \quad (3.18)$$

which is the scattered electron energy.

The results of the double angle method are expected to be good for the inelasticity range $0.05 < y < 0.3$, as it can be seen from Fig. 3.12.

The ratio E'_e/E'_{DA} is plotted in Fig. 3.13 for the range $0.05 < y < 0.3$. For this range, as well as for the entire statistics - not shown here, a nice peak close to the value of 1 is observed and the data are reasonably described by the MC.

For this analysis, the *low* Q^2 DIS regime is defined as follows:

$$2 < Q_e^2 < 100 \text{ GeV}^2; \quad (3.19)$$

$$0.05 < y_e < 0.7. \quad (3.20)$$

The selection criteria used for the scattered electron identification are presented in the next section.

3.3.2 The Scattered Electron Selection

For events with $Q^2 \leq 100 \text{ GeV}^2$ the SpaCal and the BDC are used to identify the scattered electron. The measurement of the scattered electron is input for the calculation

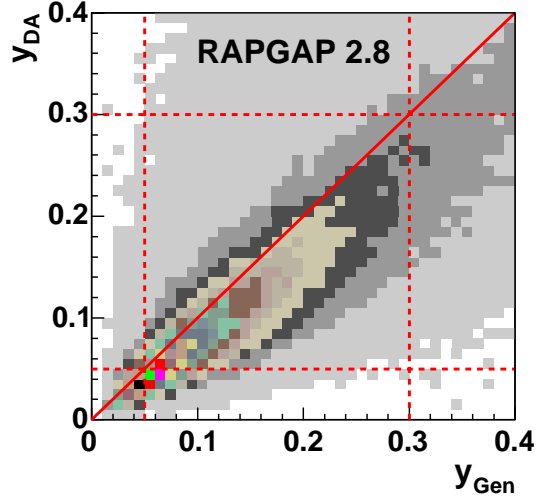


Figure 3.12: The correlation between y_{DA} at the detector level and y_{Gen} at the hadron level.

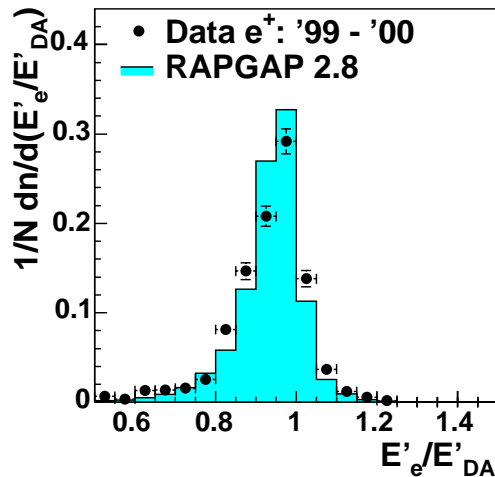


Figure 3.13: The E'_e/E'_{DA} ratio.

of the kinematic variables Q_e^2 and y_e . Two aspects are important for the selection of the scattered electron: the energy and the polar angle θ'_e to be measured with a good resolution and the rejection of misidentified electron candidates to be very efficient. As explained in Sec. 2.5, the electron resolution is very good. A charged hadron, which in photoproduction events is frequently found going into the backward direction, may be misidentified as the scattered electron. Such "fake" candidates are rejected by applying a number of cuts which are explained in the following paragraphs.

The Energy of the Scattered Electron

The scattered electron showers in the EM part of the SpaCal. The resulting cluster, consisting of cells with energy depositions from the shower, is used to calculate the energy of the electron candidate. If in an event there are two scattered electron candidates within the SpaCal acceptance, then the one with the highest p_T is chosen as being the "true" one. The scattered electron is accepted if the following conditions are fulfilled:

$$E'_e > 8 \text{ GeV}; \quad \theta_e < 178^\circ. \quad (3.21)$$

The threshold of 8 GeV is chosen in order to remove almost all misidentified electron candidates. The angle $\theta = 178^\circ$ is the upper limit of the SpaCal acceptance.

The Energy in the VETO Layer

An (x, y) view of the SpaCal inner part, is shown in Fig. 3.14. If the scattered electron is emitted with a too large angle and enters close to the beam pipe, a part of its energy will be deposited into the VETO layer cells and another part will leak into the beam pipe. Due to this leakage, the energy of the electron will not be fully reconstructed.

In order to avoid migration of events in Q_e^2 due to a wrong energy measurement, these events are rejected applying the following cut:

$$E_{VETO} < 1 \text{ GeV}. \quad (3.22)$$

This cut also rejects a fraction of events where the incoming electron radiates a photon, which may deposit energy in the cells of the VETO layer.

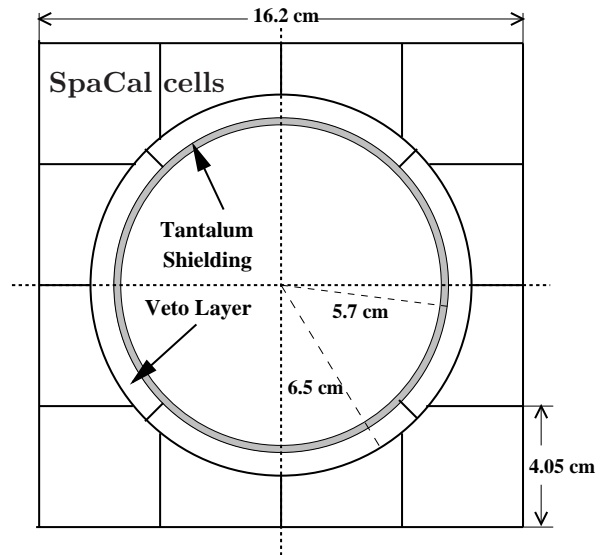


Figure 3.14: The (x, y) view of the SpaCal inner cells and the VETO layer.

The Energy in the HAD Part of the SpaCal

As already mentioned, a charged hadron, in γp and to less extent in DIS events, may shower in the SpaCal EM part such that it can fake a scattered electron. A typical hadron shower, however, does not end in the EM but rather in the HAD part of the

SpaCal. The charged hadrons detected in the SpaCal have a high probability to deposit a fraction of their energy in the HAD part. The determination of the hadronic energy of the scattered electron candidate makes possible the rejection of those which are actually hadrons. The cut applied is:

$$E'_{e, \text{HAD}} < 0.5 \text{ GeV}. \quad (3.23)$$

Even with this cut, there are cases when for a scattered electron energy of e.g. 9 GeV, the fraction of the hadronic energy can be larger than 5%. To further reduce the probability of a "fake" scattered electron candidate, an additional cut is used:

$$E'_{e, \text{HAD}}/E'_e < 3\%. \quad (3.24)$$

The Energy Fraction from the Isolation Cone

The isolation cone of the electron cluster is defined as the cone having a radius R in (η, ϕ) space which fulfills the condition:

$$R_{\text{isocone}} = \sqrt{(\eta_{\text{cl}} - \eta_{\text{cell}})^2 + (\phi_{\text{cl}} - \phi_{\text{cell}})^2} < 0.25 \quad (3.25)$$

The energy difference between the isolation cone energy and the scattered electron energy, the so-called E_{aif} quantity, has to obey the following cut:

$$E_{\text{aif}}/E'_e < 10\%. \quad (3.26)$$

The geometrical description of the electron candidate cluster in SpaCal can also be used to reject the "fake" candidates.

The z -Position of the Cluster

The front face of the EM part of the SpaCal starts at $z = -150.5$ cm and the HAD part at $z = -202$ cm. The active length of the EM part is 25 cm. A cluster which lies behind the EM part of the SpaCal cannot be attributed to an electron but rather to a hadron. Therefore the scattered electron candidate has to pass the cut:

$$z_{\text{clus}} > -180 \text{ cm}. \quad (3.27)$$

The Energy Weighted Cluster Radius

The shower of the electron in the EM part of the SpaCal does not have a uniform energy deposition in the cells. This can be used to calculate the cluster radius, E_{cra} , using as weight for the cell position the logarithm of the ratio between the cell energy and the cluster energy. The cluster radius of a hadron is much larger than the one for an electron. Another rejection of the "fake" scattered electrons is therefore achieved with the cut:

$$E_{\text{cra}} < 4 \text{ cm}. \quad (3.28)$$

The Radial Cluster Position in the SpaCal

Between the beam axis and the SpaCal z -axis there is a tilt which can shift the cluster position much closer to the beam pipe than the position read out from the SpaCal geometry alone. This effect is taken into account by cutting on:

$$R_{\text{tilt}} > 9.1 \text{ cm}. \quad (3.29)$$

The Cluster R Position Without Corrections

The electron cluster has to lie within the limits of the SpaCal radial coverage. If a cluster is at the extreme limits of the SpaCal, its barycentre can point outside of the SpaCal geometry and then the energy reconstruction is clearly not complete. These cases can be rejected by applying a cut on:

$$8.7 < R_{\text{cluster}} < 74 \text{ cm}, \quad (3.30)$$

where the R_{cluster} position of the cluster in the SpaCal (x, y) plane is calculated without considering the tilt correction.

The DCLSP Cut

The cluster of the scattered electron is also described by the so-called second radius, DCLSP. In fact the DCLSP is the sigma of the cluster xy position which has to fulfill the condition:

$$DCLSP = \sqrt{\sigma_{x, \text{cluster}}^2 + \sigma_{y, \text{cluster}}^2} < 4 \text{ cm}. \quad (3.31)$$

The Distance to the BDC Extrapolation

The backward drift chamber helps the electron identification by rejecting background due to π^0 decay into two photons, which showers in the EM part of the SpaCal. The requirement is to have a track in the BDC which, when extrapolated to the SpaCal, has a small projected distance from the centre of the cluster. The cut applied is:

$$\Delta r_{\text{BDC}} < 1.5 \text{ cm}. \quad (3.32)$$

The Number of Selected BDC Hits

In order to ensure a good extrapolation of the track using the BDC, a minimum number of hits is required:

$$N_{\text{hits, BDC}} \geq 4. \quad (3.33)$$

A summary of the selection criteria used for the scattered electron can be found in Table. 3.7. The analysis presented in this paper was performed in the object oriented analysis environment of H1 (*h100*). As in any new computing environment, not all the cuts and codes were implemented at the beginning. The scattered electron candidate selection as well the D^* -meson selection presented in Sec. 3.3.3 were updated and implemented in *h100* from the Fortran environment used until then [45].

The BDC Efficiency

For the scattered electron selection two cuts are used combining BDC information.

One of them requires that the BDC track extrapolated to the SpaCal has a projected distance to the centre of the cluster of less than 1.5 cm. Due to the dead material between the interaction point and the BDC, the electron may start to shower. This has an impact on the BDC tracking, giving a high track multiplicity. Only one of these tracks is the scattered electron track, and one has to be sure that it is efficiently reconstructed in order to reject only clusters due to photons.

Scattered Electron Variable	Threshold
Energy of the SpaCal electron	> 8 GeV
θ angle of the SpaCal electron	$< 178^\circ$
Energy of the LAr electron	> 11 GeV
Energy in the VETO layers	< 1 GeV
Energy in HAD behind the electron	< 0.5 GeV
Hadronic fraction of the electron energy	< 0.03
Energy fraction in the isolation cone	< 0.1
z -position of the SpaCal cluster	> -180 cm
Energy weighted cluster radius	< 4 cm
Radial cluster position in SpaCal	> 9.1 cm
The radius of the cluster without corrections: R_{cluster}	$8.7 \text{ cm} < R_{\text{cluster}} < 74 \text{ cm}$
DCLSP	< 4 cm
Distance between the SpaCal cluster position and BDC extrapolation	< 1.5 cm
Number of selected hits in BDC	≥ 4

Table 3.7: The selection criteria used for the scattered electron.

One can define the BDC efficiency as being the probability of finding the BDC electron track within 1.5 cm of the electromagnetic cluster in the SpaCal, when extrapolated there. The algorithm is based on the analysis chain excluding the BDC track extrapolation cut for the scattered electron candidate.

The BDC efficiency is plotted in Fig. 3.15 as a function of the cluster radius R_{cluster} .

A large fraction of the events characterised by QED radiation are rejected applying this laborious list of cuts for the scattered electron candidate as can be seen from the good description of the MC model without QED radiation and the data shown in Fig. 3.11.

Therefore, in this analysis the very small QED radiative corrections are neglected, particularly since they do not influence the structure of charm jets.

3.3.3 The D^* -meson Offline Selection

The offline selection makes use of a D^* -meson finder in the *h100* environment. The principle of this finder is the same as for the D^* -meson finder on L4. D^* -mesons are reconstructed using the CJC tracks located in the central region of the H1 detector only:

$$-1.5 < \eta_{\text{track}} < 1.5. \quad (3.34)$$

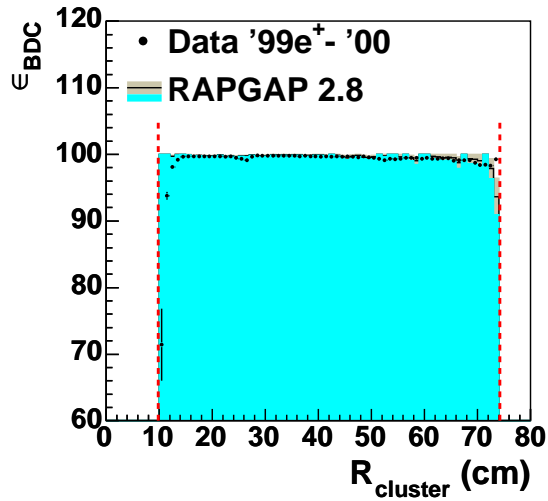


Figure 3.15: The BDC efficiency.

All tracks are attributed the pion mass as a first hypothesis. In the loop over the tracks assumed to be kaon candidates, the p_T requirement is:

$$p_{T,K} > 0.25 \text{ GeV}. \quad (3.35)$$

After a kaon candidate is found, the pion candidate has to pass the following cuts:

$$p_{T,\pi} > 0.25 \text{ GeV}; Q_K \cdot Q_\pi = -1. \quad (3.36)$$

From these two tracks, the invariant mass $m_{K\pi}$ is calculated and the following wide cut on the mass difference is applied:

$$|m_{K\pi} - m_{D^0}| < 0.25 \text{ GeV}. \quad (3.37)$$

Among the remaining tracks, the one which fulfills the following p_T and charge criteria is chosen as the π_s candidate:

$$p_{T,\pi_s} > 0.12 \text{ GeV}; Q_K \cdot Q_{\pi_s} = -1. \quad (3.38)$$

Once a D^* -meson candidate is found, additional selection cuts are applied in order to reduce the background:

$$\begin{aligned} p_{T,D^*} &> 1.5 \text{ GeV}; \\ |\eta_{D^*}| &< 1.5; \\ m_{K\pi\pi_s} - m_{K\pi} &< 0.17 \text{ GeV}. \end{aligned} \quad (3.39)$$

The D^* -meson finder is rejecting also those candidates which are considered as "bad" for the reconstructed D^* -meson as well as for D^0 -meson:

$$(|m_{K\pi} - m_{D^0}| < 0.10 \text{ GeV}) \text{ and } (m_{K\pi\pi_s} - m_{K\pi} < 0.152 \text{ GeV}). \quad (3.40)$$

As one can see from the D^* -meson finder algorithm, the method used in this analysis to identify the D^* -meson is the *mass difference method*. This method makes use of the advantage that the mass of the D^* -meson is very close to the sum of the D^0 -meson and pion mass and therefore the signal is having a falling background distribution close to the phase space boundary. In addition, part of the measurement errors of the K and π cancel in the mass difference, the error is dominated by the error of the π_s track. The mass difference distribution is given by Δm :

$$\Delta m = m_{K\pi\pi_s} - m_{K\pi}. \quad (3.41)$$

Nevertheless, some background remains under the signal. The background in the Δm distribution is combinatorial and has contributions from charm $\sim 15\%$ and light quark events $\sim 85\%$, according to MC estimations. For higher p_T cuts applied on the daughters tracks, the background can be suppressed, but then also the D^* -meson phase space is reduced. An alternative is to fit the combinatorial background with a similar one that does not have a D^* -meson signal. Since the background is combinatorial, it can be estimated using the so-called *wrong charge* combination (WrCh):

$$" D^{*+} \rightarrow K^+ \pi^+ \pi_s^- " \quad (3.42)$$

as well as the charge conjugate combination. The WrCh background has the same shape as the one given by the *right charge* combination (RiCh). A fit is applied

simultaneously to both Δm distributions to obtain the number of reconstructed D^* -mesons. More details are given in the Sec. 3.3.5.

In Sec. 3.3.4 the tracks selection criteria are presented. This is an elaborated list of cuts inherited and improved, which are applied to the daughters tracks such that more than 50% of the combinatorial background is reduced. These selection cuts are used in the selection of both types of charge combinations.

3.3.4 Track Quality Cuts

The signal to background ratio in the Δm distribution, as well as the resolution, can be substantially improved, if the tracks considered for the D^* -meson daughter candidates are well measured. An improvement of the signal to background ratio is obtained by applying the criteria presented in this section.

The first step is to make sure that only tracks which are fitted with respect to the primary vertex are accepted. This way, tracks from a secondary vertex of a B -meson or even longer lived resonance, e.g. K^0 , are rejected. The observables that characterize a track are explained in detail in Appendix C. A combination of the two track segments of CJC1 and CJC2 gives a good track quality if the total length fulfills the condition:

$$L_{\text{track}} \geq 10 \text{ cm.} \quad (3.43)$$

An enhancement of the signal with respect to the background is obtained when the radius of the track starting point is required to be:

$$R_{S, \text{track}} \leq 50 \text{ cm,} \quad (3.44)$$

which is equivalent to having the track start in the inner chamber, CJC1.

The probability that short track segments, which are not part of the same track, are linked together is reduced by requiring a minimum number of CJC hits contributing to the final fit of the track:

$$N_{\text{hits}} \geq 10. \quad (3.45)$$

The cuts presented until now allow the selection of tracks which have an accurate determination of the helix parameters. Tracks not coming from the event vertex but for example from the beam pipe or cosmic are rejected by the cut on d'_{ca} , see Appendix C:

$$d'_{\text{ca}} \leq 1.0 \text{ cm.} \quad (3.46)$$

The cuts applied on $|d'_{\text{ca}} \cdot \sin \theta_{\text{track}}|$, as well the ones applied on $|dz_0|$ and $|dz_0 \cdot \sin \theta_{\text{track}}|$, reject tracks fitted to the primary vertex, but which are found not to point to the accepted vertex area. These cuts are presented in Table 3.8.

Due to the correlation between the p_{T, D^*} and the p_{T} sum of the kaon and the pion, shown in Fig. 3.16, the cut:

$$p_{\text{T}, K} + p_{\text{T}, \pi} > 2.0 \text{ GeV} \quad (3.47)$$

reduces considerably the combinatorial background. The contributions of the kaon and the pion p_{T} sum below 2 GeV, which are not so well correlated, are rejected by this cut.

From the D^* -meson candidates that pass the track quality cuts of the daughters,

only those found in the best understood H1 detector acceptance are used in the analysis:

$$|\eta_{D^*}| < 1.5 \quad (3.48)$$

$$p_{T, D^*} > 1.5 \text{ GeV} \quad (3.49)$$

A summary of the quality cuts used to select the D^* -meson candidates is given in the Table 3.8.

More stringent values for some of the cuts are used for certain run periods depending on the criteria of the L4 finder selection, see Appendix C.

Another very efficient tool for background reduction is *particle identification* via *energy loss*: dE/dx . The charged particles passing through the CJC loose energy in the gas. The energy loss results from the scattering of the charged particles off atomic electrons.

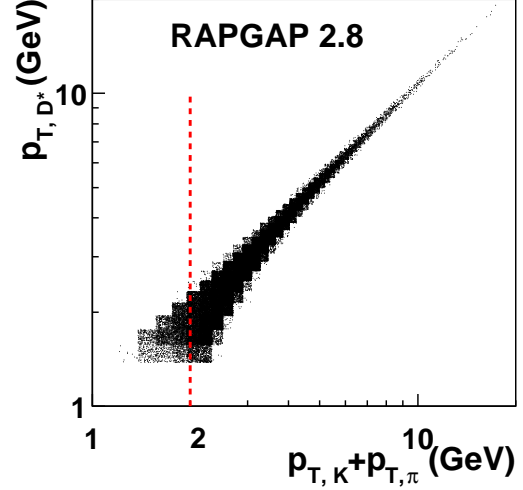


Figure 3.16: The correlation between p_{T, D^*} and the sum $p_{T, K} + p_{T, \pi}$. The dotted line shows the cut applied in this analysis.

Track Quality cuts	K	π	π_s
Transverse momentum: $p_{T, \text{track}}$	$> 0.25 \text{ GeV}$	$> 0.25 \text{ GeV}$	$> 0.12 \text{ GeV}$
Pseudorapidity: $ \eta_{\text{track}} $	< 1.5		
Primary vertex condition	<i>fulfilled</i>		
Track length	$\geq 10 \text{ cm}$		
Track starting radius	$\leq 50 \text{ cm}$		
Number of hits in CJC	≥ 10		
The distance of closest approach: d'_{ca}	$\leq 1.0 \text{ cm}$		
$ d'_{ca} \cdot \sin \theta_{\text{track}} $	$\leq 0.5 \text{ cm}$	$\leq 0.7 \text{ cm}$	
$ dz_0 = z_{d'_{ca}} - z_{vtx} $	$\leq 40 \text{ cm}$		
$ dz_0 \cdot \sin \theta_{\text{track}} $	$\leq 18 \text{ cm}$		
Additional cuts	Threshold		
$p_{T, K} + p_{T, \pi}$	$> 2.0 \text{ GeV}$		
p_{T, D^*}	$> 1.5 \text{ GeV}$		
$ \eta_{D^*} $	< 1.5		

Table 3.8: The track quality cuts applied in this analysis for the D^* -meson selection.

For heavy charged particles the energy loss dE per path dx is described by the Bethe-Bloch formula [46] :

$$-\frac{dE}{dx} = \kappa \cdot z^2 \cdot \frac{Z}{A} \cdot \frac{1}{\beta^2} \left[\frac{1}{2} \ln \left(\frac{2m_e c^2 \gamma^2 \beta^2 T_{max}}{I^2} \right) - \beta^2 - \frac{\delta}{2} \right] \quad (3.50)$$

with

$$\kappa = 4\pi \cdot N_A \cdot r_e^2 m_e c^2. \quad (3.51)$$

In the Bethe-Bloch formula, N_A denotes the number of Avogadro, r_e is the classical electron radius and m_e is the electron mass. The variable z represents the charge of

the incident particle. Z and A are the atomic and the mass number, respectively. I gives the mean excitation energy. The maximum kinetic energy that can be transferred to a free electron in a single collision of a particle with mass M is given by:

$$T_{max} = \frac{2m_e c^2 \gamma^2 \beta^2}{1 + 2\gamma \frac{m_e}{M} + \left(\frac{m_e}{M}\right)^2}. \quad (3.52)$$

The Lorentz variables are defined as:

$$\beta = \frac{p}{M}; \quad \gamma = \frac{1}{\sqrt{1 - \beta^2}}. \quad (3.53)$$

The term $\delta/2$ is the density effect correction, which is introduced to account for polarisation effects that are truncating the electric field extension of high energetic particles.

The value of dE/dx depends only on β of the particle and therefore only on the ratio p/M . As a consequence, the dE/dx curves of particles with different mass are shifted with respect to each other, if they are plotted as a function of momentum p .

The track dE/dx is determined from the values of the dE/dx attributed to its hits. The track has to fulfill the quality requirements presented previously. A mean dE/dx value of a track is calculated by transforming the energy deposition of single hits as $dE/dx \rightarrow 1/\sqrt{dE/dx}$. This is due to the fact that the dE/dx measurement has a Landau distribution. The mean of this new symmetric distribution is transformed back and multiplied with $\sin \theta$ to consider also the path length that contributes to the collected charge of each hit.

The dE/dx values measured in the CJC do not satisfy the Bethe-Bloch formula exactly. The dE/dx values are improved using run dependent constants and the following parametrisation [51]:

$$-\frac{dE}{dx} = a_1 \cdot \frac{z^2}{\beta^{a_2}} \left(1 + a_3 \cdot e^{-a_4 \log(0.25 + \beta\gamma)}\right), \quad (3.54)$$

with $a_1 = 1.4139$, $a_2 = 1.6504$, $a_3 = -0.4610$ and $a_4 = 0.56924$. The values of dE/dx are normalised using the condition $dE/dx = 1$ for minimum ionising particles (m.i.p.).

In order to have a reliable dE/dx determination, i.e. a small error on the average value, a minimum number of hits is required:

$$N_{\text{hits}, dE/dx} \geq 10. \quad (3.55)$$

The dE/dx vs. p_{track} for the tracks in the events used by this analysis are shown in the Fig. 3.17. The variable used for the particle identification is the *likelihood* of a track to be a specific particle:

$$lh = \frac{1}{\sqrt{2\pi}} \int_{\chi^2}^{\infty} dt e^{-t/2} \cdot \frac{1}{\sqrt{t}} \quad (3.56)$$

where χ^2 is the density for one degree of freedom.

In this analysis, the cuts for particle identification are applied to the so-called normalised likelihoods, which are defined, e.g. for K , as:

$$N_{lh, K} = \frac{lh_{K, K}}{lh_{K, K} + lh_{K, \pi} + lh_{K, p}}, \quad (3.57)$$

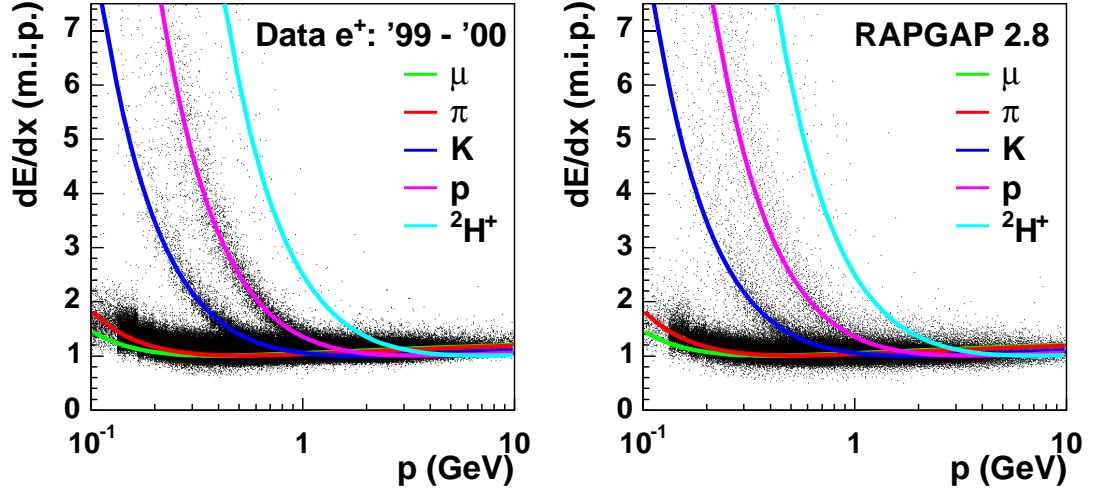


Figure 3.17: The dE/dx vs. p_{track} distribution in data, left, and in the MC simulation, right. The expectation is given by Eq. 3.54 for different particle masses.

where $lh_{K,K}$ is the likelihood that a K candidate is a "real" K . The $lh_{K,\pi}$ and $lh_{K,p}$ terms are the likelihoods for the K to be a π or a proton p , respectively.

The normalised likelihood cuts applied to the D^* -meson daughter tracks, depending on the momentum range, are shown in Table 3.9 together with the minimum number of hits used in the dE/dx measurements.

dE/dx cuts	K	π	π_s
N_{lh} for: $p_{\text{track}} < 0.7$ GeV	≥ 0.2	≥ 0.05	≥ 0.05
N_{lh} for: 0.7 GeV $< p_{\text{track}} < 1.2$ GeV	≥ 0.05	≥ 0.05	≥ 0.05
N_{lh} for: 1.2 GeV $< p_{\text{track}}$	≥ 0.02	≥ 0.02	≥ 0.05
Number of track hits used for dE/dx	≥ 10		

Table 3.9: The dE/dx requirements on normalised likelihoods for particle identification.

3.3.5 The Δm Reconstruction

In the previous section, the cuts which are used for the D^* -meson daughters tracks selection were presented. These cuts are applied in order to reduce the combinatorial background. Even if the background is minimised and the signal to background ratio is very good, the contributions given by the non D^* -mesons candidates in the final distributions are not negligible. This background can be statistically subtracted using the right charge (RiCh) combination, $K^-\pi^+\pi_s^+$, and the wrong charge (WrCh) ones, $K^+\pi^+\pi_s^-$. The charge conjugate combinations are also considered.

The best resolution for the D^* -meson measurement is obtained using the Δm distribution. The background coming from the D^0 -mesons reconstructed using the K and the π , e.g. reflections, is partially suppressed using the mass window:

$$|m_{K\pi} - m_{D^0}| \leq 0.07 \text{ GeV}. \quad (3.58)$$

The $\Delta m = m_{K\pi\pi_s} - m_{K\pi}$ distributions of the RiCh and the WrCh combinations have to pass all the quality cuts, as well as to be in the D^0 -meson mass window. The

shape of the two distributions, except for the D^* -meson signal, is the same due to the fact that the phase space of the WrCh is only slightly smaller than the one for the RiCh. If N^+ and N^- are the number of positive and respectively negative tracks, for the D^0 -meson reconstruction N^+N^- possible combinations are used in the RiCh case. For the WrCh there are $N^+(N^+ - 1)$ combinations, due to the fact that the opposite charge combinations for the D^0 -meson signal, e.g. $K^-\pi^+$, are missing.

A combined fit is applied simultaneously to the two Δm distributions, for RiCh and WrCh. The fit function consists of a Gaussian function for the D^* -meson signal:

$$f_{D^*}(\Delta m) = \frac{N_{D^*}}{\sigma\sqrt{2\pi}} \cdot e^{-\left(\frac{(\Delta m - \mu)^2}{2\sigma^2}\right)}, \quad (3.59)$$

where N_{D^*} is the number of D^* -mesons given by the fit, μ is the mean value of the signal from the Δm distribution and σ is the signal width, and of a fit function describing the shape of the combinatorial background for RiCh and WrCh:

$$f_{\text{bg}}(\Delta m) = p \cdot (\Delta m - m_\pi)^\alpha \quad (3.60)$$

where p and α are two free parameters.

The ratio between the RiCh and the WrCh combinatorial background is given by an additional parameter k_N . The total fit function used in this analysis is:

$$f_{\text{total}}(\Delta m) = b_{\text{size}} \cdot (f_{D^*}(\Delta m) + f_{\text{bg}}(\Delta m) + k_N \cdot f_{\text{bg}}(\Delta m)), \quad (3.61)$$

where b_{size} is the bin size of the Δm histogram. The RiCh and the WrCh distributions are fitted simultaneously. The parameter k_N , which gives the ratio between the WrCh and the RiCh, will be used for the statistical background subtraction, as described in Chapter 4 and Chapter 5.

The mean value of the signal in the Δm distribution signal from the fit for the full event sample is:

$$\begin{aligned} \mu &= 145.44 \pm 0.03 \text{ MeV} \\ \sigma &= 1.07 \pm 0.04 \text{ MeV}. \end{aligned} \quad (3.62)$$

In this analysis, events with D^* -meson candidates which have a Δm value within $\mu \pm 3\sigma$ are studied. The Δm spectrum is presented in Fig. 3.18b). The shaded distributions in Fig. 3.18 show the WrCh background. After the jet selection, the main effect is a decrease in statistics and a different value of the normalisation parameter k_N between the RiCh and the WrCh combinations is obtained from the new fit and used in the analysis part concerning the jets.

The results of the fit performed on the data collected during the 1999 and 2000 e^+ running periods are listed in Table. 3.10.

Fit results	Data 1999 e^+	Data 2000	Data 1999 e^+ and 2000
N_{D^*}	621 ± 36	2154 ± 72	2768 ± 81
N_{D^0}	591 ± 34	1978 ± 67	2574 ± 79

Table 3.10: The number of N_{D^*} and N_{D^0} mesons obtained from the fit.

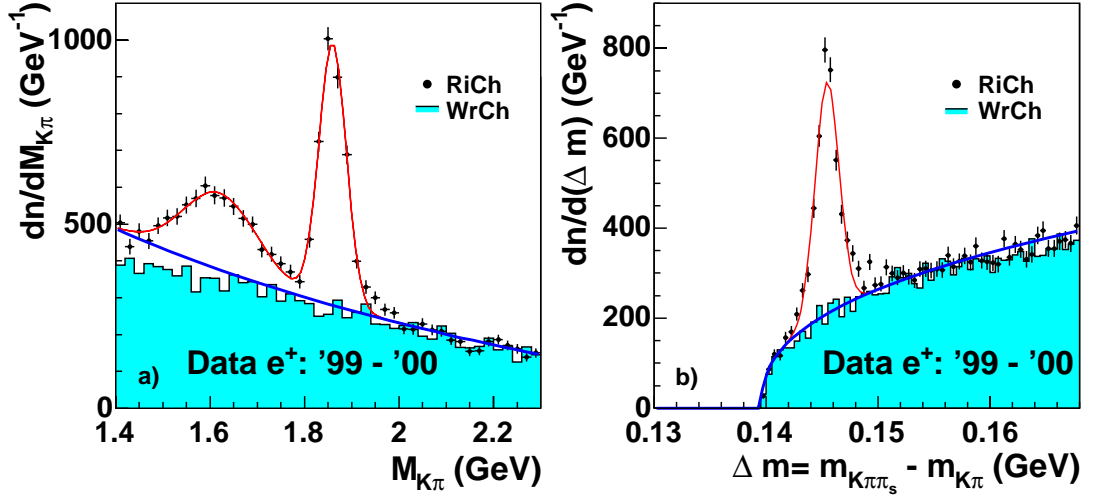


Figure 3.18: The Δm and the M_{D^0} spectra. The WrCh combinations are shown by the coloured histogram.

For a cross-check of the fit used to determine the number of D^* -mesons, the D^0 -mesons are investigated. In Fig. 3.18 a) the D^0 -meson mass spectrum is presented for the candidates which fulfill the following condition:

$$|m_{K\pi\pi_s} - m_{K\pi} - (m_{D^*} - m_{D^0})| < 2.2 \text{ MeV}. \quad (3.63)$$

The fit used for the D^0 -meson mass distribution consists of two Gaussian functions for the signals and an exponential falling function for the background. The D^0 -meson signal for the decay channel $D^0 \rightarrow K^- \pi^+$ is fitted with the function:

$$f_{D^0}(M_{K\pi}) = \frac{N_{D^0}}{\sigma_{D^0} \sqrt{2\pi}} \cdot e^{-\frac{(M_{K\pi} - \mu_{D^0})^2}{2\sigma_{D^0}^2}}. \quad (3.64)$$

The second signal, which is usually called the S^0 signal, corresponds to the decay channel $D^0 \rightarrow K^- \pi^+ \pi^0$ and is lying around the $m_{D^0} - m_{\pi^0}$ mass difference of 1.6 GeV, due to the missing π^0 . The fit function for the S^0 signal is:

$$f_{S^0}(M_{K\pi}) = \frac{N_{S^0}}{\sigma_{S^0} \sqrt{2\pi}} \cdot e^{-\frac{(M_{K\pi} - \mu_{S^0})^2}{2\sigma_{S^0}^2}}. \quad (3.65)$$

The background of the D^0 -meson mass distribution is fitted with the function:

$$f_{\text{bg}, D^0}(M_{K\pi}) = a \cdot (M_{K\pi})^{\alpha_{D^0}} + b \quad (3.66)$$

where a , b and α_{D^0} are free parameters. The parameter α_{D^0} has negative values.

The total function used to describe the D^0 -meson mass spectrum is then:

$$f_{\text{total}, D^0}(M_{K\pi}) = b_{\text{size}, D^0} \cdot (f_{D^0}(M_{K\pi}) + f_{S^0}(M_{K\pi}) + f_{\text{bg}, D^0}(M_{K\pi})) \quad (3.67)$$

and the following D^0 -meson mass value is obtained:

$$m_{D^0} = 1859.4 \pm 0.89 \text{ MeV}, \quad (3.68)$$

which is in good agreement with the Particle Data Group (PDG) value. The number of D^0 -mesons found is included in Table 3.10.

Fig. 3.18 a) indicates that the decay channels such as $D^0 \rightarrow K^- \pi^+ \pi^0$ are also contributing inside the D^0 -meson mass spectrum. This type of contribution is called *reflection*.

The effect of the reflections is giving in the D^0 -meson mass spectrum contributions shifted from the nominal mass due to the K and π mass assumption. Overall, the *reflections* contribution [52] in the Δm spectrum is of the order of $\sim 3\%$. Despite the fact that they are not coming from the $D^0 \rightarrow K^- \pi^+$ decay channel, these contributions are accepted, if they pass the Δm cut:

$$0.142 \text{ GeV} < \Delta m < 0.149 \text{ GeV}. \quad (3.69)$$

The limits of the Δm window are given by the $\mu \pm 3\sigma$ where μ and σ are obtained from the fit of the Δm distributions.

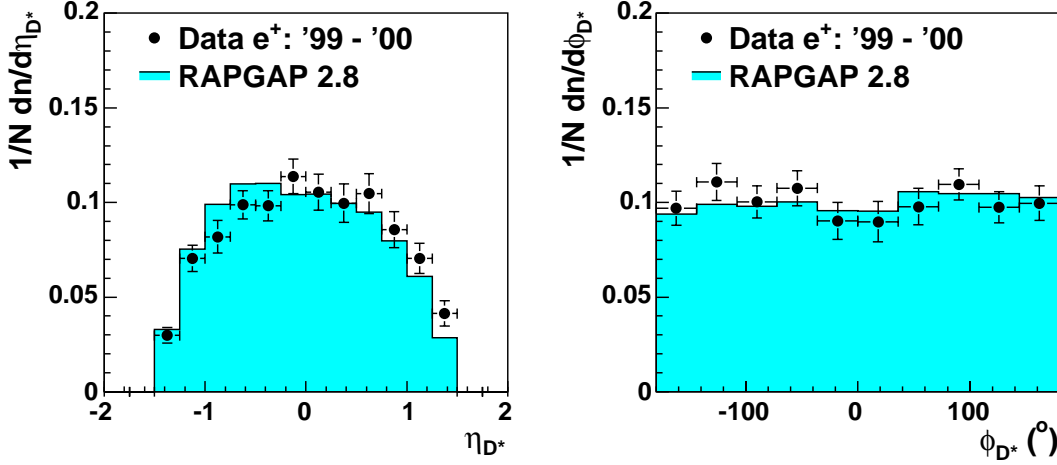


Figure 3.19: The η_{D^*} , left, and ϕ_{D^*} , right, distributions in the data and the MC model.

The η_{D^*} and the ϕ_{D^*} distributions can be seen in Fig. 3.19 and the p_{T, D^*} distribution is shown in Fig. 3.20. The MC model describes the data reasonably well.

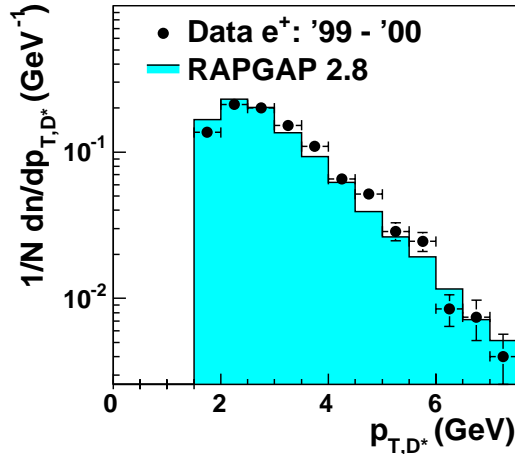


Figure 3.20: The p_{T, D^*} distribution in data and the MC model.

Chapter 4

Measurements of the Jet Shape Variables

In this chapter the results of the studies of the jet shape observables are presented. The classical approach to investigate the structure of jets is to study variables like $\langle\Psi(r, R)\rangle$ and $\langle\rho(r, R)\rangle$, which are called *jet shape variables*. An additional observable of interest is the *mean subjet multiplicity* $\langle n_{\text{subj}}(y_{\text{cut}})\rangle$. These jet observables have been presented in detail in Sec. 1.3. In this analysis, a different definition of the inner radius, which is closer to the k_{\perp} jet finder concept, is used for the first time. The inner radius defines the radius of a concentric area in which the E_{T} of the hadrons is summed up.

A new type of differential jet shape variable, $\langle\rho^*(r, R)\rangle$, is defined and studied for the jet which contains the reconstructed D^* -meson, the D^* Jet. The second charm of the *boson-gluon fusion* (BGF) event can be tagged with a high probability by the *OtherJet*, which is the second jet in the event and fulfills the selection criteria presented in Sec. 4.2. The D^* Jet and the *OtherJet* are compared. The differences between the two types of charm jets are studied. Different definitions of the D^* Jet are also used.

These studies of the charm jet structure are continued in Chapter 5 with an innovative method to analyse the emission of soft gluons by a heavy quark.

4.1 Hadronic Final State Objects

The particles produced in an ep event can be detected as tracks in the tracking detectors or as energy depositions in the calorimeters (LAr and SpaCal). Both measurements have advantages and disadvantages. The tracks can be measured precisely, especially in the region of coverage by the CJC, for transverse momenta p_{T} up to about 25 GeV. The precision decreases with increasing p_{T} [39] :

$$\frac{\sigma(p_{\text{T}})}{p_{\text{T}}} = 0.005 \cdot \frac{p_{\text{T}}}{\text{GeV}} \oplus 0.015 . \quad (4.1)$$

Only charged particles leave tracks in the detector. Neutral particles are not detected by the tracking system and, on average, about one third of the produced particles are not included if only the trackers are used. The calorimeters can detect both types of particles except neutrinos. The uncertainty of the energy measurement decreases with increasing energy, as can be seen in Sec. 2.4.

In order to make the best use of the full momentum and energy range, the information from the trackers and calorimeters are combined. The algorithm that reconstructs

the particle candidates, used in this analysis, is called HADROO2 [53]. The main feature of this algorithm is that the source of the information, which will be used for the reconstruction of a particle, is chosen on the basis of a comparison of the energy resolution of the track and the corresponding cluster. Due to this feature, the most important condition for the algorithm is to avoid double counting of energy. The double counting problem appears for those particles which are detected as tracks in the CJC and also as clusters in the calorimeters. In this situation the information with the smallest uncertainty of the energy resolution is used.

The HADROO2 algorithm defines the hadronic final state (HFS) objects. HFS objects may consist of appropriate combinations of track and cluster energy information or of only track or only cluster information. The algorithm decides if the HFS objects are determined from the four-vector defined by the transverse momentum, p_T , of the track or by the cluster energy. In the next lines a description of the HADROO2 algorithm is presented.

The first step is to select the input, the tracks and the clusters, for the algorithm. The tracks used by the algorithm are from the central region having the angular coverage $20^\circ \leq \theta \leq 160^\circ$, the so-called *central tracks*, and from the forward region, the *forward tracks* with $6^\circ \leq \theta \leq 25^\circ$. The third class of tracks are the *combined tracks* which are linking segments from central and forward region in the $6^\circ \leq \theta \leq 40^\circ$ range. The tracks can be from the primary vertex or from a secondary vertex. The order of preference for assigning one class of track to be an HFS object or to be combined with a cluster is as follows: central, combined and forward tracks. Due to the final cut on the pseudorapidity, η , of the particle candidates which are used to define the HFS, only central tracks are allowed in this analysis. Thus only the quality criteria to select central tracks are shown in the Table 4.1.

Central Track Selection
$p_T > 0.12 \text{ GeV}$
$20^\circ \leq \theta \leq 160^\circ$
$d'_{ca} < 2 \text{ cm}$
$R_{S, \text{track}} \leq 50 \text{ cm}$
$R_{E, \text{track}} - R_{S, \text{track}} > 10 \text{ cm for } \theta < 150^\circ$
$R_{E, \text{track}} - R_{S, \text{track}} > 5 \text{ cm for } \theta > 150^\circ$

Table 4.1: The central track selection criteria used by the HADROO2 algorithm. $R_{E, \text{track}}$ is the radius of the track ending point and $R_{S, \text{track}}$ is the radius of the track starting point. The d'_{ca} parameter is presented in Appendix C.

It has to be mentioned that the scattered electron candidate is searched for by the electron finder before the HADROO2 algorithm is executed. Its cluster and track are locked and are not used by the HFS algorithm. The muon candidates given by the specific finder are also locked.

The position of the cluster is aligned taking into account the geometrical position of the calorimeters with respect to the CJC. This is very important in order to make sure that the track extrapolation to the calorimeter surface will point to the corresponding cluster. One of the limitations of this algorithm is that only the clusters from LAr and SpaCal are used. The Iron and the PLUG clusters are not considered, due to their insufficient energy resolution and their non-negligible contribution of noise. For clusters which have their barycentre in the LAr, but cells also in Iron or PLUG, only

the LAr cells are used.

As a first particle hypothesis, the pion mass is used for tracks. The energy squared of a track is given by:

$$E_{\text{track}}^2 = p_{\text{track}}^2 + m_{\pi}^2 = \frac{p_{\text{T}}^2}{\sin^2 \theta} + m_{\pi}^2 \quad (4.2)$$

and the uncertainty $\sigma_{E_{\text{track}}}$ is calculated from error propagation:

$$\frac{\sigma_{E_{\text{track}}}}{E_{\text{track}}} = \frac{1}{E_{\text{track}}} \cdot \frac{p_{\text{T}}}{\sin \theta} \cdot \sqrt{\sigma_{\theta}^2 \cdot \frac{p_{\text{T}}^2}{\sin^4 \theta} \cdot \cos^2 \theta + \frac{\sigma_{p_{\text{T}}}^2}{\sin^2 \theta}}, \quad (4.3)$$

where σ_{θ} and $\sigma_{p_{\text{T}}}$ are the errors in p_{T} and θ of the track. The correlations between these two track parameters are neglected.

The error of the energy measurement in case that the particle is detected in the calorimeter is estimated by:

$$\frac{\sigma_{E_{\text{LAR, est.}}}}{E_{\text{track}}} = \frac{0.5}{\sqrt{E_{\text{track}}/\text{GeV}}}. \quad (4.4)$$

A track is considered to be of *good quality* if:

$$\frac{\sigma_{E_{\text{track}}}}{E_{\text{track}}} < \frac{\sigma_{E_{\text{LAR, est.}}}}{E_{\text{track}}}. \quad (4.5)$$

For the central region the track measurement is better than a corresponding cluster in the calorimeter up to ~ 25 GeV.

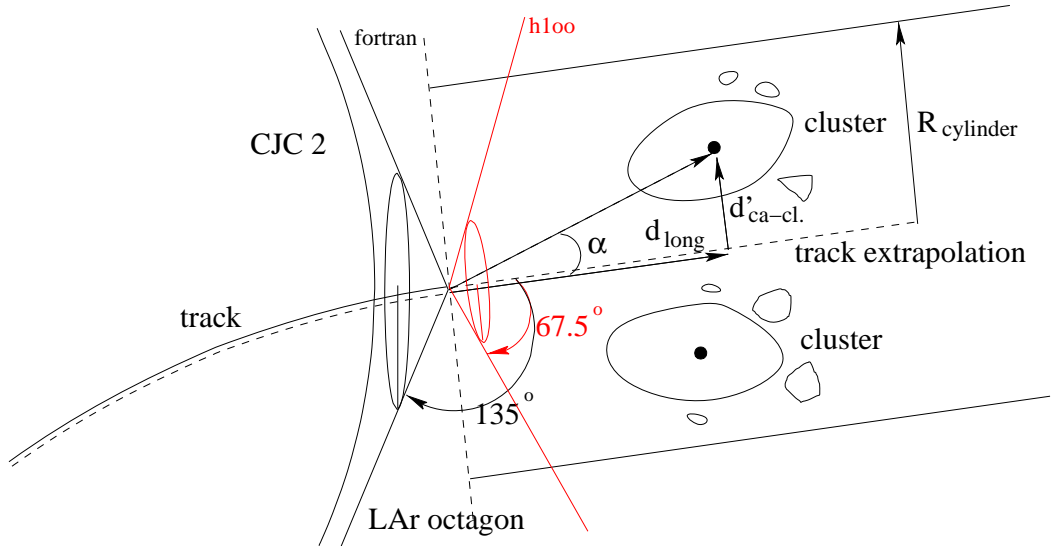


Figure 4.1: An illustration of the combination algorithm, in the $r - \phi$ view, applied in the HFS finder. The parameters d_{long} , $d'_{\text{ca-cl.}}$ and R_{cylinder} are used to select the clusters corresponding to the track.

Each track is extrapolated to the surface of the calorimeters as a helix, as illustrated in Fig. 4.1. Inside the calorimeter, the track is extrapolated as a straight line. The calorimetric energy $E_{\text{clus-tr}}$ is calculated as the sum of all cluster energies for clusters

overlapping with the volume of a cone with opening angle $\alpha = 67.5^\circ$ and a cylinder with radius of 25 cm for the EMC part and 50 cm for the HAD part¹.

The energies of the track E_{track} and its associated cluster $E_{\text{clus-tr}}$, including possible fluctuations of both measurements within their standard errors, are compared. For:

$$E_{\text{clus-tr}} < E_{\text{track}} \cdot \left[1 + 1.96 \sqrt{\left(\frac{\sigma_{E_{\text{track}}}}{E_{\text{track}}} \right)^2 + \left(\frac{E_{\text{LAR, est.}}}{E_{\text{track}}} \right)^2} \right] \quad (4.6)$$

the track is used to define the HFS object and the associated clusters are discarded. For $E_{\text{clus-tr}} - E_{\text{track}} > 0$, there is the hypothesis that one of the clusters is coming from the charged particle track and the second one from a neutral particle or another track which is extrapolated into the same calorimetric volume. The difference in energy is considered further in the algorithm as a new cluster.

If the condition of Eq. 4.5 is not fulfilled and:

$$E_{\text{clus-tr}} - 1.96 \cdot \sigma_{E_{\text{clus-tr}}} < E_{\text{track}} < E_{\text{clus-tr}} + 1.96 \cdot \sigma_{E_{\text{clus-tr}}}, \quad (4.7)$$

where $\sigma_{E_{\text{clus-tr}}} = 0.5 \sqrt{E_{\text{clus-tr}}/\text{GeV}}$ (GeV), the track energy is considered to be compatible with the calorimetric energy deposition. In this case the cluster energy is used to compute the four-vector that defines the HFS object.

After all tracks are extrapolated, the remaining clusters are used to form the neutral HFS objects. If more than 95% of the cluster energy is deposited in the EMC part and more than 50% of the energy in the first two layers of the EMC, then the cluster is most likely due to a photon. In this case, the electromagnetic energy scale is used for the cluster energy, otherwise the hadronic energy scale is applied.

The presented HFS algorithm describes the DIS charm events particles well due to the fact that they are mainly produced in the central detector region by selection and that they are dominated kinematically by relatively low energies.

In Fig. 4.2 one can observe a good correlation between the sum of the energies of generated particles and the reconstructed sum of the HFS objects at the detector level. In Appendix G more studies on HFS can be found.

Another control distribution for the HFS reconstruction algorithm is the ratio between the p_T of the HFS objects and the p_T of the scattered electron. This distribution is usually called the p_T balance distribution.

In Fig. 4.3 the p_T balance distribution is shown at the reconstructed level. One can observe that the peak position is at the value of 1 and that the MC model describes the data reasonably well.

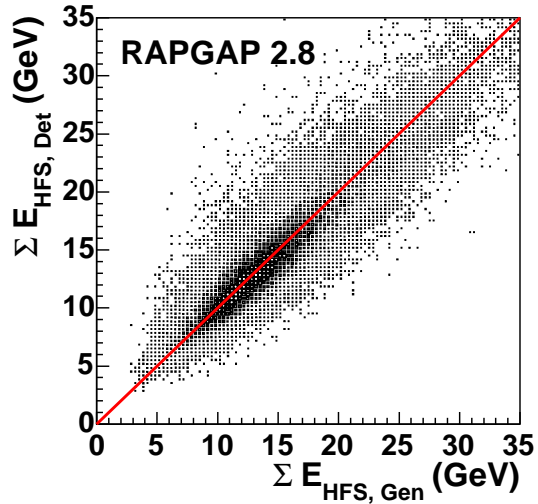


Figure 4.2: The correlation between the $\sum E_{HFS}$ on detector and the particle energies on hadron level.

¹In the Fortran environment the opening angle was 135° while in *h1oo* it is 67.5°

In this analysis the jet finder is run only over HFS objects in the central region of the H1 detector, which ensures high resolution and which is best understood:

$$p_{T,HFS} > 0.12 \text{ GeV}; \quad (4.8)$$

$$|\eta_{HFS}| < 2.0. \quad (4.9)$$

4.2 Jet Selection

The HFS objects, selected as presented in Sec. 4.1, are stored in the particle candidates array. From the HFS objects, the ones used to reconstruct the D^* -meson are discarded.

The D^* -meson, treated as a stable particle, is added to the selected particle candidates array.

The jets used in this analysis are found with the k_{\perp} cluster algorithm described in Sec. 1.3. The k_{\perp} jet finder is applied to the selected particle candidates in the laboratory frame. The advantage of using the laboratory frame is that the errors due to the boost of particle candidates into the centre of mass frame, the γ^*p -frame, are avoided.

For this classical part of the analysis the events are selected if a D^* Jet is found and fulfills the criteria:

$$p_{T, \text{Jet}} > 1.5 \text{ GeV}; \quad (4.10)$$

$$|\eta_{\text{Jet}}| < 1.5. \quad (4.11)$$

The events which have a D^* Jet form a first event sample.

The *OtherJet* is the remaining jet with the highest transverse momentum which fulfills the same $p_{T, \text{Jet}}$ and η_{Jet} requirements as above.

The azimuthal opening angle between the D^* Jet and the *OtherJet* found in the laboratory frame and then boosted into the γ^*p -frame shows the expected back-to-back topology as observed in Fig. 4.4.

A typical event is shown in Fig. 4.5.

The control plots for the found jets are presented in Fig. 4.6 and Fig. 4.7. The MC model describes the data very well in the E_{Jet} , the η_{Jet} and the ϕ_{Jet} distributions.

Another important aspect of the jet finding algorithm is the correlation between the energy and direction of the parton and the corresponding jet. The jet on detector

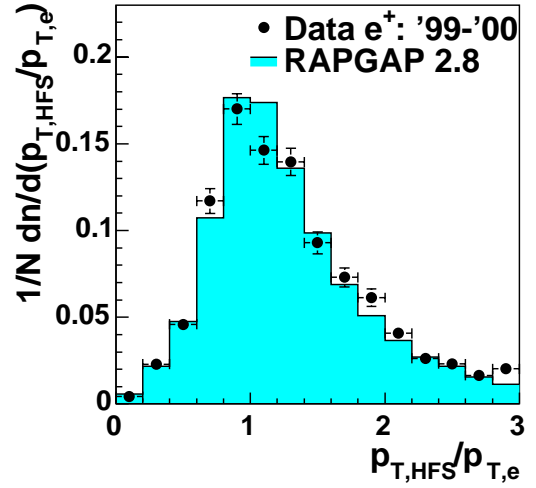


Figure 4.3: The p_T balance distribution.

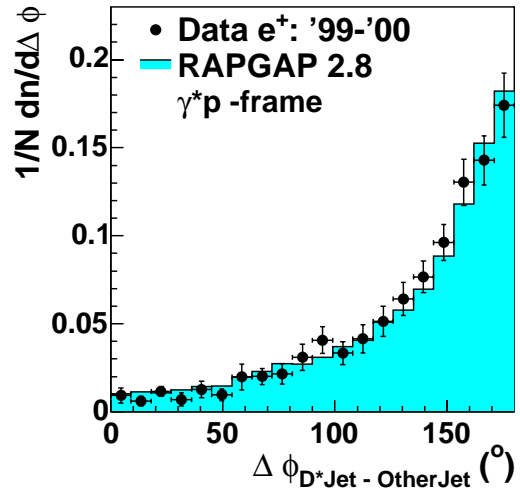


Figure 4.4: The back-to-back topology of the D^* Jet and *OtherJet* boosted into the γ^*p -frame.

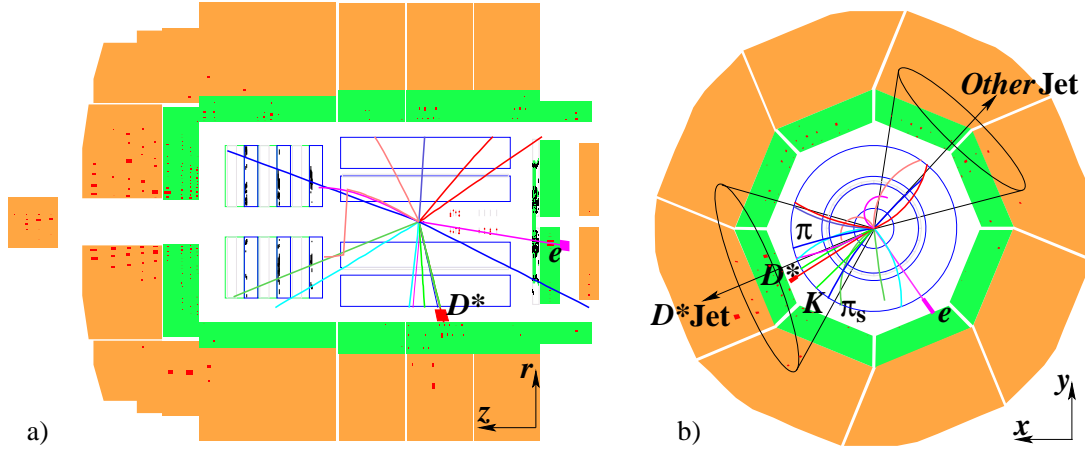


Figure 4.5: A typical event in the side view a) and the radial view b).

level is in general expected to provide a good representation of a corresponding quark or gluon on parton level. The correlations between the D^* Jet and the $OtherJet$ and the c and the \bar{c} quark are illustrated in Appendix F.

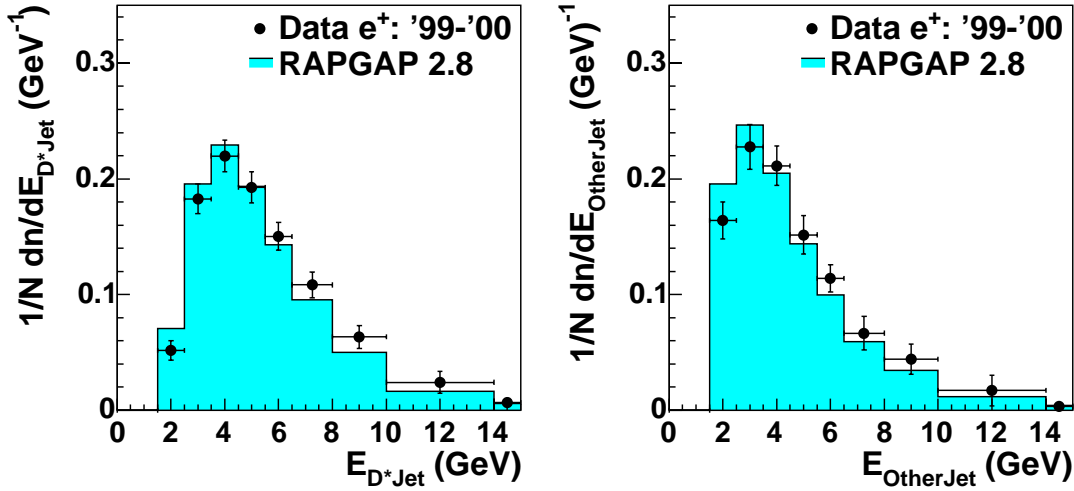


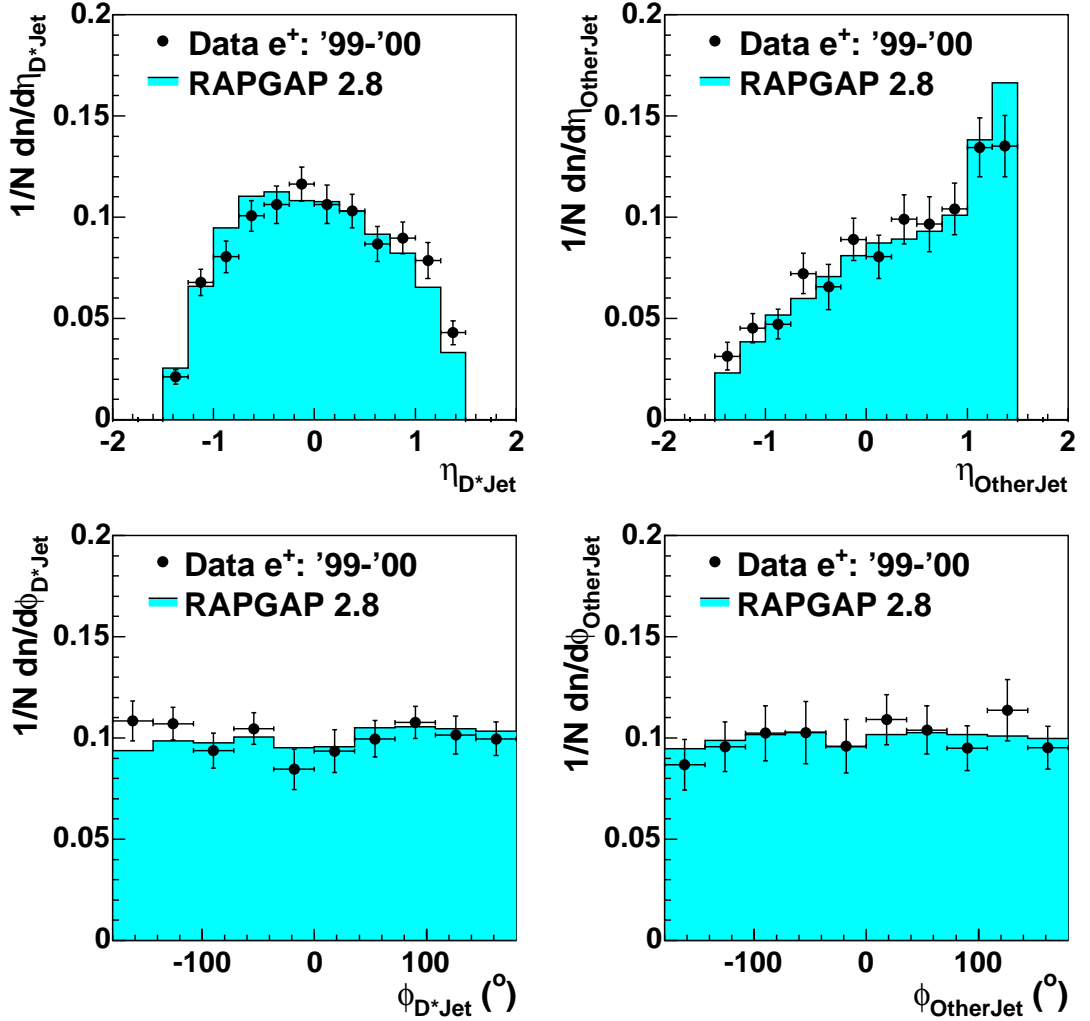
Figure 4.6: The energy distributions for the D^* Jet and the $OtherJet$.

4.3 Background Subtraction

In Sec. 3.3.3 the reconstruction of the D^* -mesons used to select the event sample for this analysis was presented. As one can observe in Fig. 4.8 a) and b), the event sample contains also background from non-charm and charm events. This background has to be statistically subtracted for the determination of the jet shape variables. The measured observables for the jet shape variables are average values obtained from the total jet sample:

$$\langle x_{\text{meas}} \rangle = \frac{1}{N_{\text{jets}}} \sum_{j=1}^{\text{jets}} x_j. \quad (4.12)$$

The relation between the background (WrCh) and the signal (RiCh) contributions


 Figure 4.7: The η and the ϕ distributions for the D^* Jet and the *OtherJet*.

can be written as:

$$\langle x_{\text{meas}} \rangle = (1 - f_{\text{bg}}^*) \cdot \langle x_{\text{sig}} \rangle + f_{\text{bg}}^* \cdot \langle x_{\text{bg}} \rangle, \quad (4.13)$$

where $f_{\text{bg}}^* = N_{\text{bg}}/N_{\text{total}}$ is the fraction of the background jet sample to the total one. The $\langle x_{\text{sig}} \rangle$ and $\langle x_{\text{bg}} \rangle$ are averages over the signal and background jet sample variables, respectively, where x stands for $\Psi(r, R)$, $\rho(r, R)$, $\rho^*(r, R)$ and $n_{\text{sbj}}(y_{\text{cut}})$.

N_{total} represents the total number of jets (separately for D^* Jet and *OtherJet*) given by the right charge (RiCh) combinations. N_{bg} is calculated using:

$$N_{\text{bg}} = \frac{1}{k_N} \cdot N_{\text{WrCh}}, \quad (4.14)$$

where N_{WrCh} is the number of jets from the wrong charge (WrCh) combinations and k_N provides the normalisation in the Δm distribution fit between the RiCh and the WrCh spectra.

The signal value is obtained by subtracting the background contribution from the

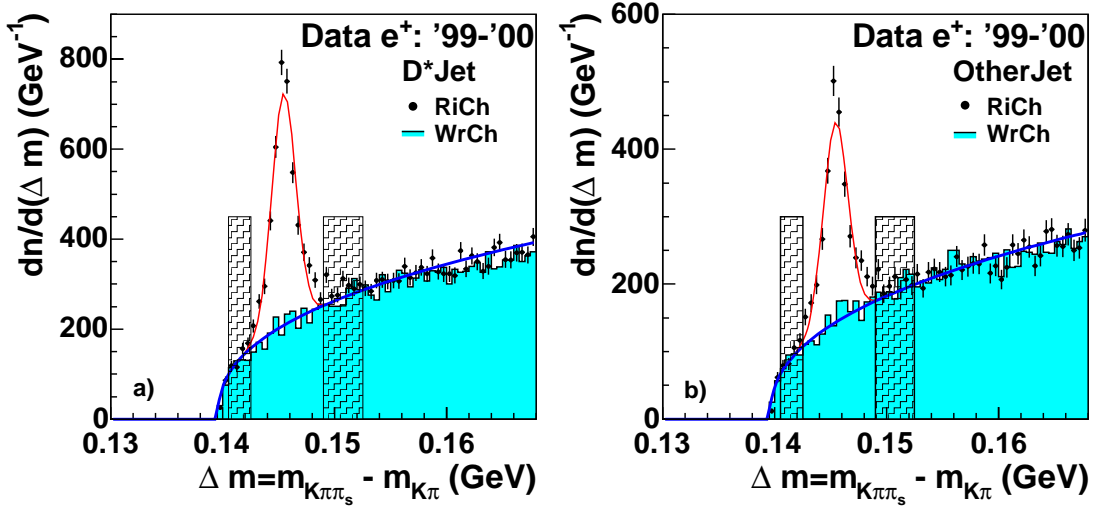


Figure 4.8: The Δm distribution for events with a D^* Jet, a), and for events with an additional *OtherJet*, b). The *side bands* used in estimating the systematic error in the determination of the background are shown by the two rectangles on both sides of the signal peak.

measured one as follows:

$$\langle x_{\text{sig}} \rangle = \frac{\langle x_{\text{meas}} \rangle - f_{\text{bg}}^* \cdot \langle x_{\text{bg}} \rangle}{1 - f_{\text{bg}}^*}. \quad (4.15)$$

4.4 Error Calculation

The errors on the jet shape observables are given by the quadratic sum of the statistical and the systematic errors. The statistical errors introduced by the background subtraction procedure are taken into account. The sources of the systematic errors are presented in Sec. 4.4.1.

The statistical errors of the RiCh and the WrCh combinations together with the normalisation factor k_N are considered to be independent. This approximation appears reasonable since k_N is given by a simultaneously fit of the RiCh and the WrCh combinations and does not depend on the total number of jets from the two samples. The error of the signal is calculated using the standard formula for error propagation applied to Eq. 4.15. The final formula is:

$$\sigma_{\langle x_{\text{sig}} \rangle} = \frac{1}{1 - f_{\text{bg}}^*} \cdot \sqrt{\sigma_{\langle x_{\text{meas}} \rangle}^2 + (f_{\text{bg}}^* \cdot \sigma_{x_{\text{bg}}})^2 + \left(\frac{\langle x_{\text{meas}} \rangle - \langle x_{\text{bg}} \rangle}{1 - f_{\text{bg}}^*} \right)^2 \cdot \sigma_{f_{\text{bg}}^*}^2} \quad (4.16)$$

where the f_{bg}^* error is given by:

$$\sigma_{f_{\text{bg}}^*} = \frac{1}{k_N \cdot N_{\text{RiCh}}} \cdot \sqrt{\sigma_{N_{\text{WrCh}}}^2 + \sigma_{N_{\text{RiCh}}}^2 \cdot \left(\frac{N_{\text{WrCh}}}{N_{\text{RiCh}}} \right)^2 + \sigma_{k_N}^2 \cdot \left(\frac{N_{\text{WrCh}}}{k_N} \right)^2} \quad (4.17)$$

and σ_{k_N} is the error of the normalisation factor given by the fit function.

4.4.1 Systematic Errors

An essential component of a measurement is the estimation of the *systematic errors*.

The jet shape variables, as well as the mean subjet multiplicity, are measured and presented in this paper at the *hadron level*. In order to correct the data obtained at the detector level to the *hadron level* one has to make use of a **MC model** and **detector simulations**. These are two classes of systematic errors that contribute to the result presented here. A third class of errors is related to the **selection cuts** which are used to reject the background and to enhance the signal.

In this section the systematic error contributions of the detector simulation and of the selection cuts are discussed. In Sec. 4.6 the contribution to the systematic error due to imperfections of the physics model of the MC are presented.

Systematic Errors Due to Detector Simulations

In order to calculate the influence of the **detector simulation** on the result, one has to estimate within which limits the reconstructed MC quantities can be varied so that they can still describe the data.

The most important quantities are the energy and the θ angle of the scattered electron and of the HFS objects.

For the possible uncertainty in the energy of the scattered electron and the HFS objects, the limits are obtained from the so-called double ratio distributions.

For the electron it is provided by the E'_e/E_{DA} distribution of the ratio between the values obtained in data and MC. In Fig. 4.9 one can observe that the MC simulation describes the data within $\pm 2\%$.

The uncertainty in the energy of the HFS objects is given by the p_T balance, see Fig. 4.3, more precisely by the ratio between data and MC. If the HFS object is formed using only cluster information, a variation of $\pm 4\%$ in energy [54] is applied to obtain the systematic error. For

the HFS objects using only track information, a $\pm 2\%$ variation in energy is used, which is a reasonable approximation of Eq. 4.1. The objects formed after a track and a cluster are combined, as presented in Sec. 4.1, have a variation of $\pm 3\%$ in energy.

The θ angle [54] of all type of objects is varied within ± 3 mrad. For the scattered electron the θ angle variation is done within ± 2 mrad.

A summary of the systematic error sources given by the **detector simulation** and their range of variation range is presented in Table 4.2.

The **mathematical formalism** used to calculate the systematic error given by the **detector simulations** is described in the following.

Let in general x be a function which depends on the parameter p . A jet observable (e.g. *subjet multiplicity*) depends on the reconstructed quantities (e.g. *energy* of the HFS objects).

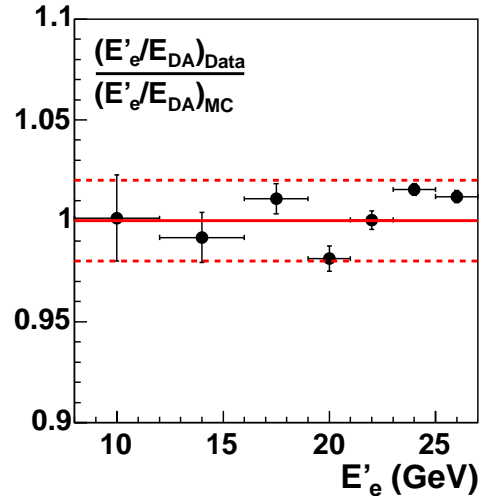


Figure 4.9: The E'_e/E_{DA} double ratio distribution vs. E'_e .

Measured Observable	Variation Range
Energy of the scattered electron	$\pm 2\%$
θ angle of the scattered electron	± 2 mrad
Energy of the HFS object: track/cluster/track-cluster	$\pm 2/4/3\%$
θ angle of the HFS object	± 3 mrad

Table 4.2: Systematic error sources due to the detector simulation and their range of variation.

The experimental results obtained at the detector level are transformed to the hadron level as follows:

$$x^{had} = x^{Det} \cdot \frac{x^{MC, Gen}}{x^{MC, Rec}}, \quad (4.18)$$

where $x^{MC, Rec}$ is the radiative MC model result at the reconstructed (detector) level, x^{Det} represents the data (at detector level) and $x^{MC, Gen}$ is the MC result obtained at the generator level. Details about the correction procedure of the data to the hadron level can be found in the Sec. 4.6.

For the systematic errors which are due to the **detector simulation**, one should vary the parameter p only in data *or* in MC, not in both. Usually, due to higher statistics, the variation in MC is chosen. From the variation of the parameter p the following result is obtained:

$$x_p^{MC, Rec} = x^{MC, Rec} \cdot (1 + \varepsilon^{MC, Rec}), \quad (4.19)$$

and the new value of the x^{had} will be:

$$x_p^{had} = x^{Det} \cdot \frac{x^{MC, Gen}}{x^{MC, Rec}(1 + \varepsilon^{MC, Rec})}, \quad (4.20)$$

where $\varepsilon^{MC, Rec}$ is the relative difference obtained for the variation of the parameter p in MC at the reconstructed level.

The variation of the x^{had} value will be:

$$\sigma_{x^{had}} = x_p^{had} - x^{had} = \underbrace{x^{Det} \cdot \frac{x^{MC, Gen}}{x^{MC, Rec}}}_{x^{had}} \cdot \frac{\varepsilon^{MC, Rec}}{1 + \varepsilon^{MC, Rec}}. \quad (4.21)$$

The relative systematic error is given by:

$$\varepsilon^{x^{had}} = \frac{\sigma_{x^{had}}}{x^{had}} = \frac{\varepsilon^{MC, Rec}}{1 + \varepsilon^{MC, Rec}}. \quad (4.22)$$

Systematic Errors Due to Selection Cuts

Another class of systematic errors is given by the **selection cuts**, which show if the events migrate in or out of the selected phase space, and the parameter R_{Jet} of the k_{\perp} jet finder algorithm, which limits the search range in the (η, ϕ) plane for the hadrons attributed to a certain jet.

Due to the fact that the variation of these cuts cannot be done in both directions, positive and negative, e.g. $|\eta_{HFS}| < 2.25$, it is assumed that the same systematic deviation is obtained for the symmetric variation of the cut.

The following selection cuts have been modified as described in Table. 4.3.

Measured Observable	Initial Cut	Varied Cut
η of the HFS object	$ \eta_{HFS} < 2$	$ \eta_{HFS} < 1.75$
η of the D^* -meson daughters	$ \eta_{K,\pi,\pi_s} < 1.5$	$ \eta_{K,\pi,\pi_s} < 1.25$
Transverse momentum of K and π	$p_{T,K,\pi} > 0.25$ GeV	$p_{T,K,\pi} > 0.3$ GeV
Transverse momentum of π_s	$p_{T,\pi_s} > 0.12$ GeV	$p_{T,\pi_s} > 0.15$ GeV

Table 4.3: Systematic errors due to selection cuts.

The **mathematics** behind the calculation of these systematic errors is different from the one used for the **detector simulations** class.

For the systematic errors given by the **selection cuts** the function x , which depends on the parameter p , the variation with the same amount of the parameter p has to be done in data and in MC, in order not to overestimate the errors. The following equations are obtained:

$$\begin{aligned} x_p^{Det} &= x^{Det} \cdot (1 + \varepsilon^{Det}) \\ x_p^{MC, Rec} &= x^{MC, Rec} \cdot (1 + \varepsilon^{MC, Rec}), \end{aligned} \quad (4.23)$$

where ε^{Det} and $\varepsilon^{MC, Rec}$ are the relative differences of the results obtained for the variation of parameter p in the data and in the MC model at the reconstructed level, respectively. This treatment of the errors can be used when there is enough statistics in data such that the contribution from statistical fluctuations is negligible.

If the results differ by an amount $\Delta\varepsilon$:

$$\varepsilon^{Det} = \varepsilon^{MC, Rec} + \Delta\varepsilon \quad (4.24)$$

the variation of the "had" values would be:

$$\sigma_{x^{had}} = \underbrace{x^{Det} \cdot \frac{x^{MC, Gen}}{x^{MC, Rec}}}_{x^{had}} \cdot \frac{\Delta\varepsilon}{1 + \varepsilon^{MC, Rec}}. \quad (4.25)$$

The relative systematic error will be given by the following formula:

$$\varepsilon^{x^{had}} = \frac{\varepsilon^{Det} - \varepsilon^{MC, Rec}}{1 + \varepsilon^{MC, Rec}}. \quad (4.26)$$

The parameter which limits the jet "radius" belongs to same class as the **selection cuts**. This parameter, R_{Jet} , see Sec. 1.3, is correlated with the charm quark that produced the jet. As a measure of this correspondence between the jet and the charm quark, the energy ratio E_c/E_{D^*Jet} and the number of "reconstructed" charm quarks, N_c , with the D^*Jet are used.

The E_c/E_{D^*Jet} distribution should have its mean value, $\mu_{E_c/E_{D^*Jet}}(R_{Jet})$, at the value of 1.

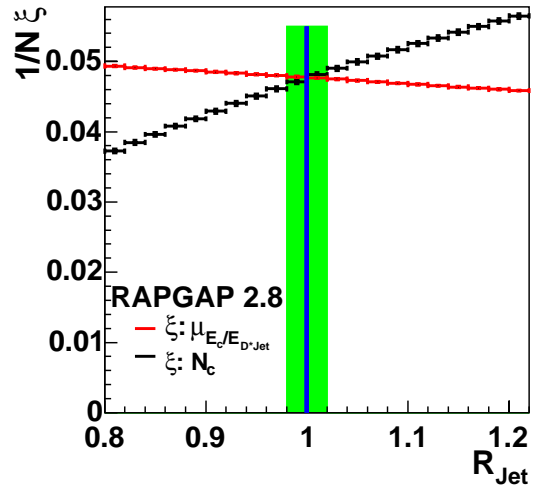


Figure 4.10: The $\mu_{E_c/E_{D^*Jet}}(R_{Jet})$ and the $N_c(R_{Jet})$ dependences normalised to 1. The two curves cross is at: $R_{Jet} = 1 \pm 0.02$.

The variation of the jet "radius" R_{Jet} of $\pm 2\%$ is used to determine a systematic error. These limits in the variation of R_{Jet} are motivated by the uncertainty of defining the value where the mean value dependence $\mu_{E_c/E_{D^* \text{Jet}}}(R_{\text{Jet}})$ crosses the number of reconstructed charm quarks $N_c(R_{\text{Jet}})$, as can be seen in Fig. 4.10.

Another source of systematic errors is due to the non-uniqueness of the background subtraction. The normalisation factor between RiCh and WrCh combinations, introduced in Sec. 3.3.5, can be determined also using the so-called *side bands*, shown in the Fig. 4.8.

The k_{SB} normalisation factor is calculated using the summation procedure:

$$k_{SB, \text{sum}} = \frac{\sum_{j=N_{1i}}^{N_{1f}} N_{j, \text{WrCh}} + \sum_{j=N_{2i}}^{N_{2f}} N_{j, \text{WrCh}}}{\sum_{j=N_{1i}}^{N_{1f}} N_{j, \text{RiCh}} + \sum_{j=N_{2i}}^{N_{2f}} N_{j, \text{RiCh}}}. \quad (4.27)$$

$N_{1i} = 0.140$ GeV and $N_{1f} = 0.142$ GeV are the boundaries of the first *side band* and $N_{2i} = 0.149$ GeV and $N_{2f} = 0.153$ GeV are the limits for the second *side band*. The boundaries are selected to be outside of the signal window but close enough to it, such that the background estimation does not need a large extrapolation. The difference $k_N - k_{SB}$ gives the systematic variation of the normalisation factor:

$$\varepsilon_k = \frac{|k_N - k_{SB}|}{k_N}. \quad (4.28)$$

For the $D^* \text{Jet}$ event sample $\varepsilon_{k, D^* \text{Jet}} = 3\%$ is obtained and for the *OtherJet* event sample the value is $\varepsilon_{k, \text{OtherJet}} = 0.6\%$. The variation will consider both signs of ε_k , positive and negative.

For the jet shape variables also the systematic errors due to the MC physics model can be estimated. This is explained in detail in Sec. 4.6. The negative and positive contributions of the different systematic errors are separately added in quadrature.

In Fig. 4.11 the total systematic errors due to the detector simulation and selection cuts for the mean subjet multiplicity of the $D^* \text{Jet}$ and *OtherJet* respectively, are presented.

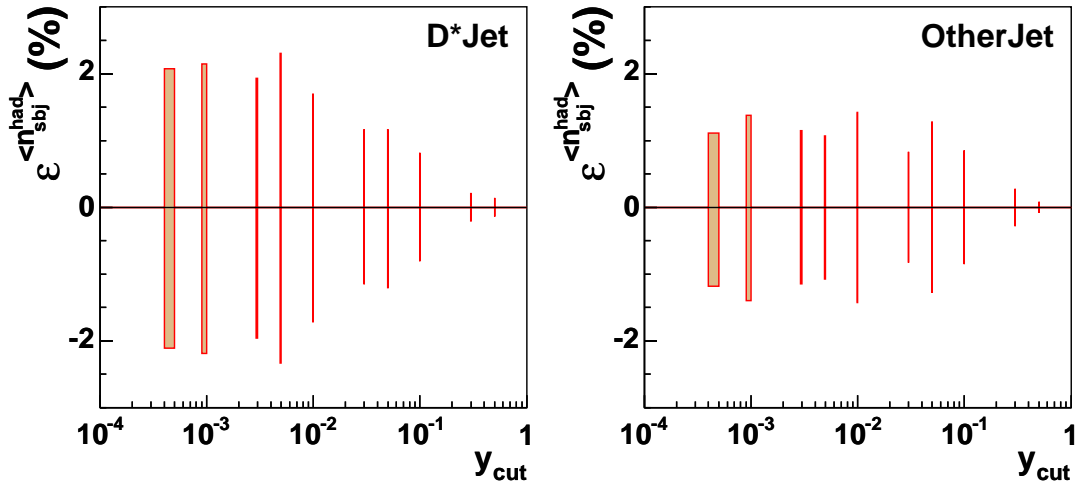


Figure 4.11: The relative systematic errors of the mean subjet multiplicity $\langle n_{\text{subj}} \rangle$.

One can observe that the total systematic error, for the detector level, is around $\pm 2\%$ for both jets. The main contribution is given by the variation of the parameter R_{Jet} of the k_{\perp} jet algorithm and the variation of the π_s selection cuts.

A complete overview of the various contributions can be found in Appendix H.

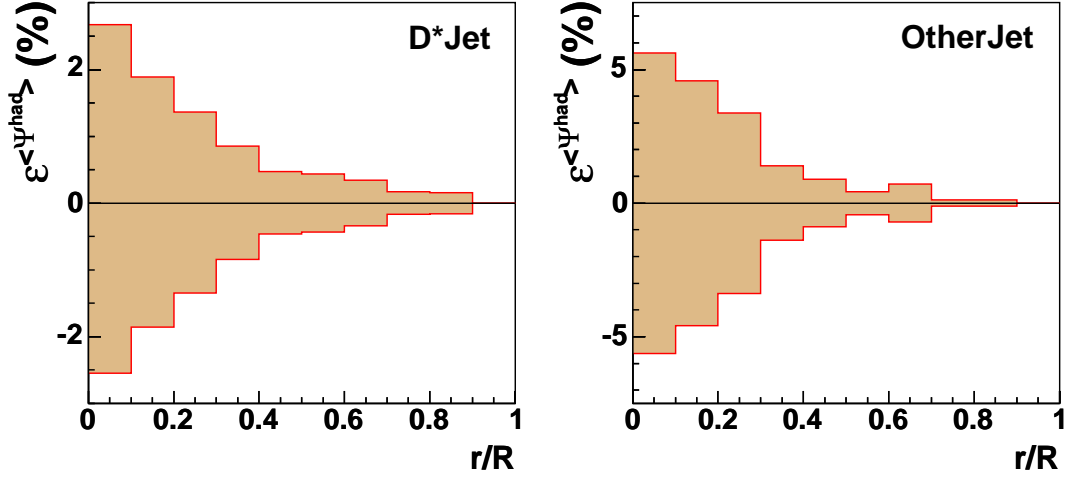


Figure 4.12: The relative systematic errors of the integrated jet shape variable $\langle \Psi(r/R) \rangle$ where $R = 1$.

The systematic errors for the integrated jet shape variable, $\langle \Psi(r/R) \rangle$, are shown in Fig. 4.12. On average, the systematic errors at the detector level for $\langle \Psi(r/R) \rangle$ of the $D^* \text{Jet}$ is around 1%. For the inner part of the jet, the systematic error reaches $\sim 2.5\%$ and decreases to $\sim 0\%$ at the upper limit of the jet radius because $\langle \Psi(r/R) \rangle$ approaches 1 for $r \rightarrow R$ by definition. For the bins with $r/R < 0.9$, the energy of the jet particles and their direction can vary and a systematic shift is observed. The shift decreases from the inner part to the outer side because $\langle \Psi(r/R) \rangle$ is summing the energy bin after bin.

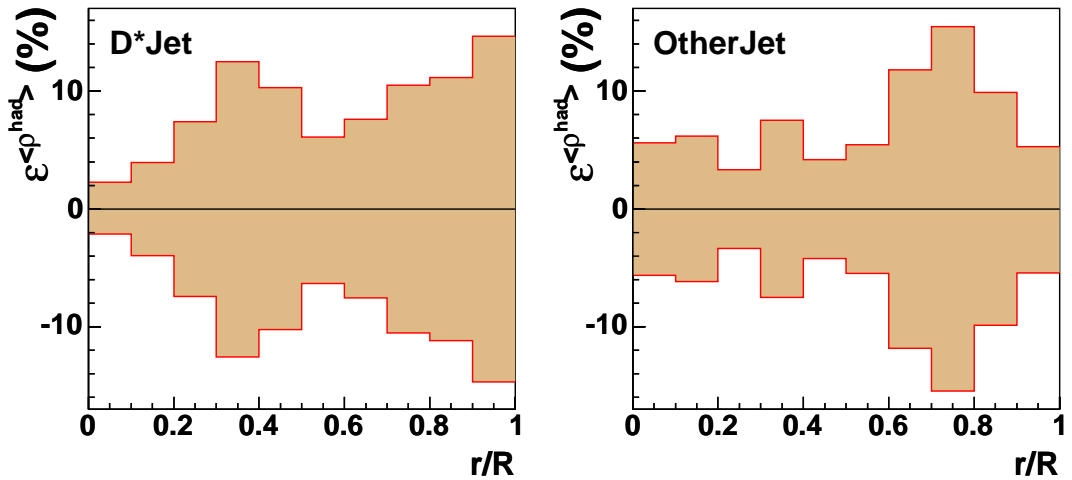


Figure 4.13: The relative systematic errors of the differential jet shape variable $\langle \rho(r/R) \rangle$ where $R = 1$.

The main contributions are given by the parameter R_{Jet} , the π_s selection cuts and the normalisation factor k_N . For the $Other \text{Jet}$, the systematic errors are doubled due

to the fact that the precision of the D^* -meson energy measurement is missing.

The systematic errors for the differential jet shape variable, $\langle \rho(r/R) \rangle$, are shown in Fig. 4.13. The average of the systematic errors for the D^* Jet and the *OtherJet* is $\sim 8\%$. The main contributions are given by the R_{Jet} , the π_s selection cuts, the η range of the K and the π , as well as k_N .

The systematic errors for the jet shape variable $\langle \rho^*(r/R) \rangle$, with an average of $\sim 12\%$, are presented in Fig. 4.14. The main contributions are given by the same parameters as for the $\langle \rho(r/R) \rangle$ jet shape variable.

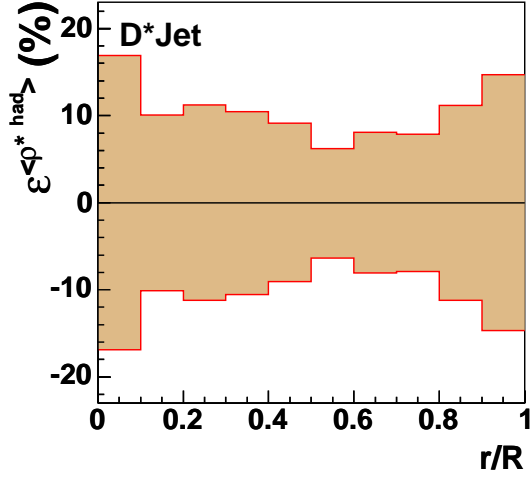


Figure 4.14: The relative systematic errors of $\langle \rho^*(r/R) \rangle$ where $R = 1$.

4.5 Results at the Detector Level

In this section the jet shape observables at detector level are presented. The statistical and systematic errors are added in quadrature.

In the Fig. 4.15 the results of the mean subjet multiplicity, $\langle n_{\text{subj}} \rangle$, at the detector level, are presented as a function of y_{cut} .

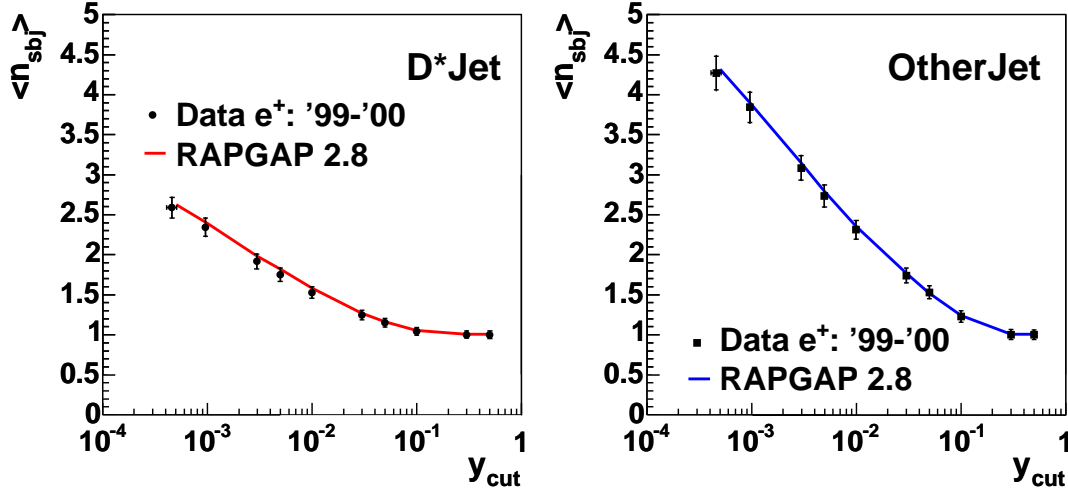


Figure 4.15: The mean subjet multiplicity $\langle n_{\text{subj}} \rangle$ at the detector level as a function of y_{cut} .

The boundaries of the concentric jet fraction, used for the measurement of jet shape variables, are given by the parameter r which is defined as:

$$r = \sqrt{(\eta_h - \eta_{\text{Jet}})^2 + (\phi_h - \phi_{\text{Jet}})^2} \quad (4.29)$$

where the index h is used for the hadrons which are forming the Jet.

The integrated and the differential jet shape variables are shown in Fig. 4.16 and Fig. 4.17, respectively.

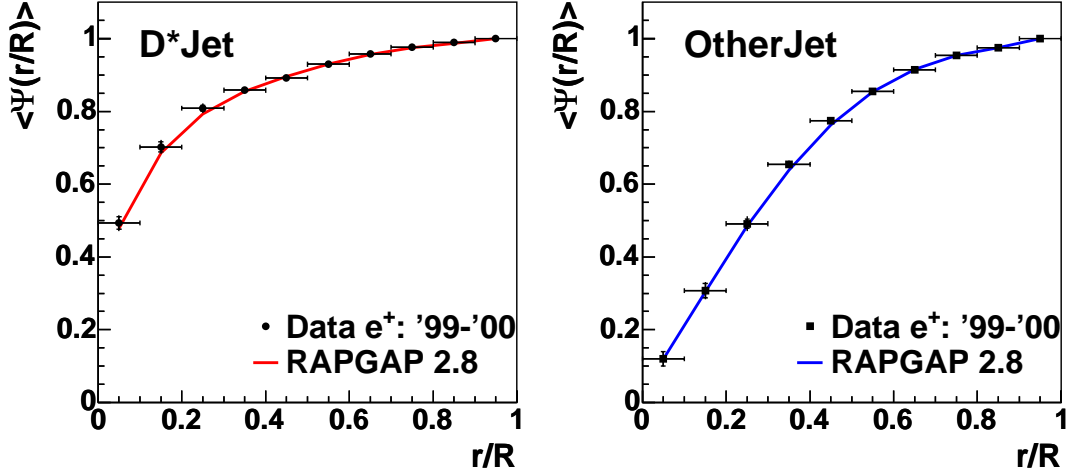


Figure 4.16: The integrated jet shape variable $\langle \Psi(r/R) \rangle$ at the detector level ($R = 1$).

One can observe that the MC model used in this analysis, RAPGAP 2.8, describes the data reasonably well for the classical jet shape observables. Another important observation is that although the two jets are coming from charm or anti-charm quarks they are quite different in shape. A study of these differences is presented in Sec. 4.8.

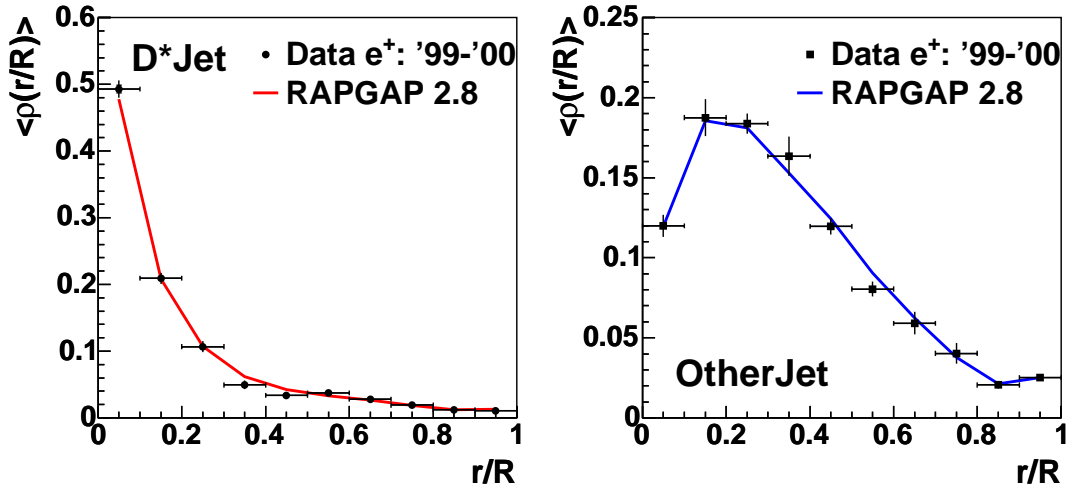


Figure 4.17: The differential jet shape variable $\langle \rho(r/R) \rangle$ at the detector level ($R = 1$).

An additional differential jet shape variable, $\langle \rho^*(r/R) \rangle$, can be defined for the D^* Jet by excluding the D^* -meson candidate from the sum over the hadrons. The E_T of the D^* Jet is kept unchanged. This variable shows the flow of the E_T around the D^* -meson within its jet, see Fig. 4.18.

4.6 Correction of the Data to the Hadron Level

In order to make these results available for comparison with theoretical predictions or with the results from other experiments, one has to correct them for different detector effects, such as detector efficiency and resolution, geometrical acceptance, interactions with dead material, and effects of the trigger and event selection.

Before the corrections are performed, particularly when applying bin by bin corrections, one should check the *stability* and *purity* of the distributions.

They are defined as:

$$S = \frac{N_{\text{had \& det}}}{N_{\text{had}}} \quad \text{and} \quad P = \frac{N_{\text{had \& det}}}{N_{\text{det}}}, \quad (4.30)$$

where N_{had} and N_{det} are the number of events found within a given bin using the selection criteria on hadron and on detector level, respectively. The N_{det} is often referred to as N_{rec} , the number of events at the *reconstructed* level; the detector and the *reconstructed* level are the same. $N_{\text{had \& det}}$ is the number of events which pass the selection cuts on both levels simultaneously for the given bin.

The stability is a measure of how many events from hadron level are reconstructed on detector level within the same bin. For events populating a given bin at detector level, the fraction of events which are found in the same bin at hadron level is defined as purity.

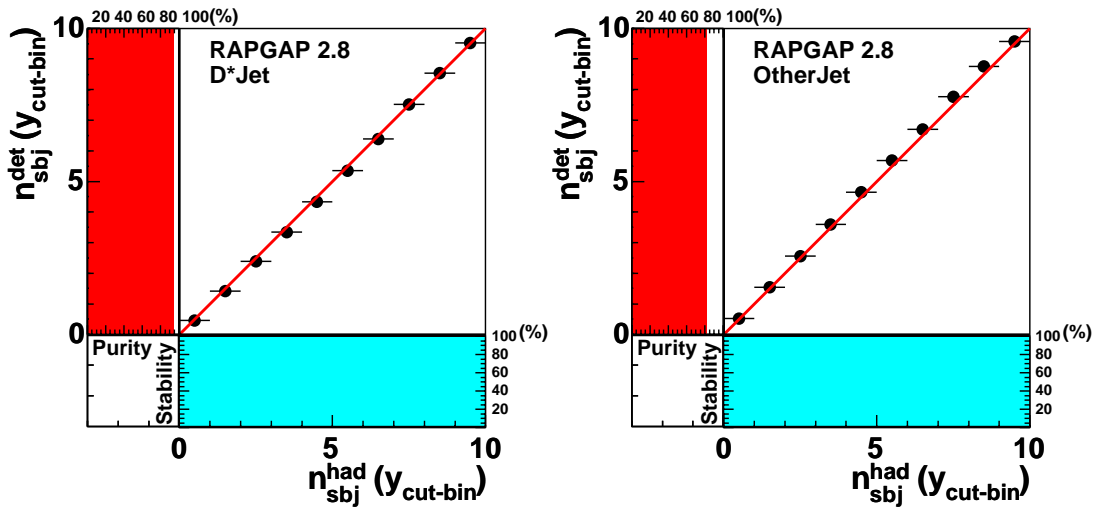


Figure 4.19: The purity, stability and the correlation for the mean subjet multiplicity, $\langle n_{\text{subj}} \rangle$, between hadron and detector level for the D^* Jet and the *OtherJet*, in bins of y_{cut} .

The values of purity and stability are in general above 50% in each bin of the

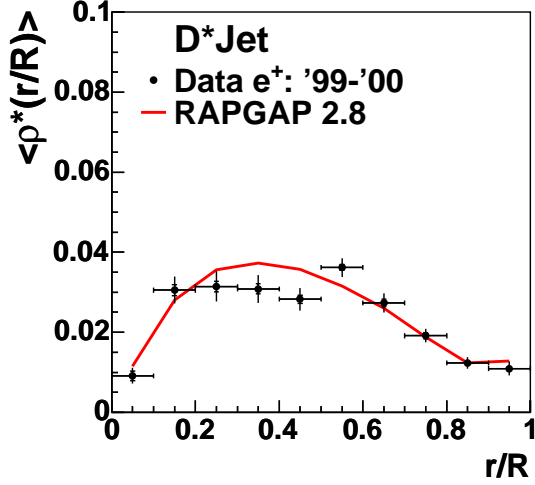


Figure 4.18: The $\langle \rho^*(r/R) \rangle$, ($R = 1$).

various distributions, which is a reasonable requirement in order to apply the so-called bin-by-bin correction. The additional condition that the data are reasonably described by the MC simulations is also fulfilled.

In Fig. 4.19, the correlation between $\langle n_{\text{sbj}} \rangle$ at hadron level and at the detector level is presented. The closer the point is in a y_{cut} bin to the first bisecting line, the better the results of $\langle n_{\text{sbj}} \rangle$ at hadron and detector level are correlated. Parallel with the x -axis, the stability, in percent, is plotted in bins of y_{cut} . The purity is plotted parallel with the y -axis.

The purity, the stability and the hadron-detector level correlation for the integrated jet shape variable, $\langle \Psi(r/R) \rangle$, are illustrated in Fig. 4.20.

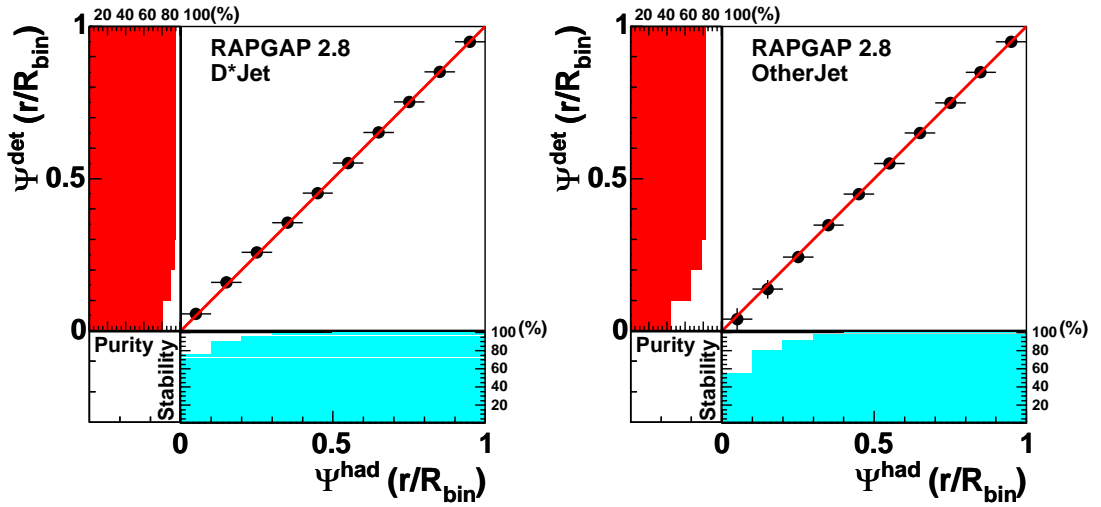


Figure 4.20: The purity, stability and the correlation for the integrated jet shape variable, $\langle \Psi(r/R) \rangle$, between hadron and detector level for the D^* Jet and the *OtherJet*, in bins of r/R .

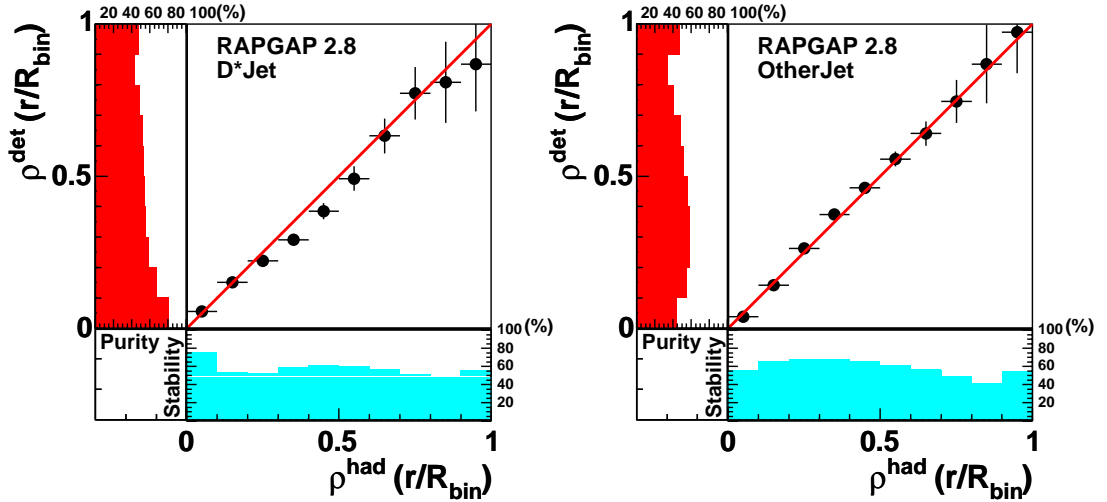


Figure 4.21: The purity, stability and the correlation for the differential jet shape variable, $\langle \rho(r/R) \rangle$, between hadron and detector level for the D^* Jet and the *OtherJet*, in bins of r/R .

For the differential jet shape variable, $\langle \rho(r/R) \rangle$, one observes in Fig. 4.21 a general reduction of stability and purity to the $\sim 60\%$ level compared to $\langle \Psi(r/R) \rangle$, where only the first three bins of r/R indicate a slight reduction.

For $\langle \rho(r/R) \rangle$ also the correlation becomes slightly worse, and the error increases in the larger bins of r/R , where only a small fractional energy of the jet is found at the edge of the cone.

In Fig. 4.22 the same quantities as before are presented for $\langle \rho^*(r/R) \rangle$. One observes that stability decreases below 40% for the first two bins in r/R .

The corrected data are given by:

$$x^{\text{had}} = x_{\text{det}} \cdot f_{\text{corr}} \quad , \quad (4.31)$$

where

$$f_{\text{corr}} = \frac{x_{\text{had}}}{x_{\text{det}}} \Big|_{\text{MC}} \quad . \quad (4.32)$$

The value of x_{had} is calculated using the MC model at hadron level, applying the same selection as for the detector level. The correction factors f_{corr} are calculated individually for each bin and are shown in Fig 4.23.

For the first two bins of $\langle \rho^*(r/R) \rangle$ the correction factors are relatively large due to removing of the dominant D^* -meson contribution. Here the distribution is sensitive to small energies.

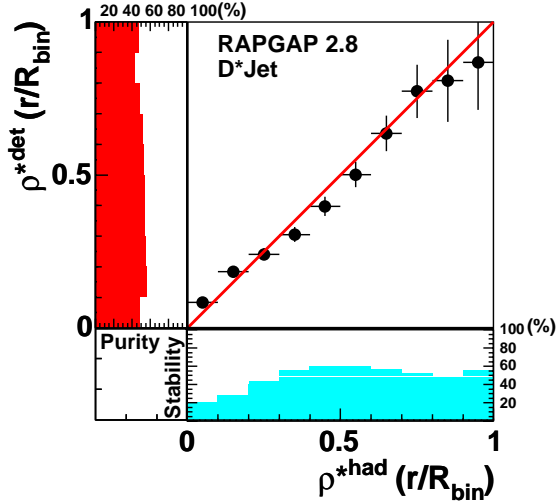


Figure 4.22: The purity, stability and the correlation for $\langle \rho^*(r/R) \rangle$ between hadron and detector level for the D^* Jet, in bins of r/R .

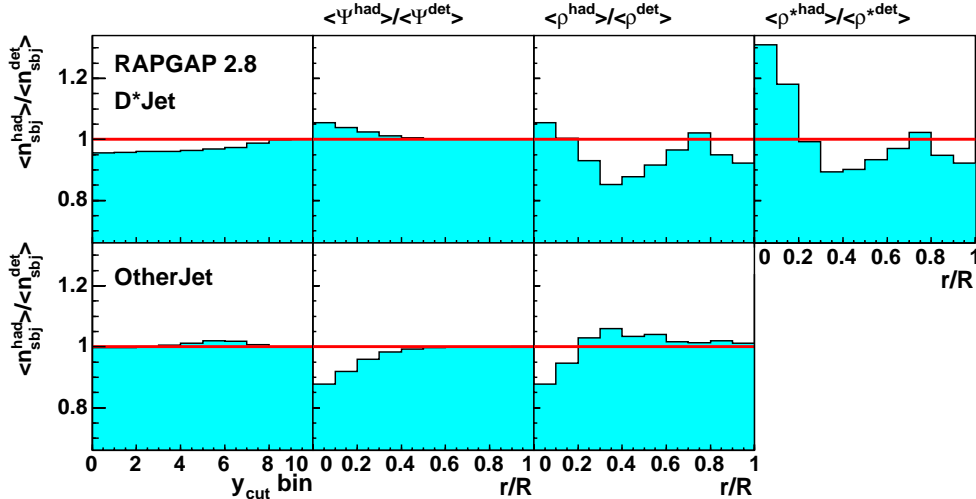


Figure 4.23: The correction factors for the jet shape observables.

The relative difference of the results obtained with two MC models, HERWIG and RAPGAP, is included in the estimation of the systematic errors of the corrected distributions:

$$\varepsilon_{\text{model}} = \frac{x_{\text{corr, H}} - x_{\text{corr, R}}}{x_{\text{corr, R}}} \quad . \quad (4.33)$$

The systematic errors of the jet shape observables including the MC model systematic errors are presented in Fig. 4.24. The various sources of systematic errors are assumed to be independent. For the differential jet shape variable, the errors for the D^* Jet and the $OtherJet$ are anti-correlated due to the fact that the E_T sum is performed over a much larger number of particles for the $OtherJet$ than for the D^* Jet in the range of $r/R \in (0.2; 0.5)$.

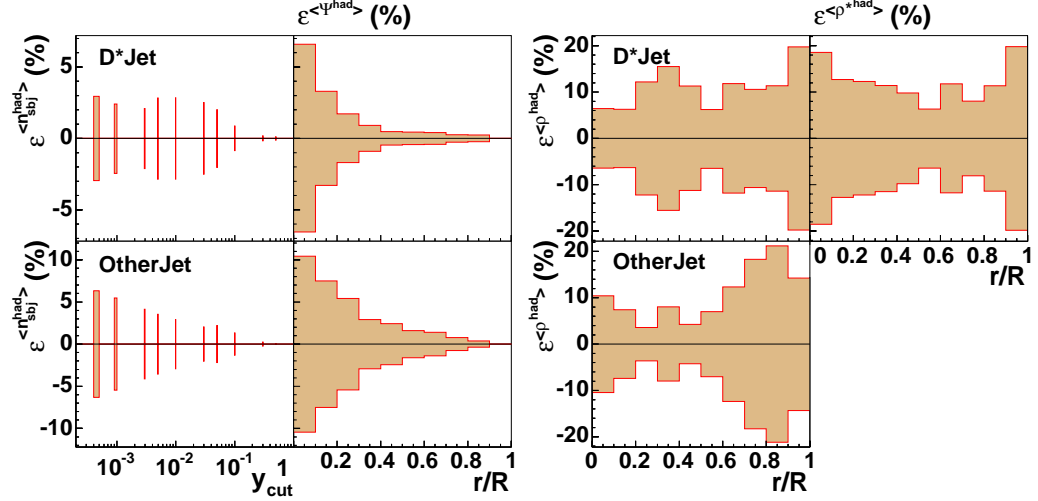


Figure 4.24: The systematic errors for jet shape observables.

4.7 Results at the Hadron Level

The results at the detector level, presented in the Sec. 4.5, are now shown corrected to the hadron level and compared to the QCD based model of RAPGAP 2.8 for direct charm production in DIS. The systematic error from the MC model is also added in quadrature to the total error.

Fig. 4.25 shows the $\langle n_{sbj} \rangle$ distribution.

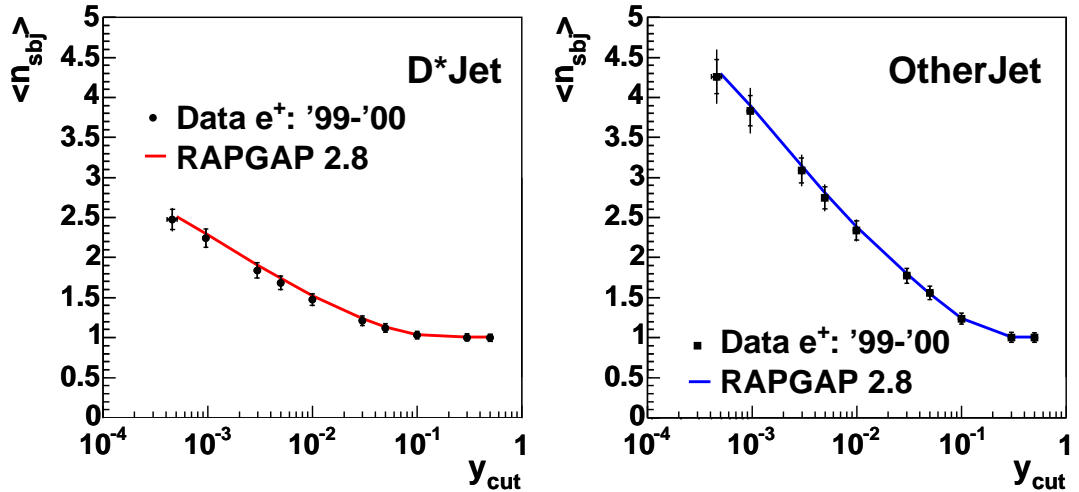


Figure 4.25: The mean subjet multiplicity $\langle n_{sbj} \rangle$ corrected to hadron level.

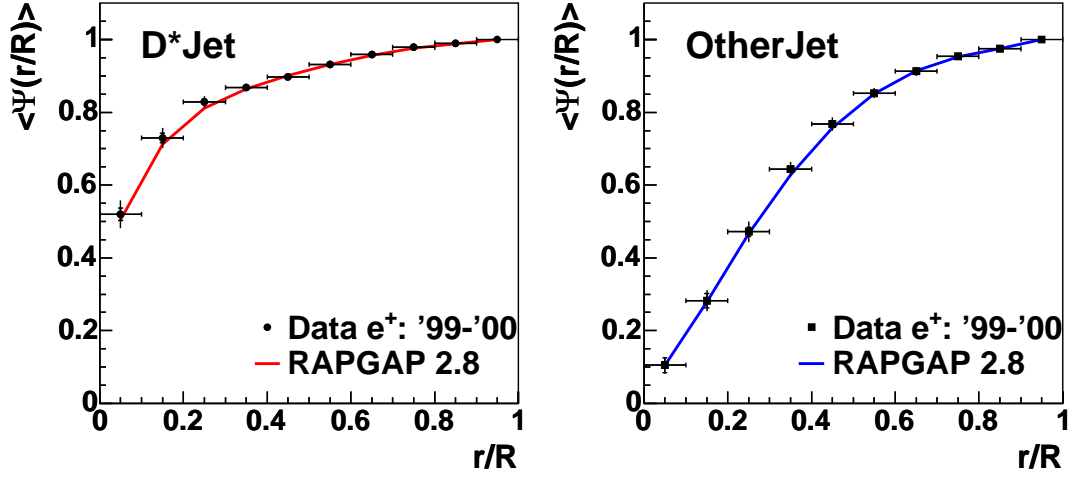


Figure 4.26: The integrated jet shape variable $\langle \Psi(r/R) \rangle$ corrected to hadron level ($R = 1$).

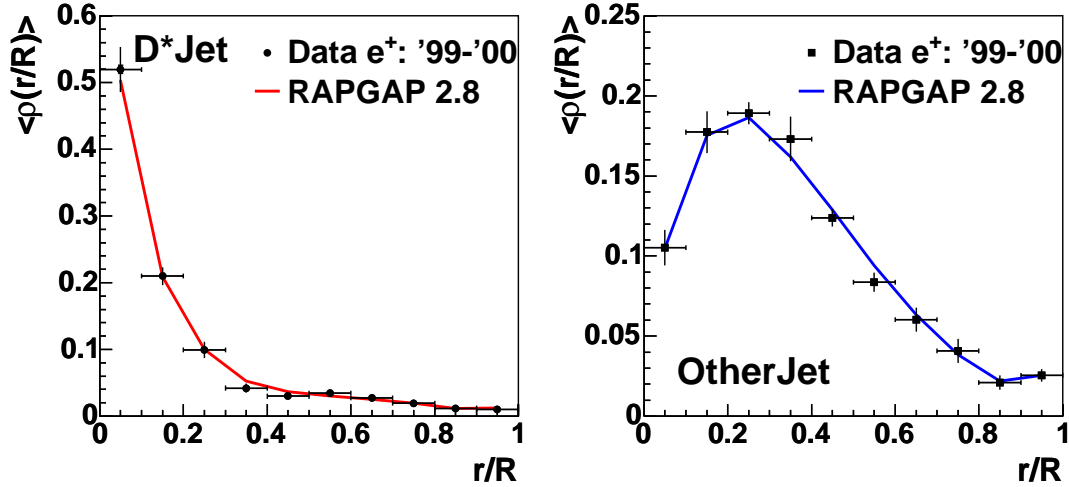


Figure 4.27: The differential jet shape variable $\langle \rho(r/R) \rangle$ corrected to hadron level ($R = 1$).

Fig. 4.26 and Fig. 4.27 show that the differences between the D^* Jet and the *OtherJet*, already observed at detector level, remain at hadron level. Studies of these differences are presented in Sec. 4.8.

The variable $\langle \rho^*(r/R) \rangle$ corrected to hadron level is shown in Fig. 4.28.

4.8 Investigation of the Difference between the D^* Jet and *OtherJet*

In previous sections, clear differences between the D^* Jet and the *OtherJet*, at detector and hadron level, have been observed.

It is interesting to establish the nature of these differences given that *both jets* are assumed to be predominantly *charm jets* produced in the process of boson-gluon fusion to a $c\bar{c}$ pair.

In this section various D^* Jet definitions are presented. In addition, an innovative definition for the boundaries of the concentric jet fraction is introduced. This new definition makes use of a more k_{\perp} like radius, r^* .

In the last part of this section the jet shape observables are shown as a function of different η_{Jet} , E_{Jet} and $E_{T,\text{Jet}}$ ranges.

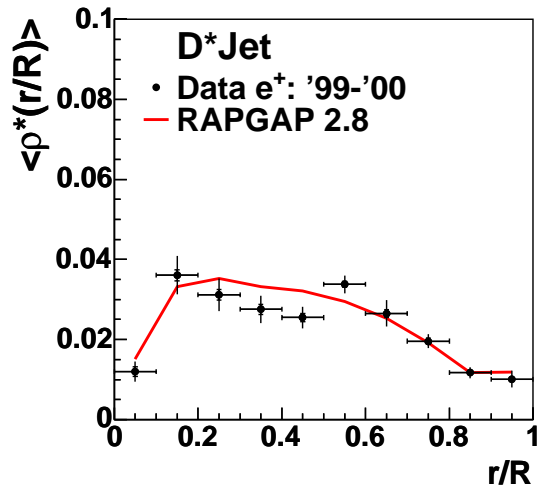


Figure 4.28: The $\langle \rho^*(r/R) \rangle$ variable corrected to the hadron level ($R = 1$).

4.8.1 Different D^* Jet Definitions

One possible reason for the differences between the D^* Jet and the *OtherJet* could be the selection criteria for the jet which contains the D^* -meson.

For this check an alternative definition of the D^* Jet, which was already used in a previous analysis [56], was considered. Not the D^* -meson is used as a stable particle within the HFS objects, but rather its stable daughter particles.

From the jets found with this new HFS configuration, the jet closest in the azimuthal angle ϕ to the D^* -meson direction and with a $\Delta\phi$ angle less than 60° , is considered as D^* Jet:

$$\min |\Delta\phi(D^*, \text{jet})| < \frac{\pi}{3}. \quad (4.34)$$

A third possibility is to use a new definition which requires a match of the D^* Jet with a D^* -meson also in η , making use of the above HFS objects.

The jet closest in (η, ϕ) space to the D^* -meson direction and with $r_{\text{jet}} < 1$ is called the D^* Jet:

$$\min r_{\text{jet}}(D^*, \text{jet}) < 1, \quad (4.35)$$

where

$$r_{\text{jet}} = \sqrt{(\eta_{\text{jet}} - \eta_{D^*})^2 + (\phi_{\text{jet}} - \phi_{D^*})^2}. \quad (4.36)$$

Results using these two new definitions and the standard D^* Jet definition of this analysis are compared in Fig. 4.29. The data are corrected to hadron level and the errors include systematic errors. One can observe that the differences between the two charm jets become smaller.

However, even if the D^* -meson is not included in the HFS objects as a stable particle, some differences remain. They are probably due to the fact that the *OtherJet* is not always fully reconstructing the charm quark jet and that in addition it has a significant probability, $\simeq 20\%$, to be due to a hard gluon instead of a charm quark, as indicated by the MC studies, see Fig. F.4 and F.5 in Appendix F.

The correlations between the charm quarks and the corresponding jets are presented in Appendix F. Distributions of the purity, stability, correction factors to hadron level and systematic errors of the new D^* Jet definition are shown in Appendix H.

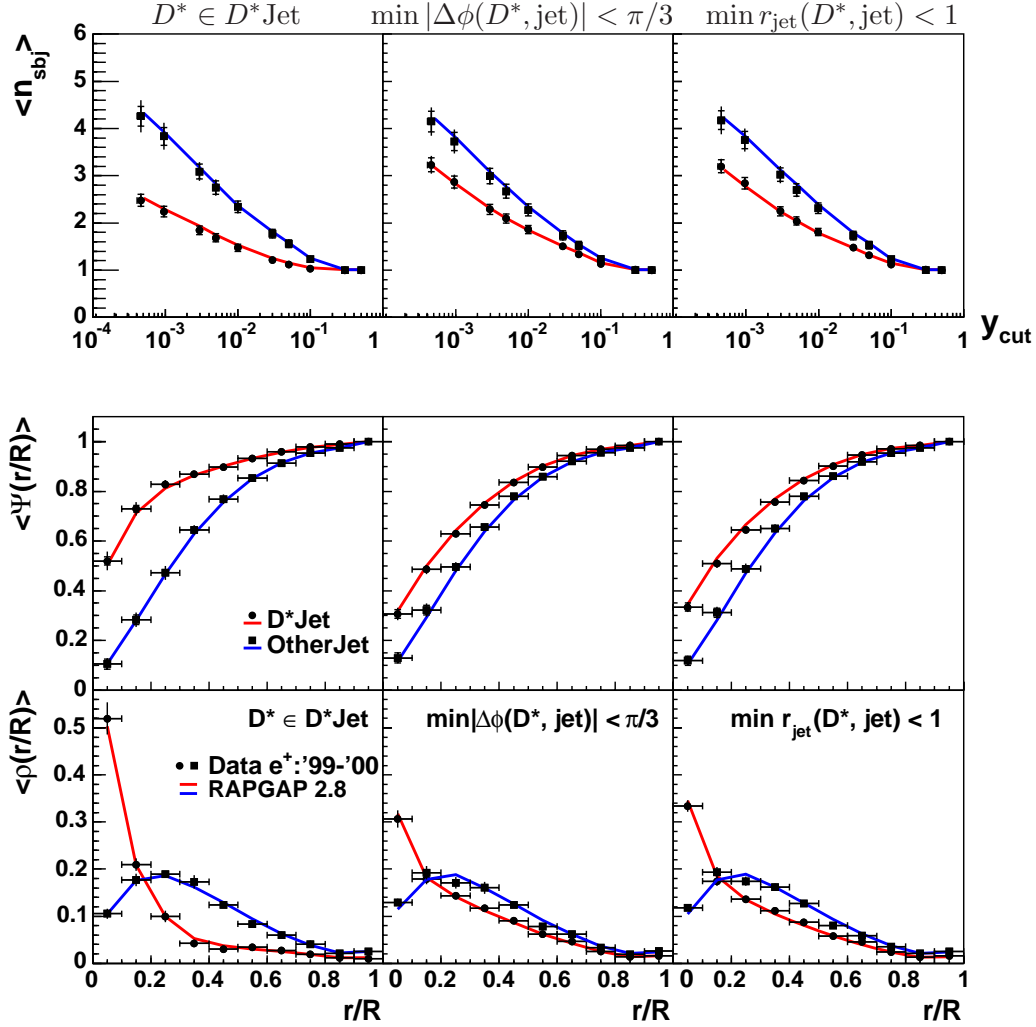


Figure 4.29: The jet shape observables for different $D^*\text{Jet}$ definitions corrected to hadron level ($R = 1$). The default definition used in this analysis is $D^* \in D^*\text{Jet}$.

4.8.2 Alternative Radius Definition

The jet shape variables are defined summing the E_T of the hadrons in concentric cones around their respective jet axis using the following radius definition:

$$r = \sqrt{(\eta_{\text{jet}} - \eta_h)^2 + (\phi_{\text{jet}} - \phi_h)^2}, \quad (4.37)$$

which is historically related to the cone algorithm concept.

Nowadays, the k_\perp cluster algorithm is mostly used to perform the jet finding, see Sec. 1.3. For this algorithm a more natural definition would be:

$$r^* = p_h \cdot \sin \alpha_{h-\text{jet}}, \quad (4.38)$$

where p_h is the momentum of the HFS object contained in the jet. The angle between the HFS object and the jet direction is $\alpha_{h-\text{jet}}$. The variable r^* has the meaning of a relative transverse momentum.

The results of the jet shape observables using this new definition are illustrated in Fig. 4.30 at the hadron level. The D^* Jet definition used is the default one from this analysis, the D^* -meson is used as a stable particle and the jet which contains it is called the D^* Jet. The correction factors to hadron level, the purity, stability as well as systematic errors are presented in Appendix H.

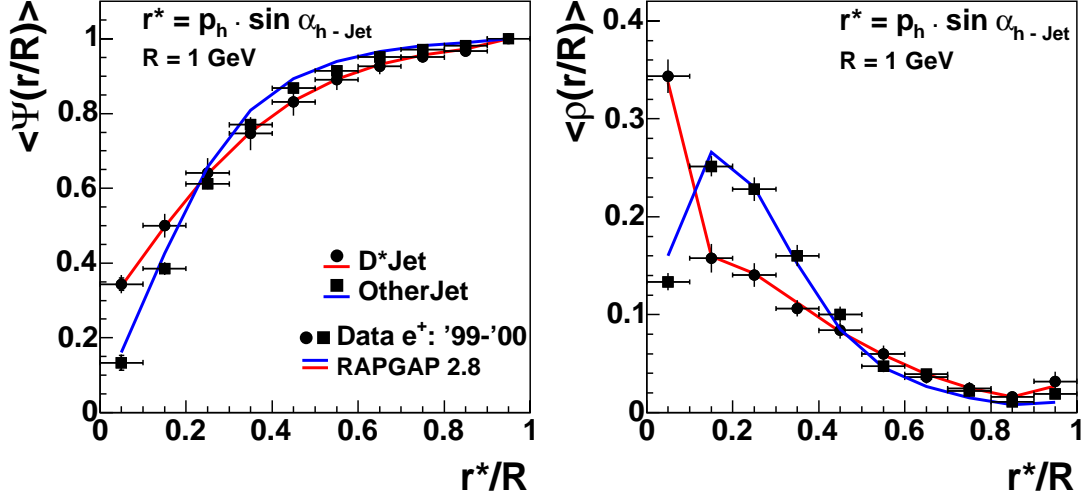


Figure 4.30: The jet shape variables using a k_{\perp} -like radius r^* corrected to hadron level. Here $R = 1 \text{ GeV}$.

With this new r^* definition, the two charm quark jets are more similar in $\langle \Psi \rangle$. This is a new vision of the jet shape variables which makes use of a k_{\perp} -like radius that is consistent with the jet finder. The differences, especially in the first two bins, are due to the gluon jet contributions which confirm previous observations of the fact that gluon jets are broader than the quark ones.

4.8.3 Dependence of Jet Shape Variables on Jet Kinematics

In this section the jet shape variables are studied as a function of $E_{T,\text{jet}}$, E_{jet} and η_{jet} , in order to observe if the reconstructed jets have a quark or a gluon signature.

In Fig. 4.31, the jet shape variables are plotted in different bins of $E_{T,\text{jet}}$ at the hadron level and their errors include the systematic errors. The higher $E_{T,\text{jet}}$ is, the higher is the probability to reconstruct a charm quark using the *OtherJet*.

The shape of the *OtherJet* distributions for the highest $E_{T,\text{jet}}$ bin are similar to the one in the backward η_{jet} bin, presented in Fig. 4.32:

$$-1.5 < \eta_{\text{jet}} < -0.5 \quad (4.39)$$

even if the charm quark is in this case not completely reconstructed. This is supported by the correlation plots shown in Appendix F, where one can observe that in the backward direction the charm quark contributions are approximatively the same for the D^* Jet and the *OtherJet*.

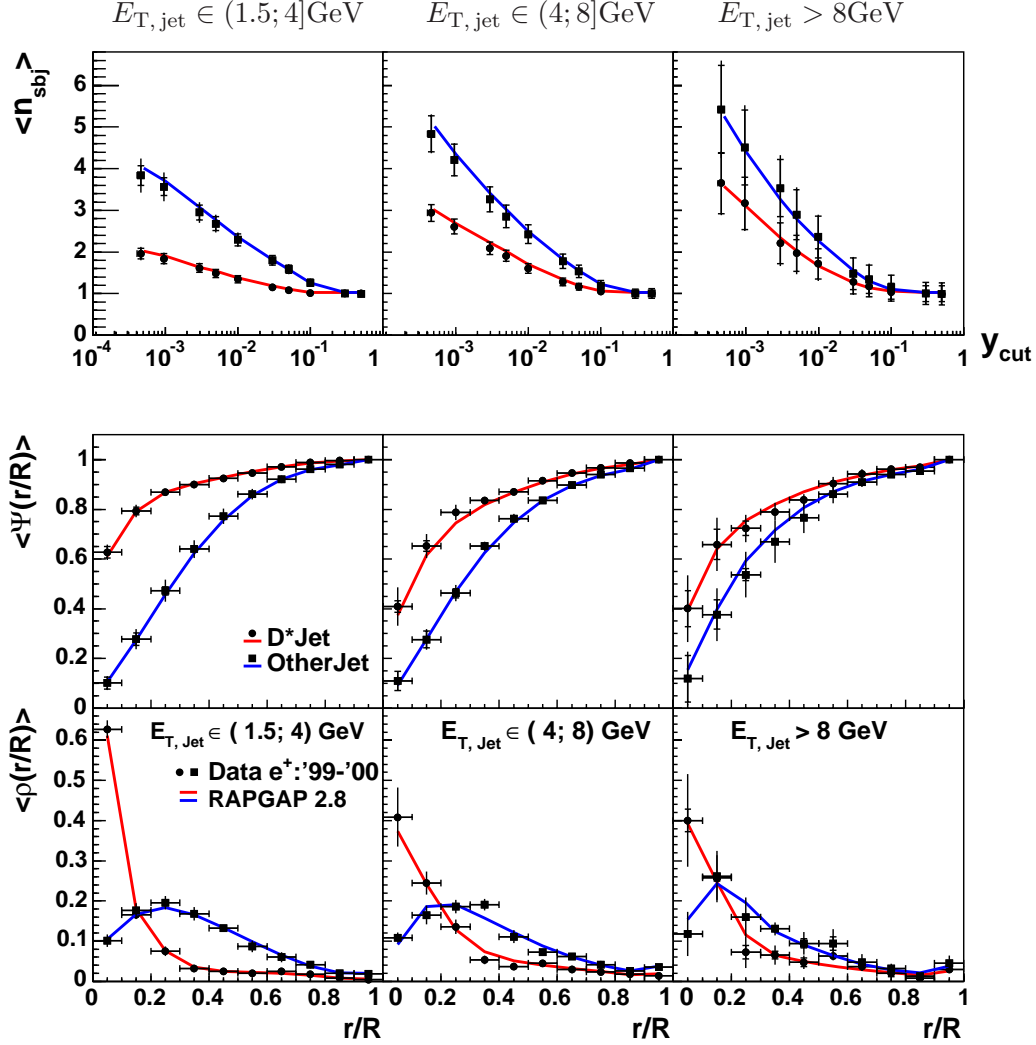


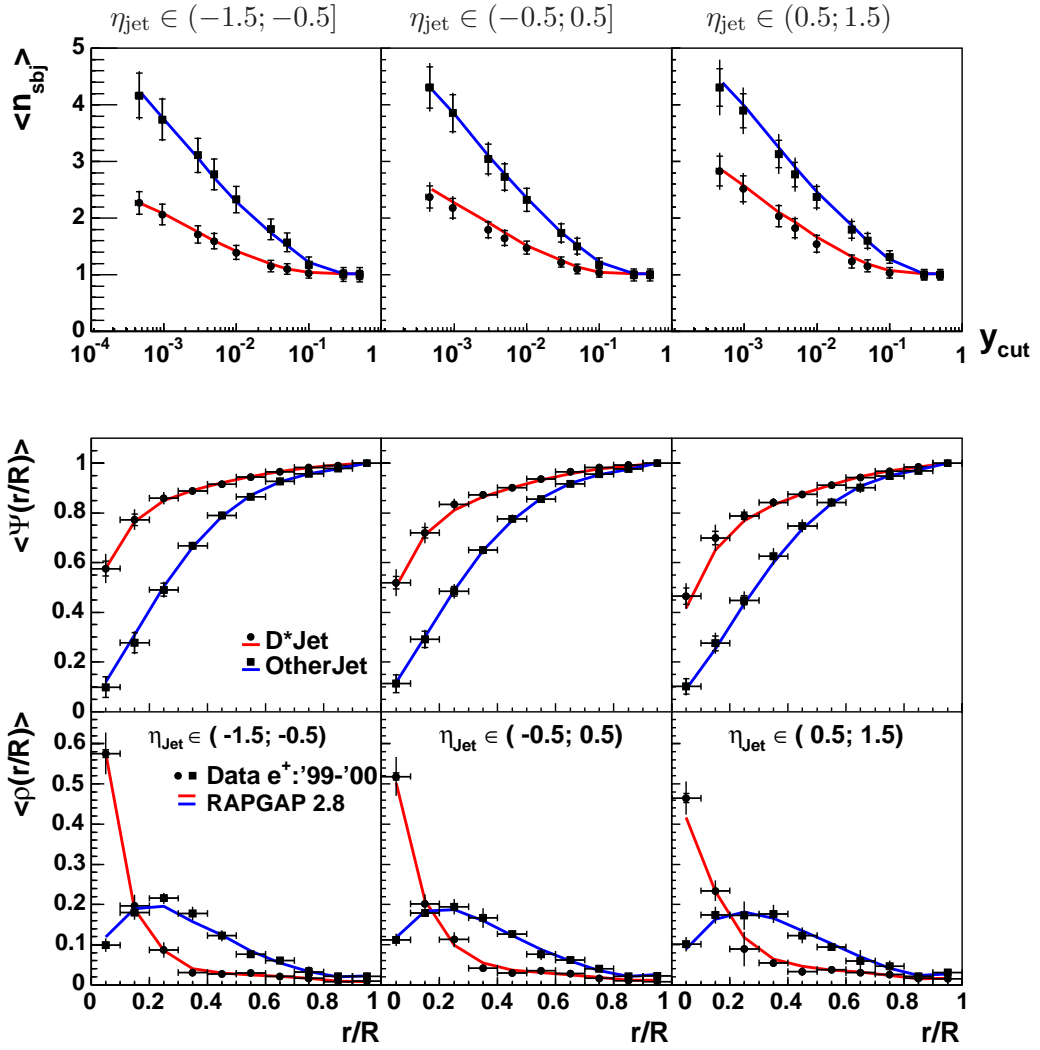
Figure 4.31: The jet shape observables for different bins in $E_{T,\text{jet}}$ corrected to hadron level ($R = 1$).

The distributions of jet shape variables for different bins in E_{jet} , shown in the Fig. 4.33 also confirm the $E_{T,\text{jet}}$ observation.

One can conclude from the various comparisons and the correlations shown in Appendix F that for low energies of the charm jets only the D^* Jet can reconstruct the charm quark properly and the *OtherJet* is affected by hard gluon contributions, $\simeq 20\%$, as well as by the missing reconstructed energy of the charm quark.

The purity, stability, correction factors to hadron level and the systematic errors corresponding to the distributions shown in Figs. 4.31, 4.32 and Fig. 4.33 are presented in Appendix H.

Having understood the parton likely contributions resulting in differences between the two types of charm jets, in the next chapter an innovative perspective is explored: a subjet of the charm jet, subjet assumed to originate from a soft gluon radiated by the charm quark that generates the jet, is used to measure the *dead cone effect*, which is a step further in understanding the structure of the charm jets.


 Figure 4.32: The jet shape observables for different bins in η_{Jet} corrected to hadron level ($R = 1$).

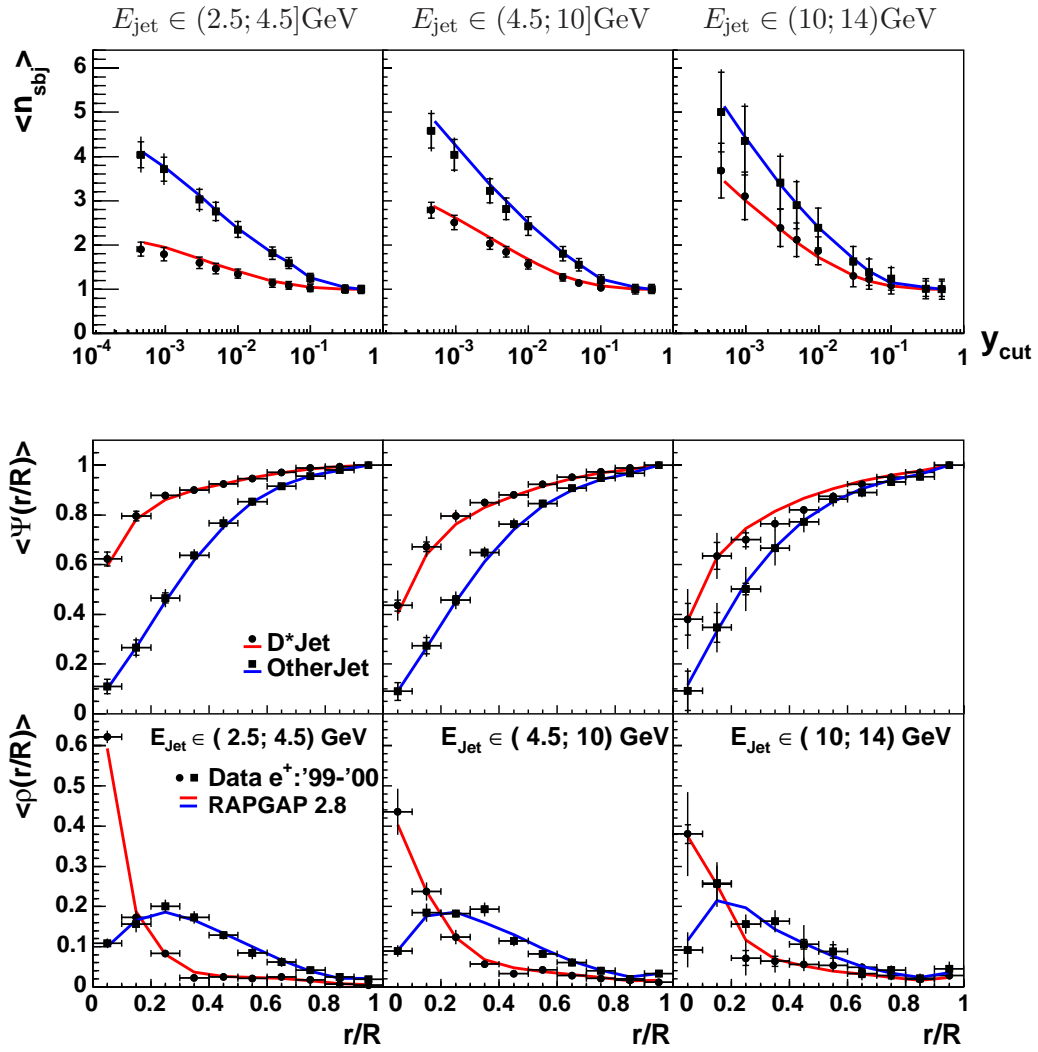


Figure 4.33: The jet shape observables for different bins in E_{jet} corrected to hadron level ($R = 1$).

Chapter 5

The *Dead Cone* Effect

In this chapter an innovative method to investigate the structure of charm jets is presented. The idea of this method is to use a specific angular distribution and its dependence on the jet energy. The method is expected to be sensitive to the suppression of soft perturbative¹ gluons emitted by heavy quarks close to their flight direction. For these gluons, the differential cross section [25] is written as:

$$\frac{d\sigma_{Q \rightarrow Q+g}}{d\alpha} \approx C \frac{\alpha^3}{(\alpha^2 + \alpha_0^2)^2} \quad (5.1)$$

with:

$$\alpha_0 = \frac{M_Q}{E_Q}, \quad (5.2)$$

where M_Q is the mass of the heavy quark and E_Q its energy.

The angle between the radiated gluon and the primary heavy quark momentum is denoted by α . From Eq. 5.1 it follows that the emission of soft gluons is suppressed in the region of small α . Therefore this region is called the "dead cone". The *dead cone effect* is characterised by an opening angle α_0 which depends on the mass and energy of the heavy quark. In Sec. 5.2 an attempt is made to define an experimentally accessible angle which should approximate the parton level angle α .

In this chapter the nomenclature is as follows. The charm quark coming from the hard BGF process is called the *primary heavy quark* or the **BGFQ**. The gluon radiated by the BGFQ is called **BGFg**. The charm quark after gluon radiation is named **aBGFQ**, as illustrated in Fig. 5.1.

Indirect evidence for the presence of the dead cone, based on comparing multiplicities in light-quark and heavy-quark jets has been reported by the DELPHI collaboration [55].

At HERA, in ep collisions at $\sqrt{s} \simeq 318$ GeV, the charm quarks are produced mainly via the boson-gluon fusion process, as described in Sec. 1.2. The charm quarks are produced in pairs and, in contrast to e^+e^- experiments, close to kinematic threshold. This allows to study the effect of the charm mass on the jet structure at low jet momenta, in a region of phase space where these effects are expected to be measurable with the detector resolution of the H1 experiment.

In the next section the possible approaches to study the *dead cone effect* are discussed. The motivation for choosing the *Energy Variation* approach is also presented.

¹The gluon radiation, to which this analysis is referring, can still be calculated perturbatively. Only its *soft* part, close to quarks direction, is studied.

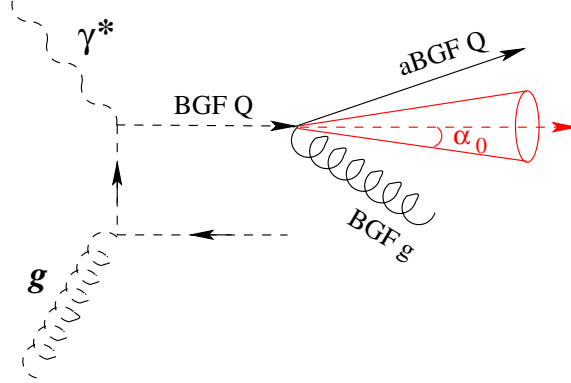


Figure 5.1: The representation of the radiated soft gluon by the BGFQ.

5.1 Two Approaches to Study the Dead Cone Effect

On the basis of Eq. 5.2, two approaches can be used to study the *dead cone effect*.

One of them is to keep the energy of the quarks constant and to compare two quark flavours that have significantly different masses. This will be called the *Mass Variation* approach, and it is explained in detail in Sec. 5.1.1. In the second approach the quark mass is kept the same, making use of one quark flavour only, and the energy of the quark is varied. This approach will be referred to as the *Energy Variation*. It is presented in Sec. 5.1.2.

A third possibility is to combine the two approaches in the following fashion. The *Energy Variation* can be applied to the *c* and *b*-quarks and their results can be compared to see the difference due to the mass of the two quarks, as in the *Mass Variation* approach.

5.1.1 The Mass Variation Approach

Two quark flavours with a significant mass difference are the *u* and the *c*-quarks. Due to the fact that it is difficult to discriminate the BGF processes for *u*, *d* and *s* production, respectively, one can include, for a comparison with charm, all three of these flavours in one class.

This is possible since their mass is of order 10 to 100 MeV and is significantly smaller than the charm quark mass of 1400 MeV. Therefore, the *u*, *d* and *s*-quarks are grouped together as *light* quarks.

The *Mass Variation* approach is based on a comparison of *light* quarks with charm quarks.

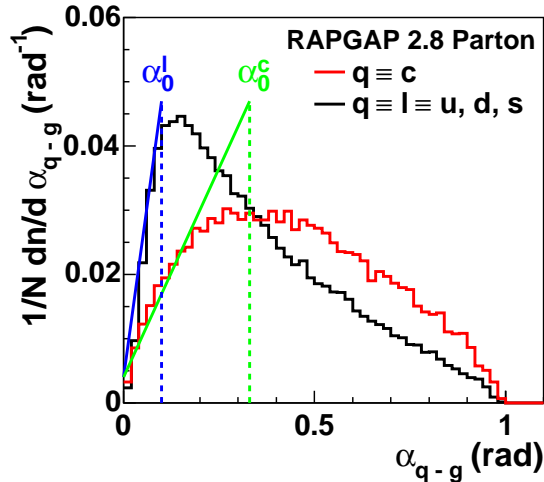


Figure 5.2: The Monte Carlo predictions for the *dead cone effect* for light and charm quarks.

The α_0 angle can be written for the two classes as:

$$\alpha_0^c \cong \frac{m_c}{E_c} \quad \text{and} \quad \alpha_0^l \cong \frac{m_l}{E_l}. \quad (5.3)$$

The relation between the quark masses is $m_c \gg m_l$ which implies that:

$$\alpha_0^c \gg \alpha_0^l. \quad (5.4)$$

This can be nicely observed in the MC model at the parton level, see Fig. 5.2.

An experimental method [57] for the *Mass Variation* approach compares the angular distribution of the hadrons around the highest E_T jet direction. Fig. 5.3 shows the results of MC simulations for the proposed method.

The difference between the full line (u -quarks) and the dashed one (c -quarks) is considered as evidence of the *dead cone effect*.

The dashed line in Fig. 5.3, which includes also the D^* -meson, is different from the one obtained in [57].

The red histogram shows the same distribution as the dashed one but excluding the D^* -meson and it is in good agreement² with the dashed one from [57].

The difference which could be considered evidence for the *dead cone effect* is rather small. Another problem with this comparison of light and heavy quark jets is that for the D^* Jet the daughter particles are discarded and the D^* -meson is

used while for the *light*-quark jets no such procedure can be performed. Therefore the light and heavy quark jets cannot be compared in this way on the same footing. An alternative is to study only one flavour type of quarks.

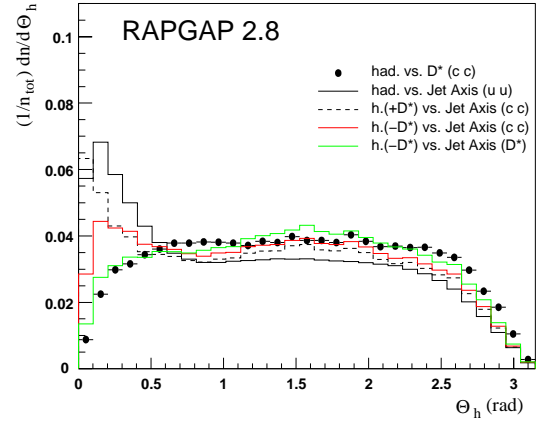


Figure 5.3: Cross-check of experimental method proposed for the *Mass Variation* approach.

5.1.2 The Energy Variation Approach

In Fig. 1.13 it was observed that the phase space for gluon emission is suppressed for charm and bottom quarks at HERA production energies. At HERA the cross section for charm production is at least two orders of magnitude higher than the one for bottom production. For reasons of statistics the appropriate quark flavour for this study is charm.

The idea of the *Energy Variation* approach is to keep the quark mass constant and to vary the energy of the quark jet. For two bins in the energy of the quark $E_{Q,i}$ and $E_{Q,j}$ one can write:

$$\alpha_{0,i}^Q \cong \frac{m_Q}{E_{Q,i}} \quad \text{and} \quad \alpha_{0,j}^Q \cong \frac{m_Q}{E_{Q,j}}. \quad (5.5)$$

²Unfortunately in the legend of Fig.7 of [57] an error, confirmed by the author, occurred and $+D^*$ became $-D^*$.

If the relation between the energies is:

$$E_{Q,j} > E_{Q,i} \Rightarrow \alpha_{0,j}^Q < \alpha_{0,i}^Q \quad (5.6)$$

the following relations can be written:

$$\alpha_{0,i}^Q \cdot E_{Q,i} \cong \alpha_{0,j}^Q \cdot E_{Q,j} \cong m_Q. \quad (5.7)$$

The distribution $\alpha_{0,i}^Q \cdot E_{Q,i}$ vs. $E_{Q,i}$ is expected to be a flat distribution with a constant value which is a reasonable measure of the quark mass.

The predictions of the MC model at the parton level are shown in Fig. 5.4 for the charm and the bottom quarks.

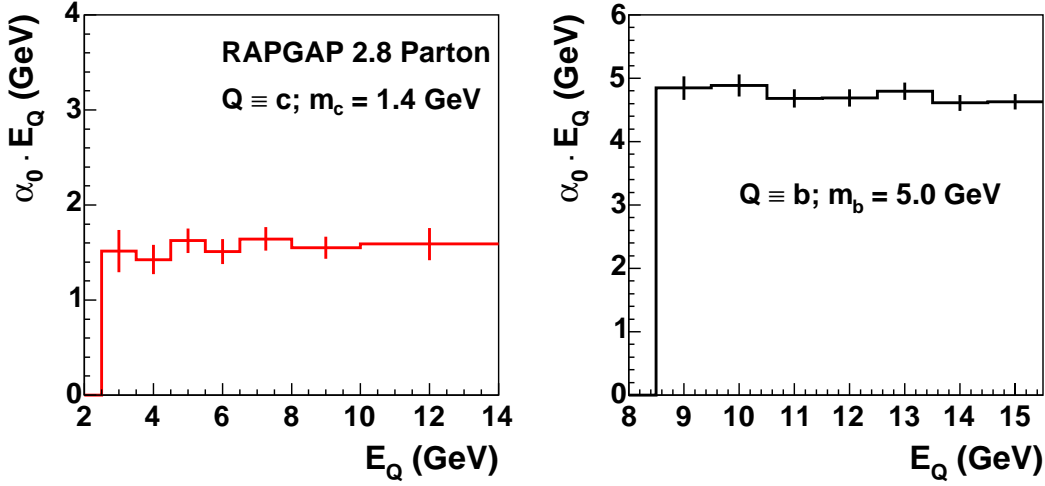


Figure 5.4: The MC predictions at the parton level for the *Energy Variation* approach in case of *c*-quarks, left, and *b*-quarks, right.

For the light quarks *u*, *d* and *s* one can observe in Fig. 5.5 a constant level, which will be called *pseudo-mass* level of around 1 GeV, indicating a *pseudo dead-cone effect*.

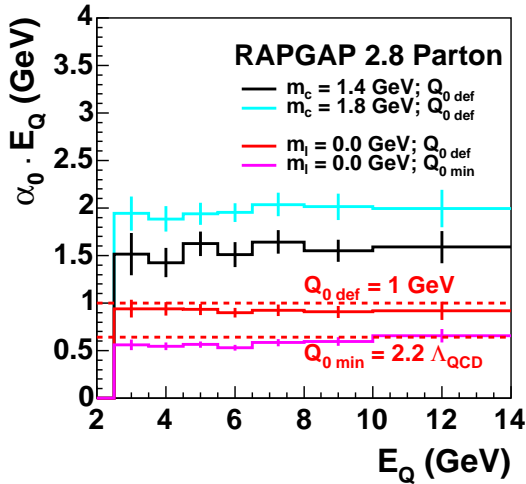


Figure 5.5: The MC predictions for light quarks compared with those for *c*-quarks for the *Energy Variation* approach.

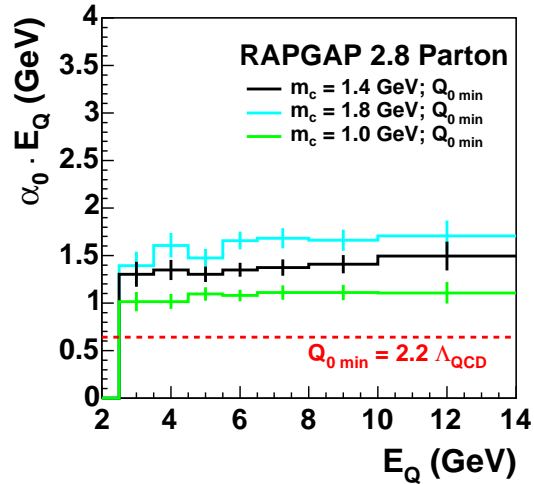


Figure 5.6: The MC predictions for the *c*-quarks in the *Energy Variation* approach when using $Q_{0\min}$ instead of $Q_{0\text{def}}$.

The flatness and the 1 GeV level of the distribution is due to the invariant mass *cut-off*, Q_0 , where typically the parton shower development is stopped in MC and the non-perturbative fragmentation starts. The default value of the invariant mass *cut-off* is $Q_0 = 1$ GeV. Its value and the fragmentation parameters have been tuned to e^+e^- data. Below this mass *cut-off*, the partons are assumed not to radiate.

The *pseudo-mass* level of the light quarks decreases to the same level of the mass *cut-off* when the latter is lowered. This behaviour is not seen for the charm quark as one can see in Fig. 5.6. The lower limit of the invariant mass *cut-off* is given by $Q_{0\min} = 2.2 \Lambda_{\text{QCD}}$, where $\Lambda_{\text{QCD}} = 0.29$ GeV. However, the level of charm quark slightly deviates for low energies due to lower threshold of Q_0 when larger m_c are used.

This approach makes use of one quark flavour only, and the comparison in different energy bins at hadron and at detector level is on the same footing. If not all the energy of the quark is reconstructed by its jet, or the jet is not well correlated with the quark direction, these should appear in the $\alpha_{0,i}^{\text{jet}} \cdot E_{\text{jet},i}$ vs. $E_{\text{jet},i}$ histogram as deviations from the normal flat distribution.

5.2 The Experimental Method

The event sample for the study of the *dead cone effect* is approximately the same as the one used for the study of the jet shape variable. The kinematical regime and the D^* -meson selection are identical. The jets are found using the k_{\perp} -jet algorithm, and the jet which contains the D^* -meson is called D^* Jet. The differences in the event selection are due to the D^* Jet requirements:

$$p_{\text{T}, D^*\text{Jet}} > 1.5 \text{ GeV} \quad \text{and} \quad |\eta_{D^*\text{Jet}}| < 1.5. \quad (5.8)$$

An additional criterium to be fulfilled is:

$$N_{\text{hadrons}} \geq 3, \quad (5.9)$$

where N_{hadrons} is the number of hadrons, HFS objects, required for the D^* Jet.

A BGF charm quark (BGFc) radiates a BGF gluon (BGFg) and the charm quark (aBGF) then fragments into a D^* -meson. The BGFg splits further, perturbatively or non-perturbatively, into a $q\bar{q}$ -pair. The two quarks from the BGFg are fragmenting into hadrons as illustrated in Fig. 5.7.

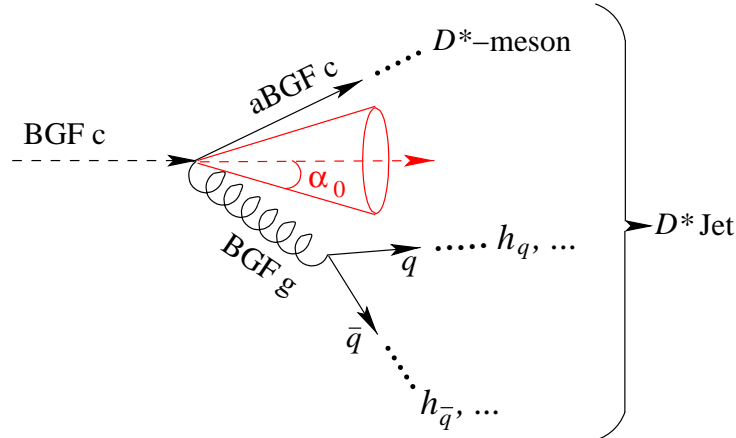


Figure 5.7: An illustration of the principle of the method.

By requiring that the D^* Jet, which should have reconstructed the original BGF c , contains at least two hadrons in addition to the D^* -meson, one allows for the possibility of the D^* Jet to be a signature of a BGF charm quark and a soft gluon. After the new jet selection is applied, the particles which compose the D^* Jet are used further in the analysis.

On this array of particles, the k_{\perp} -jet algorithm is rerun varying the resolution parameter y_{cut} such that only two subjects are found. The D^* Jet is approximating the BGF c and one of the found subjects the BGF g .

The selection criteria for the subject assumed to be the gluon, the *gluon subjet*, are different for the D^* Jet and the *OtherJet*. They are presented in Sec. 5.2.1 and in Sec. 5.2.2, respectively.

Once the *gluon subjet* is established, a new variable can be defined to study the *dead cone effect*. This variable is called the *gluon subjet angle* α , which is defined as the angle between the direction of the D^* Jet and the direction of the *gluon subjet*. An analogous angle is defined for the *OtherJet*.

5.2.1 The Gluon Subjet of the D^* Jet

For the D^* Jet case, the selection of the gluon subjet is simple. Out of the two subjects found, the one which does not contain the D^* -meson is assumed to be due to the BGF g and is named the *gluon subjet*.

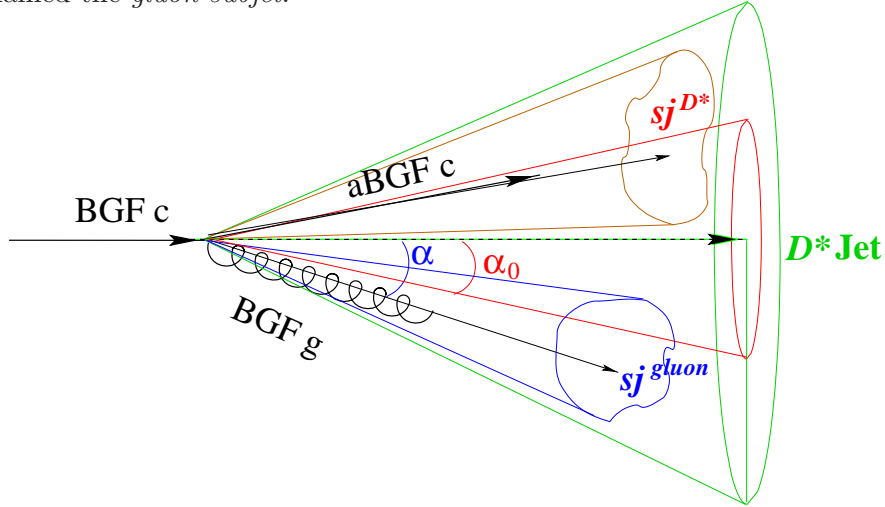


Figure 5.8: The relation between the partons and the D^* Jet with its subjects.

In Fig. 5.8 the analogy between the partons and the jet, respectively the subjects, is illustrated for the D^* Jet case. One can write the following:

$$\begin{aligned} D^*\text{Jet} &\rightarrow \text{sj}_{D^*} + \text{sj}_{\text{gluon}} \\ \text{BGF}c &\rightarrow \text{aBGF}c + \text{BGF}g, \end{aligned} \quad (5.10)$$

where "sj" stands for subjet.

The *gluon subjet angle* is given by:

$$\alpha = \sphericalangle(D^*\text{Jet}, \text{sj}_{\text{gluon}}). \quad (5.11)$$

With the requirement of two subjects, the y_{cut} distribution shown in Fig 5.9, is found to peak at $\sim 2 \cdot 10^{-3}$, which is a good value for the resolution parameter. For

$y_{\text{cut}} > 10^{-2}$ the resolution of the found subjects is worse and one can observe in Fig. 4.25 that on average only one subject is found. The y_{cut} distribution has to be checked in order to make sure that the method is not suffering from a worse resolution given by a high mean value of the y_{cut} .

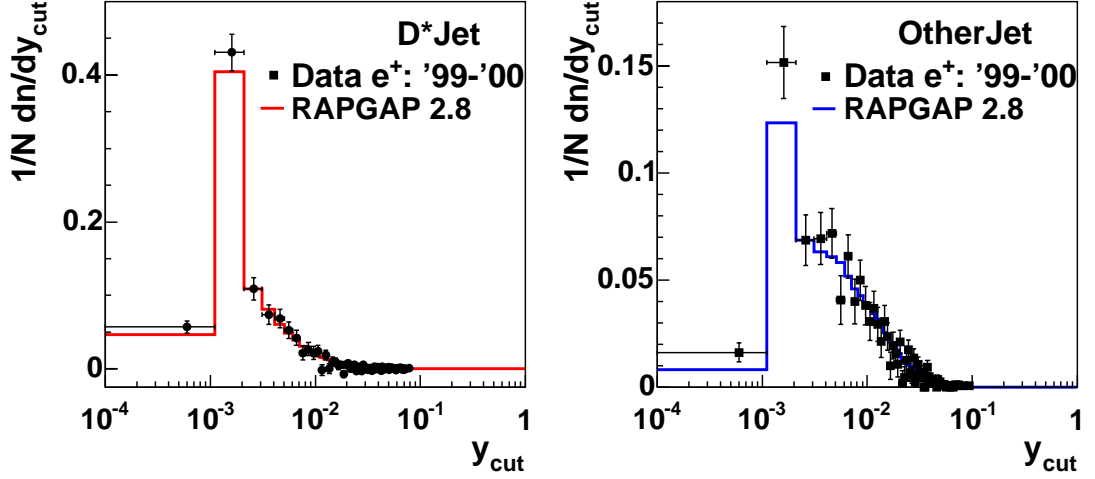


Figure 5.9: The distribution of resolution parameter y_{cut} for the D^* Jet and the *OtherJet*.

5.2.2 The Gluon Subject of the *OtherJet*

The *OtherJet* has to fulfill the same criteria as the D^* Jet. The subjects of the *OtherJet* are found applying the same algorithm.

The *gluon subject* in case of the *OtherJet* is selected on the basis of the following analogy with the D^* Jet. In the D^* Jet two subjects are found and the one containing the D^* -meson has always the highest energy, as was observed in MC studies. Therefore, in case of the *OtherJet*, the subject with the highest energy is taken to be the charm subject (aBGFc), while the *gluon subject* is the subject with the lowest energy.

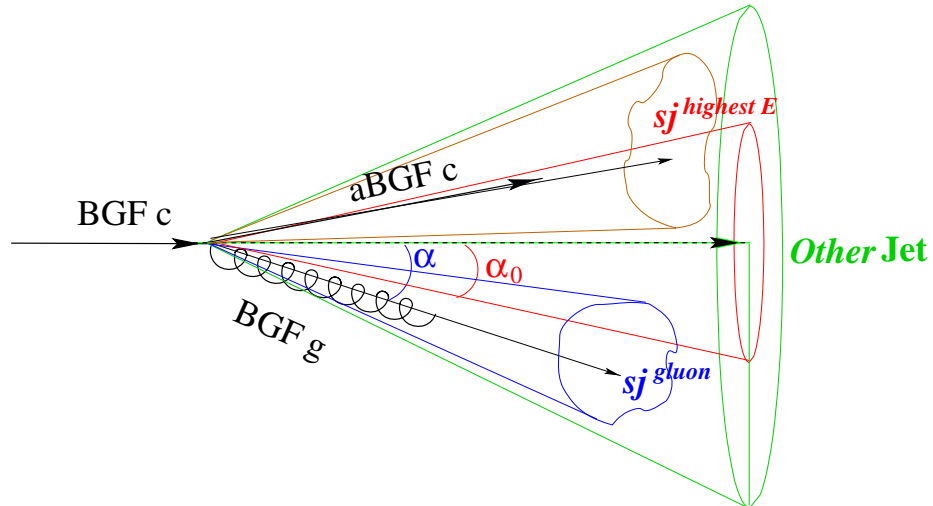


Figure 5.10: The analogy between the partons and the *OtherJet* with its subjects.

This is illustrated in Fig. 5.10. For the *OtherJet* the following relations can be written:

$$\begin{aligned} \text{OtherJet} &\rightarrow \text{sj}_{\text{highestE}} + \text{sj}_{\text{gluon}} \\ \text{BGFc} &\rightarrow \text{aBGFc} + \text{BGFg} \end{aligned} \quad (5.12)$$

and for the *gluon subjet angle*:

$$\alpha = \langle (\text{OtherJet}, \text{sj}_{\text{gluon}}) \rangle. \quad (5.13)$$

5.3 Results

The gluon subjet angle, α , measured as described in the previous section, is plotted in bins of jet energy. The background subtraction procedure is similar to the one used for the jet shape observables. The α distribution given by the wrong charge (WrCh) combinations is subtracted from the one given by the right charge (RiCh) combinations as:

$$x_{\text{sig}} = x_{\text{RiCh}} - \frac{1}{k_N} \cdot x_{\text{WrCh}}, \quad (5.14)$$

where k_N is determined using the fit function of Eq. 3.61. The fit function is applied to the new Δm distributions, shown in Fig. 5.11 a) for the *D*Jet* and in b) for the *OtherJet* event samples, respectively.

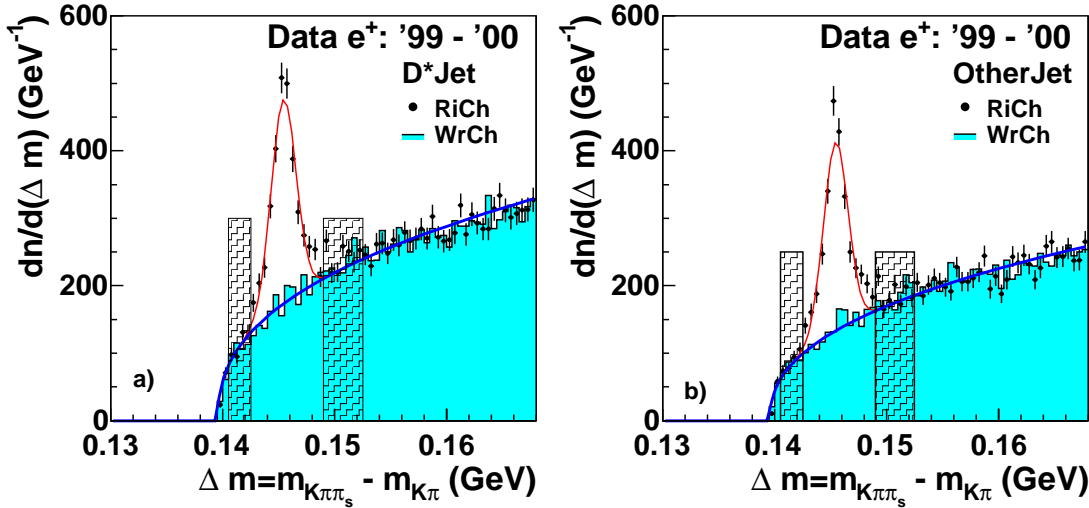


Figure 5.11: The Δm spectrum for the *D*Jet* and *OtherJet* event sample used to study the *dead cone effect*.

The statistical errors of the signal determination, x_{sig} , are calculated using the standard error propagation. The error calculation is performed with the formula:

$$\sigma_{\text{sig}} = \frac{1}{k_N} \cdot \sqrt{\sigma_{x_{\text{RiCh}}}^2 \cdot k_N^2 + \sigma_{k_N}^2 \cdot \frac{x_{\text{WrCh}}^2}{k_N^2} + \sigma_{x_{\text{WrCh}}}^2}. \quad (5.15)$$

The systematic errors for this measurements are presented in Sec. 5.3.2. The final errors are calculated adding the statistical and systematic errors in quadrature.

5.3.1 The α_0 Determination

Once the gluon subjet angle, α , is measured in different bins of the jet energy the *dead cone angle*, α_0 , can be determined.

The α distribution is fitted with the following function:

$$fit_\alpha = p_1 \cdot \frac{\alpha^3}{(\alpha^2 + p_2^2)^2}, \quad (5.16)$$

where p_1 and p_2 are free parameters of the fit. One can observe the analogy with the theoretical cross section of Eq. 5.1. The parameter p_2 is exactly the α_0 angle. The α distributions and the fit used to determine the α_0 angle are shown in Fig. 5.12 for the first four bins of the jet energy and in Fig. 5.13 for the last three bins.

The range where the fit applies is given by the applicability of the function fit_α from Eq. 5.16 which is an approximation of the cross section for small angles.

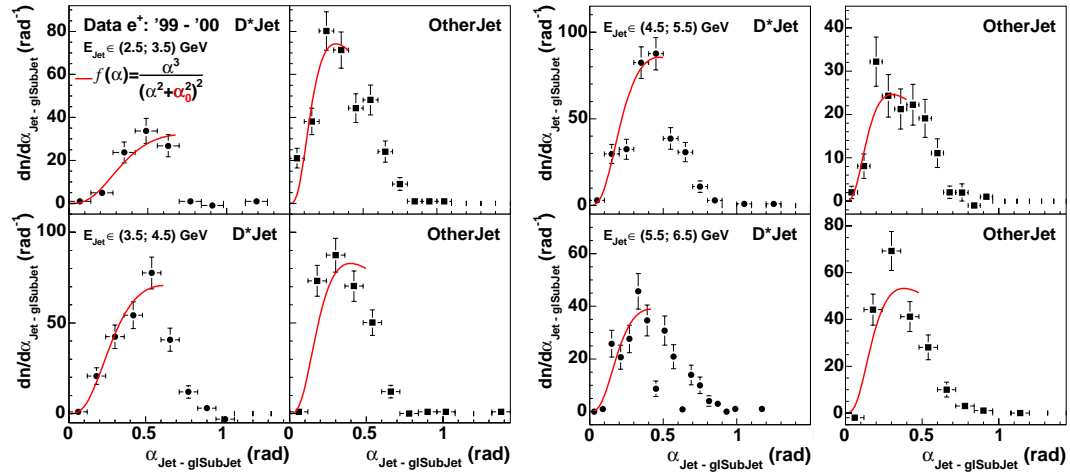


Figure 5.12: The α distributions and the fit function fit_α in the first bins of jet energy.

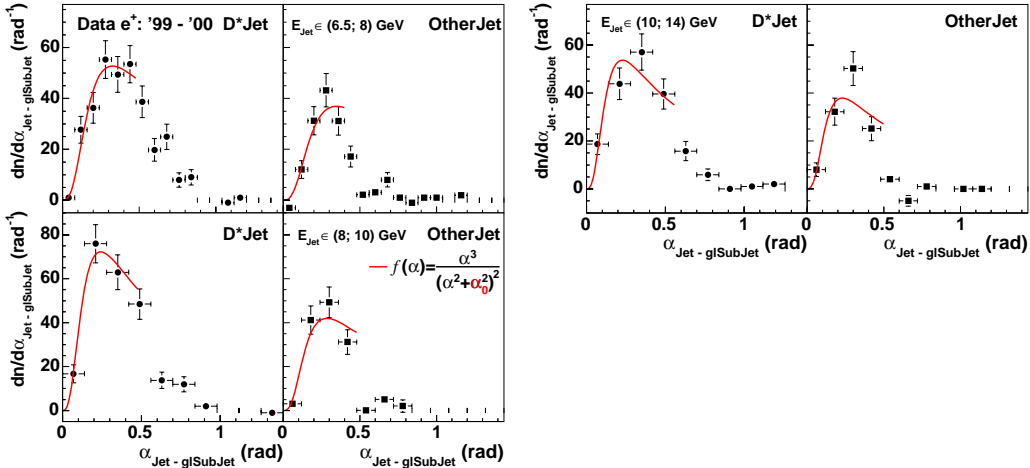


Figure 5.13: The α distributions and the fit function fit_α in the last bins of jet energy.

In order to estimate the systematic error of the α_0 measurement, a second method, which is a very intuitive one, is used. For every α distribution the peak position can be established. The α value at the fraction fr of the peak height is considered as the corresponding α_0 in the jet energy bin. The fraction fr of the peak is determined in the first bin in jet energy as follows: the peak position, max , is found, then, using the α_0 given by the fit method, the value of fit_α is calculated. The ratio:

$$fr = fit_\alpha(\alpha_0)/max \quad (5.17)$$

is used afterwards for the α_0 determination in the rest of the energy bins.

To avoid statistical fluctuations, the MC model was used. The α_0 value is given by the point where the horizontal line $fr \cdot max$ crosses the α distribution as shown in Fig. 5.14 for the second bin in jet energy. Similarly, the fraction³ fr is determined in a higher bin in the jet energy and is then used to find α_0 for the first bin in jet energy. The difference obtained in α_0 from the two methods is used as systematic error.

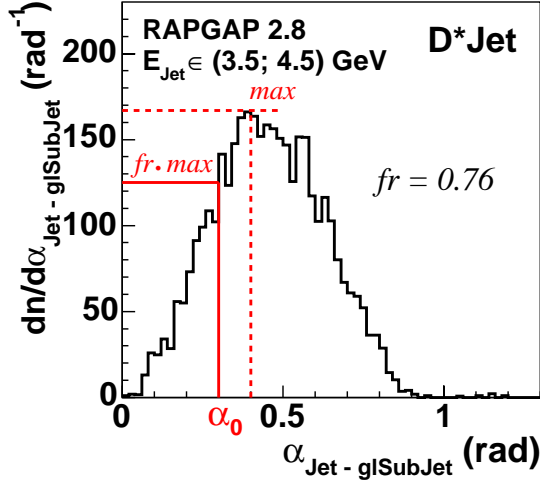


Figure 5.14: The second method used to determine the α_0 .

5.3.2 The Systematic Errors

The sources of the systematic errors are similar to the ones considered for the jet shape measurements.

The energy of the HFS objects is varied from 2% to 4 % as presented in Sec. 4.4.1. The θ angle of the HFS objects is varied within ± 3 mrad.

The sensitivity of the measured distributions to detector cuts is considered as a source of systematic errors. The selection cuts are shown in Table 4.3. Also the background subtraction given by the k_N term is considered as a source of systematic errors. The parameter that limits the jet "radius" R and the MC model are also included in the systematic error calculation. Due to the lower statistics in the data only the MC model at the detector level was used. No corrections to hadron level are performed.

The calculation of the systematic uncertainty is based on the description presented in Sec. 4.4.1. The negative and positive contributions are added in quadrature separately. The *dead cone angle*, α_0 , determination is giving an additional source of systematic errors. The difference between the results of the two methods for the α_0 determination, see Sec. 5.3.1, are used to estimate the systematic error.

In Fig. 5.15 the total systematic errors, including the MC model systematic uncertainty, for $\alpha_0 E_{\text{Jet}}$ as a function of E_{Jet} for the D^* Jet and the *OtherJet*, respectively, are presented.

³The value of fr obtained from the fit_α derivative is compatible with the one of the method presented here.

For the D^* Jet in the *laboratory* frame the main contribution to the systematic errors are given by the method to determine α_0 ($\sim 6\%$), the MC model ($\sim 5\%$), the R_{Jet} ($\sim 2\%$) and the cut on the η_{π_s} ($\sim 2\%$).

For the *OtherJet* the systematic error has as main contributions the cut on η_{HFS} ($\sim 8\%$), the method to determine α_0 ($\sim 6\%$), the MC model ($\sim 5\%$) and the R_{Jet} ($\sim 3\%$).

In the $n\gamma^*p$ frame, see Sec. 5.3.3, the D^* Jet systematic errors are dominated by the MC model ($\sim 7\%$), the method to determine α_0 ($\sim 6\%$), R_{Jet} ($\sim 4\%$) and the energy of the scattered electron E'_e ($\sim 2\%$), due to the boost of the HFS objects into this frame.

The systematic contributions are shown in detail in Appendix H.

5.3.3 The Distribution of $\alpha_0 E_{\text{Jet}}$ vs. E_{Jet} .

The distribution used to conclude about the *dead cone effect* makes use of the correlations with the distributions on parton level shown in Sec. 5.1.2. The assumed correlation is the following:

$$\begin{aligned} E_{Q,i} &\Leftrightarrow E_{\text{Jet},i} \\ \alpha_{0,i}^Q &\Leftrightarrow \alpha_{0,i}^{\text{Jet}} \end{aligned} \quad (5.18)$$

where "Jet" refers to the D^* Jet and *OtherJet*, respectively, and the heavy quark Q to the charm quark.

The distribution of $\alpha_0 E_{\text{Jet}}$ vs. E_{Jet} can be seen in Fig. 5.16.

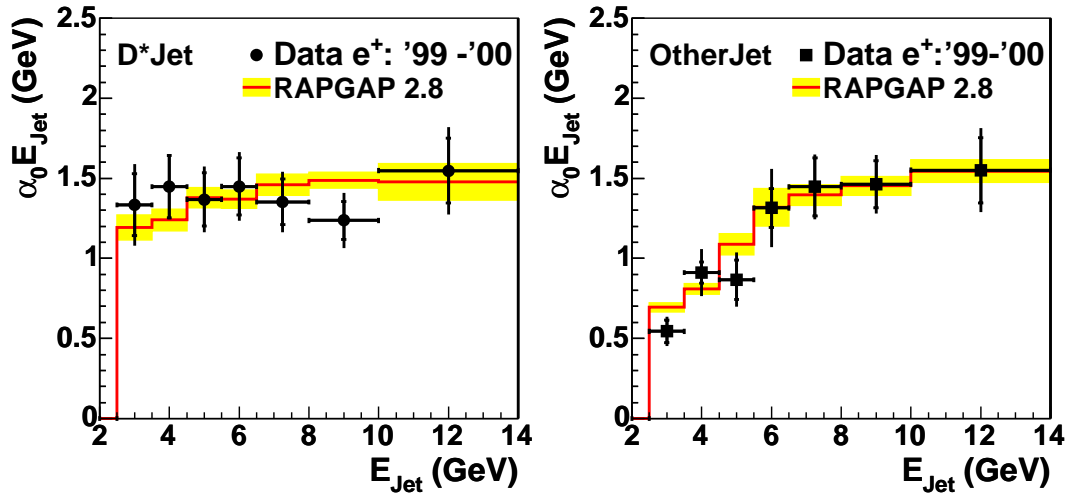


Figure 5.16: The distributions of $\alpha_0 E_{\text{Jet}}$ vs. E_{Jet} for the D^* Jet and the *OtherJet* in the laboratory-frame.

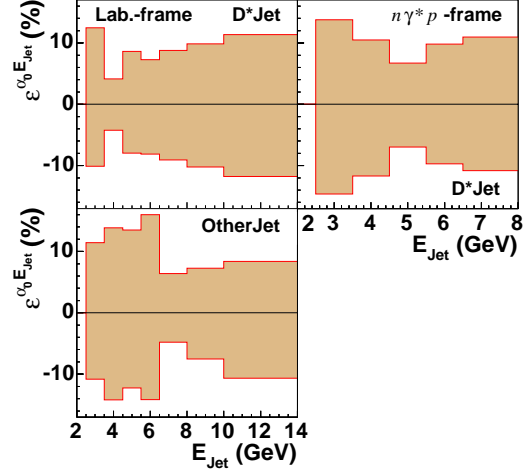


Figure 5.15: The systematic errors of $\alpha_0 E_{\text{Jet}}$ as function of the jet energy E_{Jet} .

The MC model which contains an implementation of the *dead cone effect* describes the data reasonably well. The yellow band indicates the statistical error from the MC model. When comparing the two charm jets one notices a clear difference in the lower bins in jet energy.

This difference at low jet energies can be understood to be due to a deteriorating correlation of the c -quark with the charm jet and to the fact that hard gluons can be the "real" partonic nature of the *OtherJet*, as it can be observed in the Appendix F.

According to the theory of the *dead cone effect*, the suppression of soft gluons emitted by heavy quarks is independent from the frame of reference [58]. To check this, the distribution of $\alpha_0 E_{\text{Jet}}$ vs. E_{Jet} is obtained in a frame different from the laboratory one, e.g. in a frame where the respective jet is always normal to the γ^*p -direction.

This frame is referred to as $n\gamma^*p$ -frame [58], and it is defined by boosting the respective jet and its subjects first to the γ^*p -frame and then in the $-p_{z,\text{Jet}}$ direction. An illustration of the $n\gamma^*p$ -frame is shown in Fig. 5.18. The results in the $n\gamma^*p$ -frame are presented in Fig. 5.17, confirming the frame independent behaviour.

Based on Eq. 5.2 one can consider $\alpha_0 E_{\text{Jet}}$ as a measurement of the charm quark mass. In Table 5.1 the charm *mass* obtained from the data and the MC model at detector level are presented.

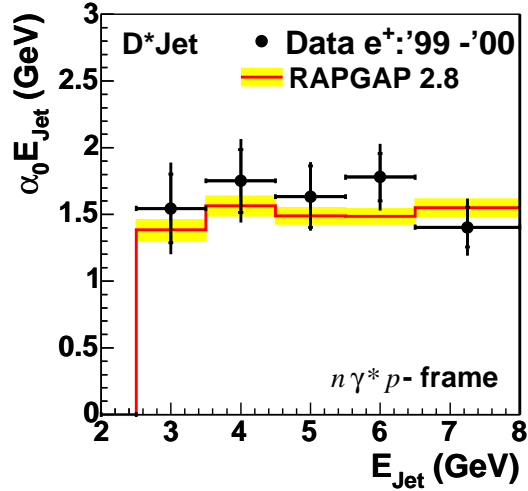


Figure 5.17: The distribution of $\alpha_0 E_{\text{Jet}}$ vs. E_{Jet} for the $D^*\text{Jet}$ in the $n\gamma^*p$ -frame.

Jet	Data				MC		
	m_c (GeV)	σ_{stat} (GeV)	σ_{sys} (GeV)	$\overline{m}_c \pm \sigma_{stat}^{\overline{m}_c} \pm \sigma_{sys}^{\overline{m}_c}$ (GeV)	m_c (GeV)	σ_{stat} (GeV)	$\overline{m}_c \pm \sigma_{stat}^{\overline{m}_c}$ (GeV)
$D^*\text{Jet}$	1.33	0.19	0.16	$1.39 \pm 0.05 \pm 0.03$	1.19	0.07	1.40 ± 0.02
	1.44	0.19	0.06		1.24	0.06	
	1.36	0.16	0.11		1.37	0.06	
	1.44	0.17	0.11		1.36	0.05	
	1.35	0.14	0.12		1.46	0.06	
	1.23	0.11	0.12		1.48	0.04	
	1.54	0.20	0.18		1.47	0.11	
$Other\text{Jet}$	1.31	0.12	0.21	1.31	0.11		
	1.44	0.18	0.09	1.39	0.06		
	1.46	0.14	0.10	1.45	0.05		
	1.55	0.20	0.16	1.54	0.07		

Table 5.1: The $\alpha_0 E_{\text{Jet}} \approx m_c$ values from data and the MC model at detector level. The input value $m_c = 1.4$ GeV was used in the MC model. The rows represent the measurements from different jet energy bins and \overline{m}_c is the weighted average.

The mass used in the MC model simulations for the charm quark was:

$$m_c = 1.4 \text{ GeV}. \quad (5.19)$$

A dedicated study of heavy quark mass measurement can be considered using this method. The mass of the heavy quarks like charm, bottom or top could be determined using certain jets energies and, of course, enough statistics, as presented in the MC study shown in Sec. 5.3.5 and Sec. 1.4.

In the next section, a series of checks that have been performed in order to discriminate the influence of different effects and assumptions on the distribution of $\alpha_0 E_{\text{Jet}}$ vs. E_{Jet} are presented.

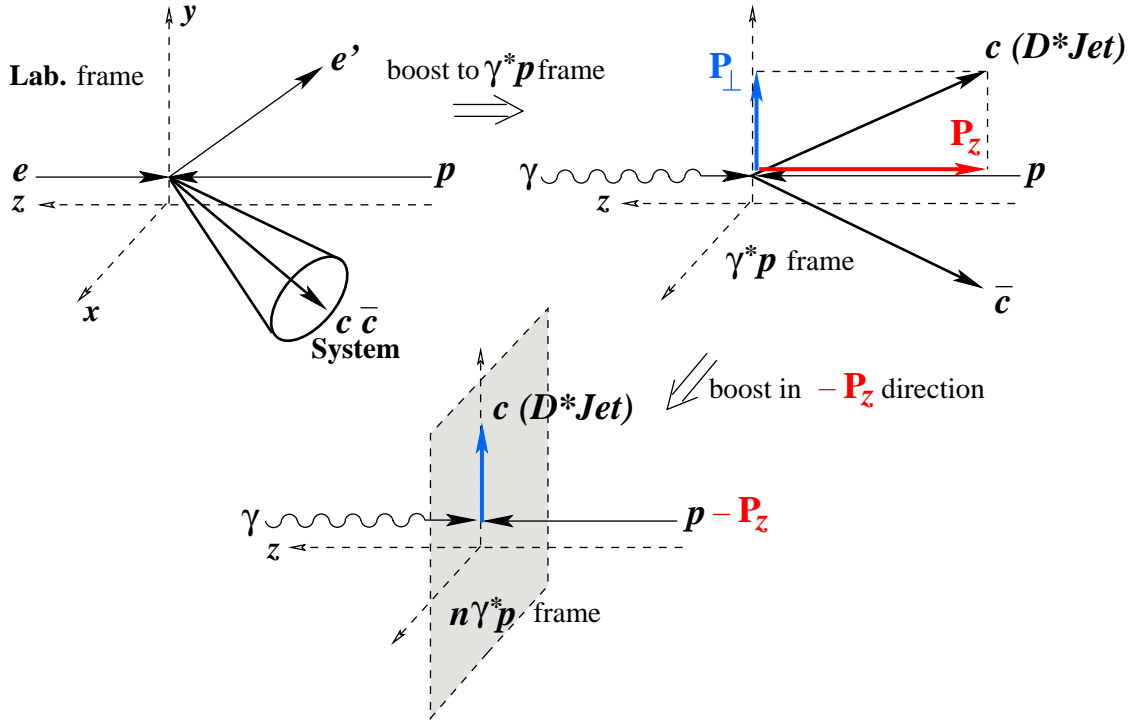


Figure 5.18: An illustration of the $n\gamma^*p$ -frame.

5.3.4 Checks of the Experimental Method

Checks were performed in order to establish the influence of other effects besides the *dead cone effect* on the distribution of $\alpha_0 E_{\text{Jet}}$ vs. E_{Jet} :

- the jet energy profiles for the $D^* \text{Jet}$ and the *OtherJet*;
- the influence of a fixed y_{cut}
- the influence of the fragmentation;
- the colour flow effect;
- a possible constant p_T of the gluon subjet with respect to the $D^* \text{Jet}$;
- the influence of the phase space.

a) The motivation to look at the jet energy profiles as a function of η and ϕ was that the depletion around the jet axis could have been produced by a wrong description of the particles in the jet. As it can be seen in Fig. 5.19, the distributions for the two

energy ranges shown here are similar and the MC model describes the data reasonably well.

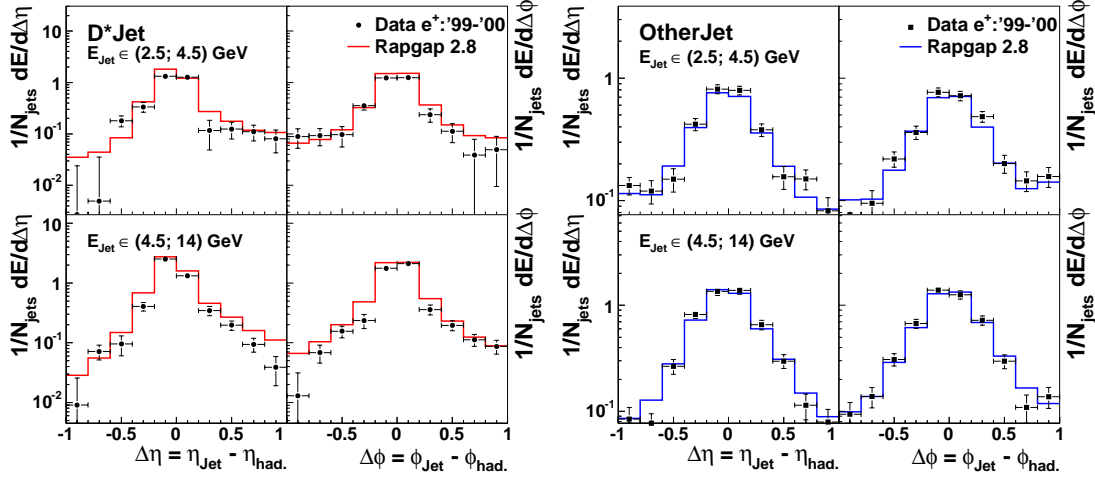


Figure 5.19: The jet energy profiles for the D^* Jet and the *OtherJet* in two ranges of jet energy. The difference $\Delta\phi$ is expressed in radians.

The η range of the D^* Jet was split into two ranges: a forward region, $0 < \eta < 1.5$, and a backward region, $-1.5 < \eta < 0$. The distribution of $\alpha_0 E_{\text{Jet}}$ vs. E_{Jet} was compared for the two ranges.

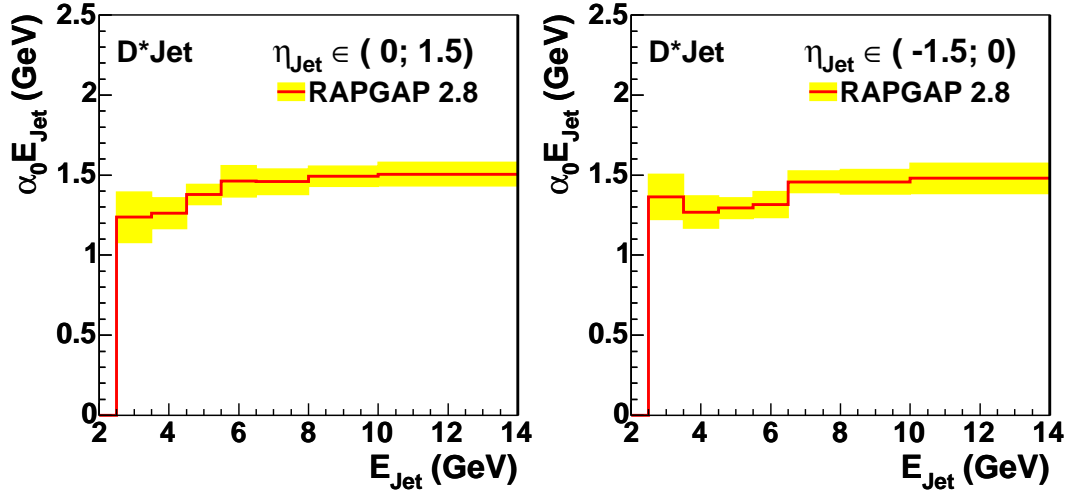


Figure 5.20: The distributions of $\alpha_0 E_{\text{Jet}}$ vs. E_{Jet} for the D^* Jet in the forward region, left, and in the backward region, right.

A difference between the two distributions might indicate a problem in the reconstruction of the HFS objects for the two regions of the detector. The results are shown in Fig. 5.20.

b) Due to the principle of the method, the resolution parameter y_{cut} is chosen such that exactly two subjects are identified. Another interesting check is performed by studying the influence of a fixed y_{cut} on the distribution of $\alpha_0 E_{\text{Jet}}$ vs. E_{Jet} when more than two subjects are found. In this case the angle α is plotted between the D^* Jet

and all subjects which do not contain the D^* -meson. The histograms are presented in Fig. 5.21 for two different y_{cut} values. The observed variation for $y_{\text{cut}} = 2 \cdot 10^{-3}$ in low jet energy bins is due to those subjects which have only one HFS object.

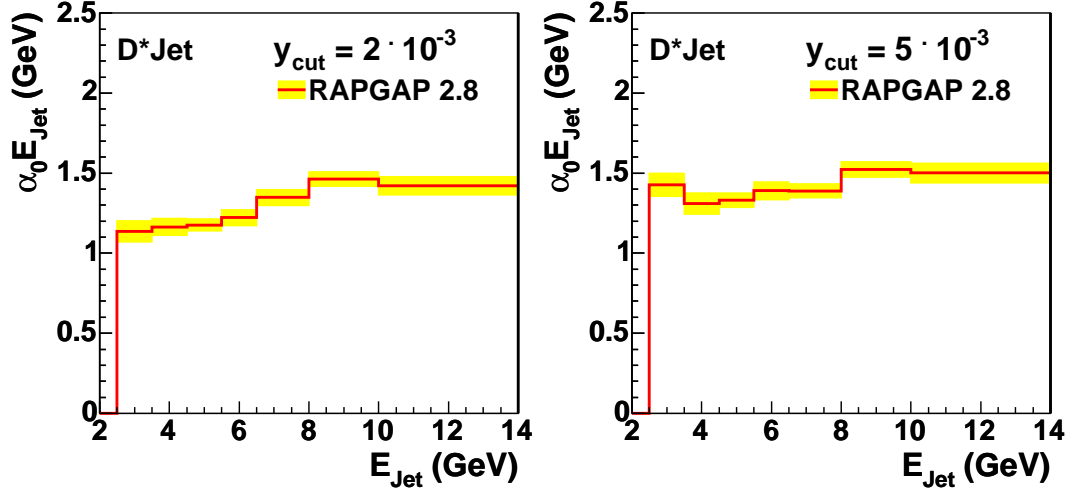


Figure 5.21: The distributions of $\alpha_0 E_{\text{Jet}}$ vs. E_{Jet} of the D^* Jet for two different fixed y_{cut} values.

c) Another concern is the influence of the fragmentation model on the comparison of data and MC. For this the HERWIG MC model was used and the results shown in Fig. 5.22 when compared to Fig. 5.16 indicate that the distribution of $\alpha_0 E_{\text{Jet}}$ vs. E_{Jet} do not depend significantly on the fragmentation model.

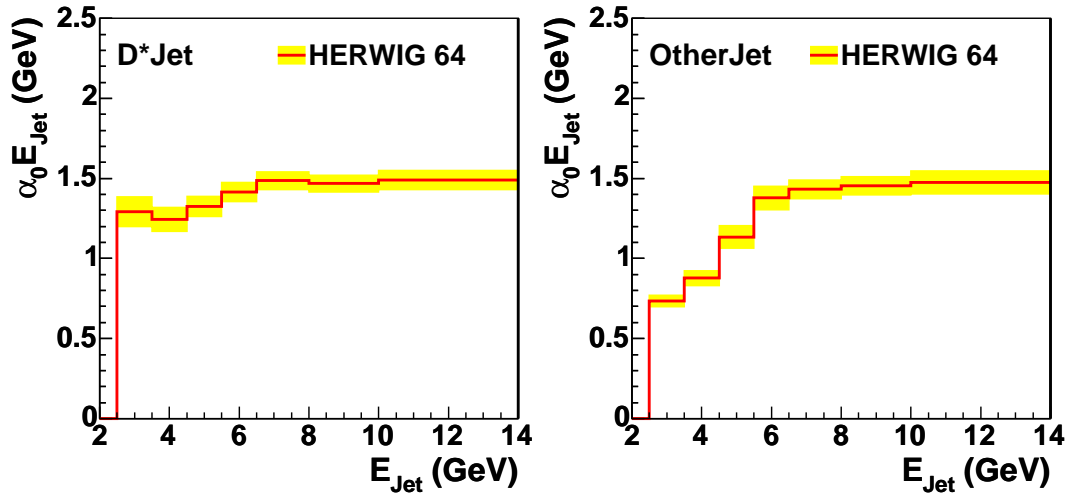


Figure 5.22: The $\alpha_0 E_{\text{Jet}}$ vs. E_{Jet} distribution using the HERWIG MC model for the D^* Jet and the *OtherJet*.

d) The distribution of $\alpha_0 E_{\text{Jet}}$ vs. E_{Jet} could be also influenced by the colour flow effect, also called colour drag effect, which is illustrated in Fig. 5.23. The charm meson from the string made of the \bar{c} and one of the light quarks from the proton should not be influenced by the colour flow. For the other charm quark, which forms the string with the remaining pair of light quarks from the proton, one might expect the emitted

soft gluon to be dragged more towards the proton direction than the c -quark. If this would be the case, a clear difference should be observed in the MC model when one compares the D^{*-} -meson with the D^{*+} -meson contribution.

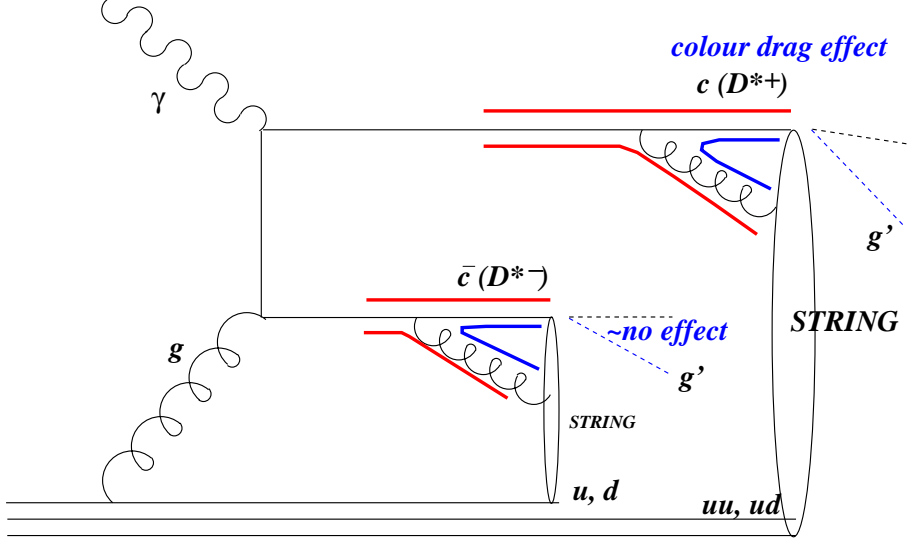


Figure 5.23: An illustration of the colour flow for the D^* -mesons.

This comparison is presented in Fig. 5.24. One observes a small difference between the positive and the negative D^* -mesons at low energy bins, but within the errors of the MC model one can conclude that there is no significant influence from the colour flow spoiling the interpretation of this distribution in terms of the *dead cone effect*.

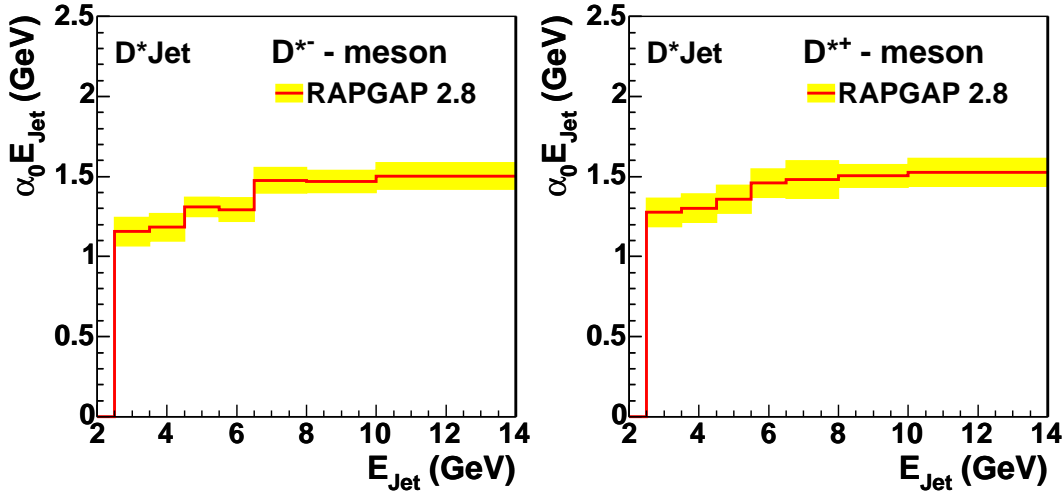


Figure 5.24: The distributions of $\alpha_0 E_{\text{Jet}}$ vs. E_{Jet} of the D^* Jet for the D^{*-} -mesons, left, and for the D^{*+} -mesons, right.

e) There is also another hypothesis to explain the distribution of $\alpha_0 E_{\text{Jet}}$ vs. E_{Jet} for the D^* Jet: if the relative p_T of the gluon subject to the jet direction is a constant of 1.5 GeV, this leads to the flatness of the distribution of $\alpha_0 E_{\text{Jet}}$ vs. E_{Jet} . The results shown in Fig. 5.25 do not support this hypothesis.

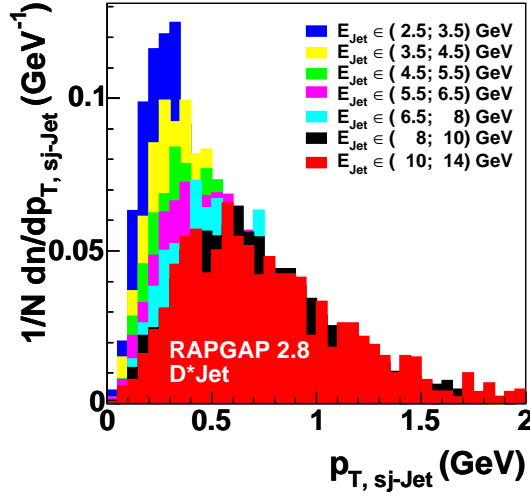


Figure 5.25: The distribution of the relative p_T of the gluon subjet to the D^* Jet in different bins of jet energy for the MC.

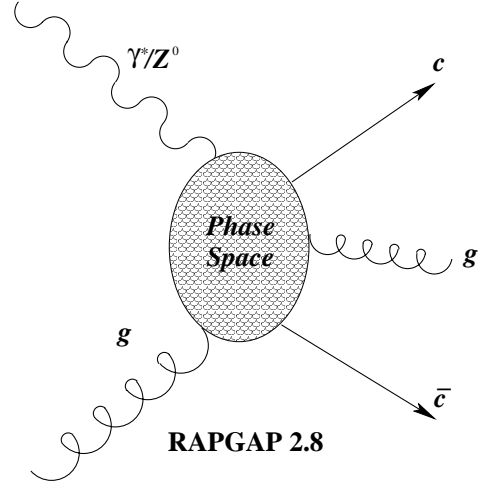


Figure 5.26: Illustration of $c\bar{c}g$ production according to phase-space.

f) The MC model was modified to generate $c\bar{c}g$ events according to *phase-space* as indicated in Fig. 5.26.

In Fig. 5.27, the distribution of $\alpha_0 E_Q$ vs. E_Q for the *phase-space* generated events is presented. One can observe that when the gluon is not radiated by the BGF heavy quark, the distribution is no longer flat.

Another observation is that gluons of the events generated according to *phase-space* are in general mainly *hard* gluons which produce their own jet on the hadron level and they cannot be found anymore as subjets. The investigation of these jets is not relevant for the experimental method proposed in this analysis.

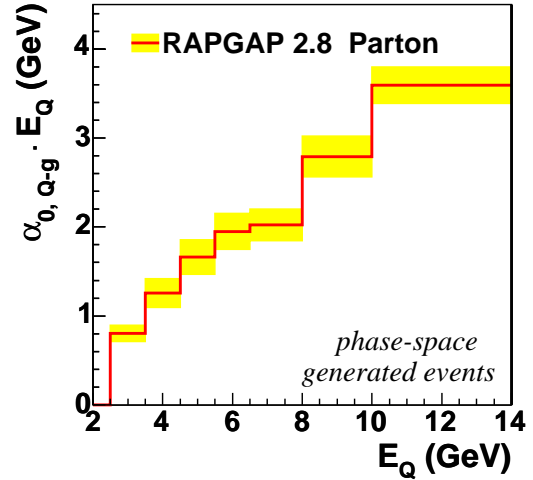


Figure 5.27: The distribution of $c\bar{c}g$ events $\alpha_0 E_Q$ vs. E_Q generated according to *phase-space*.

5.3.5 Monte Carlo Study of b -jets vs. c -jets

A Monte Carlo study using c -quarks and b -quarks⁴ with their respective masses on parton and hadron level was also performed. In the c -quark case the distribution of $\alpha_0 E_{\text{Jet}}$ vs. E_{Jet} at hadron level for the D^* Jet is presented in Fig. 5.28.

The bins in energy of the b -quark were chosen according to the ratio:

$$\frac{m_c}{E_c} = \frac{m_b}{E_b}. \quad (5.20)$$

⁴In principle one can increase artificially the charm mass. But the charmed mesons masses and the fragmentation need relative adjustments. Therefore this study is done with b -quarks.

If the energy of the b -quark becomes too large, the soft gluon radiation phase space becomes similar to the *light* quark one, see Sec. 1.4.

At hadron level, the B^0 -meson was assumed to have been reconstructed from its decays and therefore chosen for the b quark jet reconstruction.

The *OtherJet*, with a similar definition as in case of the c -quark jets, was used to reconstruct also the second b -quark from the BGF process.

For the *OtherJet*, the reconstruction of the b -quark is more complete than for the c -quark.

As a consequence, the distribution of $\alpha_0 E_{\text{Jet}}$ vs. E_{Jet} for the *OtherJet* is similar to the one from the B^0 Jet.

The results of the MC model simulation for the b -quark at parton level are shown in Fig. 5.4 for a b -quark mass of 5 GeV.

The distribution of $\alpha_0 E_{\text{Jet}}$ vs. E_{Jet} at hadron level for the B^0 Jet and the *OtherJet* are presented in Fig. 5.29.

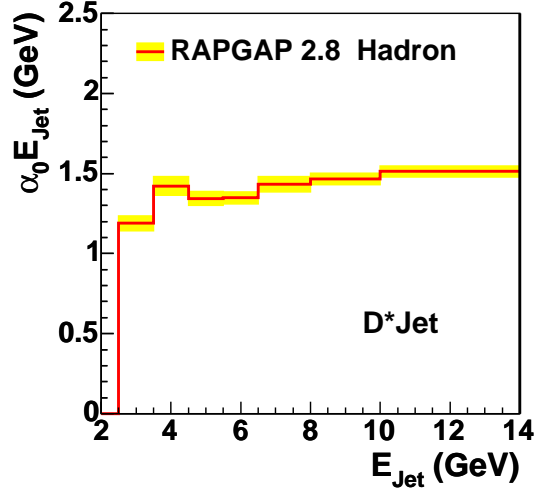


Figure 5.28: The distribution of $\alpha_0 E_{\text{Jet}}$ vs. E_{Jet} at hadron level for the D^* Jet.

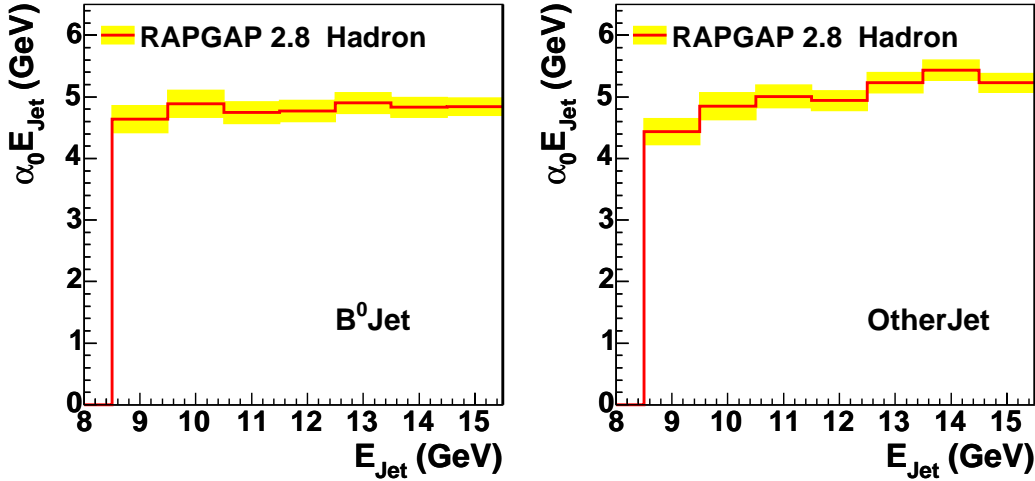


Figure 5.29: The distributions of $\alpha_0 E_{\text{Jet}}$ vs. E_{Jet} for the B^0 Jet and the *OtherJet* for the b -quark generated events.

More, for the charm quark the correlation in the (η, ϕ) plane between the radiated BGF gluons and the corresponding subjects are presented in Fig. 5.30. One can observe that the correlation between the gluon radiated by the BGFQ and the gluon subject found in the D^* Jet is better than the one for the *OtherJet*, as expected.

In the next section, the distribution of $\alpha_0 E_{\text{Jet}}$ vs. E_{Jet} for charm jets and jets for a di-jet (2Jet) sample are compared. The latter is dominated by light quarks. For comparison the "fake" D^* Jet is used for to reconstruct the light quark.

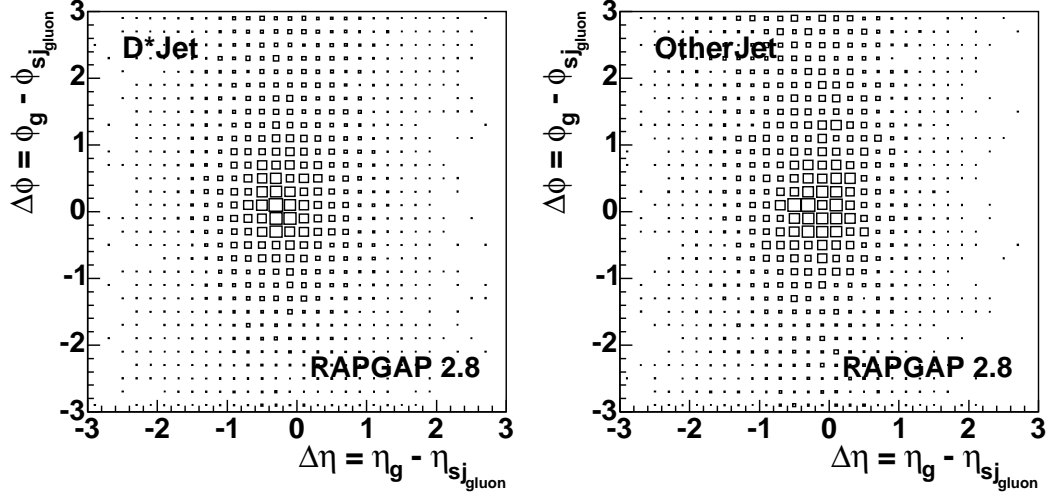


Figure 5.30: The correlations at hadron level between the BGF gluon and the corresponding gluon subjet for the D^* Jet, left, and the *OtherJet*, right.

5.3.6 A Comparison of Charm Jets with Jets from a $2Jet$ Sample

One can also plot the distribution of $\alpha_0 E_{Jet}$ vs. E_{Jet} for the side bands of the spectrum of the RiCh combinations, as well as for the WrCh combinations⁵. The idea behind this comparison is that the background in the Δm distribution should be mainly dominated by light quark events contributions. This comparison would also clarify the influence of using the D^* -meson as a stable particle in case of the D^* Jet. The results can be seen in Fig. 5.31.

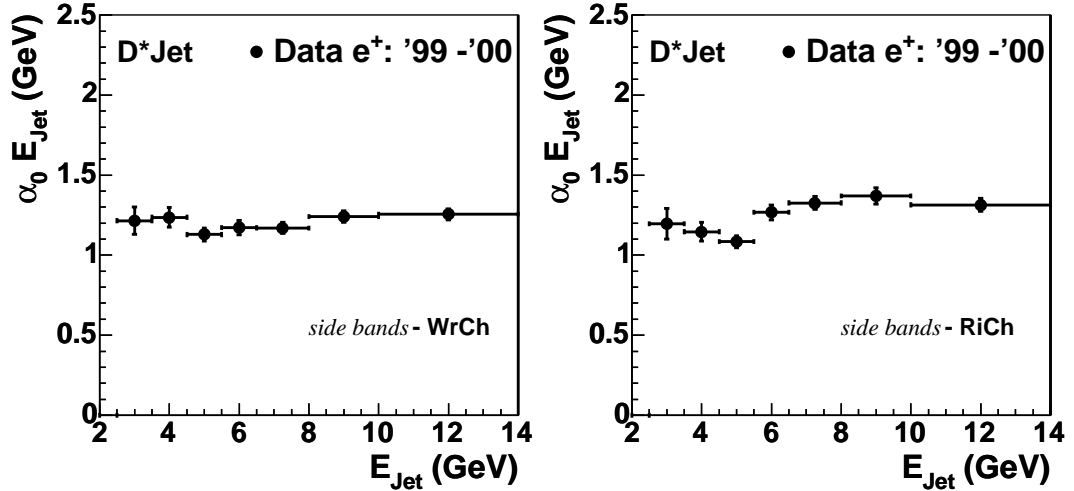


Figure 5.31: The distributions of $\alpha_0 E_{Jet}$ vs. E_{Jet} for the D^* Jet for the side bands in the Δm background of WrCh, the left plot, and the RiCh, the right plot. The side bands are defined here as $\Delta m \in (0.14; 0.142)$ GeV and $\Delta m > 0.149$ GeV.

One can see a small difference between the distribution of $\alpha_0 E_{Jet}$ vs. E_{Jet} from the Δm signal region, see Fig. 5.16, and the distribution from the Δm side bands.

The expected level for the side bands distribution is the one from the *pseudo-mass* of the light quarks at the parton level, see Fig. 5.5, due to the fact that the

⁵In both cases the *side bands* shown in Fig. 5.11, i.e. close to the Δm peak of the D^* -meson, are used.

background in the Δm distribution was assumed to be dominated by the contribution of light quarks.

The reason why the distributions of $\alpha_0 E_{\text{Jet}}$ vs. E_{Jet} for the side bands of the Δm spectrum are above the *pseudo-mass* of the light quarks is that the charm contributions in the Δm spectrum, which is obtained with the selection presented in Sec. 3.3.4, is still of the order of $\sim 33\%$, as can be seen in Fig. 5.32.

The MC model DJANGO 62 was used to generate fully inclusive DIS events. The charm contribution is significant and the level of the distribution of $\alpha_0 E_{\text{Jet}}$ vs. E_{Jet} increases.

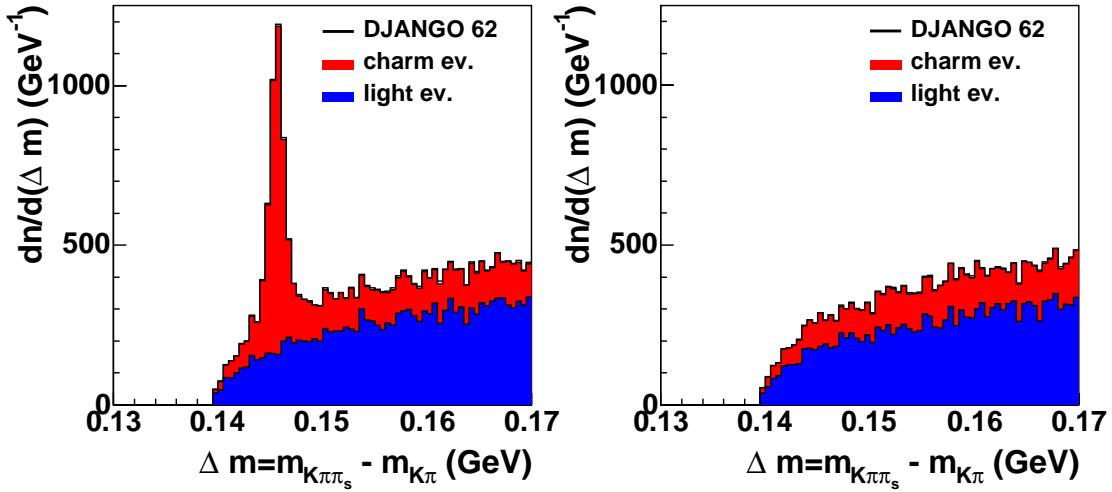


Figure 5.32: The Δm spectra for the RiCh, left, and the WrCh, right, obtained from events generated events with the inclusive MC model DJANGO.

A solution to this problem is to make use of a 2Jet event sample. The 2Jet events were selected from the 1999 and 2000 e^+ data taking periods using the cuts presented in Table 5.2.

The 2Jet sample cuts:
ST0 ST3 ST61
$2 \text{ GeV}^2 < Q_e^2 < 100 \text{ GeV}^2$
$0.05 < y_e < 0.7$
$E'_e > 8 \text{ GeV}$
$40 \text{ GeV} < E - p_z < 75 \text{ GeV}$
$N_{\text{jets}} \geq 2$
$ \eta_{\text{jets}} < 1.5$
$p_{\text{T,jets}} > 1.5 \text{ GeV}$

Table 5.2: The selection criteria for the 2Jet event sample.

The Δm distribution for the 2Jet event sample, without the selection cuts for the D^* -meson candidates that enrich the signal with respect to the background, is presented in Fig. 5.33. One can observe that the signal is swamped by the background. MC studies show that the Δm distribution in this case is dominated by light quarks, $\gtrsim 85\%$, see Fig 5.34.

In order to compare the charm jets with the jets from the 2Jet event sample on the same footing, the "fake" D^* -meson candidates which contribute in the Δm ranges:

$$0.140 < \Delta m < 0.142 \text{ GeV} \text{ or } \Delta m > 0.149 \text{ GeV} \quad (5.21)$$

were used. Outside the signal window, the light quark contributions to the Δm spectra increase.

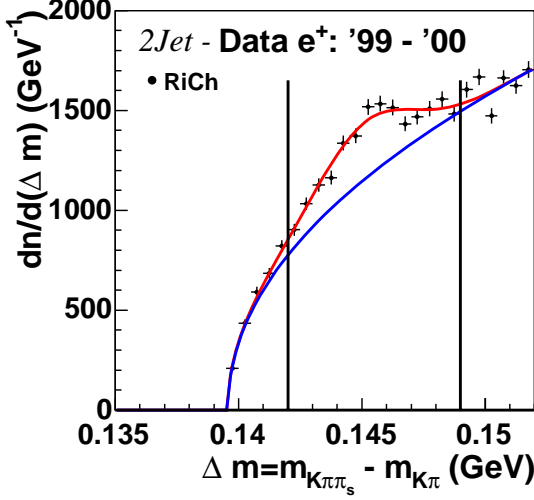


Figure 5.33: The Δm spectra for the $2Jet$ event sample.

After a fake D^* -meson candidate was found, the inclusive k_{\perp} jet finder algorithm is run in the same manner as for the charm jets, see Sec. 5.2. From the jets found, the one which contains the fake D^* -meson is called "fake" D^* Jet. For the $2Jet$ sample, only the "fake" D^* Jet is studied in order to establish whether there are two different $\alpha_0 E_{Jet}$ levels: for the charm jets and respectively the light quark jets.

With this method one can compare the charm jet event sample with a light quark jet dominated event sample on the same level.

The systematic errors were estimated using the DJANGO MC model. In Fig. 5.35, the systematic errors of the distribution of $\alpha_0 E_{Jet}$ vs. E_{Jet} for the "fake" D^* Jet of the $2Jet$ event sample are presented. The systematic error sources are the same as for the charm sample.

In Fig. 5.36 the α distributions of the $2Jet$ sample in bins of the "fake" D^* Jet energy are presented. The MC model describes the data reasonably well as one can observe from Fig. 5.37. Finally the comparison between the charm jets (D^* Jet) and the light quark jets ("fake" D^* Jet) from the $2Jet$ event sample is presented in Fig. 5.38.

In the first four bins of Fig. 5.38, a difference between the charm jets and the light quark jets from the $2Jet$ event sample can be seen. In the last three bins the statistical and systematic errors are larger. Also for the $2Jet$ event sample, the influence of the energy is dominant and the $\alpha_0 E_{Jet}$ values in the last three bins are getting larger with

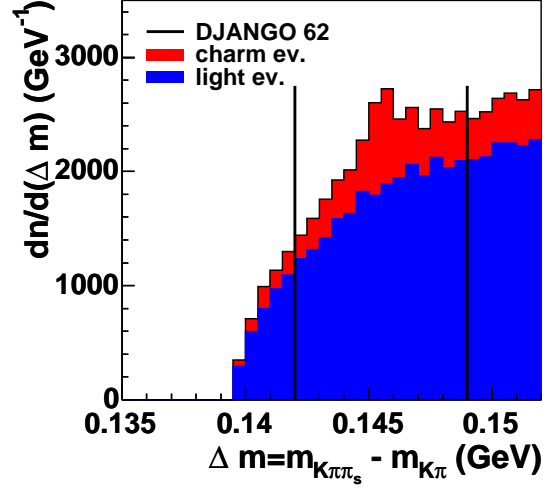


Figure 5.34: The Δm spectra for the $2Jet$ event sample in MC model DJANGO.

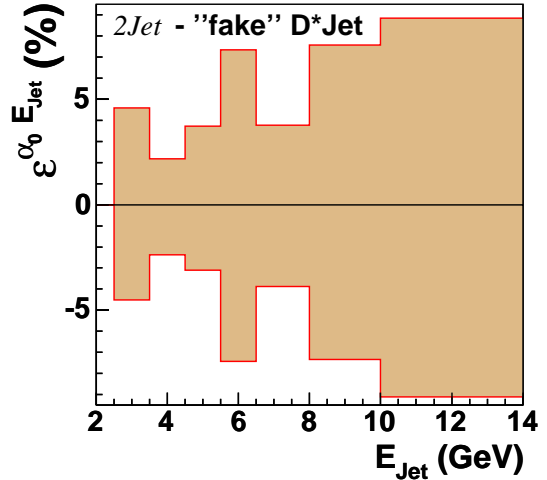


Figure 5.35: The systematic errors for the distribution of $\alpha_0 E_{Jet}$ vs. E_{Jet} for the "fake" D^* Jet in the $2Jet$ sample.

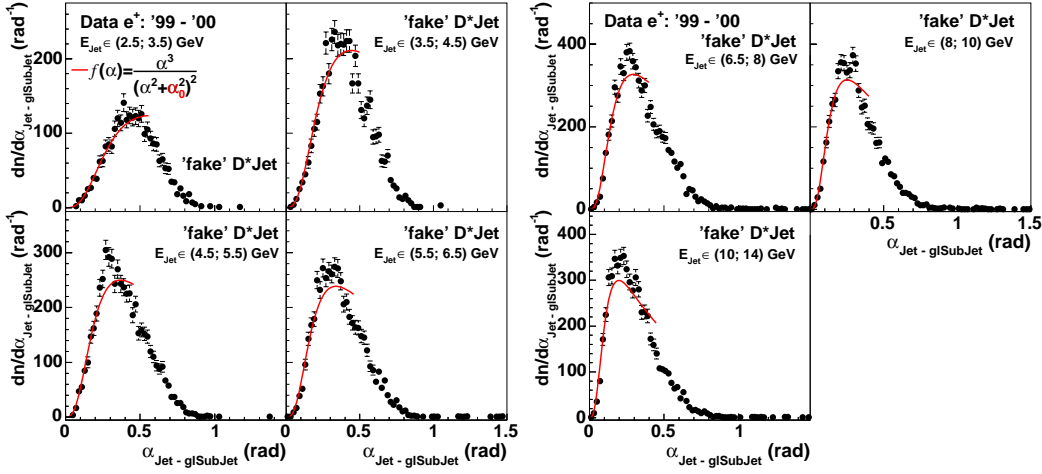


Figure 5.36: The α distributions and the fit function fit_α in bins of jet energy for the "fake" D^* Jet of the $2Jet$ sample.

increasing energy. Starting with the last bin the method is probably no longer sensitive to $\alpha_0 E_{Jet}$ product but rather to E_{Jet} alone.

The value for the weighted average *pseudo-mass* level of the "fake" D^* Jet of the $2Jet$ event sample is presented in Table 5.3.

The weighted average value obtained for the *pseudo-mass* level is consistent with the default value of the Q_0 in MC if one considers that the $2Jet$ event sample still has contributions from the charm quarks of about $\sim 10\%$. Q_0 is the invariant mass *cut-off* which gives the level of $\alpha_0 E_Q$ at parton level, see Sec. 5.1.2. The result obtained for $\overline{m_c} - 3\sigma^{\overline{m_c}}$ is different from the one of $\overline{m_{pseudo}} + 3\sigma^{\overline{m_{pseudo}}}$:

$$(\overline{m_c} - 3\sigma^{\overline{m_c}}) - (\overline{m_{pseudo}} + 3\sigma^{\overline{m_{pseudo}}}) = 0.08 \quad (5.22)$$

where $\sigma = \sqrt{\sigma_{stat}^2 + \sigma_{sys}^2}$.

Jet (Data)	m_{pseudo}	σ_{stat}	σ_{sys}	$\overline{m_{pseudo}} \pm \sigma_{stat}^{\overline{m_{pseudo}}} \pm \sigma_{sys}^{\overline{m_{pseudo}}}$
$e^+ : '99 - '00$	(GeV)	(GeV)	(GeV)	(GeV)
"fake" D^* Jet	1.01	0.03	0.04	$1.07 \pm 0.01 \pm 0.02$
	1.02	0.02	0.02	
	1.06	0.02	0.04	
	1.16	0.01	0.09	
	1.22	0.02	0.05	
	1.28	0.02	0.10	
	1.33	0.02	0.12	

Table 5.3: The $\alpha_0 E_{Jet} \approx m_{pseudo}$ values from data of "fake" D^* Jet of the $2Jet$ event sample. The rows represent the measurements from different jet energy bins. The $\overline{m_{pseudo}}$ is the weighted average.

In order to establish this difference more clearly, one needs to use larger statistics for the charm jets. This is presented in the next section.

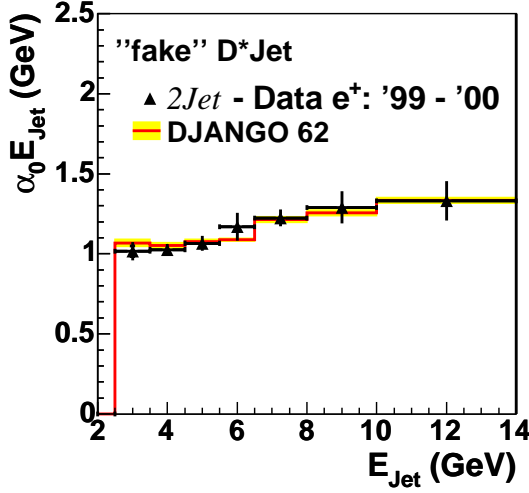


Figure 5.37: The distribution of $\alpha_0 E_{\text{Jet}}$ vs. E_{Jet} for the "fake" D^* Jet in the 2Jet sample.

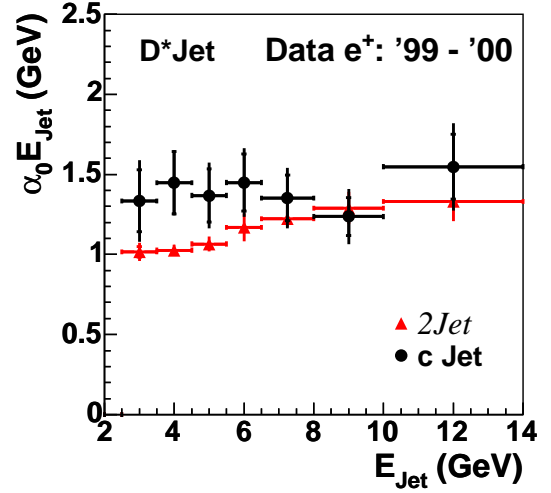


Figure 5.38: The comparison between the D^* Jet of the charm event sample and the "fake" D^* Jet of the 2Jet sample.

5.3.7 Higher Statistics '96-'04

To reduce the statistical errors, all available statistics was analysed. For the years 1996 and 1997 the subtrigger was chosen according to the corresponding trigger setup. A similar selection to the one used for the 1999 and 2000 e^+ data taking periods was applied to the entire data sample. The Δm spectrum can be seen in Fig. 5.39. The distribution of $\alpha_0 E_{\text{Jet}}$ vs. E_{Jet} is presented in Fig. 5.40.

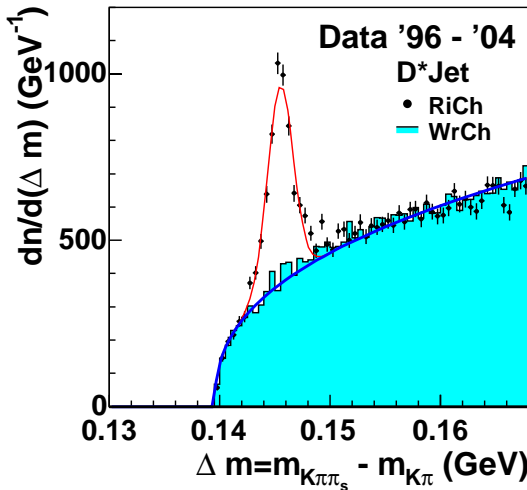


Figure 5.39: The Δm spectrum for the event sample from '96-'04 used to study the *dead cone effect* ($N_{D^*} = 4126 \pm 127$).

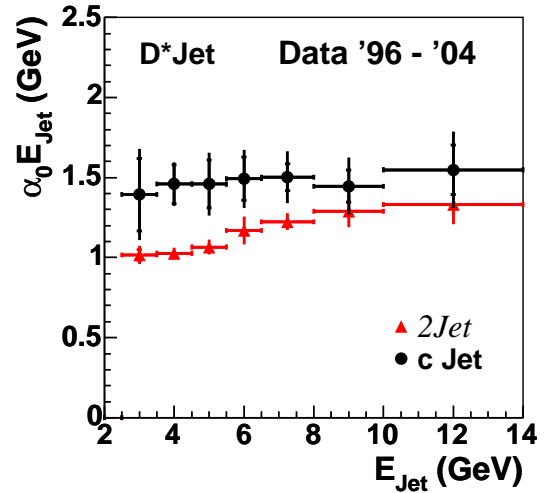


Figure 5.40: The comparison between the '96-'04 charm event sample and the 2Jet sample.

With this, the difference between distribution of $\alpha_0 E_{\text{Jet}}$ vs. E_{Jet} for the charm from the one for the 2Jet event sample can be seen rather clearly.

The difference becomes even clearer when one applies the following correction. As

mentioned above, the $2Jet$ sample still contains a charm contribution of $\sim 10\%$. One can perform the analysis using only *light* quark events from MC. The ratio between the $\alpha_0 E_{Jet}$ values obtained from the *light* event sample and the total event sample, *light* and *charm* events, can be considered a correction factor for the $2Jet$ data sample:

$$f_{corr} = \frac{\alpha_0 E_{Jet, light}}{\alpha_0 E_{Jet, light \& charm}}. \quad (5.23)$$

With this correction, based on the reasonably good description of the data by MC, one can obtain a prediction for a *light* quark jet sample only, $2Jet^{light}$. In Fig. 5.41 the correction factors obtained from the MC model are shown. They are also given in Table 5.4.

E_{Jet} (GeV)	(2.5;3.5)	(3.5;4.5)	(4.5;5.5)	(5.5;6.5)	(6.5;8)	(8;10)	(10;14)
f_{corr}	0.99	1.00	1.00	0.99	0.97	0.94	0.94

Table 5.4: The correction factors for the $2Jet^{light}$ distribution.

The comparison between the charm event sample and the $2Jet^{light}$ event sample is presented in Fig. 5.42.

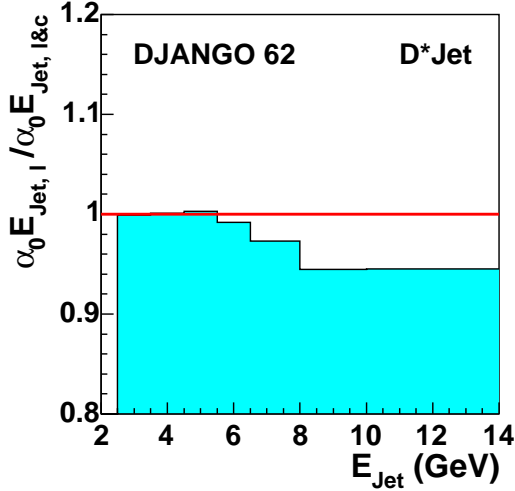


Figure 5.41: The correction factors for a $2Jet^{light}$ event sample obtained from the MC model.

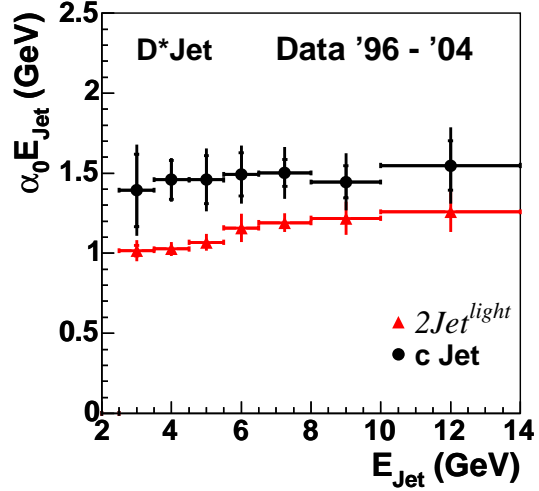


Figure 5.42: The comparison between the '96-'04 charm event sample and the $2Jet^{light}$ event sample.

Including this correction, the result obtained for the difference defined in Eq. 5.22 between the two data sets, the D^*Jet and the "fake" D^*Jet of the $2Jet^{light}$ event sample, is:

$$(\overline{m_c} - 3\sigma^{\overline{m_c}}) - (\overline{m_{pseudo}} + 3\sigma^{\overline{m_{pseudo}}}) = 0.15, \quad (5.24)$$

which corresponds to more than 5σ deviation.

One can conclude that differences between the charm jets and the light quark jets can be observed in data and that the MC model prediction describes these differences reasonably well. The distribution of $\alpha_0 E_{Jet}$ vs. E_{Jet} can provide a nice and unique possibility to observe *dead cone effect*, the effect of the mass on the gluon radiation, in a direct way.

Chapter 6

Conclusions

The subject of this thesis is the study of charm jets in DIS. Charm quarks can be investigated using the corresponding jet, called charm jet, which is made out of the hadronic final state objects. Charm jets are traditionally described by jet shape variables and the mean subjet multiplicity. An innovative way to study charm jets is to make use of the soft gluon radiation of the quarks as explained in the first chapter of this thesis.

In analogy with electrodynamics, the theory of quantum chromodynamics stipulates that soft gluon radiation of heavy quarks is suppressed towards the quark direction. This suppression is called the *dead cone effect*.

The data used in this analysis were taken with the H1 detector at the HERA collider as described in the second chapter.

The selection of charm events is presented in the third chapter. A careful and detailed selection of the electron and the D^* -meson candidates ensures that background is highly suppressed.

In the fourth chapter, the study of the charm jets using the jet shape variables and the mean subjet multiplicity is presented. The jet selection and the HFS algorithm which uses the reconstructed hadrons of the final state are described. For the reconstruction of the two charm quarks from a *boson gluon fusion* event, two different jet requirements are employed: the D^* Jet and the *OtherJet*. Jets are found using the k_{\perp} -jet algorithm. The D^* Jet is the jet which contains the reconstructed D^* -meson which is treated as a stable particle. If additional jets are found, the one with the highest p_T , excluding the D^* Jet, has a high probability to be the second charm quark in the event. This jet is called the *OtherJet*. Interesting differences between the two types of charm jets are observed for the jet shape variables and the mean subjet multiplicity.

In order to investigate if the observed differences depend on the way the D^* Jet is defined, two alternative definitions are also studied. The differences between the two types of charm jets do not vanish if the D^* Jet definition is changed.

In another systematic study a new definition of the E_T jet fraction radius, r^* , which enters the calculation of jet shape variables is used. The r^* is defined in the spirit of the inclusive k_{\perp} finder:

$$r^* = p_h \cdot \sin \alpha_{h-\text{Jet}}.$$

In this case, the observed differences are rather small. Therefore the choice of using the reconstructed D^* -meson candidate as a stable particle is not the major source of the observed differences between the two types of charm jets. On the other hand this definition ensures the best correlation in terms of energy and direction between the

charm quark and its corresponding jet, as one can observe from MC studies presented in Appendix F. A reasonable good correlation is even observed for low energetic jets in the energy range between 2.5 and 4 GeV.

The dependence of these differences between the D^* Jet and the *OtherJet* as a function of E_{Jet} , η_{Jet} and $E_{\text{T,Jet}}$ is also studied. These distributions and the correlation with the charm quarks show that the main sources of these differences are the incomplete reconstruction of the charm quark by the *OtherJet* plus the fact that the parton that generates the *OtherJet* is in some regions of phase space a hard gluon.

Using the definition of the D^* Jet, which, as demonstrated, gives the best charm quark - jet correlation, the *dead cone effect* is studied in the fifth chapter. The *Energy Variation* approach, presented in Sec. 5.1, is used to study this effect. This approach is based on the equation:

$$\alpha_0 E_{\text{Jet}} \simeq m_Q. \quad (6.1)$$

The experimental method used to measure the *dead cone* angle, α_0 , is presented in Sec 5.2.1 and Sec 5.2.2 for the D^* Jet and the *OtherJet*, respectively. The dependence of the variable $\alpha_0 E_{\text{Jet}}$ on E_{Jet} is well described by the MC model used in this analysis, which includes the *dead cone effect*. The results for the two types of charm jets show differences only in the energy range where the *OtherJet* cannot reconstruct the properties of the charm quark as well as the D^* Jet. This can be observed in the correlation plots from the MC studies.

The possible influences of other effects than the *dead cone effect* on the distribution of $\alpha_0 E_{\text{Jet}}$ vs. E_{Jet} are studied showing however only small contribution to it. A MC study showed a nice consistency of the method, when bottom quarks and their corresponding jets containing a B^0 -meson are used instead of charm quarks and their D^* Jet.

A comparison of the charm quarks with light quarks is also performed. In order to perform the analysis for both quark flavours on the same footing, the following method is used. In a di-jet (*2Jet*) event sample D^* -meson candidates are selected without applying the requirements which enhance the signal with respect to the background. This way, the light quark contribution in the Δm spectrum of the D^* -meson candidates is increased to above 85%. Furthermore, the Δm signal region is excluded from the analysis and only the side bands are used for the distribution of $\alpha_0 E_{\text{Jet}}$ vs. E_{Jet} . The "fake" D^* -meson is considered as a stable particle, like in the standard analysis, and the corresponding jet is called the "fake" D^* Jet, such that the same criteria are used for the jets of both flavours. Comparing the results of charm and light flavour jets, a difference between the two distributions of $\alpha_0 E_{\text{Jet}}$ levels is observed.

Finally, including HERA-II data in the analysis the statistical error can be further reduced and the differences between light quarks and charm quarks become even clearer. The difference obtained in weighted averages between the two distributions of $\alpha_0 E_{\text{Jet}}$ is more than 5σ . These differences can be interpreted as being due to the *dead cone effect*: the α_0 angle yields a measure of the size of the angular region of suppressed gluon emission close to the quark direction and it is seen to depend on the heavy quark energy as predicted by QCD.

Appendix A

QCD Environment

The strong interaction is mediated by the gluons. The name of Quantum Chromodynamics (QCD) is coming from the *colour* of the quarks and the gluons, which has the role of an elementary charge in the strong interactions. QCD is a non-Abelian group and the gluons can couple also to each other.

The cross-sections can be calculated in perturbative QCD (pQCD) as power series in the strong coupling constant α_s . The calculations have different levels of accuracy. In the so called *leading order* (LO) calculations, the internal loops as the ones shown in Fig. A.1 are neglected, but these are giving additional contributions in the *next to leading order* (NLO) ones.



Figure A.1: Loops in QCD: a) the gluon loop and b) the fermion loop.

The contributions of a particular loop are calculated integrating over all particle momenta p in the loop. For $p \rightarrow \infty$ the *ultraviolet divergences* are reached. In a renormalisation these divergences are absorbed into the *running* of the strong coupling constant. A new arbitrary renormalisation scale μ_R needs to be introduced.

The μ_R scale can be interpreted as the momentum for which the subtraction that removes the divergences is performed.

Taking into account the arbitrariness of the scale μ_R , the physical observable which has to be calculated to all orders in α_s needs to be independent of μ_R . From the mathematical point of view, the upper condition is given by the renormalisation group equation (RGE):

$$\mu_R^2 \frac{dR}{d\mu_R^2} = \mu_R^2 \frac{\partial R}{\partial \mu_R^2} + \mu_R^2 \frac{\partial \alpha_s}{\partial \mu_R^2} \frac{\partial R}{\partial \alpha_s} = 0 \quad (\text{A.1})$$

where R is the independent observable of μ_R .

One can re-write the differential equation as a power series in $\alpha_s(\mu_R^2)$ and the β functions in the following way:

$$\mu_R^2 \frac{\partial \alpha_s}{\partial \mu_R^2} = \alpha_s \beta(\alpha_s) = -\beta_0 \alpha_s^2 - \beta_1 \alpha_s^3 - O(\alpha_s) \quad (\text{A.2})$$

with

$$\beta_0 = 11 - \frac{2}{3} \cdot n_f; \quad \beta_1 = 102 - \frac{38}{3} \cdot n_f. \quad (\text{A.3})$$

The number of active flavours is indicated by n_f .

For the one loop approximation when only the β_0 term is considered the following relation is obtained for α_s :

$$\alpha_s(\mu_R^2) = \frac{1}{\frac{\beta_0}{4\pi} \cdot \ln\left(\frac{\mu_R^2}{\Lambda_{QCD}^2}\right)} \quad (\text{A.4})$$

The Λ_{QCD} is the scale where α_s gets large enough and the perturbative series in α_s no longer converges. At this scale the pQCD is not applicable any longer. The Λ_{QCD} is experimentally determined to be about 200 MeV. A more convenient estimation of α_s is at the Z^0 mass scale. The experimental value [14] is:

$$\alpha_s(M_Z) = 0.119 \pm 0.004. \quad (\text{A.5})$$

Another type of divergences that appear in the NLO calculations are the *infrared* divergences which are also a consequence of the α_s behavior (for small scales μ^2 , α_s is large). A typical example of divergency is the collinear gluon radiation. The transverse momentum of the emitted gluon $k_\perp \rightarrow 0$ leads to a divergency due to $d\sigma/dk_\perp^2 \sim 1/k_\perp^2$. This type of divergences are removed in the integration over the k_\perp making use of an artificial *cut-off* limit μ_F . The scale μ_F is a non-perturbative scale where the pQCD breaks down. These divergences are absorbed into the parton densities. One could say in analogy with the *running* of the α_s that here one has a *running* of the parton densities $f_{i/p}(x, \mu_F)$. For *hard* processes with $\mu^2 > \mu_F^2$, the pQCD can be applied due to small α_s , but the *soft* processes with $\mu^2 \leq \mu_F^2$ are absorbed in $f_{i/p}(x, \mu_F)$ which are also called *renormalised parton densities*. This classification in *hard* and *soft* processes is called *factorisation*. The μ_F is factorisation scale. An intuitive drawing of the factorisation principle is shown in Fig. A.2.

The treatment of the singularities is given by the factorisation scheme, but the one of the finite terms is arbitrary. Nevertheless the factorisation scheme determines the amount of finite terms which factorise into renormalised quark distributions. For the DIS scheme all finite contributions are absorbed in the quark density. The structure function F_2 in this case is given by:

$$F_2(x, \mu_F^2) = x \sum_q e_q^2 \cdot (f_{q/p}(x, \mu_F^2) + f_{\bar{q}/p}(x, \mu_F^2)). \quad (\text{A.6})$$

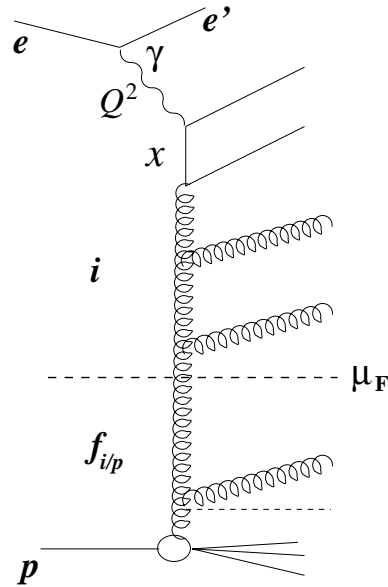


Figure A.2: The factorisation principle with μ_F the factorisation scale.

The ep cross section is the convolution between the *renormalised parton density function* $f_{i/p}(\mu_F^2)$, which depends on the factorisation scale μ_F^2 , and the *hard boson parton cross section* $\hat{\sigma}_i(\hat{s}, \alpha_s(\mu_R), \mu_R, \mu_F)$, which is calculable in pQCD:

$$d\sigma^{ep \rightarrow e'X} = \sum_{\text{partons}} \int_0^1 dx f_{i/p}(\mu_F^2) \cdot \hat{\sigma}_i(\hat{s}, \alpha_s(\mu_R), \mu_R, \mu_F). \quad (\text{A.7})$$

An important observation is, as the factorisation theorem says, that the renormalised parton density functions depend only on the hadron type and they are *universal*. Once the parton densities of the proton are determined at HERA, they can be plugged in descriptions of all type of proton collisions, e.g. at Large Hadron Collider (LHC).

The renormalised parton densities depend on scale due to the included soft processes up to factorisation scale μ_F . For μ_F^2 in DIS a commonly used value is the Q^2 , but for heavy quarks another choice is needed because the mass itself can be large enough to be considered as a scale. There is no fundamental prediction for the parton densities. Once the parton densities are known at an arbitrary scale μ_0 , they can be determined at any other scale using the QCD evolution equations. The models used for QCD evolution are DGLAP, BFKL and CCFM. The input of the initial parton densities are provided by experimental results.

The evolution models consider the gluon radiation and the gluon splitting processes as shown in Fig. A.3. The splitting function $P_{ij}(z)$ gives the probability of a parton j , with four-momentum k and longitudinal momentum fraction x , to radiate another parton carrying the momentum fraction $(1-z)x$ and to continue as parton i with momentum fraction zx . For the situation shown in Fig. A.3 a), the cross section

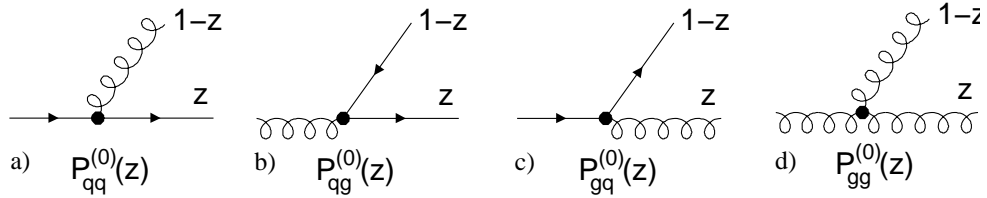


Figure A.3: The splitting function $P_{ij}(z)$.

$d\sigma_{q \rightarrow qg}/dk^2 \sim 1/k^2$ and has a singularity for $k^2 \rightarrow 0$. In Fig. A.3 d) the gluon splits into two gluons and $d\sigma_{q \rightarrow qg}/dk^2 \sim 1/k^2 \cdot 1/z$ has two singularities for $k^2 \rightarrow 0$ and $z \rightarrow 0$. The three evolution models treat these singularities differently.

The DGLAP model performs the parton densities evolution in k^2 assuming that the emission of gluons is ordered in k^2 . This assumption implies that the emitting partons should be ordered at small z in the square transverse momentum k_{\perp}^2 as well as the emitted partons in p_{\perp}^2 .

The gluon ladder in DGLAP approach is shown in Fig. A.4 a). The DGLAP model is based on a collinear factorisation.

The DGLAP evolution equations can be applied for large scales μ^2 and moderate Bjorken x and can be written as:

$$\frac{\partial f_{qj/p}(x, \mu^2)}{\partial \ln(\mu^2)} = \int_x^1 \frac{dz}{z} \frac{\alpha_s}{2\pi} \left(\hat{P}_{qq}(z) f_{qj/p}\left(\frac{x}{z}, \mu^2\right) + \hat{P}_{qg} g\left(\frac{x}{z}, \mu^2\right) \right) \quad (\text{A.8})$$

$$\frac{\partial g(x, \mu^2)}{\partial \ln(\mu^2)} = \sum_{q, \bar{q}} \int_x^1 \frac{dz}{z} \frac{\alpha_s}{2\pi} \left(\hat{P}_{gg}(z) g\left(\frac{x}{z}, \mu^2\right) + \hat{P}_{gq} f_{qj/p}\left(\frac{x}{z}, \mu^2\right) \right) \quad (\text{A.9})$$

The BFKL model has an evolution in x and can be used for moderate μ^2 and small x . The model assumes that the momentum fraction carried by the parton, z , after emission is very small. The leading contribution is given by the $1/z$ term and the model needs a resummation of the $\ln(1/x)$ terms. In the gluons ladder of the BFKL model the partons are unordered. The hard scattering cross-section is calculated off-shell. This means that the virtuality of the parton contributing to the cross-section cannot be neglected as in DGLAP model where the hard cross-section is calculated on-shell. The BFKL model is based on the k_\perp factorisation. The gluon density in BFKL $F(x, k_\perp^2, \mu_0^2)$ can be related to the DGLAP one $g(x, \mu^2)$ as:

$$xg(x, \mu^2) \simeq \int_0^{\mu^2} F(x, k_\perp^2, \mu_0^2) \frac{dk_\perp^2}{k_\perp^2}. \quad (\text{A.10})$$

The CCFM model combines the DGLAP and BFKL approaches such that for large scales μ^2 and moderate x it is equivalent with DGLAP, and for moderate μ^2 and small x is equivalent with BFKL. The model is based on the resummation of the singularities in z and in k^2 without requiring a strong k_\perp^2 ordering. This leads to a hard cross-section which depends on k_\perp . The CCFM model is based on a k_\perp factorisation as the BFKL one. The gluon emission is performed in a region where the emission angle is increased, an evolution in angle as shown in Fig. A.4 b).

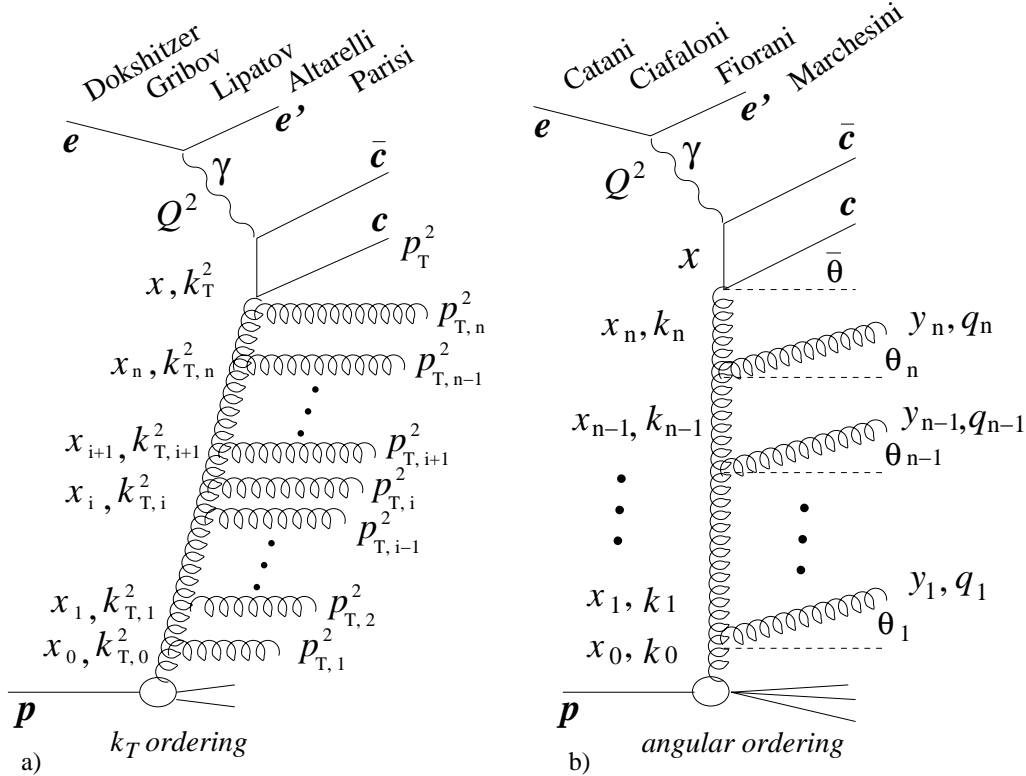


Figure A.4: The gluon ladder for a) DGLAP model and b) CCFM model.

The gluon density $A(x_g, k_\perp, \vec{q}'_t)$ in CCFM depends on the maximum angle allowed for any emission \vec{q}'_t which has the meaning of the factorisation scale μ_F^2 .

The CCFM evolution equation [10] is:

$$\vec{q}'_t \frac{d}{d\vec{q}'_t{}^2} \frac{x A(x, k_\perp, \vec{q}'_t)}{\Delta_S(\vec{q}'_t, \mu_0)} = \int dz \frac{d\phi}{2\pi} \frac{\tilde{P}\left(z, \frac{\vec{q}'_t}{z}, k_\perp\right)}{\Delta_S(\vec{q}'_t, \mu_0)} x' A(x', k'_\perp, \frac{\vec{q}'_t}{z}) \quad (\text{A.11})$$

where x' and k'_\perp are the momentum fraction and the transverse momentum before the last gluon emission. The Δ_S is the Sudakov form factor:

$$\Delta_S(\mu^2) = e^{-\int_{\mu_0}^{\mu^2} \frac{d\mu'^2}{\mu'^2} \int dz \frac{\alpha_s}{2\pi} \tilde{P}(z)} \quad (\text{A.12})$$

with \tilde{P} being the gluon splitting function in the CCFM model.

Appendix B

Mandelstam Variables

In a scattering process with two particles in the initial state and two in the final state, as in the Fig. B.1, one identifies the following types of channels:

- i)* $1 + 2 \rightarrow 3 + 4$;
- ii)* $1 + \bar{3} \rightarrow \bar{2} + 4$;
- iii)* $1 + \bar{4} \rightarrow \bar{3} + 2$.

where the numbers stand for the particles and the over-lined numbers for the antiparticles. The particle labeled 2 is in the first channel in the initial state. In the

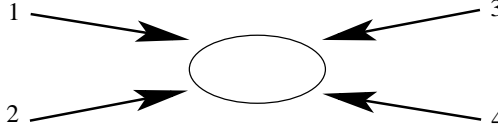


Figure B.1: The process with two initial state particles and two final state particles.

second channel it is in the final state which implies that the temporal component of the four-vector has changed the sign, actually it is the corresponding antiparticle.

For all the three channels, the energy-momentum four-vector as well as the charge and other quantum numbers have to be conserved:

$$\mathbf{p}_1 + \mathbf{p}_2 + \mathbf{p}_3 + \mathbf{p}_4 = 0. \quad (\text{B.1})$$

One can define the following quantities:

$$s = (\mathbf{p}_1 + \mathbf{p}_2)^2 = (\mathbf{p}_3 + \mathbf{p}_4)^2 \quad (\text{B.2})$$

$$t = (\mathbf{p}_1 + \mathbf{p}_3)^2 = (\mathbf{p}_2 + \mathbf{p}_4)^2 \quad (\text{B.3})$$

$$u = (\mathbf{p}_1 + \mathbf{p}_4)^2 = (\mathbf{p}_2 + \mathbf{p}_3)^2 \quad (\text{B.4})$$

which are called the *Mandelstam variables* [59]. The three variables are related via:

$$s + t + u = m_1^2 + m_2^2 + m_3^2 + m_4^2 \quad (\text{B.5})$$

where m_i with $i = \overline{1,4}$ are the masses of the particles.

The variable s represents the total energy of the system in the centre of mass reference system of the channel *i*). The same physical meaning have t and u for the channels *ii*) and *iii*) respectively.

For this reason the three channels are usually called s , t and u channels as in the Fig. B.2. These variables initially introduced by Mandelstam are now used to describe kinematics of the multi-body final states interpreted as two incident and two outgoing systems.

A graphical representation of the Mandelstam variables and their values domain are shown in Fig. B.3.

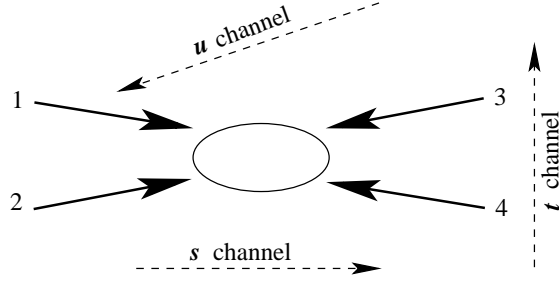


Figure B.2: The s , t and u channels.

The coordinate system of this representation is a triangular one in a plane. The axes of the system are given by the three sides of an equilateral triangle. The s , t and u coordinates are positive if they point to the interior of the triangle and negative otherwise.

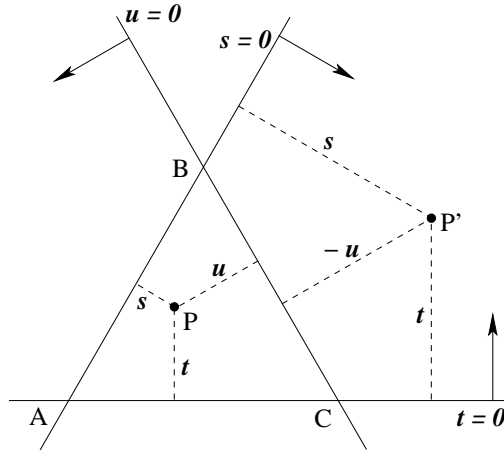


Figure B.3: The representation of the Mandelstam variables using the triangular coordinates in plane.

One should mention also the existence of a fourth type of channel reaction, a decay channel:

$$iv) \quad 1 \rightarrow \bar{2} + 3 + 4 \quad (\text{B.6})$$

which takes place if the following mass condition is fulfilled:

$$m_1 > m_2 + m_3 + m_4.$$

For this channel, one can write in the system of the decaying particle:

$$\begin{cases} s = m_1^2 + m_2^2 - 2m_1 E_2; \\ t = m_1^2 + m_3^2 - 2m_1 E_3; \\ u = m_1^2 + m_4^2 - 2m_1 E_4. \end{cases} \quad (\text{B.7})$$

Appendix C

The Track Reconstruction

In the uniform longitudinal magnetic field of the H1 solenoid, charged particles move on helical trajectories due to the Lorentz force. Therefore track finding and track reconstruction are based on a helical track model.

The five helix parameters used in the reconstruction are:

- the signed *curvature* $|\kappa| = R^{-1}$, which is defined to be positive if the direction Φ coincides with a counter clockwise propagation along the circle in the (x, y) plane;
- the signed *distance of closest approach* from the origin in the (x, y) plane, d_{ca} , which is positive if the vector from the origin to the point of *closest approach* and the trajectory direction form a right handed system;
- the azimuthal angle Φ , which is the angle between the x axis and the transverse momentum vector at the point of *closest approach*;
- the θ angle at the point of *closest approach* defined as the angle between the z -direction and the momentum vector at the point of closest approach;
- the z value of the track at the point of *closest approach*, z_0 .

The helix parameters d_{ca} and z_0 are defined with respect to the nominal event vertex position $(0, 0, 0)$. A more appropriate definition of these two parameters is with respect to the actual event vertex position (x_{ac}, y_{ac}, z_{ac}) , this being different from event to event with respect to the nominal one, see Fig. C.1.

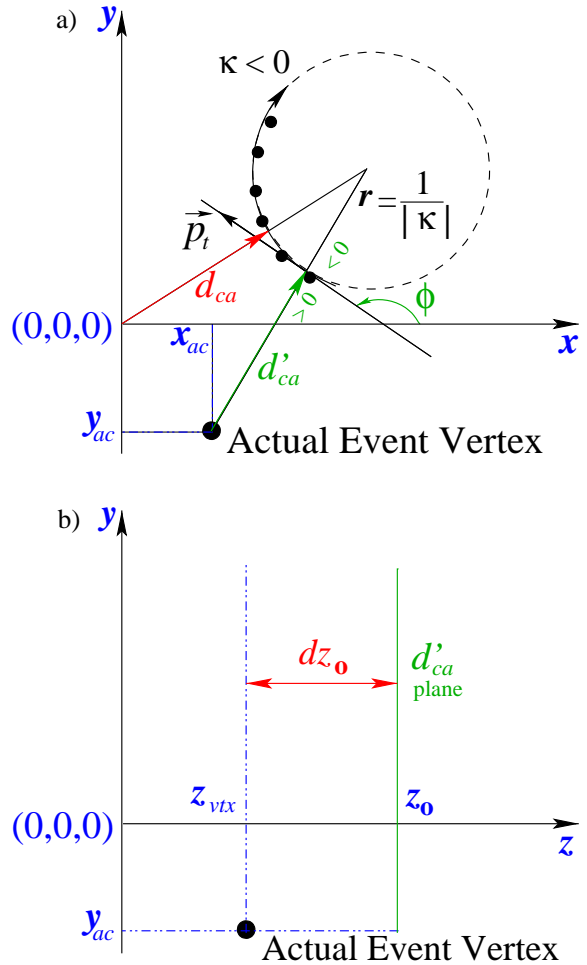


Figure C.1: Definition of track parameters in the (x, y) plane and of d'_{ca} .

The first three parameters of the helix can be determined by a circle fit to the CJC hits in the (x, y) plane using the Karimäki algorithm [44].

The equation of a circle with radius R and centre (x_0, y_0) describing the projection of the trajectory in the (x, y) plane is given by:

$$(x - x_0)^2 + (y - y_0)^2 = R^2 \quad (\text{C.1})$$

where (x_0, y_0) is the centre of the circle which describes the projection of the trajectory in the (x, y) plane.

If one wants to use the track parameters, one should perform the following variable transformation:

$$R, x_0, y_0 \rightarrow |\kappa| = \frac{1}{R}, d'_{ca}, \Phi \quad \text{and} \quad x, y \rightarrow r_i, \varphi_i \quad (\text{C.2})$$

where R and r_i are not related one to each other. The r_i is the distance of a hit to the ep event vertex position in the (r, ϕ) plane. The φ_i is defined as the angle between the x direction and the r_i direction, as shown in Fig C.2.

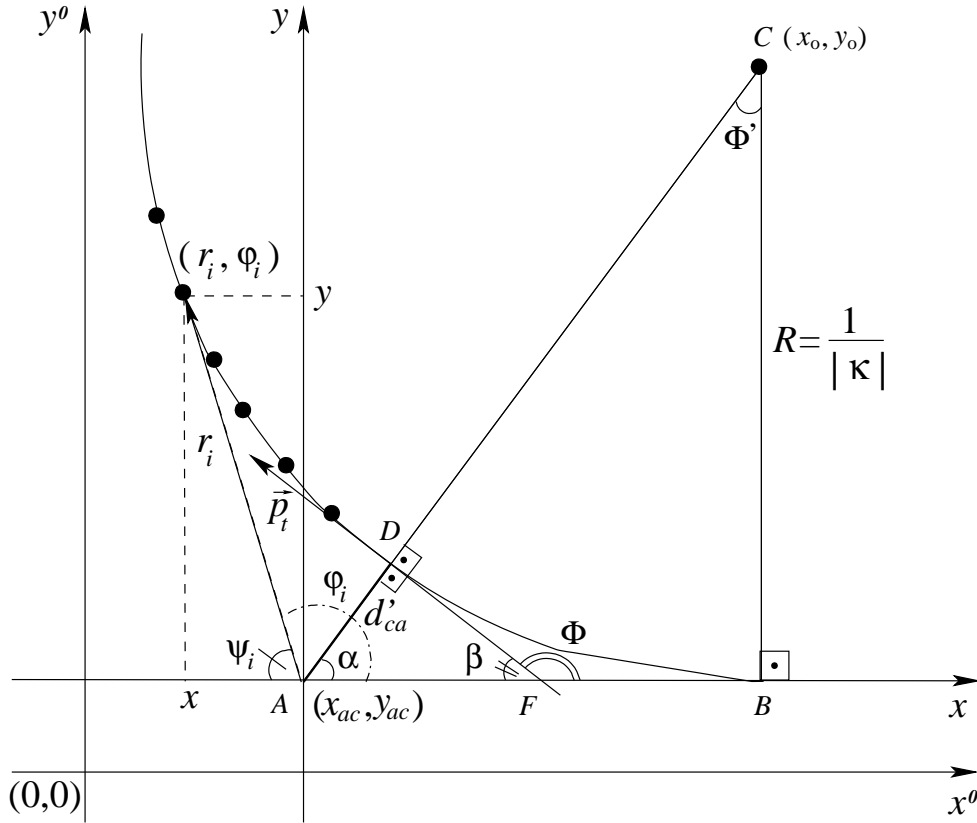


Figure C.2: The track geometry using the r_i and the φ_i coordinates.

From the Fig C.2 one can observe the following relations:

$$\left. \begin{array}{l} \Delta ADF : m(\sphericalangle ADF) = \pi/2 \Rightarrow \alpha + \beta = \pi/2 \\ A, F, B : \text{collinear points} \Rightarrow \beta + \Phi = \pi \end{array} \right\} \Rightarrow \alpha = \Phi - \pi/2 \quad \left. \begin{array}{l} \Delta ACB : m(\sphericalangle ABC) = \pi/2 \Rightarrow \alpha + \Phi' = \pi/2 \end{array} \right\} \Rightarrow \frac{\pi}{2} - \Phi' = \Phi - \frac{\pi}{2}$$

$$\Rightarrow \Phi' = \pi - \Phi \quad (\text{C.3})$$

and also:

$$\sin \Phi' = \frac{x_0}{d'_{ca} + R} \quad \text{and} \quad \cos \Phi' = \frac{y_0}{d'_{ca} + R}. \quad (\text{C.4})$$

From Eq. C.3 and Eq. C.4, the x_0 and y_0 coordinates of the circle centre of the track projection in the (x, y) plane can be written as:

$$\begin{cases} x_0 = (d'_{ca} + R) \sin \Phi \\ y_0 = -(d'_{ca} + R) \cos \Phi \end{cases} \quad (\text{C.5})$$

where the trigonometrical relations:

$$\begin{cases} \sin(\pi - \Phi) = \sin \Phi \\ \cos(\pi - \Phi) = -\cos \Phi \end{cases} \quad (\text{C.6})$$

have been used.

At this point one can write the relations between $x, y \leftrightarrow r_i, \varphi_i$:

$$\begin{cases} x = -r_i \cos \psi'_i & \text{where } \psi'_i = \pi - \varphi_i \\ y = r_i \sin \psi'_i \end{cases} \quad \Rightarrow \quad \begin{cases} x = r_i \cos \varphi_i \\ y = r_i \sin \varphi_i \end{cases}. \quad (\text{C.7})$$

The Eq. C.1 can be written using the helix parameters as follows:

$$(r_i \cos \varphi_i - (R + d'_{ca}) \sin \Phi)^2 + (r_i \sin \varphi_i + (R + d'_{ca}) \cos \Phi)^2 = R^2. \quad (\text{C.8})$$

Using the trigonometrical relation: $\sin^2 a + \cos^2 a = 1$,
the circle equation becomes:

$$\begin{aligned} \Rightarrow r_i^2 + (R + d'_{ca})^2 - R^2 - 2(R + d'_{ca}) \cdot r_i \underbrace{(\sin \Phi \cos \varphi_i - \cos \Phi \sin \varphi_i)}_{=\sin(\Phi - \varphi_i)} &= 0; \quad R = \frac{1}{|\kappa|} \\ \Rightarrow r_i^2 + 2\frac{d'_{ca}}{|\kappa|} + d'_{ca}{}^2 + R^2 - R^2 - 2\left(\frac{1}{|\kappa|} + d'_{ca}\right) \cdot r_i^2 \sin(\Phi - \varphi_i) &= 0. \end{aligned} \quad (\text{C.9})$$

If one divides the Eq. C.9 by $|\kappa|/2$, then the trajectory projection in the (x, y) plane can be fitted using:

$$\frac{|\kappa|}{2} (r_i^2 + d'_{ca}{}^2) + d'_{ca} - (1 + |\kappa| \cdot d'_{ca}) \cdot r_i \cdot \sin(\Phi - \varphi_i) = 0 \quad (\text{C.10})$$

The other two parameters of the track helix are determined by a linear least-squares fit of the track projection to a (r, z) plane which is a *right line* described by the equation:

$$z_i = z_0 + S_i^{xy} \left(\frac{dz}{dS} \right) \quad (\text{C.11})$$

where S_i^{xy} is the track length for the point z_i in the (x, y) plane, with $S^{xy} = 0$ corresponding to the d'_{ca} plane shown in the Fig. C.1.

The slope parameter dz/dS is giving the θ angle by:

$$\theta = \arctan \left(\frac{1}{dz/dS} \right). \quad (\text{C.12})$$

The tangent of the θ angle is:

$$\tan \theta = \frac{r_i - r_s}{z_i - z_0} \quad (\text{C.13})$$

where:

$$r_i - r_s = S_i^{xy} \Rightarrow z_i - z_0 = \frac{S_i^{xy}}{\tan \theta}. \quad (\text{C.14})$$

One can write the same thing for $i + 1$:

$$z_{i+1} - z_0 = \frac{S_{i+1}^{xy}}{\tan \theta}. \quad (\text{C.15})$$

Subtracting i from $i + 1$ one obtains:

$$z_{i+1} - z_i = \frac{S_{i+1}^{xy} - S_i^{xy}}{\tan \theta} \quad \text{and at the limit:} \quad \tan \theta = \frac{dS}{dz}. \quad (\text{C.16})$$

At the H1 experiment there are two versions of track finding and fitting algorithms [37]. One version is fast and efficient for tracks with momentum $p_{track} > 100$ MeV which originate from the primary vertex. This version, H1FAST, is implemented on the L4 trigger farm to reject the background and to classify the events. This first version is ~ 10 times faster than the standard version, H1REC, which has higher efficiency and is used in the final reconstruction.

In the first phase of the track finding, the search for short track elements is performed independently in the angular cells of the CJC wires. The curvature of these short track elements is negligible and they do not depend, within angular sectors, on the Lorentz angle or on the drift velocity. The track finding is based almost exclusively on the drift time data in the (x, y) plane. In the fast finding version it is sufficient to determine the t_0 bunch crossing time of an event from the threshold of the drift time histogram.

The short track elements are defined by three hits within angular cells found on three wires that are at two wire distance. The pairs of hits at wire $n \pm 2$ with the wire index n are tried first. Possible values of drift distances \bar{d}^n at the wire n are calculated by $(d_i^{n-2} + d_k^{n+2})/2$ and $|d_i^{n-2} - d_k^{n+2}|/2$ where i, k are the hits indices. If the direction of the pair does not deviate too strongly from the radial direction, the drift distances are stored in a list. Regions with too many hits are not analysed at this stage. The list is compared with measured values d_j^n and the indices of the hits at the three wires for which $|d_j^n - \bar{d}^n|$ is small are stored as a possible track element. The curvature κ and the angle Φ can be determined from the hit triplets assuming $d_{ca} \equiv 0$. The drift sign ambiguity is not solved at this stage. If the values of $|\kappa|$ are too large, the triplets hits are rejected. At this point the charge information of the two wire ends is used to calculate a z value and a dE/dx one are assigned to the triplets. The circle fit in the (x, y) plane using the helix parameters as described in Fig. C.2 is performed and also a z fit in order to obtain the triplets coordinates. After the fit values are obtained, the track elements are clustered and a first track definition is obtained. The track candidates are checked in the order of decreasing number of triplets. The tracks which have triplets already used by other track candidates are rejected. Now the drift sign ambiguities are solved.

The standard track finding uses as input the results of the fast algorithm. In the standard algorithm the steps are similar to the fast track finding. The first step is to

search for track elements defined also by three hits, but this time they should be on adjacent wires. The dense regions are again rejected. The triplets with common hits are connected and they are extracted when all hits of an angular cell are analysed. These chains of hits are checked and the drift sign ambiguities are solved for the long ones. A merging algorithm is applied to connect the short track elements using a χ^2 fit in the (x, y) plane. In order to improve the track finding efficiency and precision, the expected drift length is calculated for all possible wires and also for the track elements ordered by their length. The hits at the expected wires which are not used by another track are collected. The difference between the measured and the expected drift length is used to reject the incompatible hits. The fits are performed once more using all the accepted hits. The track candidates which are very short are rejected excepting the case when they are starting from the first few wires on a ring. The energy loss dE/dx for a given track is determined from the mean of single hits values not including the ones close to another track.

The tracks used for D^* -meson selection in this analysis had to fulfill the L4 trigger conditions depending on the running time periods. Due to these changes of the L4 D^* -meson finder, in the offline selection harder requirements, than the ones shown in Table 3.8, have to be fulfilled by the tracks, as it is shown in the Table C.1.

L4 Track cuts	Threshold		
	K	π	π_s
Track starting radius	≤ 50 cm		
for $212884 \leq \text{Run} \leq 236646$	≤ 25 cm	≤ 50 cm	
Track length	≥ 10 cm		
for $212884 \leq \text{Run} \leq 236646$	≥ 25 cm	≥ 10 cm	
for $236646 \leq \text{Run} \leq 238955$	≥ 15 cm		≥ 10 cm
for $244968 \leq \text{Run}$	≥ 15 cm		≥ 10 cm
The distance to closest approach: d'_{ca}	≤ 1.0 cm		
for $212884 \leq \text{Run} \leq 236646$	≤ 0.4 cm	≤ 1.0 cm	
$ dz_0 = z'_{ca} - z_{vtx} $	≤ 40 cm		
for $212884 \leq \text{Run} \leq 236646$	≤ 12 cm	≤ 40 cm	
for $238955 \leq \text{Run} \leq 244968$	≤ 20 cm	≤ 40 cm	

Table C.1: The adjusted track quality cuts for D^* -meson selection depending on L4.

Appendix D

The ST61 Efficiency

In this appendix the trigger element (TE) efficiencies as well as the subtrigger (**ST61**) one for the control distribution are presented. The efficiencies are of the order of $\sim 90\%$ and the MC model agrees reasonable well with the data within the errors.

The efficiencies are used just to control the data selection and different variables that can have a high influence on the results of this analysis.

Due to the reasonable good agreement between the data and the MC model, no corrections are needed for the results concerning the trigger efficiency.

In the Fig. D.1 one can see that the main influence for the **ST61** efficiency is coming from the TE **zVtx_sig** which can be considered the weakest in efficiencies from the TE used.

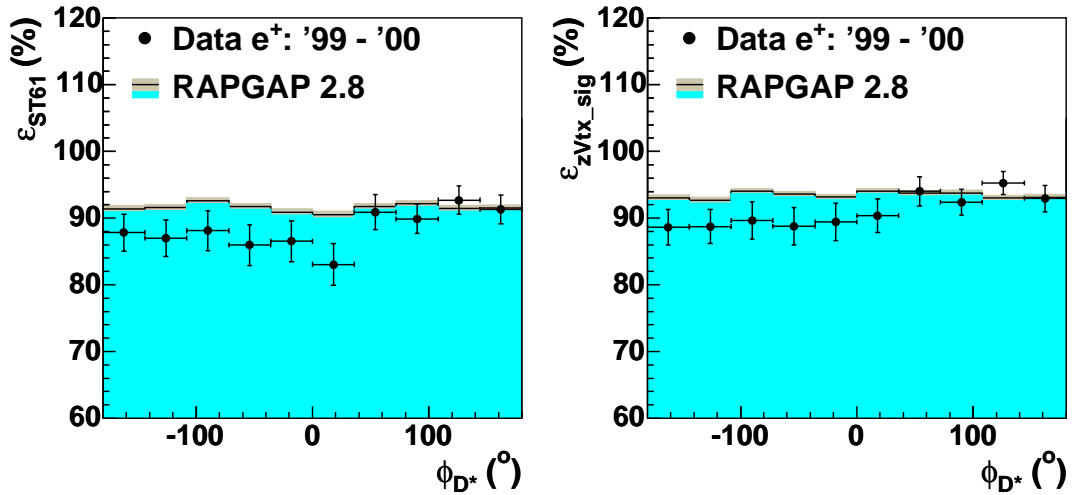


Figure D.1: The efficiency of the **ST61** and the **zVtx_sig** for the ϕ_{D^*} distribution. The shift seen in the range $-180^\circ \leq \phi \leq 40^\circ$ of $\sim 2\%$ is propagated also in the $\phi_{D^*_{Jet}}$ distribution.

The **SPCLe_IET** efficiencies are presented in the Fig. D.2, the **DCRPh_THig** efficiencies in the Fig. D.3 and the **zVtx_sig** efficiencies in the Fig. D.4.

The **ST61** efficiency for several control variables can be seen in Fig. D.5.

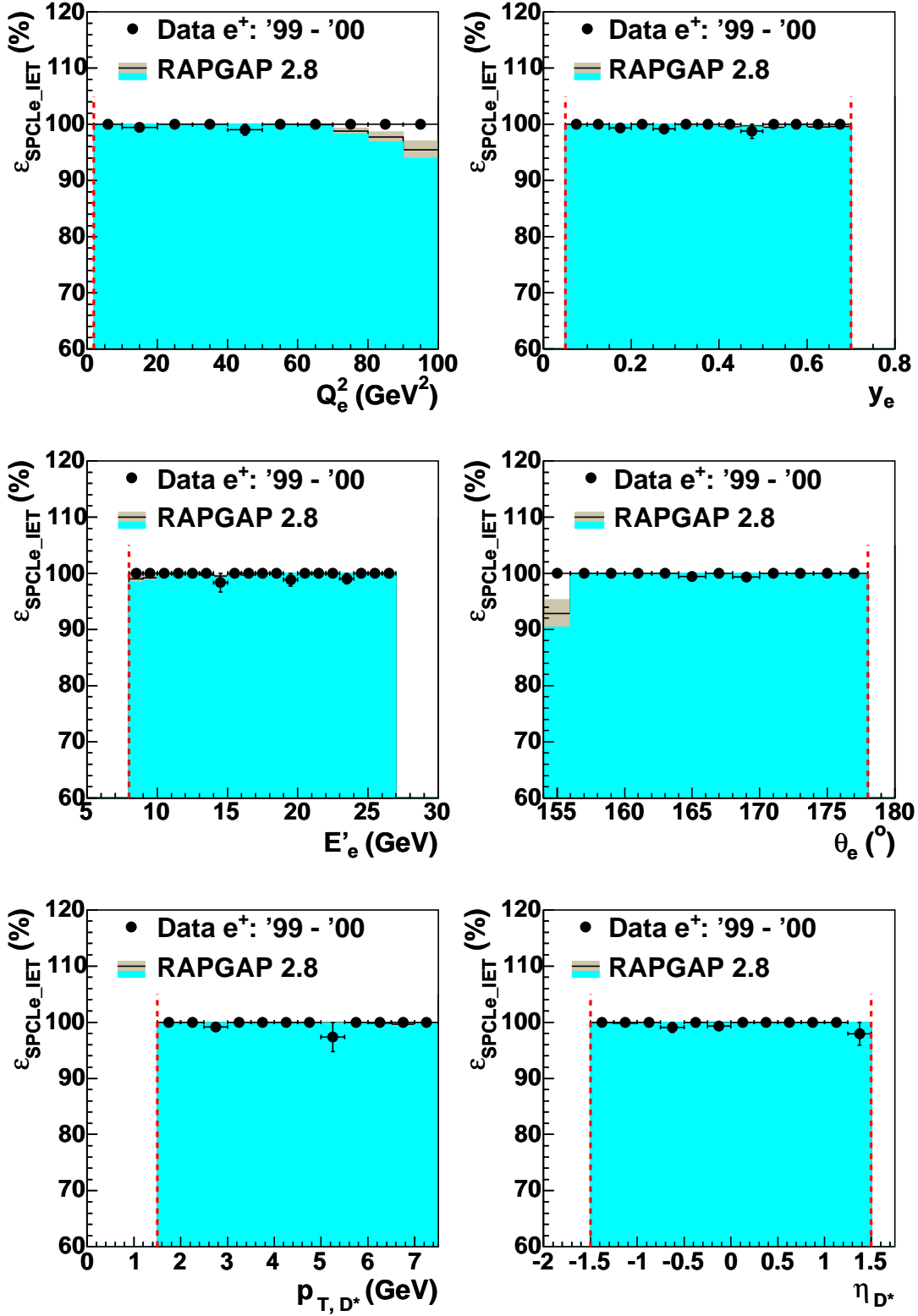


Figure D.2: The SPCLe_IET efficiency for the control variables Q_e^2 , y_e , E'_e , θ_e , p_{T,D^*} and η_{D^*} . The errors are the statistical ones. The dotted lines show the cuts applied in this analysis.

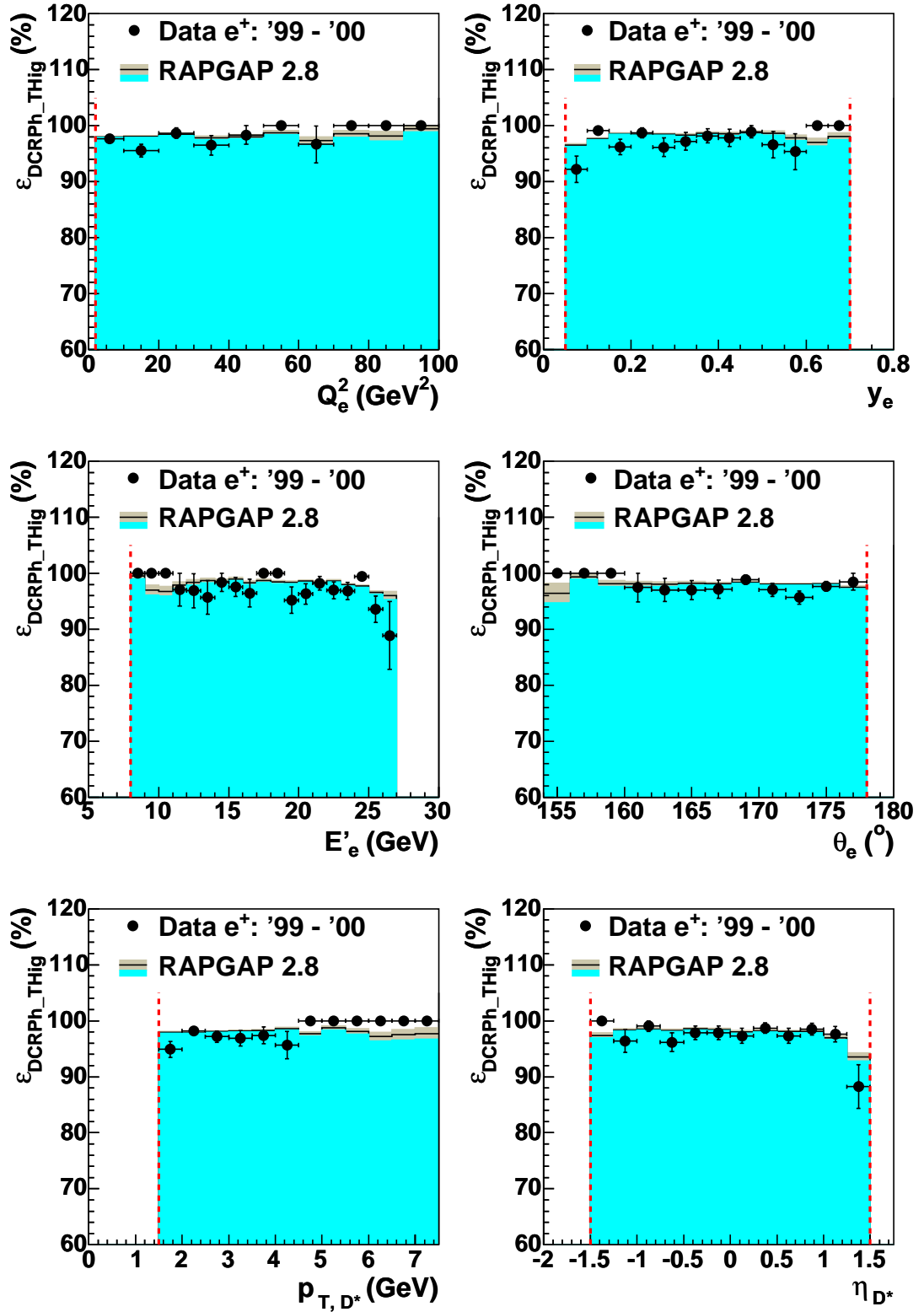


Figure D.3: The DCRPh_THig efficiency for the control variables Q_e^2 , y_e , E'_e , θ_e , p_{T,D^*} and η_{D^*} . The errors are the statistical ones. The dotted lines show the cuts applied in this analysis.

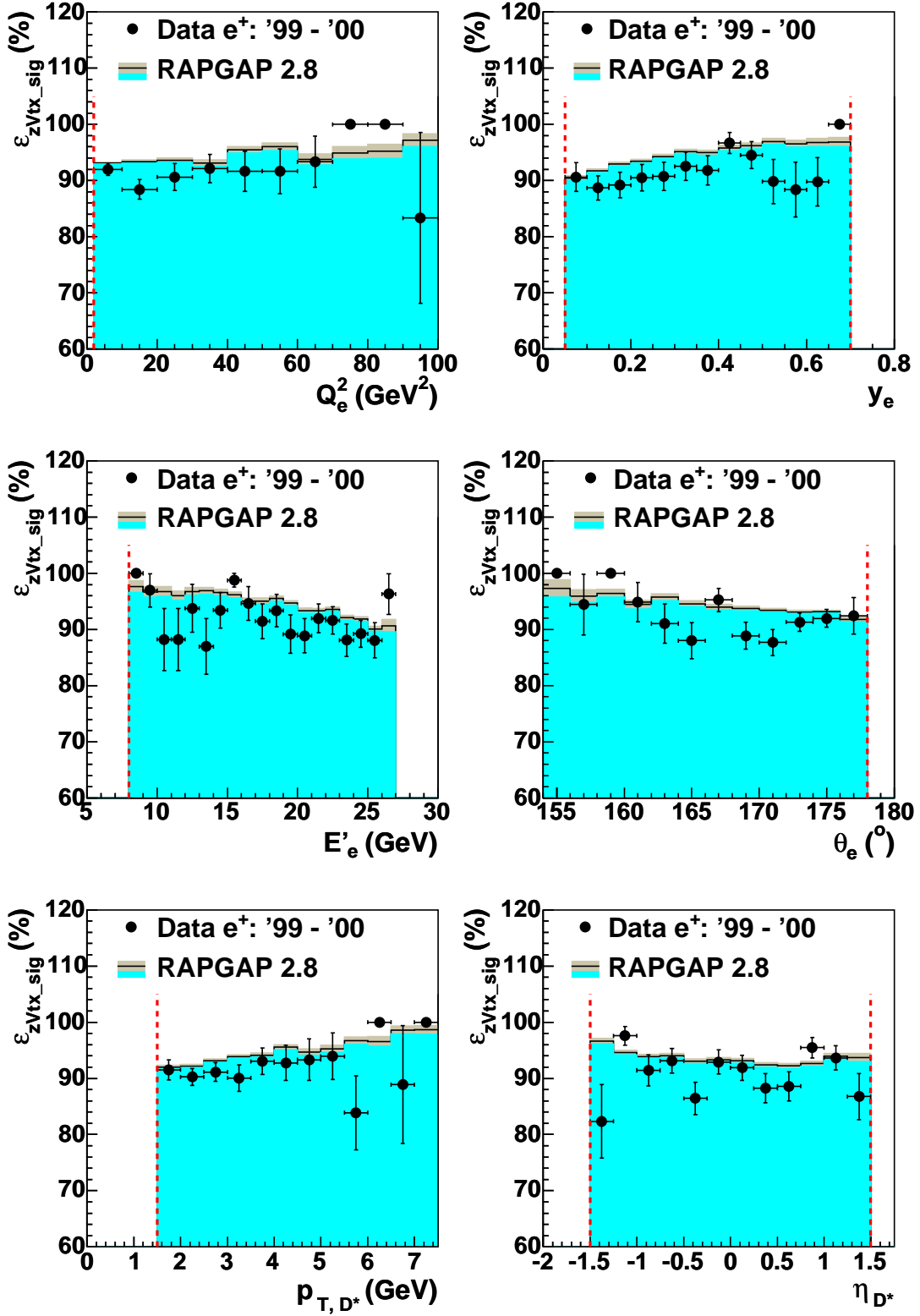


Figure D.4: The $zVtx_sig$ efficiency for the control variables Q_e^2 , y_e , E'_e , θ_e , p_{T,D^*} and η_{D^*} . The errors are the statistical ones. The dotted lines show the cuts applied in this analysis.

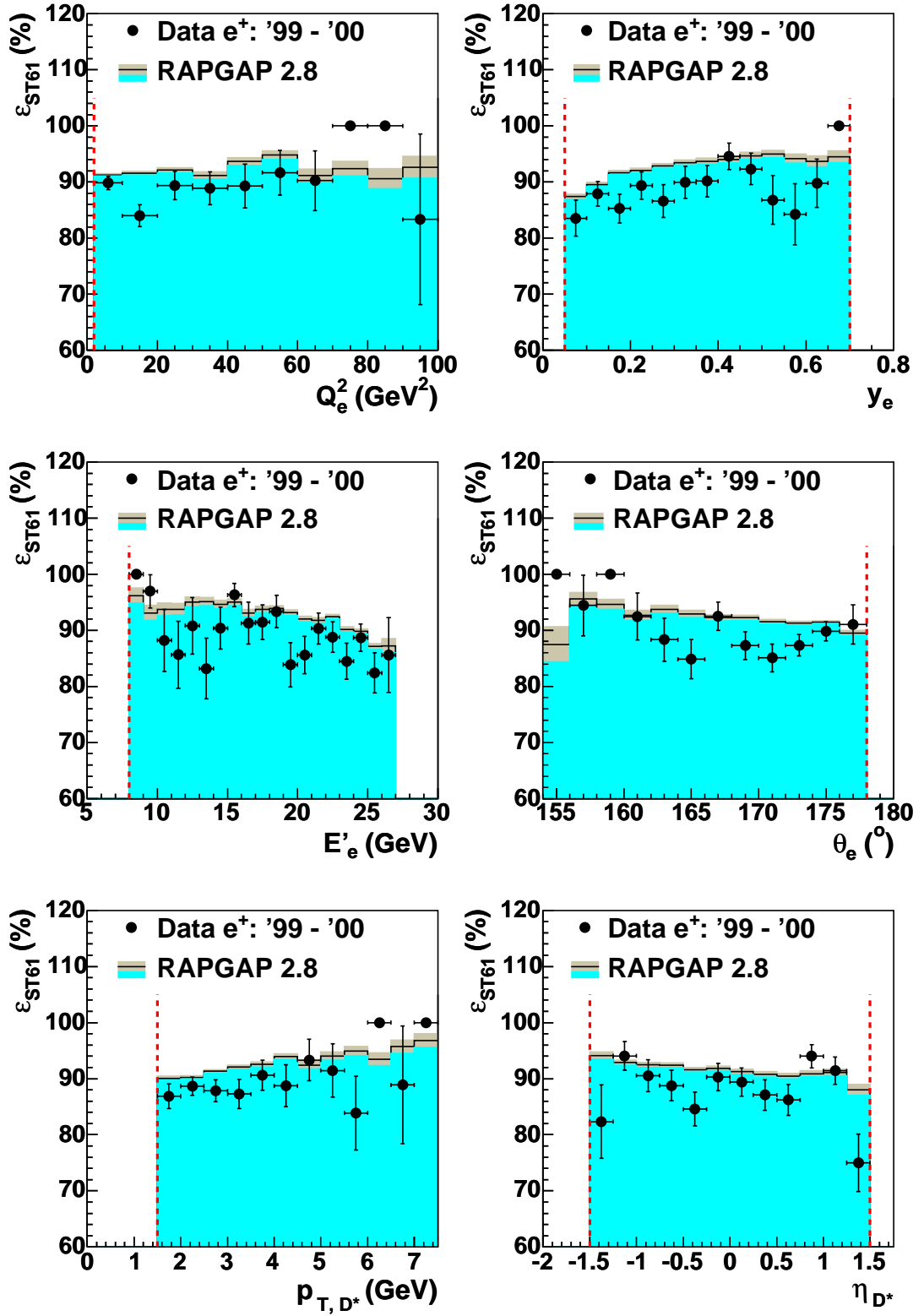


Figure D.5: The ST61 efficiency for the control variables Q_e^2 , y_e , E'_e , θ_e , p_{T,D^*} and η_{D^*} . The errors are the statistical ones. The dotted lines show the cuts applied in this analysis.

Appendix E

The Sigma Method

The sigma method calculates the kinematic variables Q_Σ^2 and y_Σ taking into account the QED radiation emitted by the incoming electron. Due to the electron energy loss, related to the QED radiation, the energy of the electron beam is replaced in this method by the electron energy at the event vertex position. The value of the later energy is given by:

$$E_e = \frac{E - p_z}{2} \quad (\text{E.1})$$

where $E - p_z$ is calculated using the Eq. 3.13.

In the sigma method, the E_e calculated from the Eq. E.1 is replaced in the Eq. 3.15 as follows:

$$Q_\Sigma^2 = 4 \frac{E - p_z}{2} E'_e \cos^2 \left(\frac{\theta_e}{2} \right);$$

$$y_\Sigma = 1 - \frac{E'_e}{\frac{E - p_z}{2}} \sin^2 \left(\frac{\theta_e}{2} \right); \quad x_\Sigma = \frac{Q_\Sigma^2}{s \cdot y_\Sigma}. \quad (\text{E.2})$$

where the most appropriate choice for s would be $s = 2(E - p_z)E_p$.

Due to the errors of the quantities used to calculate $E - p_z$, for s the definition from the electron method ($s = 4E_e E_p$) is used. In this analysis only a check is done using the sigma method. The y_Σ can be written also as:

$$y_\Sigma = 1 - \frac{E'_e}{\frac{E - p_z}{2}} \sin^2 \left(\frac{\theta_e}{2} \right) = \frac{E - p_z - E'_e(1 - \cos \theta_e)}{E - p_z} = \frac{E_{had} - p_{z, had}}{E - p_z} \quad (\text{E.3})$$

from where the:

$$Q_\Sigma^2 = \frac{(E'_e \sin \theta_e)^2}{1 - y_\Sigma} \quad \text{and} \quad x_\Sigma = \frac{Q_\Sigma^2}{y_\Sigma \cdot 4E_e E_p} \quad (\text{E.4})$$

can be used.

The ratio y_e/y_Σ is shown in the Fig. E.1. The MC model describes the data. The distribution has a nice peak at the value of 1, showing that the QED radiative correction can be neglected.

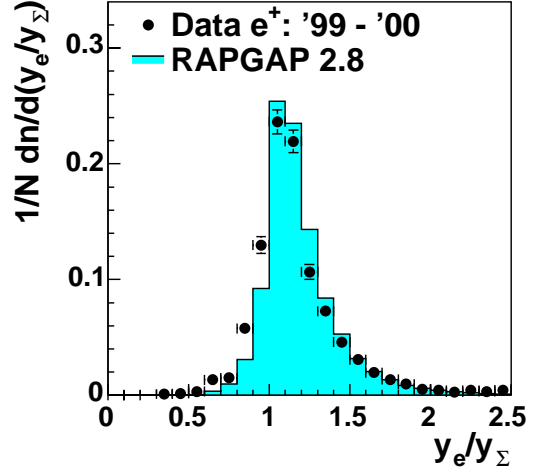


Figure E.1: The y_e/y_Σ distribution.

Appendix F

The $c \Leftrightarrow$ Jets Correlations

In the Chapter 4 the jet shape observables are presented. Because both jets, the D^* Jet and the *OtherJet*, are charm jets, it is important to know how well are they correlated with the corresponding c quarks.

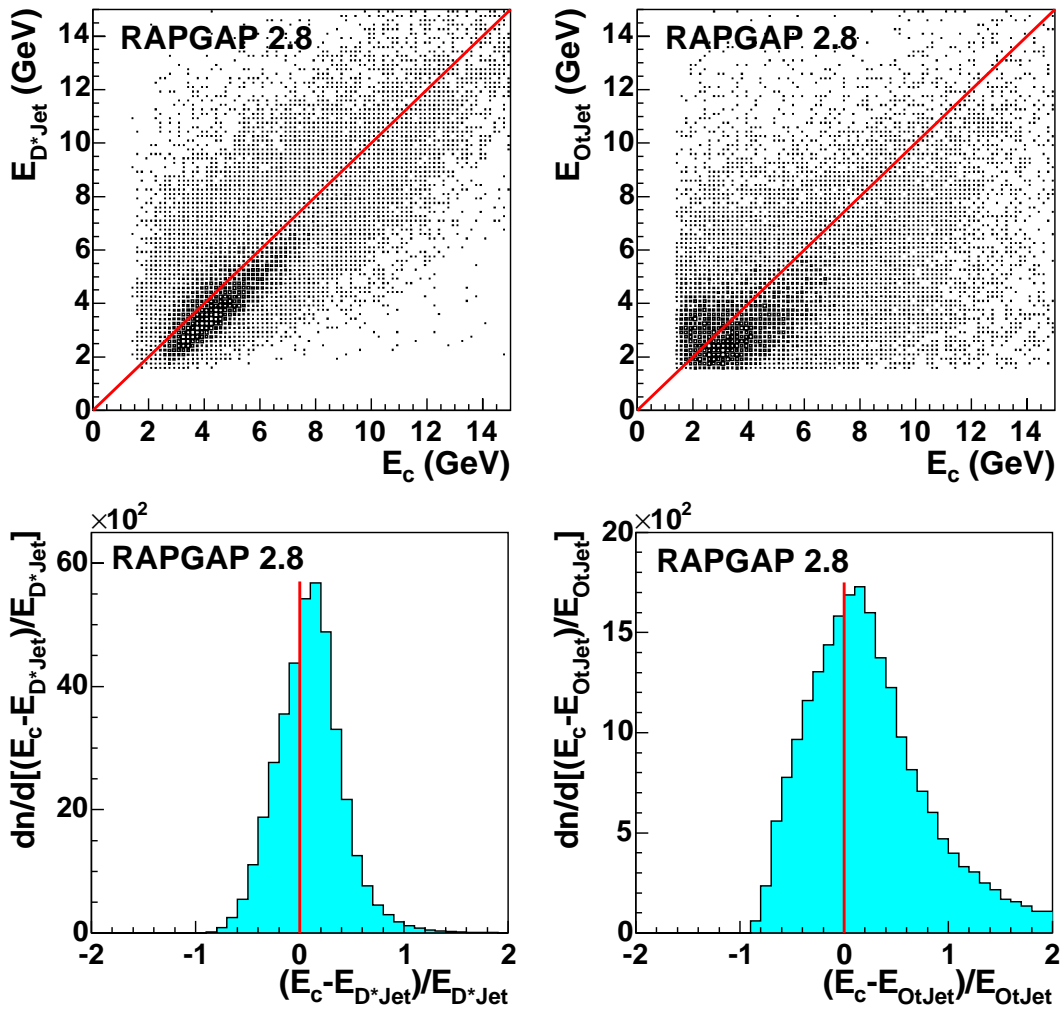


Figure F.1: The energy correlations between the Jet and the corresponding c quark.

One can observe that the correlation in energy, shown in the Fig. F.1, between the *OtherJet* and the corresponding c quark is not as good as the one between the D^* Jet and its corresponding c quark.

The correlation in η and ϕ are better than the E one, see the Fig. F.2 and the Fig. F.3, respectively. Nevertheless, the quality of the D^* Jet \Leftrightarrow c quark correlation is still not achieved in the *OtherJet* case.

The profiles, showed in the dashed histograms, have also large tails for the *OtherJet* correlations.

This hint concerning the c quark reconstruction can partly explain the differences in jet shape variables observed between the D^* Jet and the *OtherJet*.

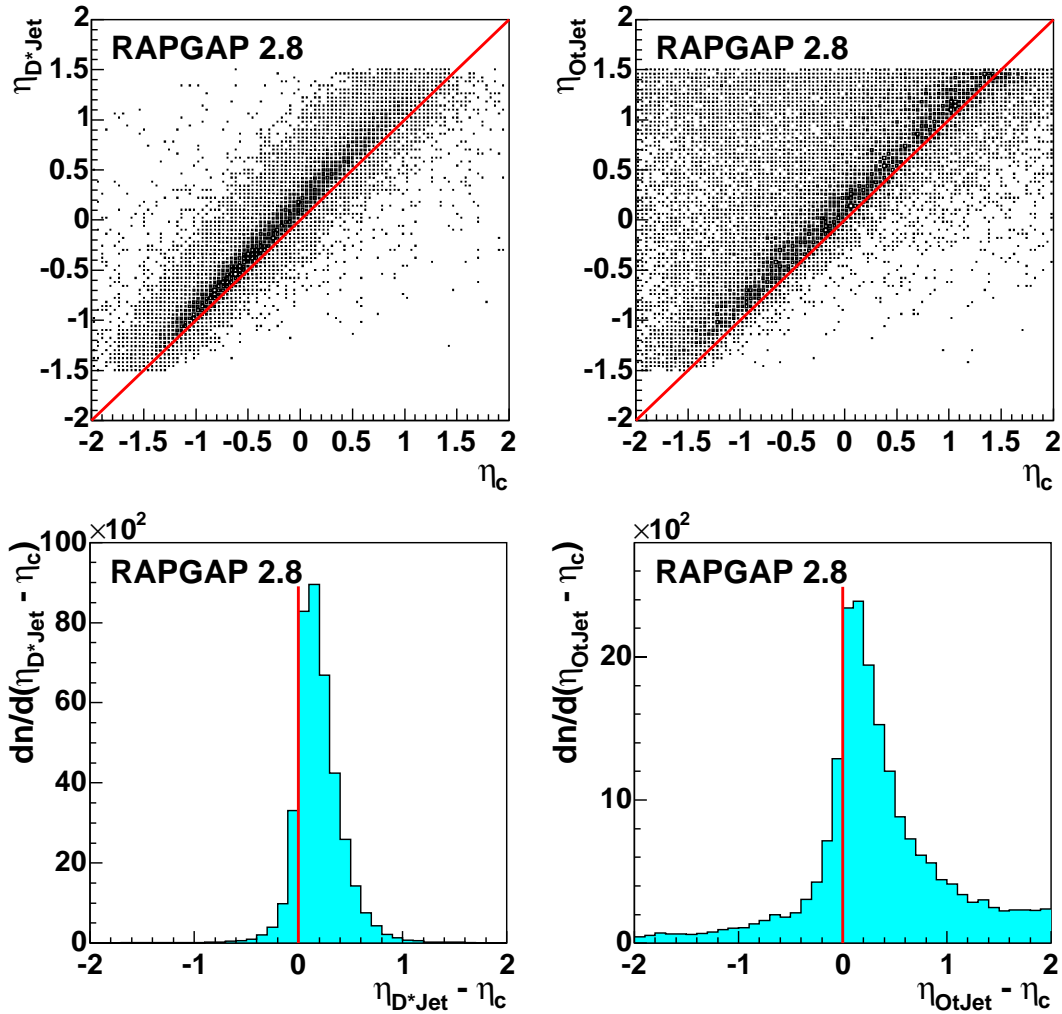


Figure F.2: The pseudorapidity correlation between the Jet and the corresponding c quark.

The asymmetric peak for the η correlations is due to the non fully invariance of the η with respect to the longitudinal boost.

In the ϕ correlation distributions, a symmetric peak at the zero value can be seen. This is due the invariance of the azimuthal angle ϕ to the longitudinal boost in the z direction.

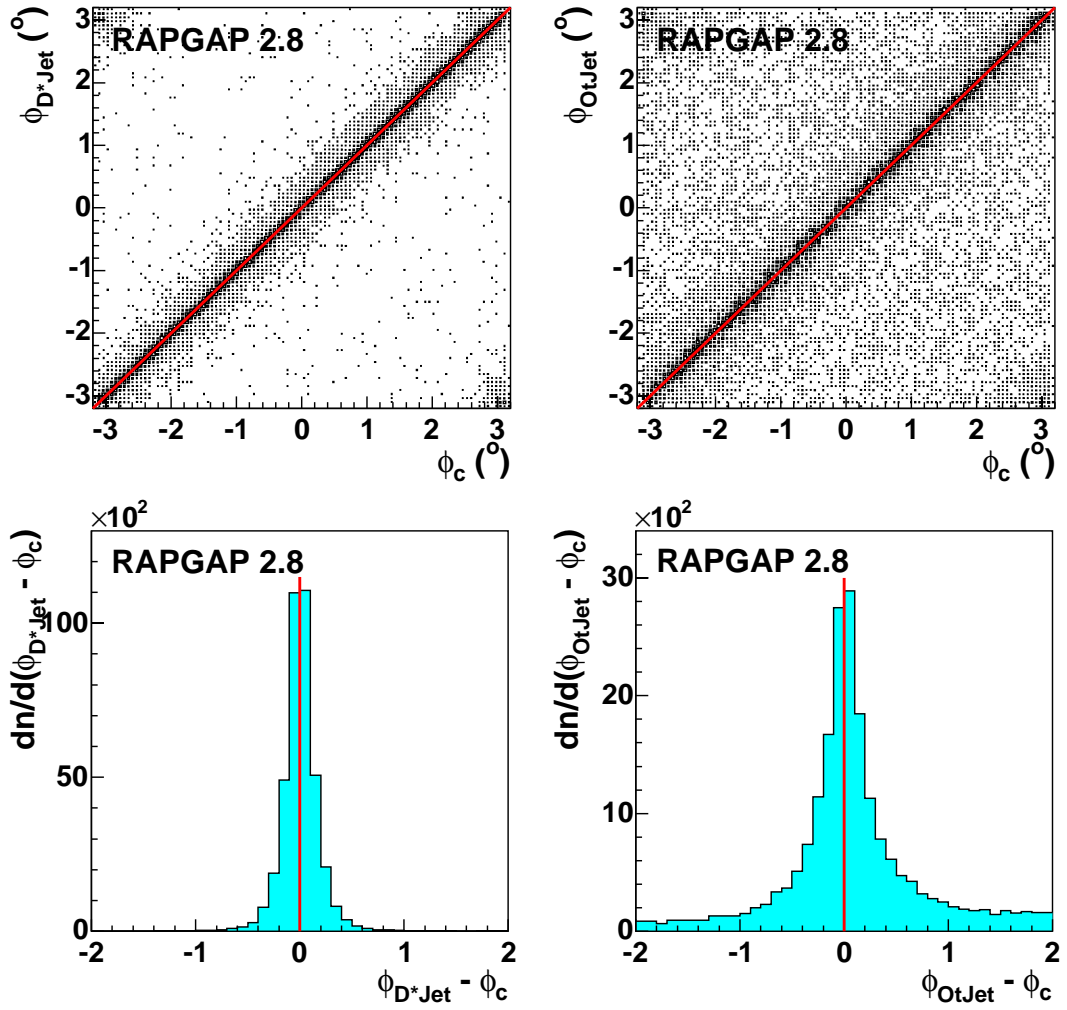


Figure F.3: The ϕ correlation between the Jet and the corresponding c quark.

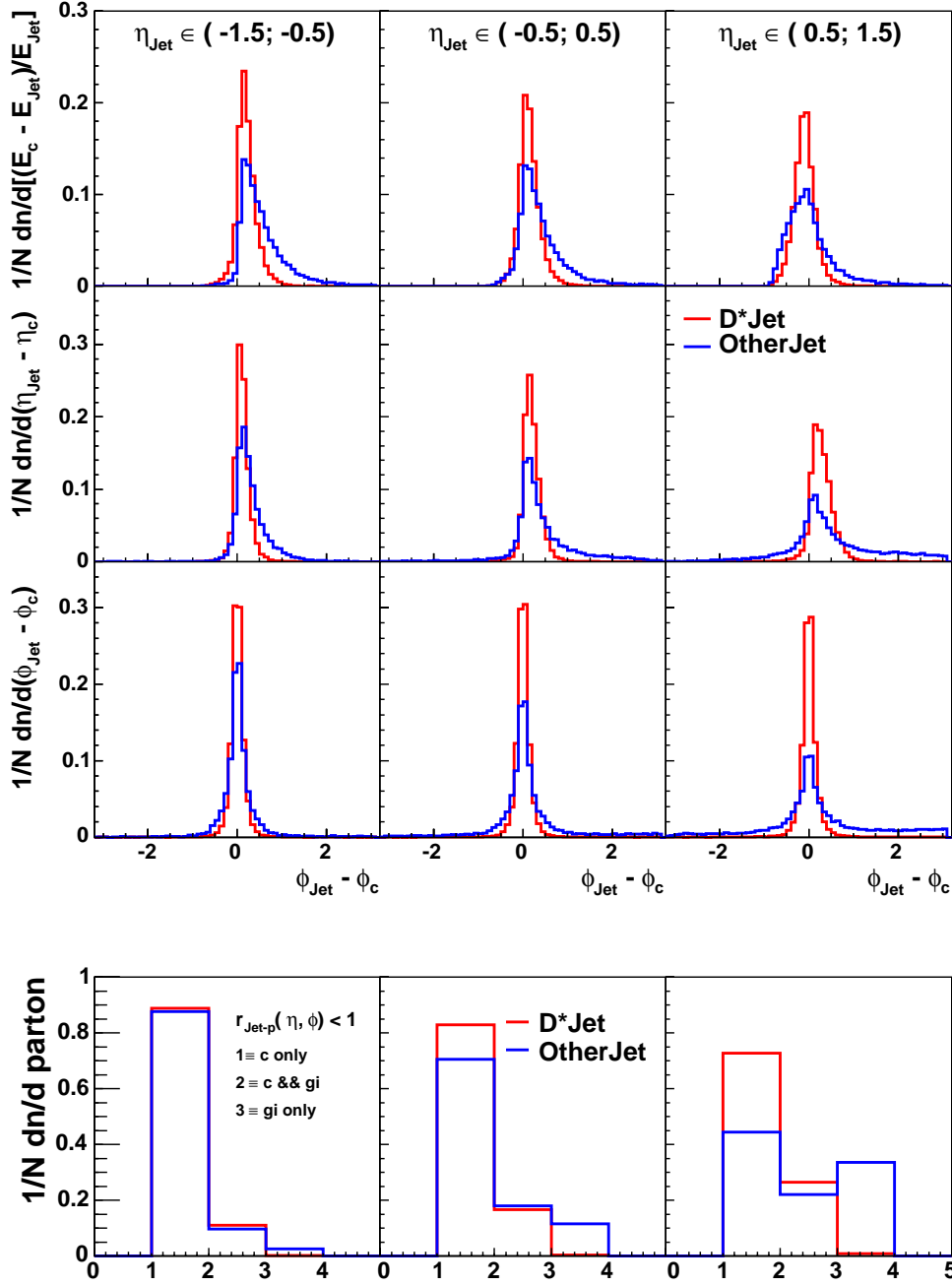


Figure F.4: The jet shape observables for different η_{Jet} bins corrected to the hadron level ($R = 1$).

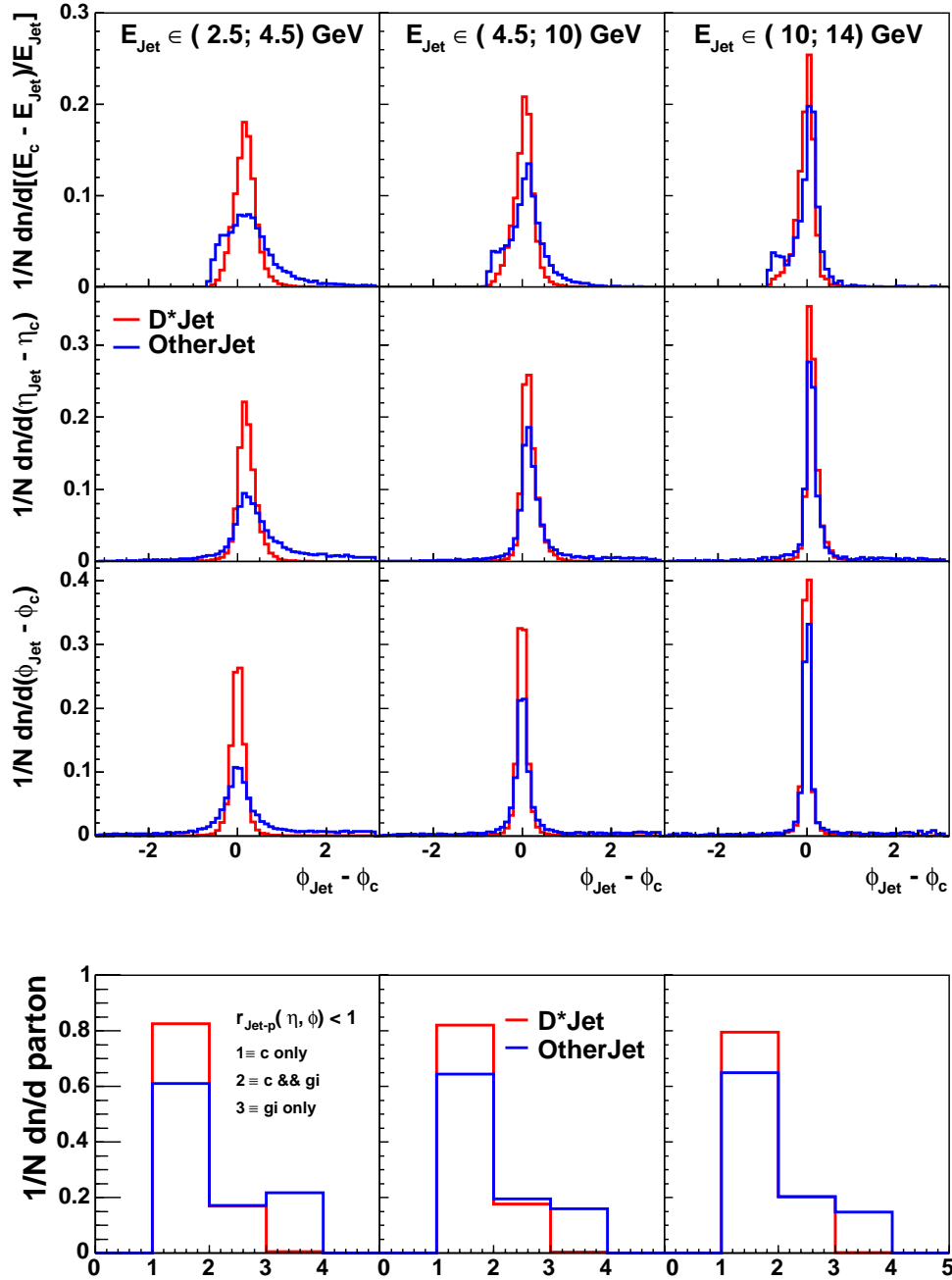


Figure F.5: The jet shape observables for different E_{Jet} bins corrected to the hadron level ($R = 1$).

Appendix G

HFS and Jet Control Distributions

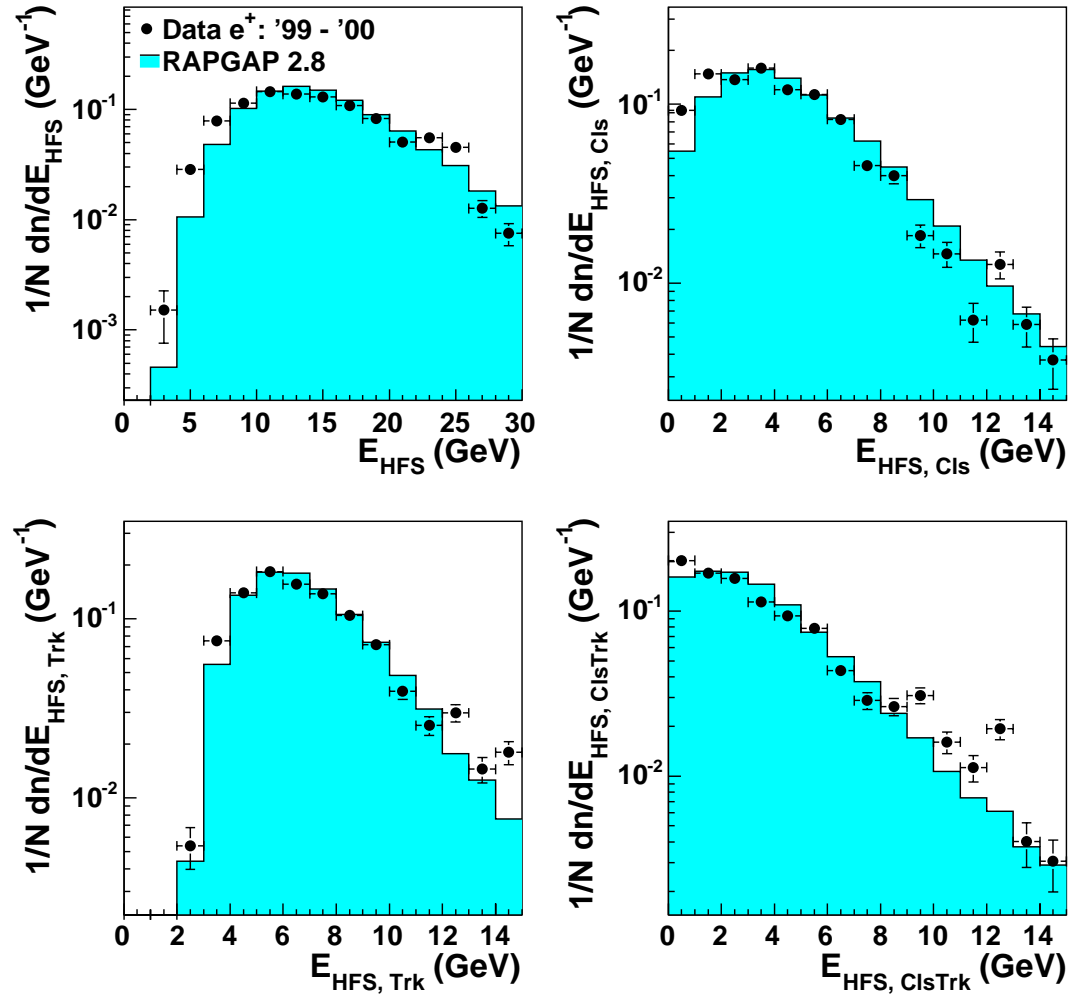


Figure G.1: The total energy and the contributions from clusters, tracks and combined cluster-track objects to the total hadronic final state (HFS) energy.

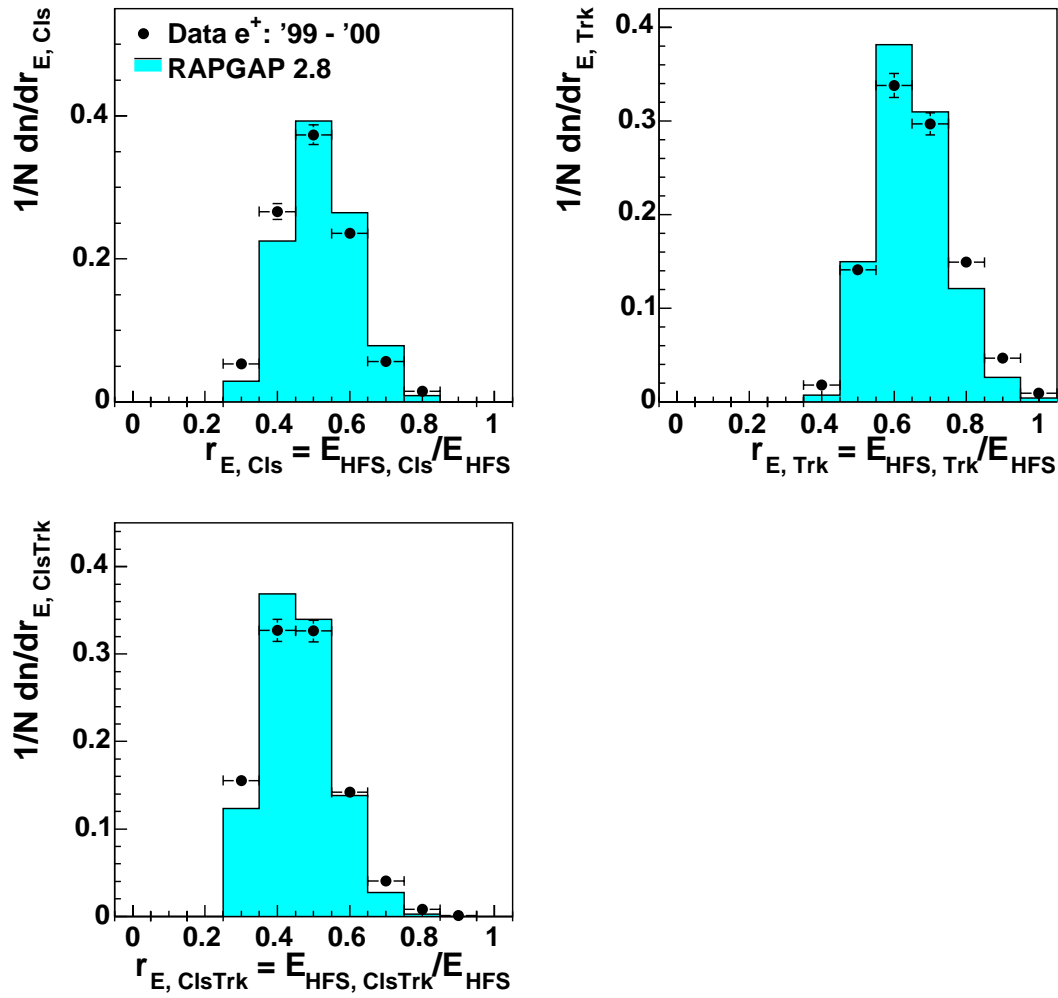


Figure G.2: The energy fraction contributions from clusters, tracks and combined cluster-track objects to HFS.

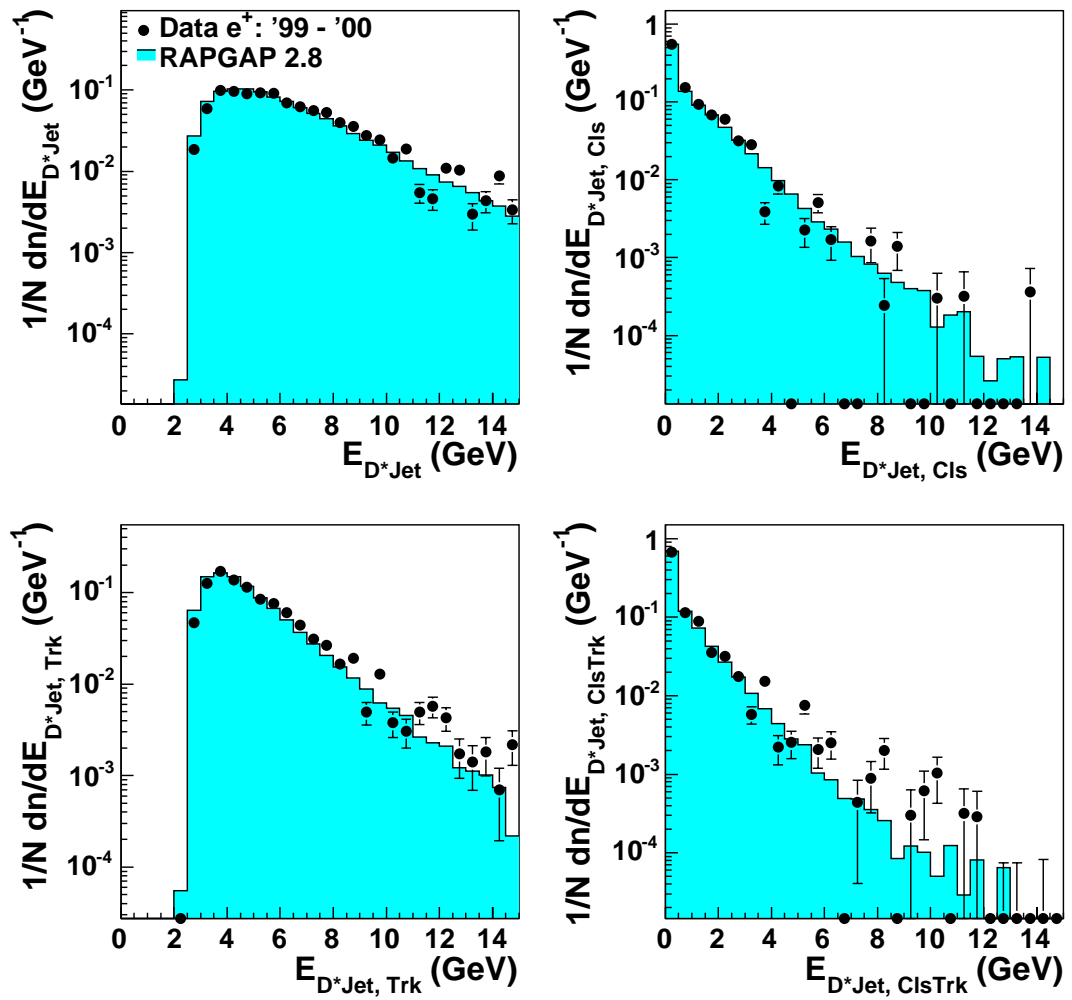


Figure G.3: The total energy and the contributions from clusters, tracks and combined cluster-track objects to the total D^* Jet energy.

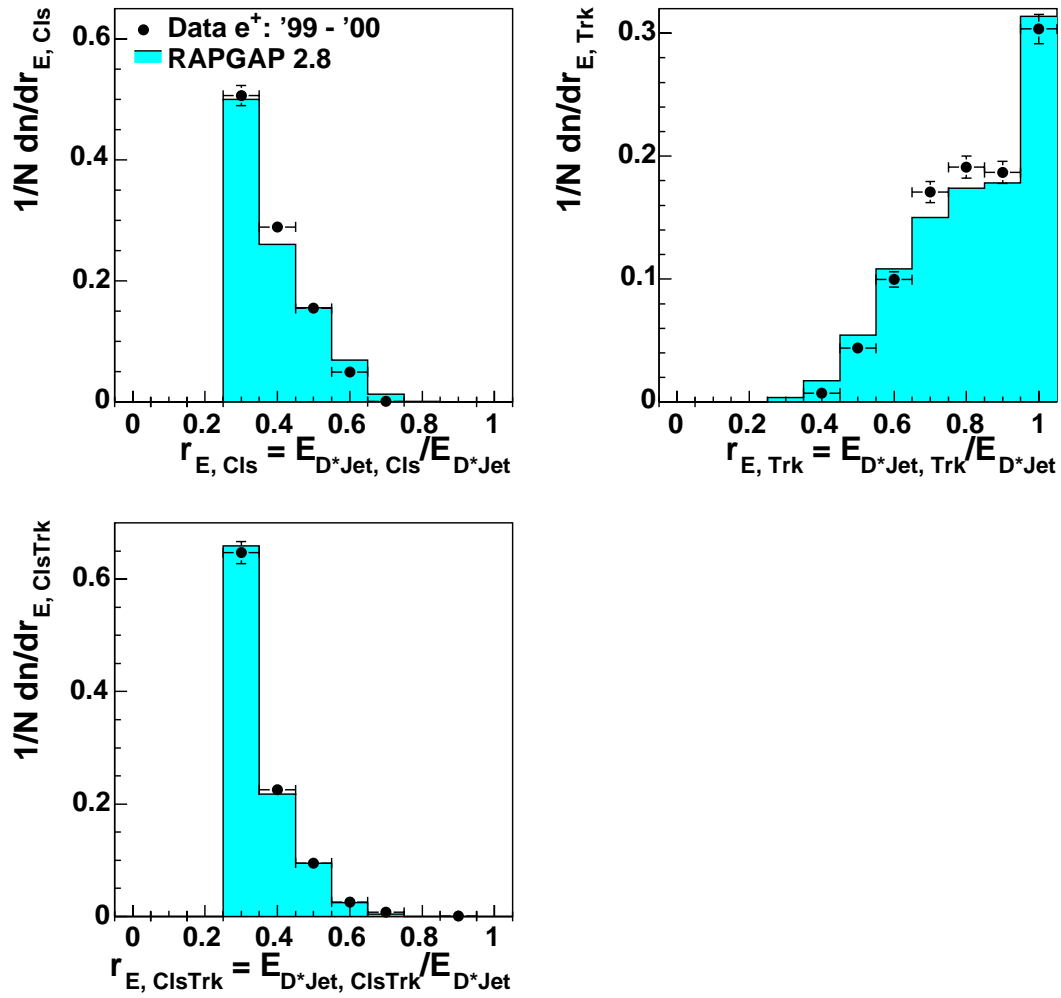


Figure G.4: The energy fraction contributions from clusters, tracks and combined cluster-track objects to $D^* \text{Jet}$.

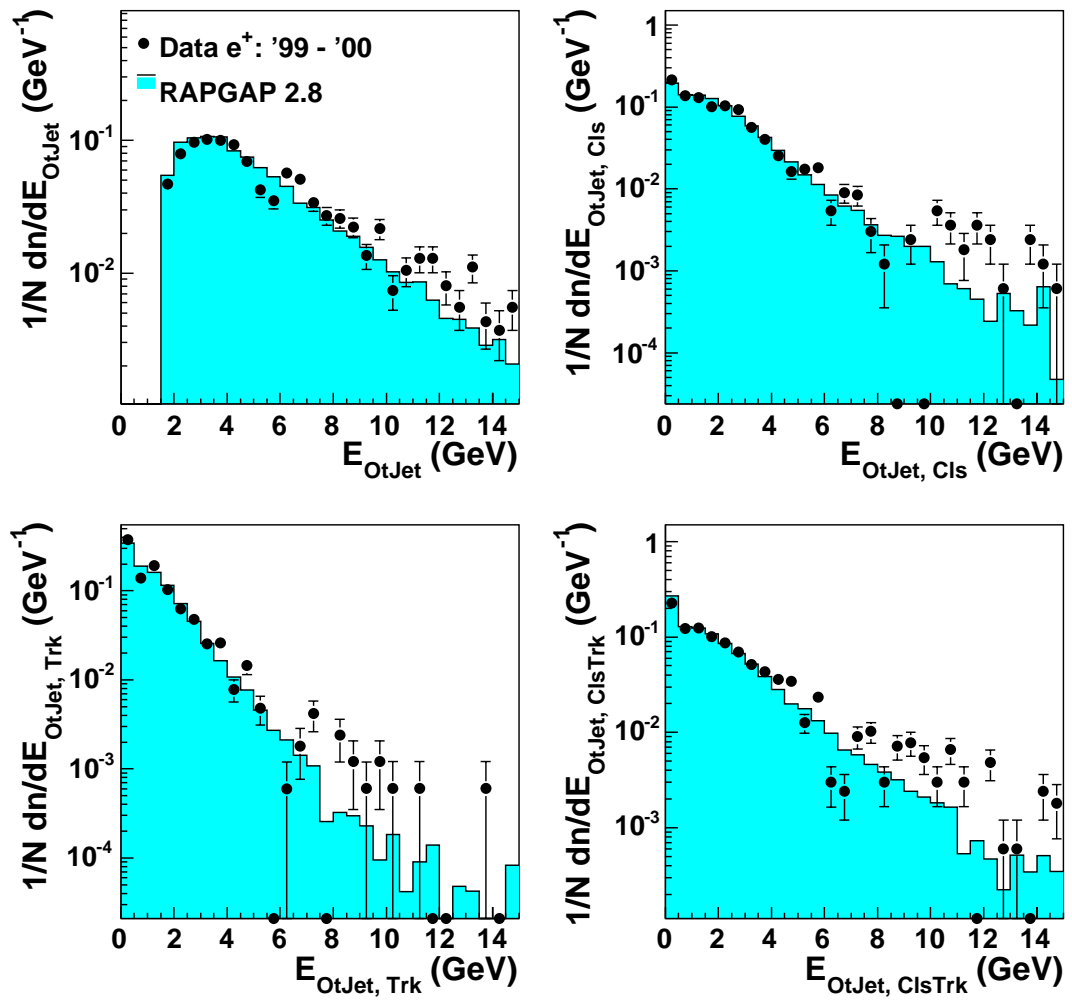


Figure G.5: The total energy and the contributions from clusters, tracks and combined cluster-track objects to the total *OtherJet* energy.

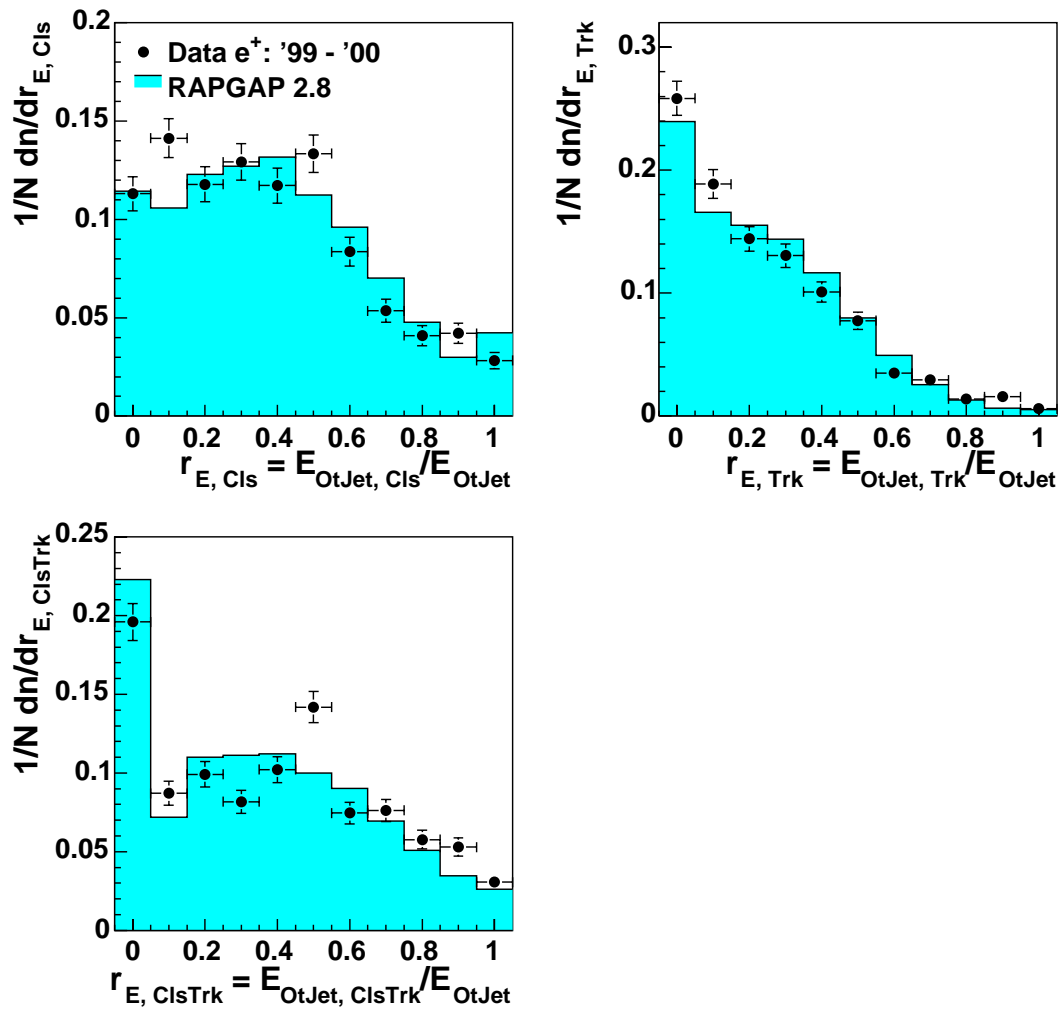


Figure G.6: The energy fraction contributions from clusters, tracks and combined cluster-track objects to *OtherJet*.

Appendix H

The Systematic Error Contributions

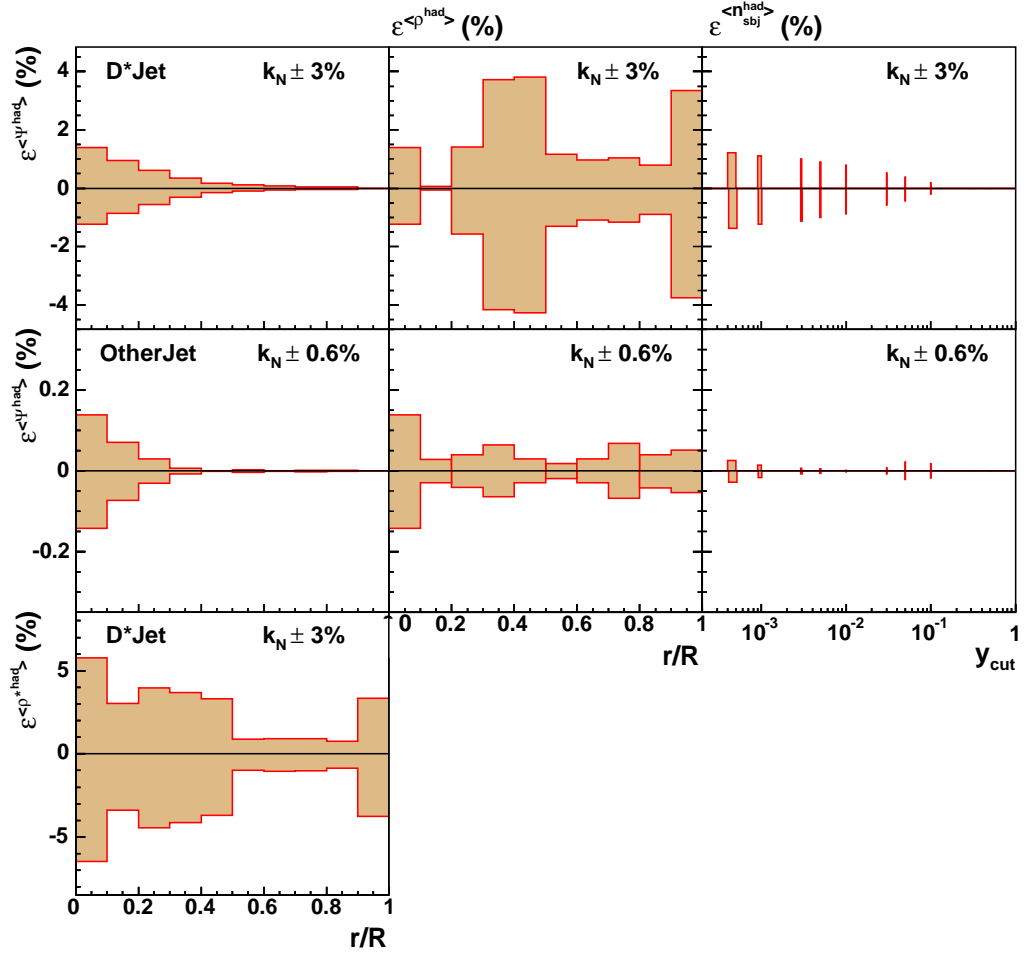
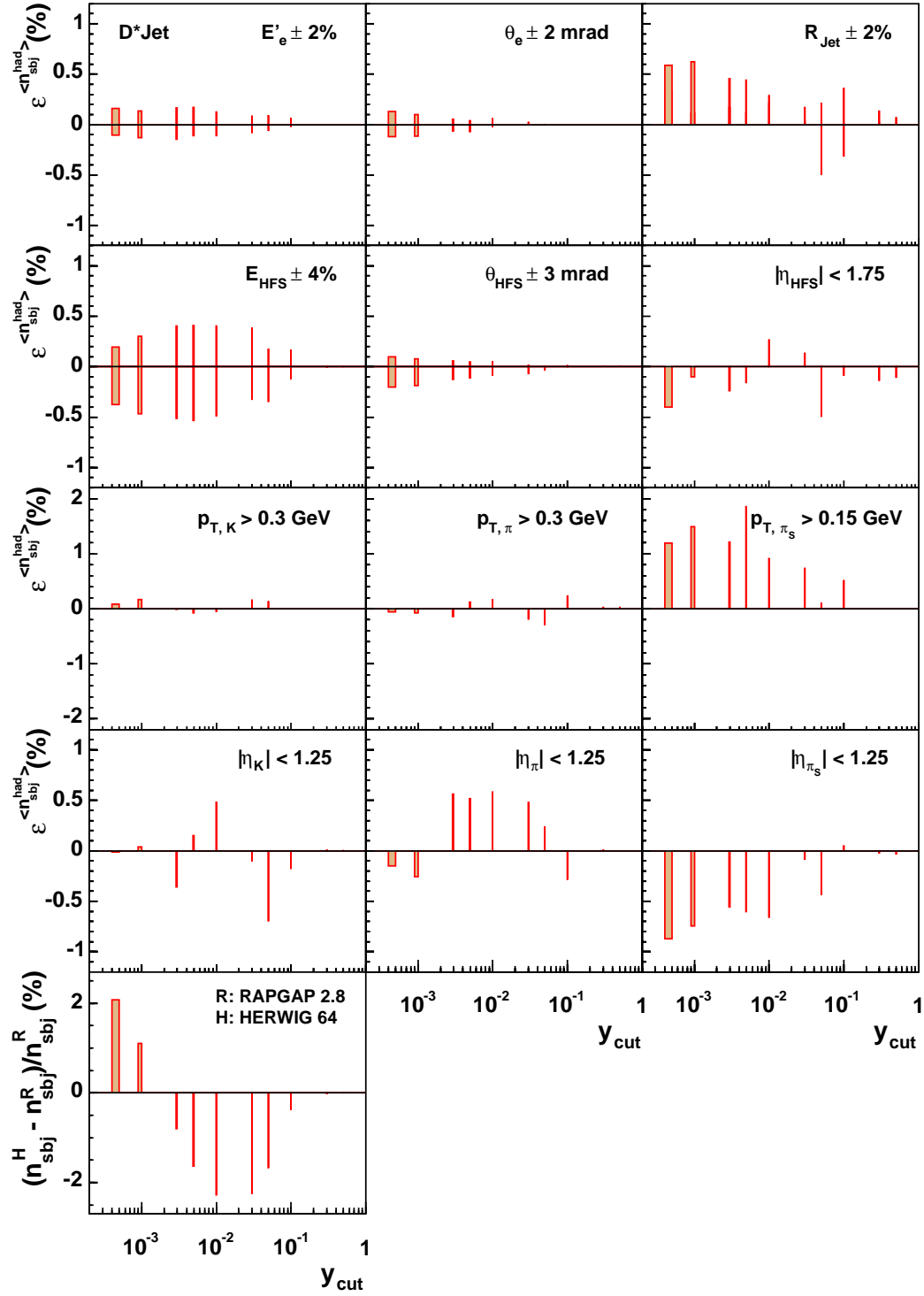


Figure H.1: The systematic errors of the jet shape variable from the k_N variation, see Sec. 3.3.5.

Figure H.2: The systematic errors of the mean subject multiplicity $\langle n_{\text{subj}} \rangle$ for the D^* Jet.

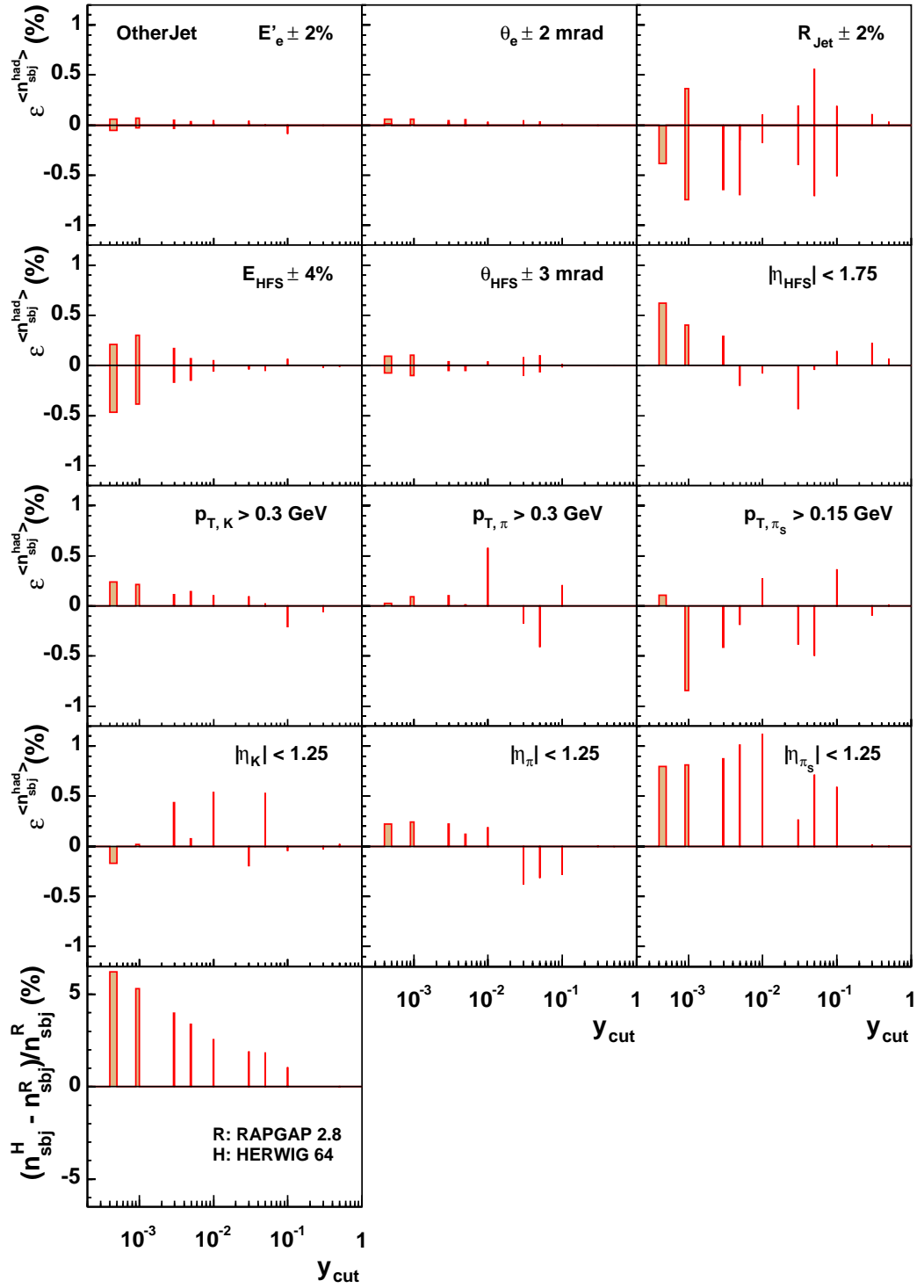


Figure H.3: The systematic errors of the mean subjet multiplicity $\langle n_{\text{subj}} \rangle$ for the *OtherJet*.

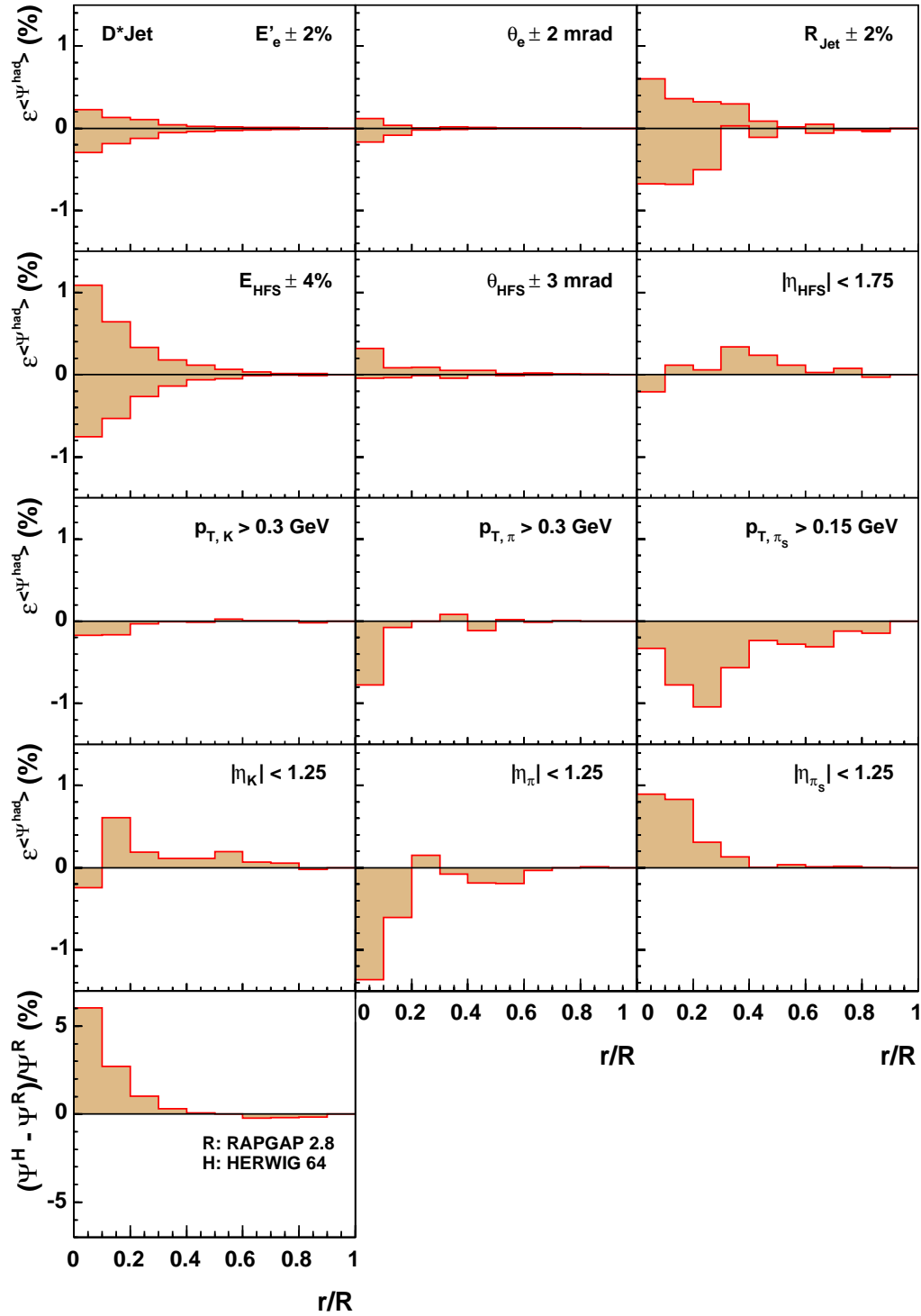


Figure H.4: The systematic errors of the integrated jet shape variable $\langle \Psi(r/R) \rangle$ for the D^* Jet where $R = 1$.

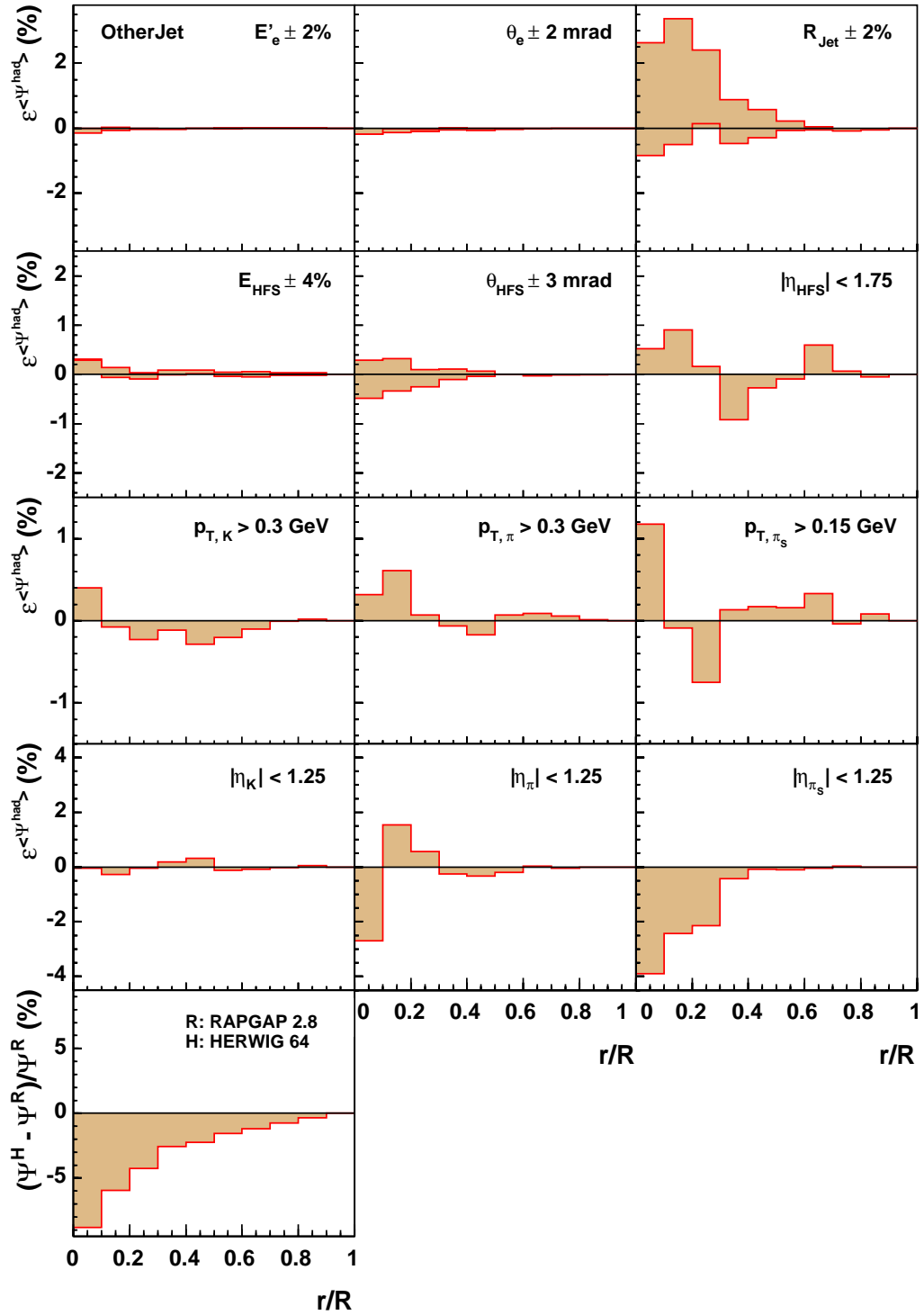


Figure H.5: The systematic errors of the integrated jet shape variable $\langle \Psi(r/R) \rangle$ for the *OtherJet* where $R = 1$.

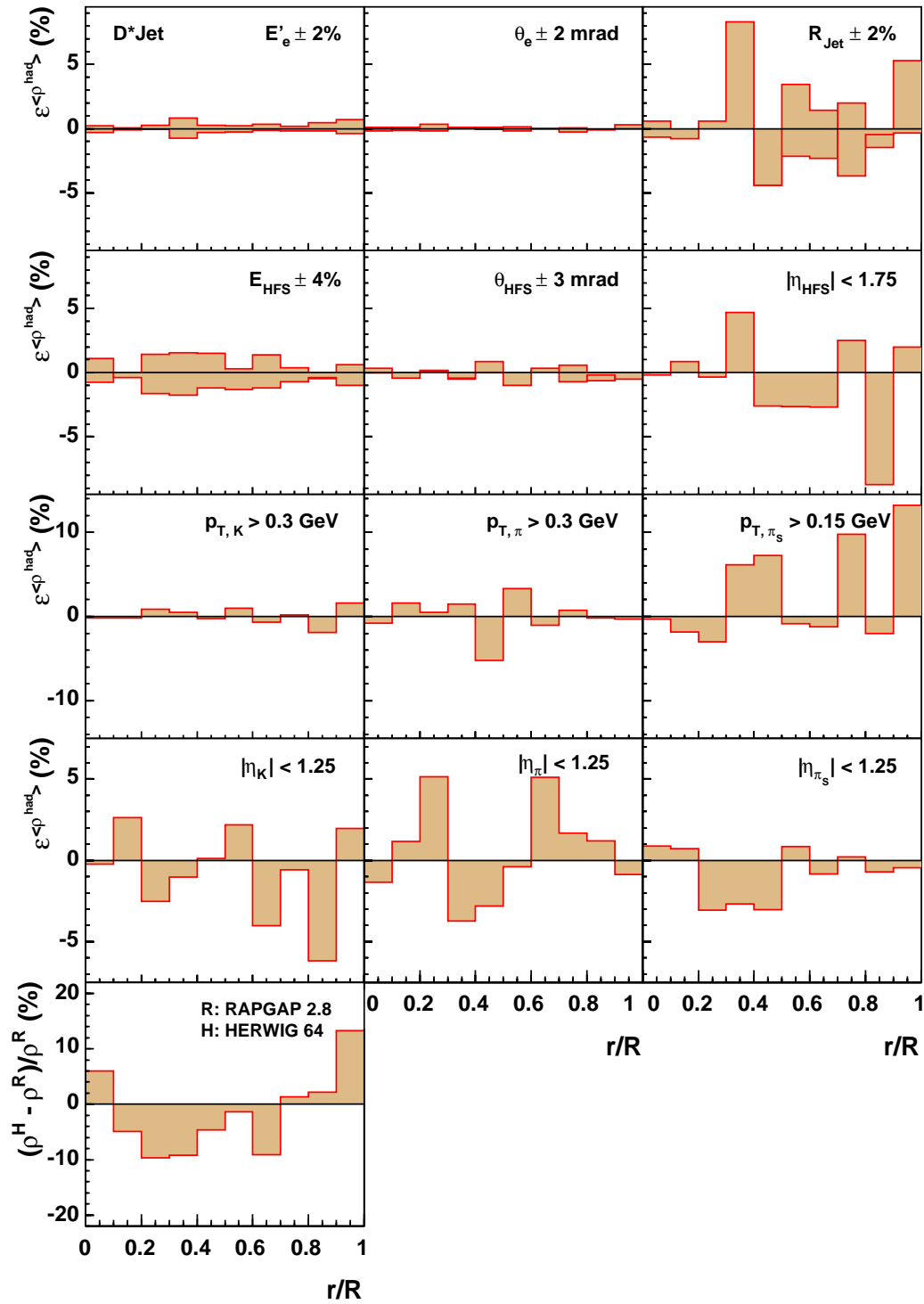


Figure H.6: The systematic errors of the differential jet shape variable $\langle \rho(r/R) \rangle$ for the D^* Jet where $R = 1$.

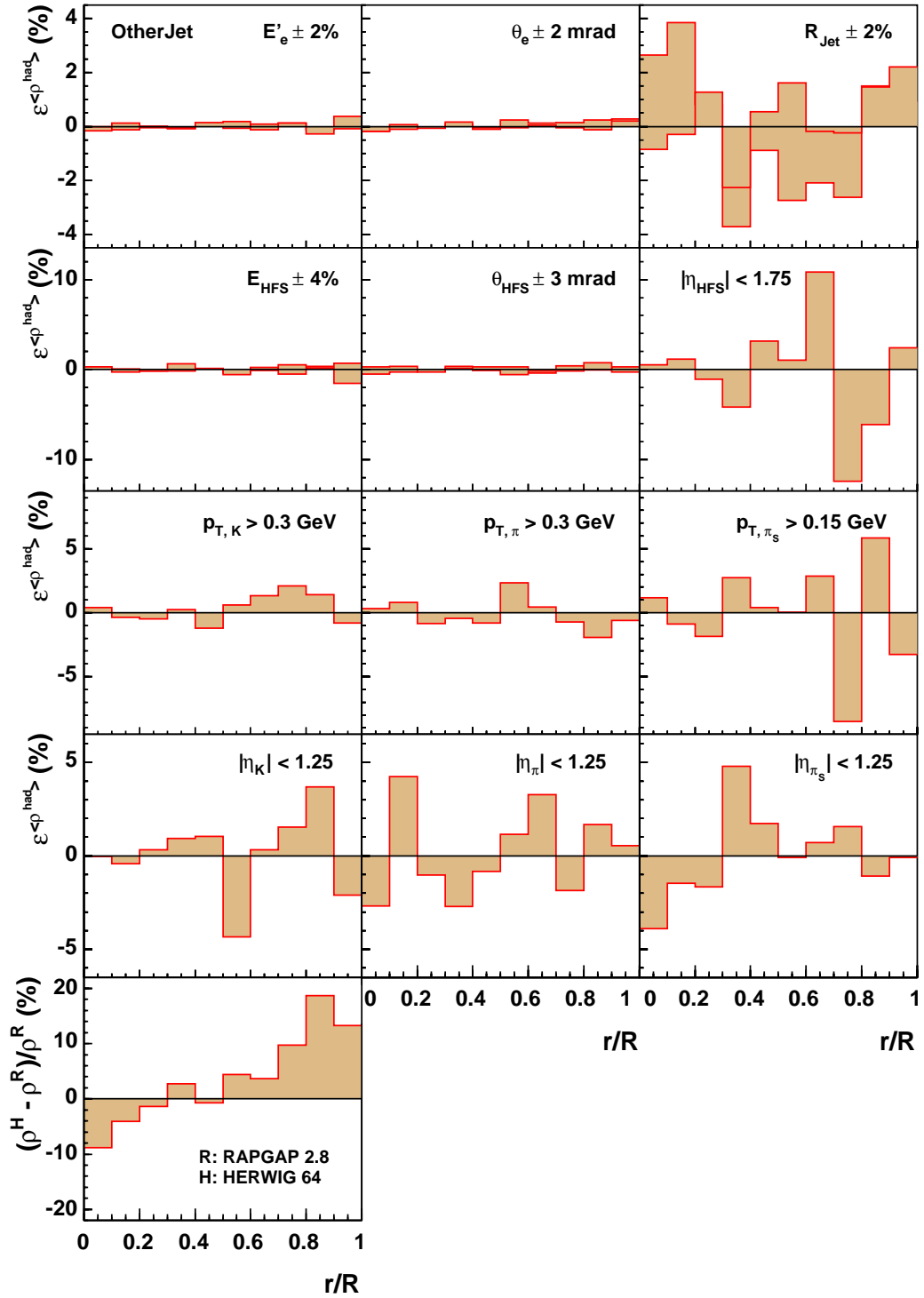


Figure H.7: The systematic errors of the differential jet shape variable $\langle \rho(r/R) \rangle$ for the *OtherJet* where $R = 1$.

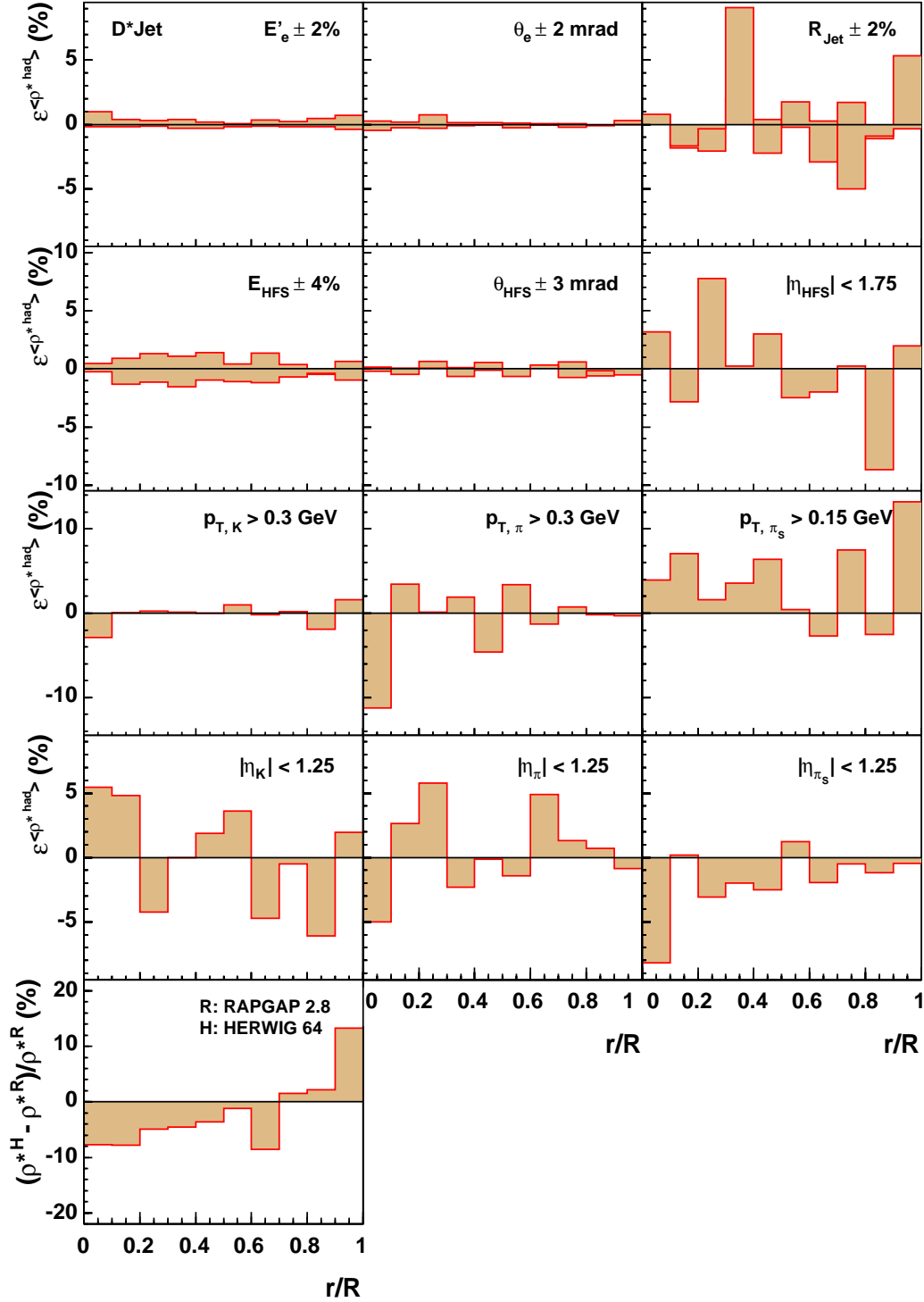


Figure H.8: The systematic errors of the differential jet shape variable $\langle \rho^*(r/R) \rangle$ for the D^* Jet where $R = 1$.

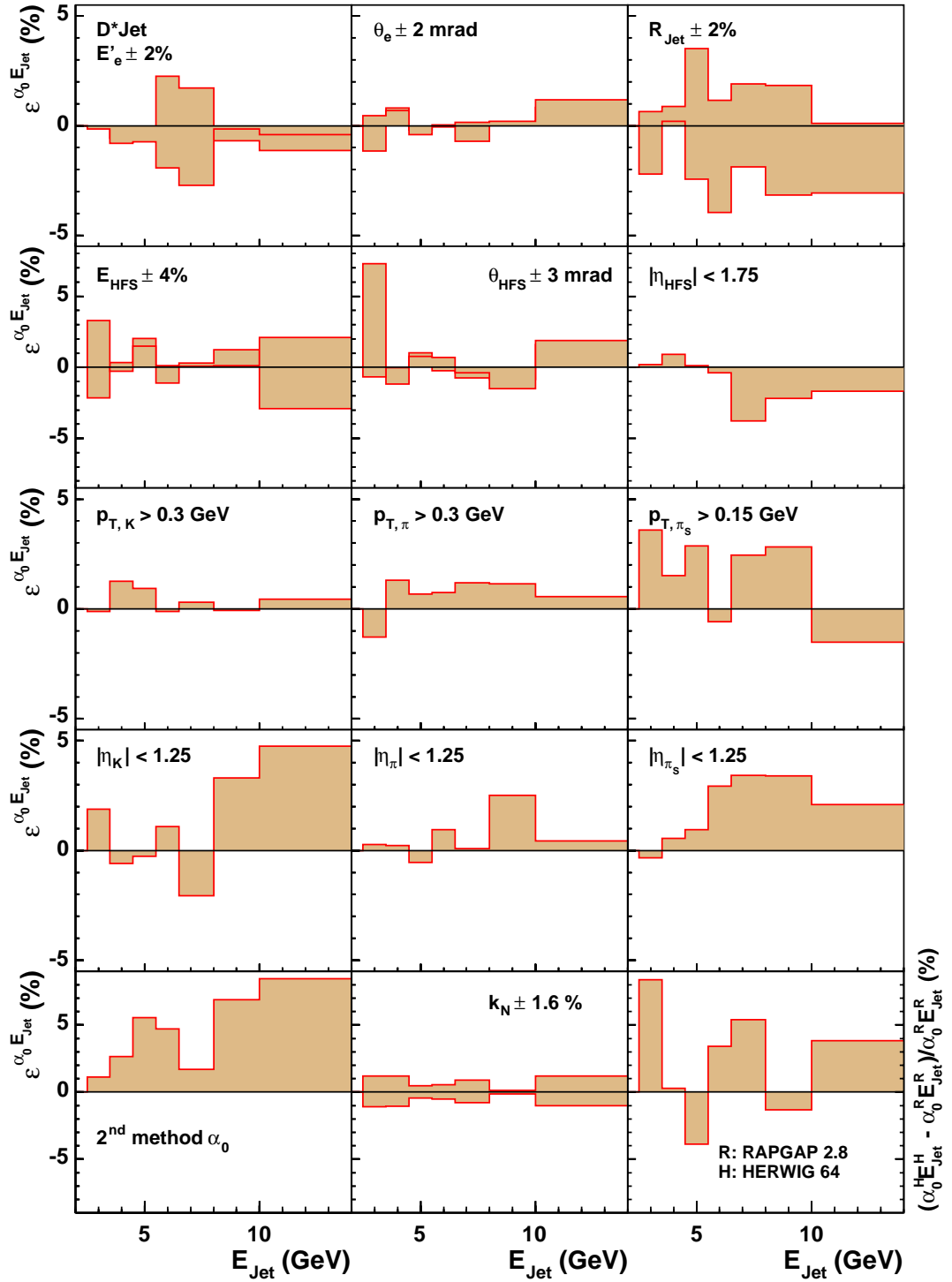


Figure H.9: The systematic errors of the $\alpha_0 E_{\text{Jet}}$ in bins on jet energy, E_{Jet} , for the $D^* \text{Jet}$ in the laboratory frame.

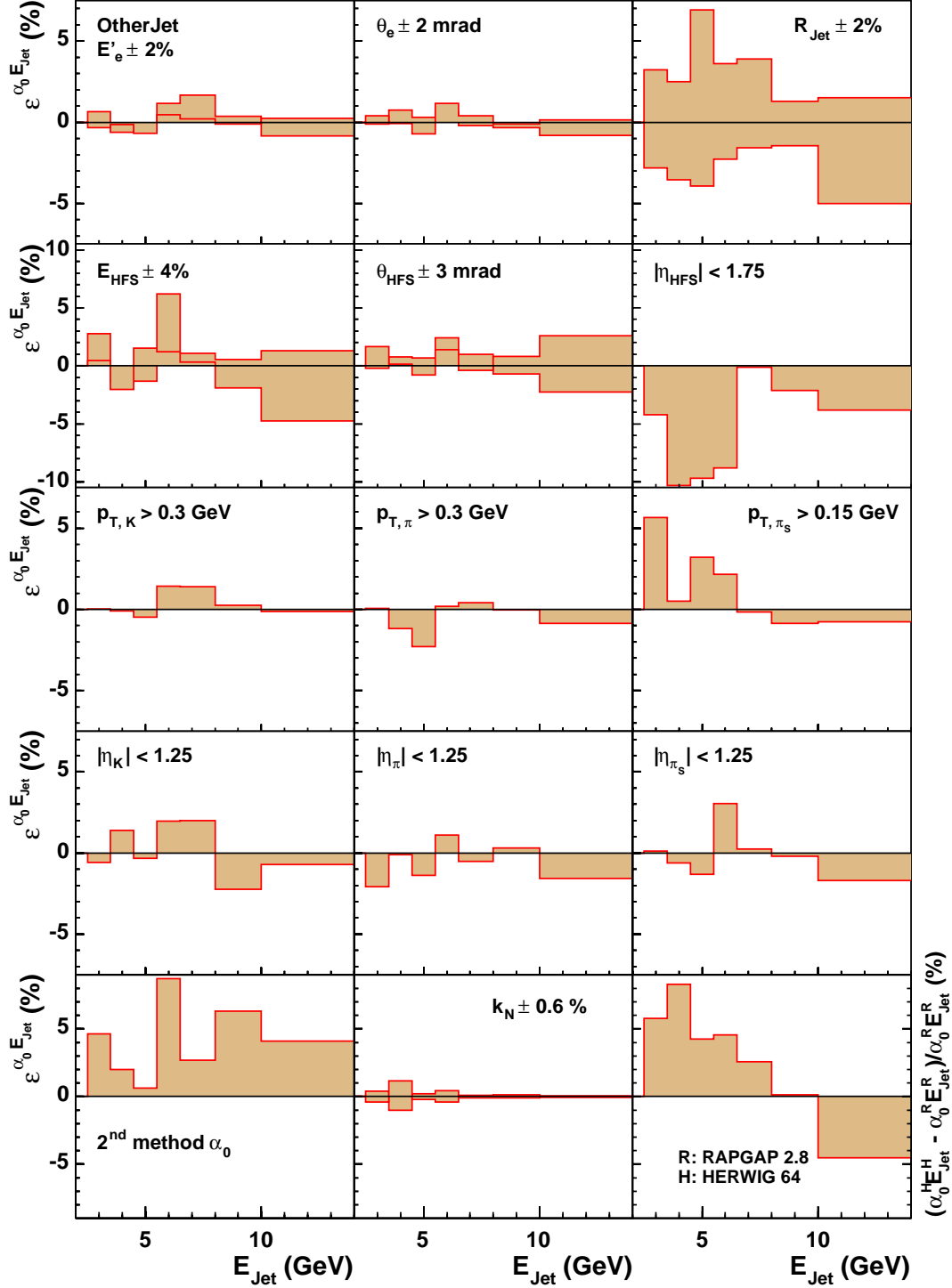


Figure H.10: The systematic errors of the $\alpha_0 E_{\text{Jet}}$ in bins on jet energy, E_{Jet} , for the *OtherJet* in the laboratory frame.

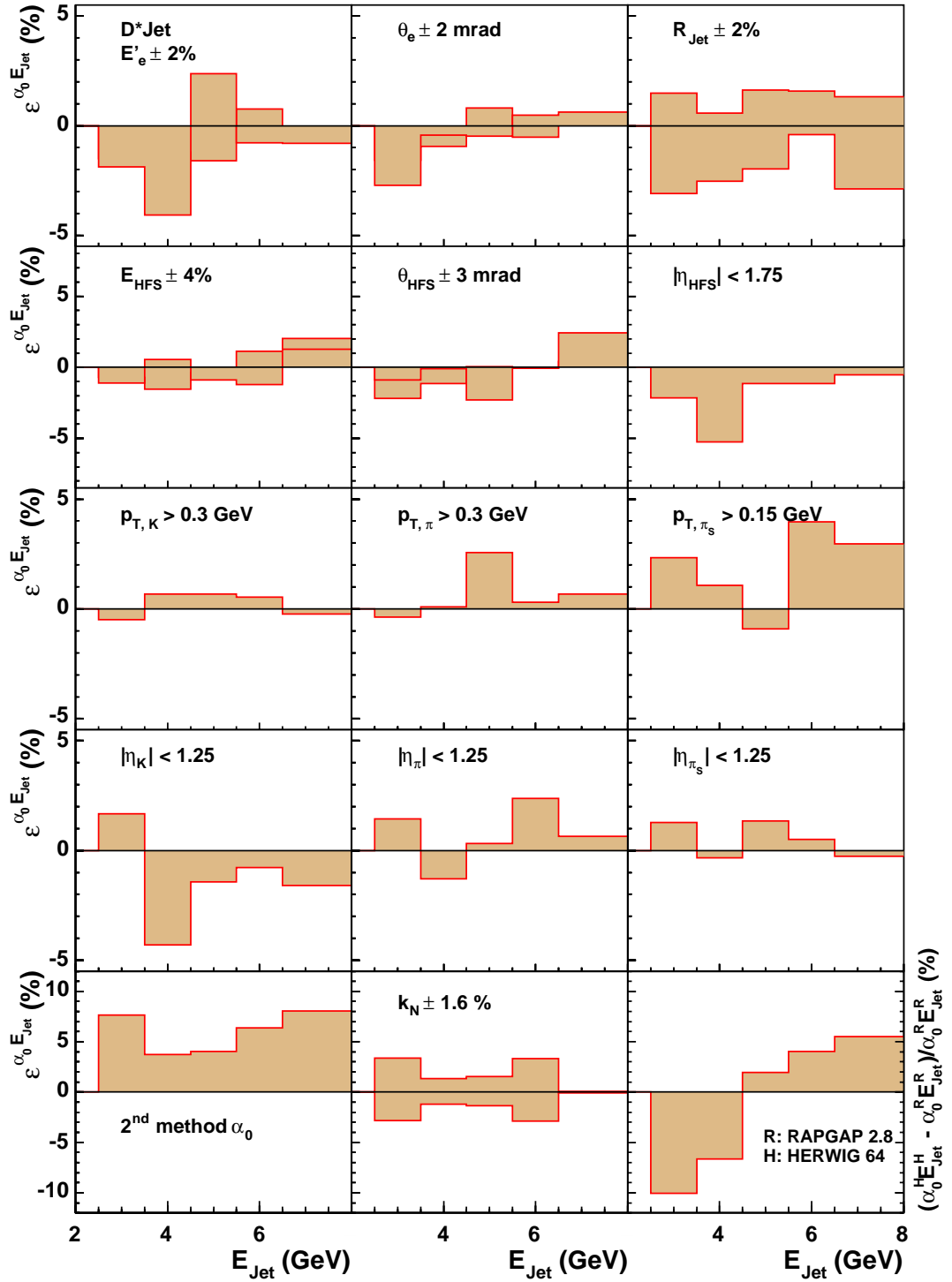


Figure H.11: The systematic errors of the $\alpha_0 E_{\text{Jet}}$ in bins on jet energy, E_{Jet} , for the D^* Jet in the $n\gamma^*p$ - frame.

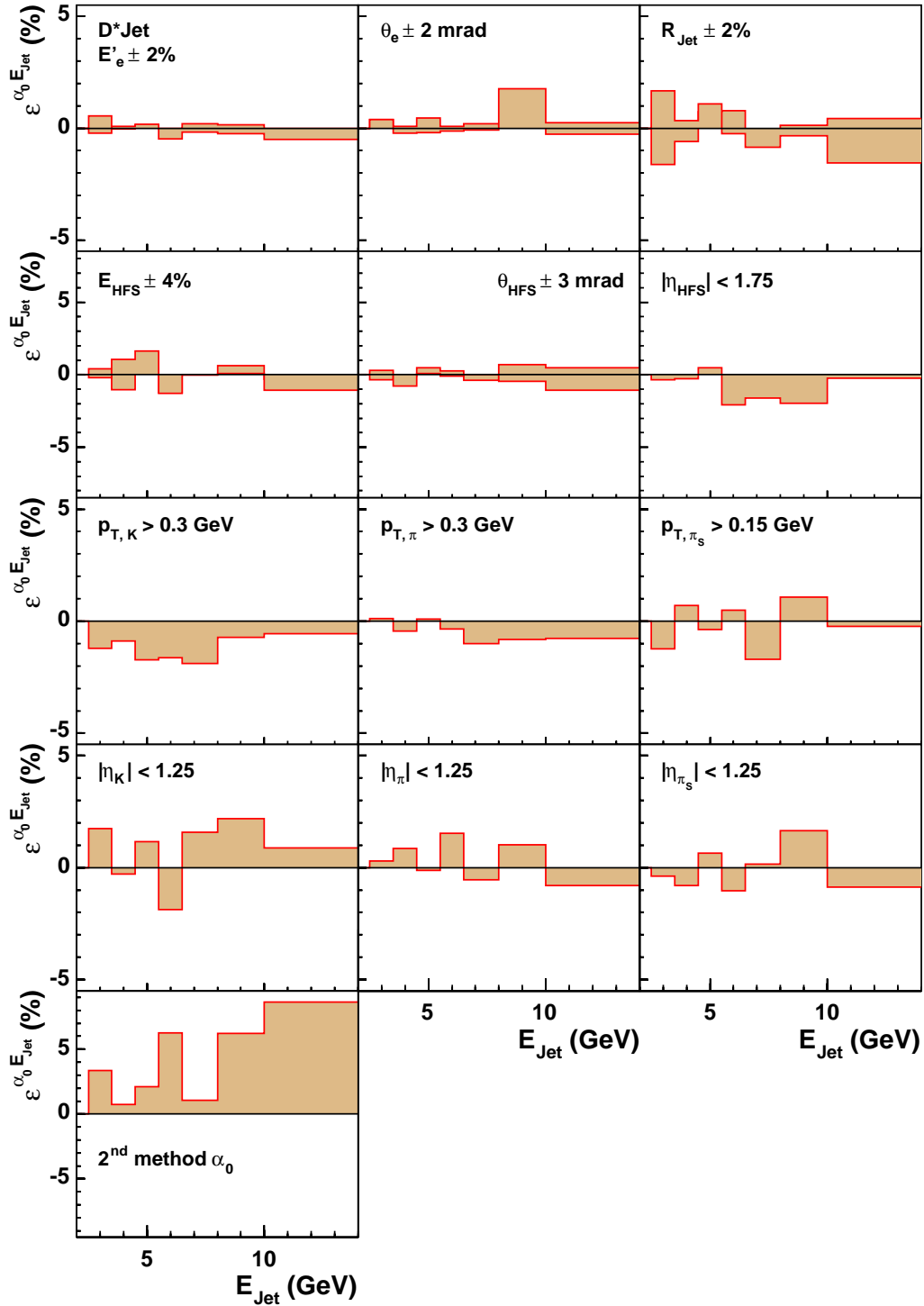


Figure H.12: The systematic errors of the $\alpha_0 E_{\text{Jet}}$ in bins on jet energy, E_{Jet} , for the "fake" D^* Jet in 2Jet event sample.

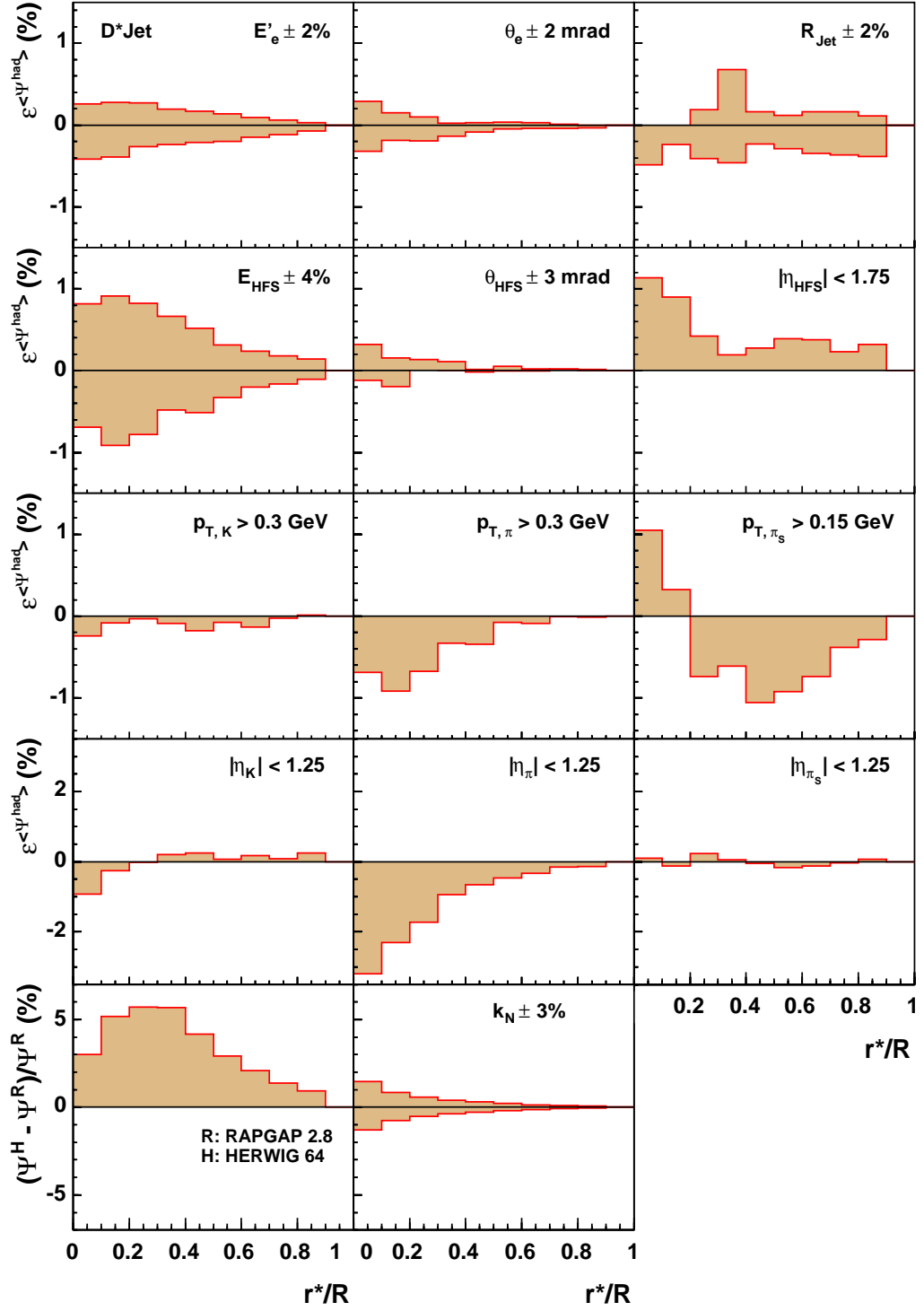


Figure H.13: The systematic errors of the integrated jet shape variable $\langle \Psi(r^*/R) \rangle$ for the D^* Jet where $R = 1$ GeV.

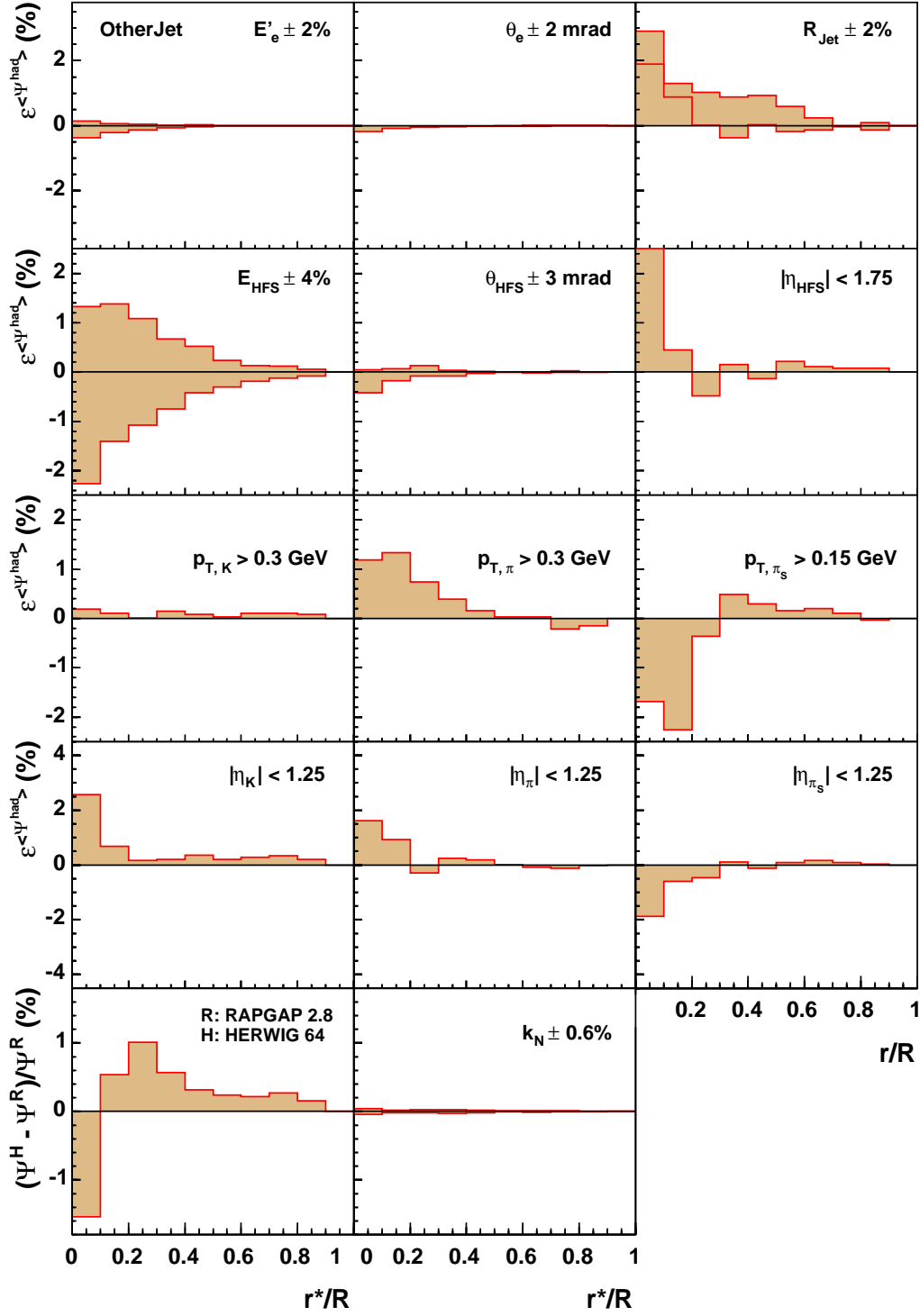


Figure H.14: The systematic errors of the integrated jet shape variable $\langle \Psi(r^*/R) \rangle$ for the *OtherJet* where $R = 1$ GeV.

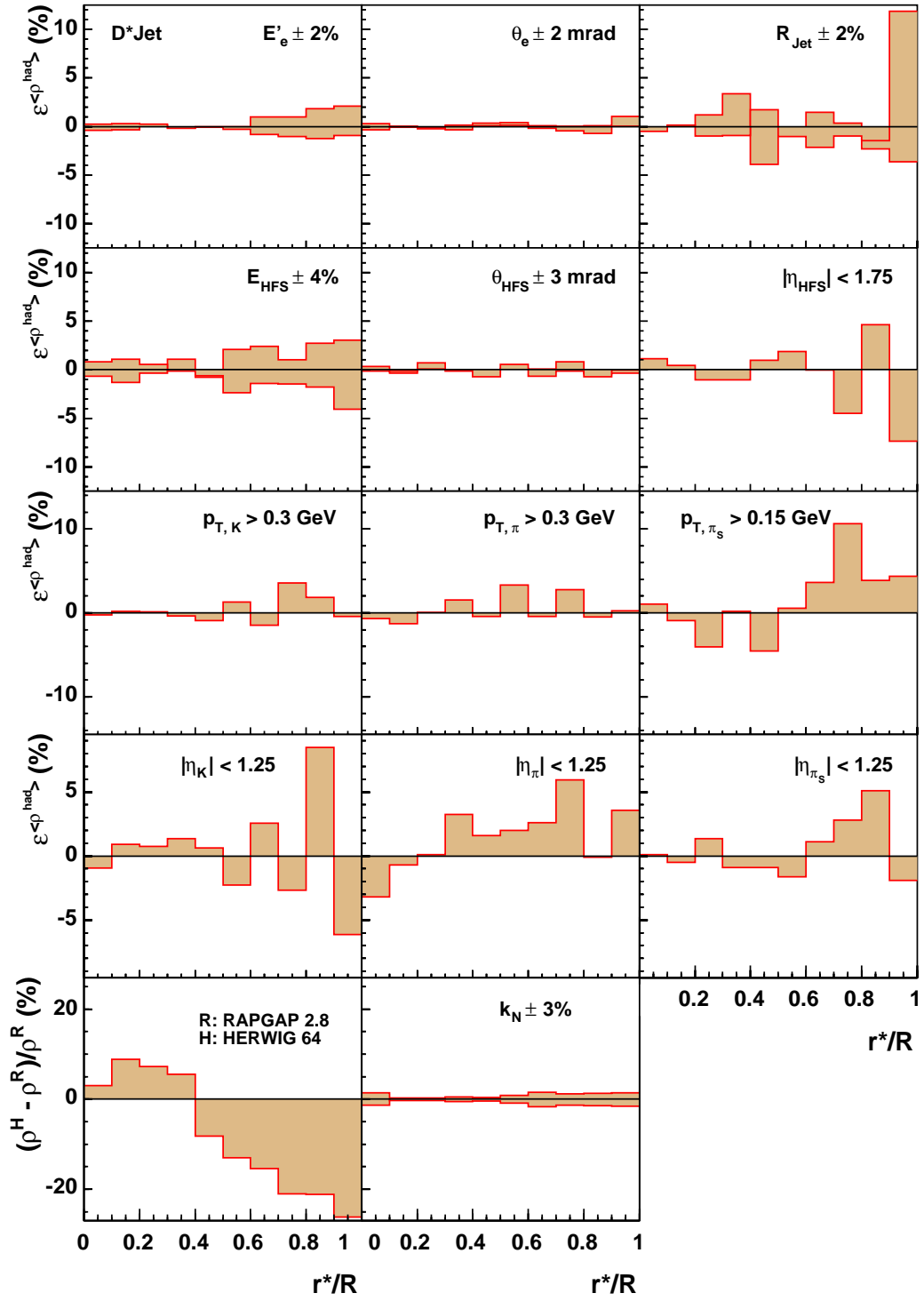


Figure H.15: The systematic errors of the differential jet shape variable $\langle \rho(r^*/R) \rangle$ for the D^* Jet where $R = 1$ GeV.

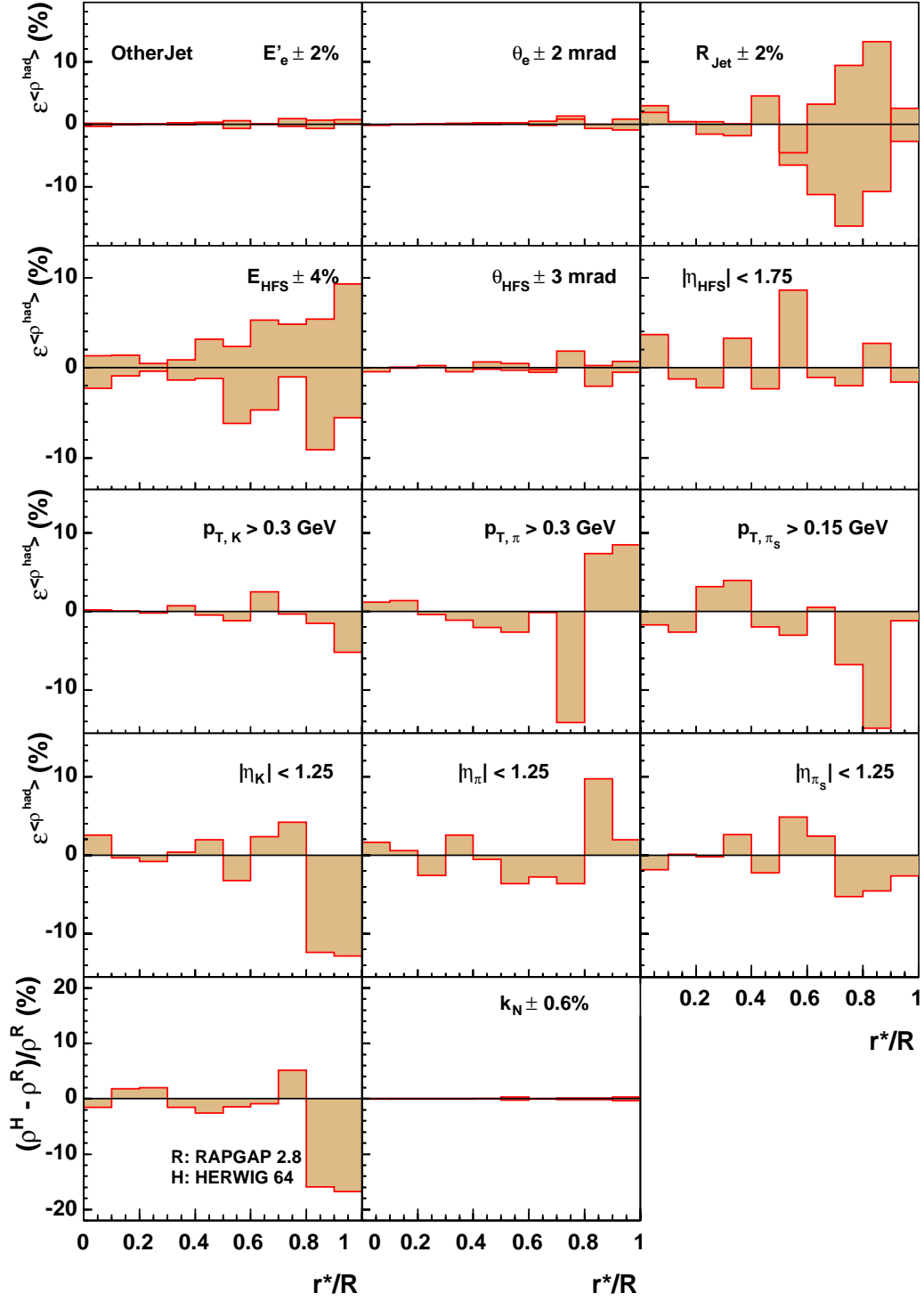


Figure H.16: The systematic errors of the differential jet shape variable $\langle \rho(r^*/R) \rangle$ for the *OtherJet* where $R = 1$ GeV.

Purity and Stability

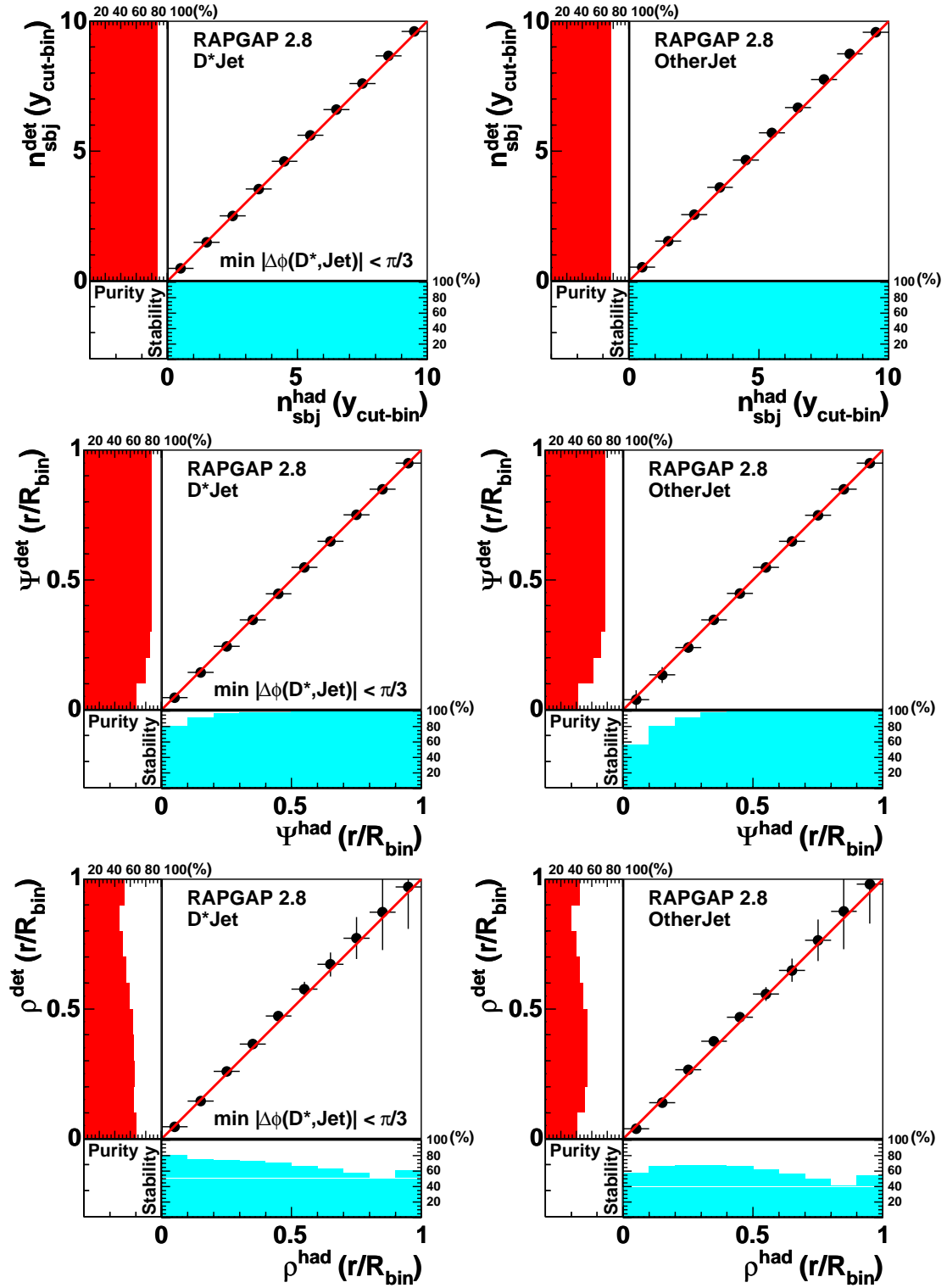


Figure H.17: The purity and the stability of the jet shape observables using $\min |\Delta\phi(D^*, \text{Jet})| < \pi/3$ as D^* Jet definition, see Sec. 4.8.

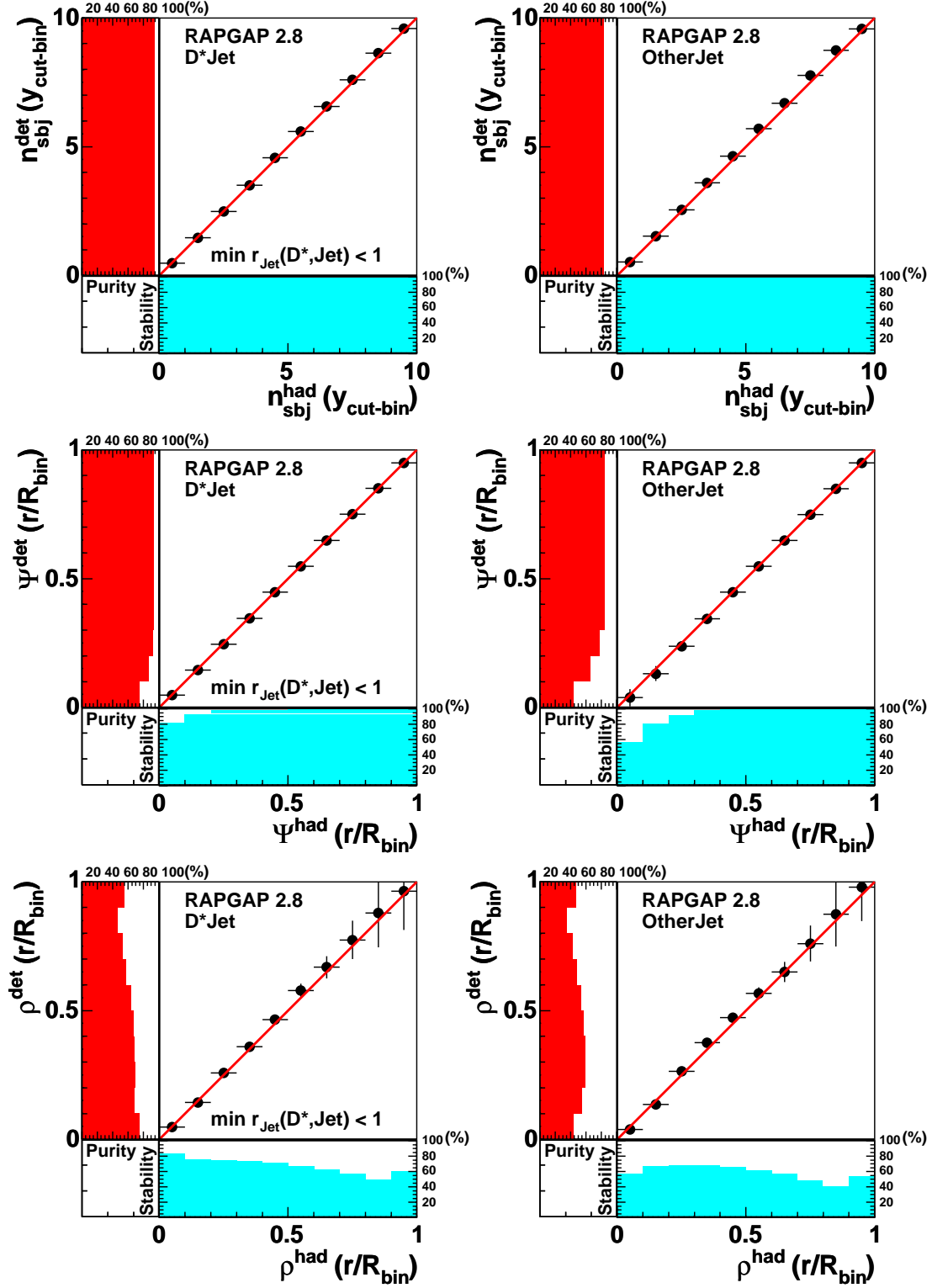


Figure H.18: The purity and the stability of the jet shape observables using $\min r_{Jet}(D^*, Jet) < 1$ as D^* Jet definition.

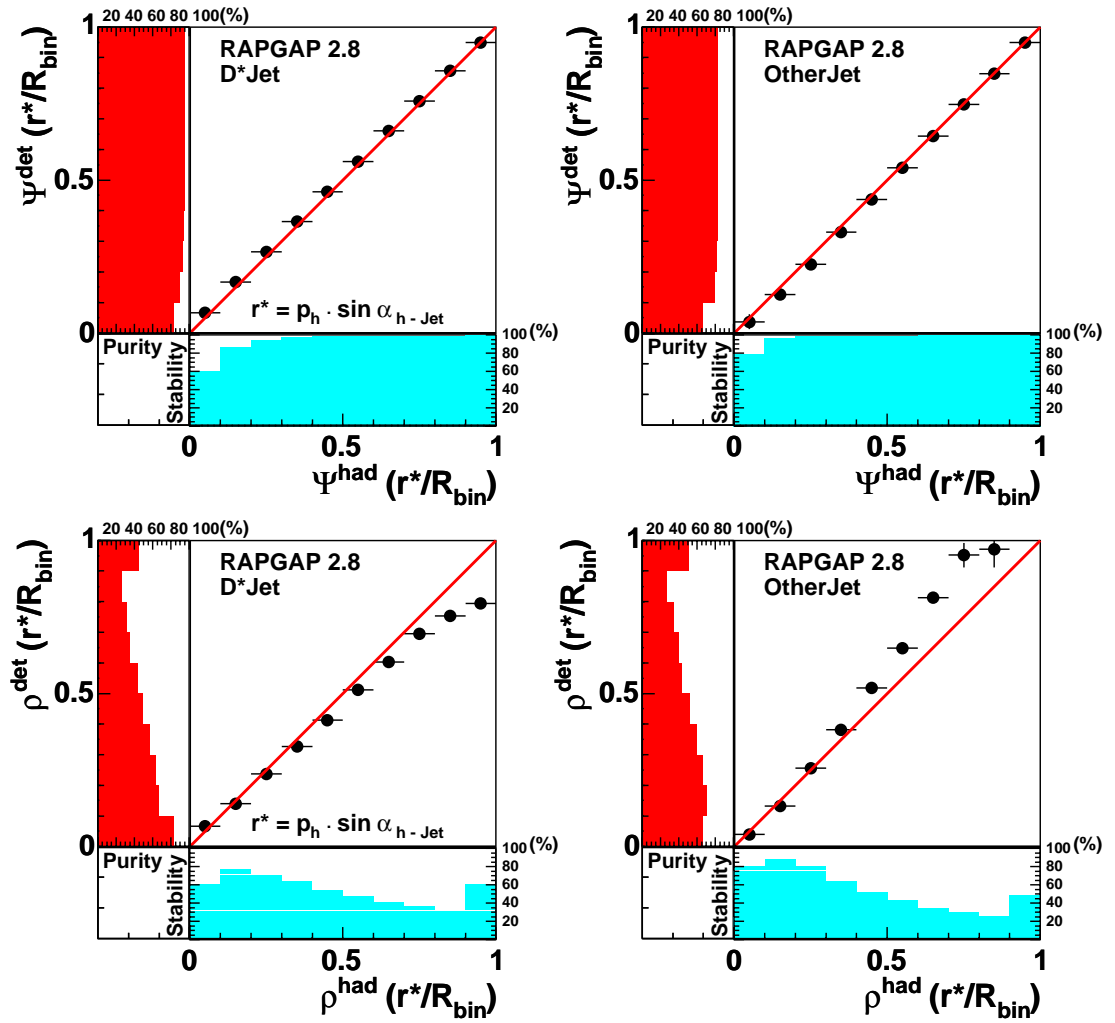


Figure H.19: The purity and the stability of the jet shape observables using the new definition $r^* = p_h \cdot \sin \alpha_{h-Jet}$ where $D^* \in D^*Jet$.

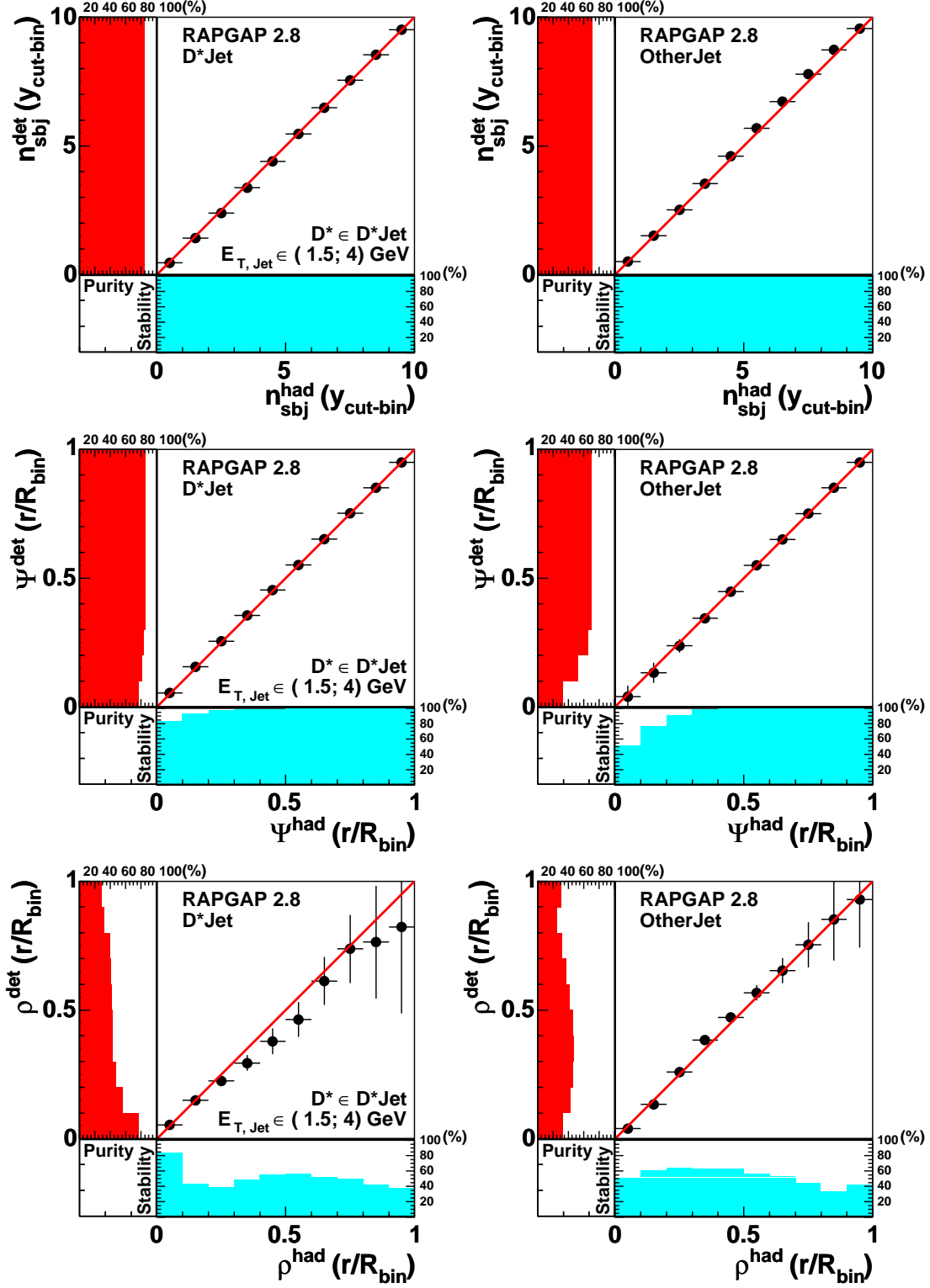


Figure H.20: The purity and the stability of the jet shape observables using for the D^* Jet definition: $D^* \in D^*$ Jet in $E_{T, \text{Jet}} \in (1.5; 4) \text{ GeV}$ bin.

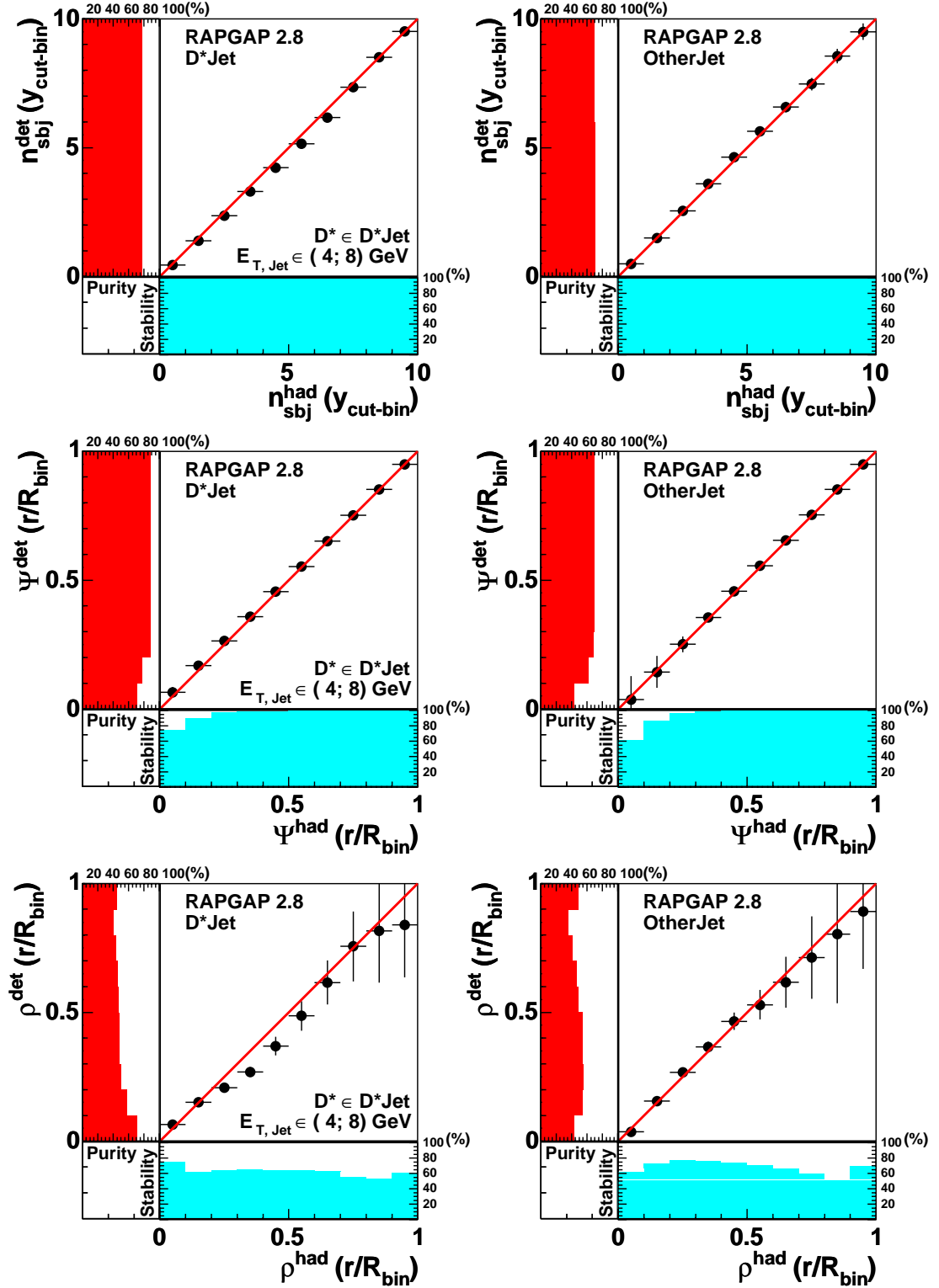


Figure H.21: The purity and the stability of the jet shape observables using for the D^* Jet definition: $D^* \in D^*$ Jet in $E_{T, \text{Jet}} \in (4; 8)$ GeV bin.

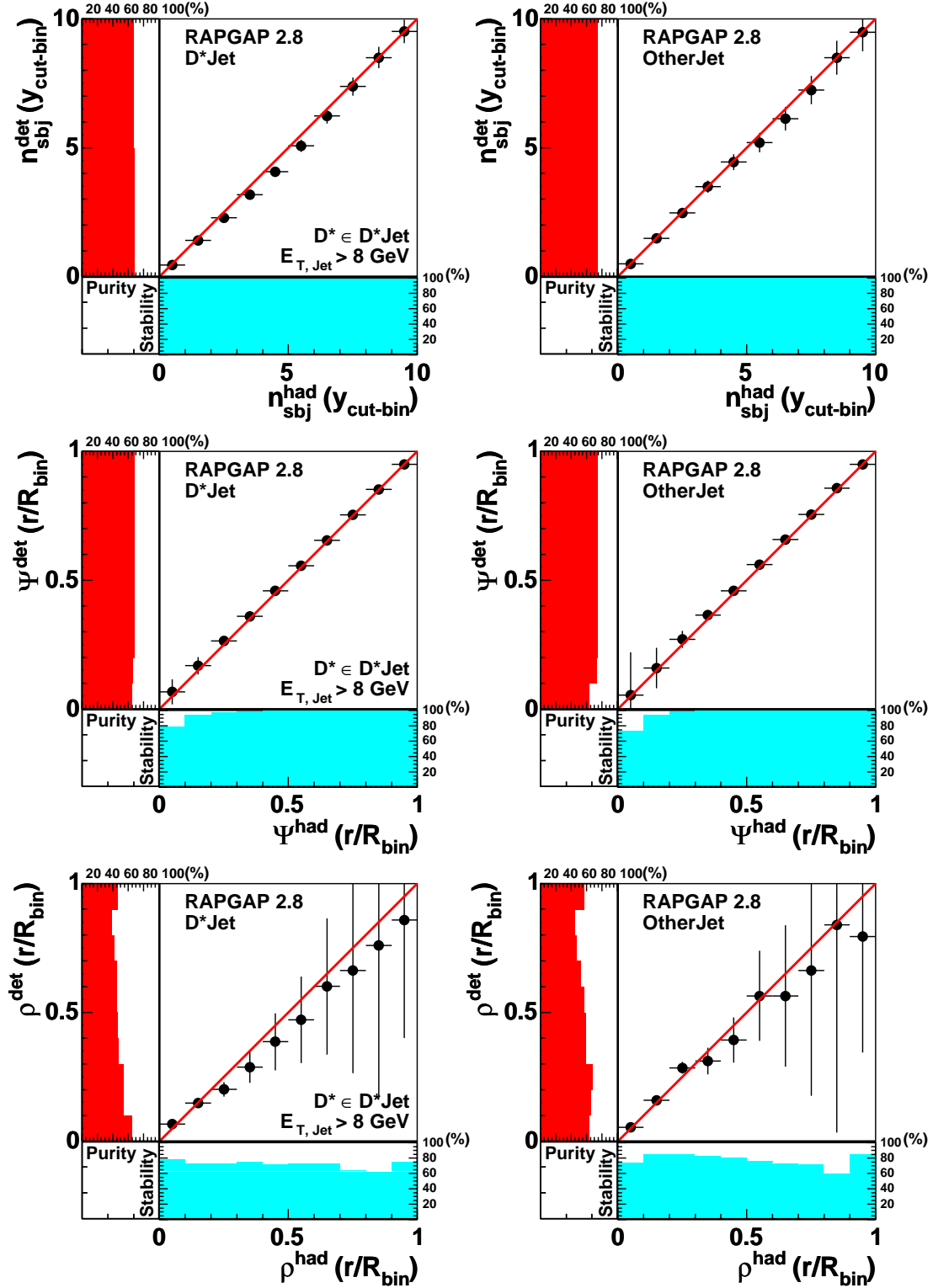


Figure H.22: The purity and the stability of the jet shape observables using for the D^* Jet definition: $D^* \in D^*\text{Jet}$ in $E_{T,\text{Jet}} > 8 \text{ GeV}$ bin.

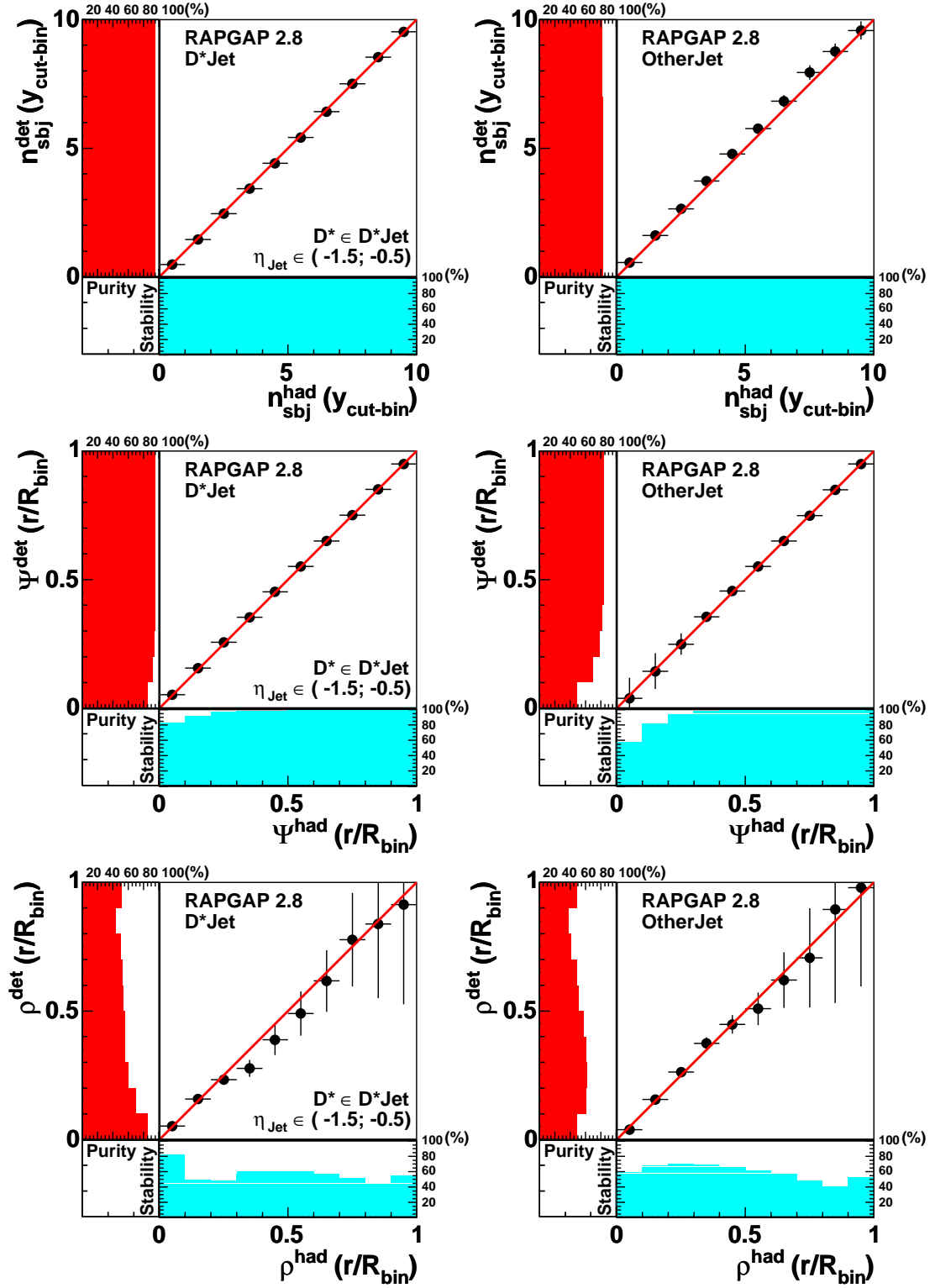


Figure H.23: The purity and the stability of the jet shape observables using for the D^* Jet definition: $D^* \in D^*$ Jet in $\eta_{\text{Jet}} \in (-1.5; -0.5)$ bin.

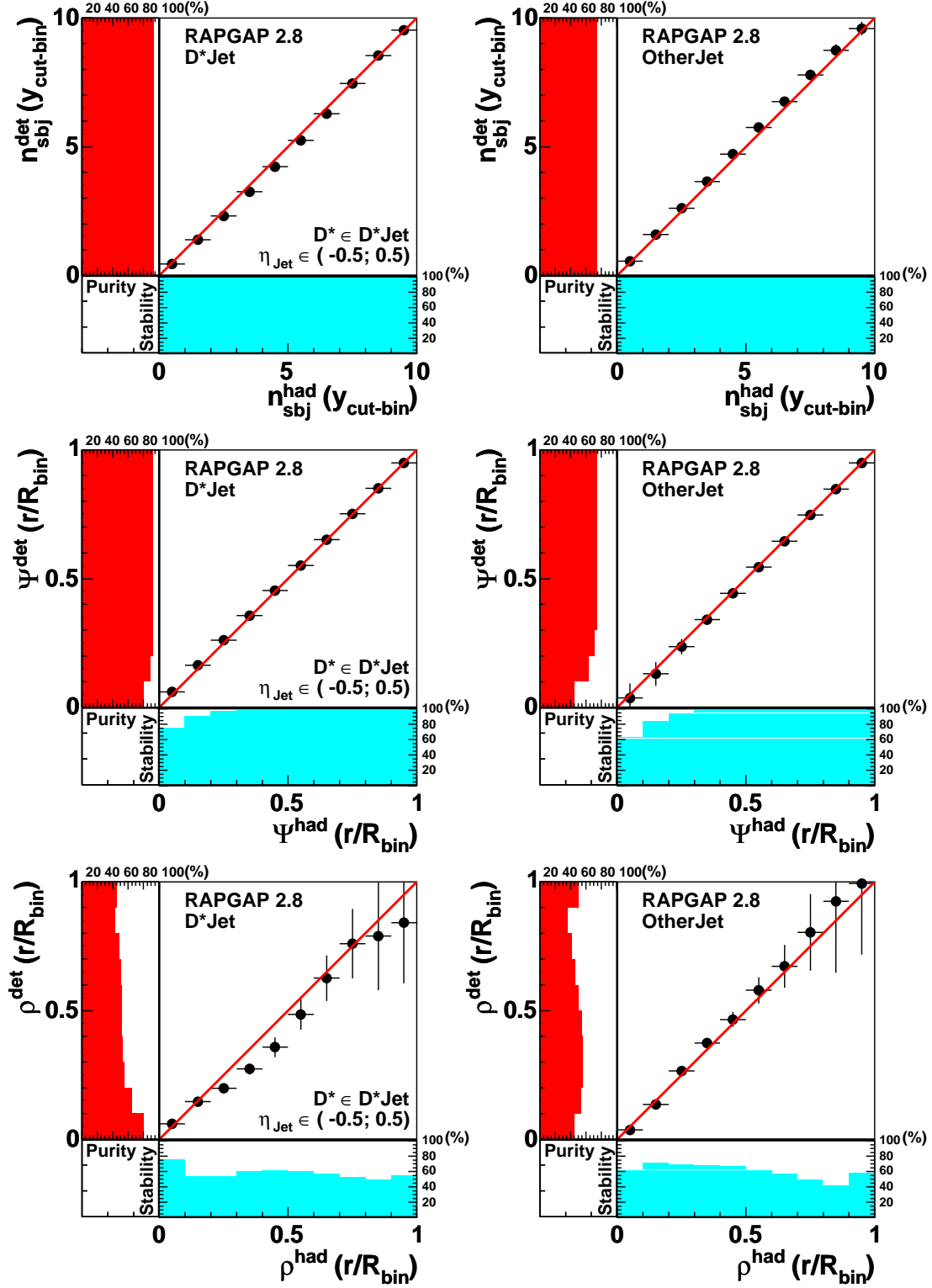


Figure H.24: The purity and the stability of the jet shape observables using for the D^* Jet definition: $D^* \in D^*$ Jet in $\eta_{\text{Jet}} \in (-0.5; 0.5)$ bin.

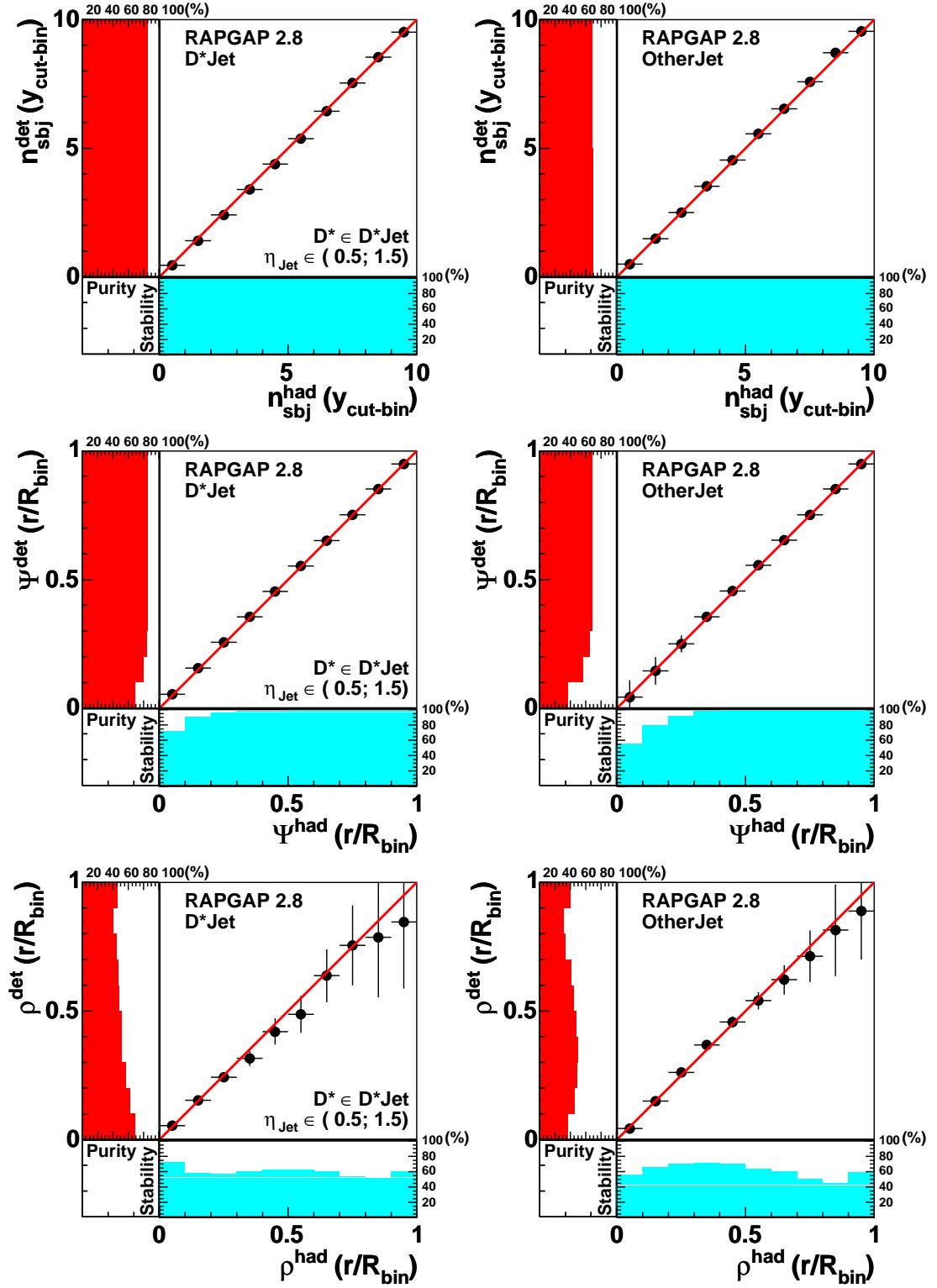


Figure H.25: The purity and the stability of the jet shape observables using for the D^* Jet definition: $D^* \in D^*$ Jet in $\eta_{\text{Jet}} \in (0.5; 1.5)$ bin.

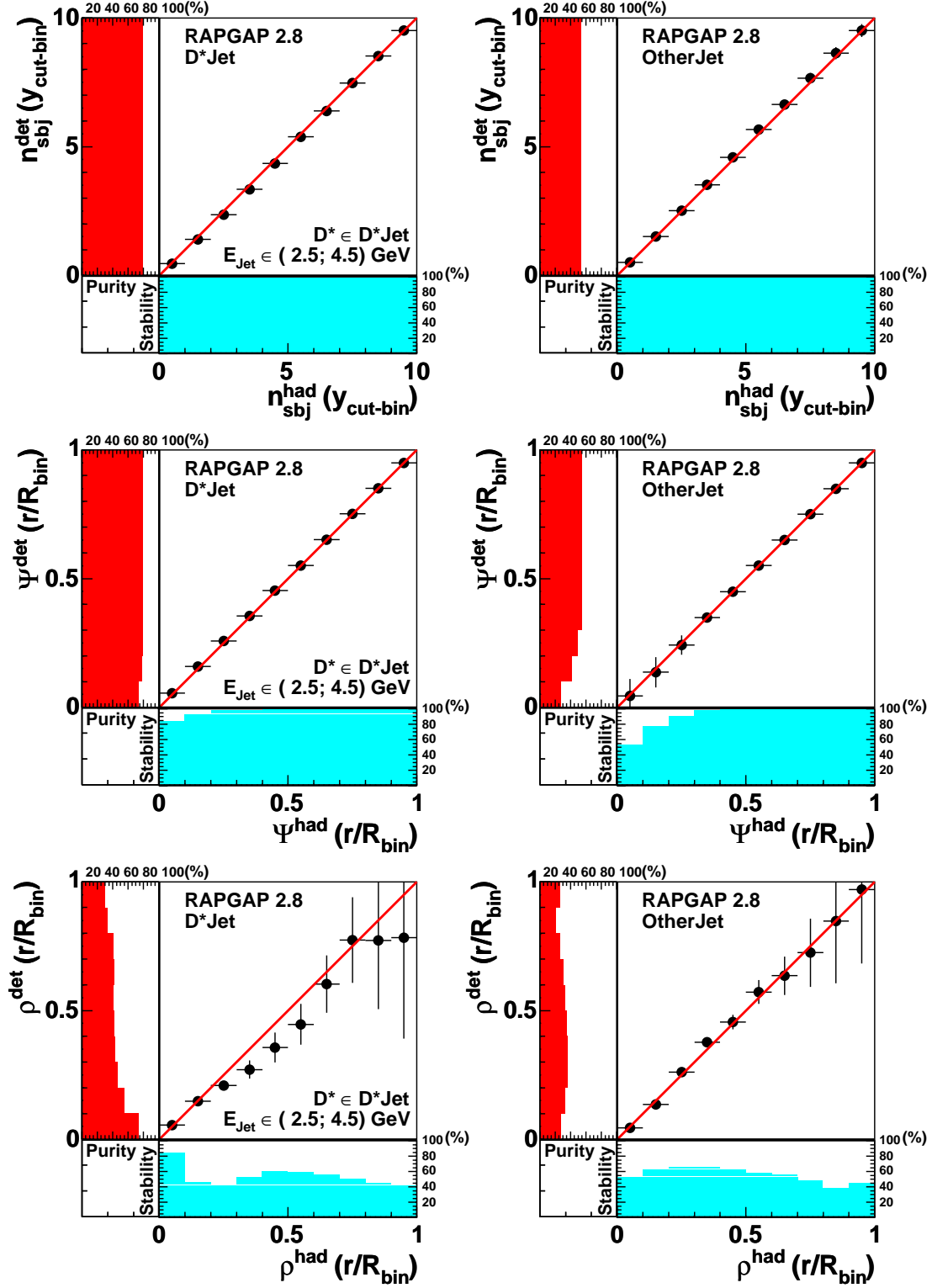


Figure H.26: The purity and the stability of the jet shape observables using for the D^* Jet definition: $D^* \in D^*$ Jet in $E_{\text{Jet}} \in (2.5; 4.5)$ GeV bin.

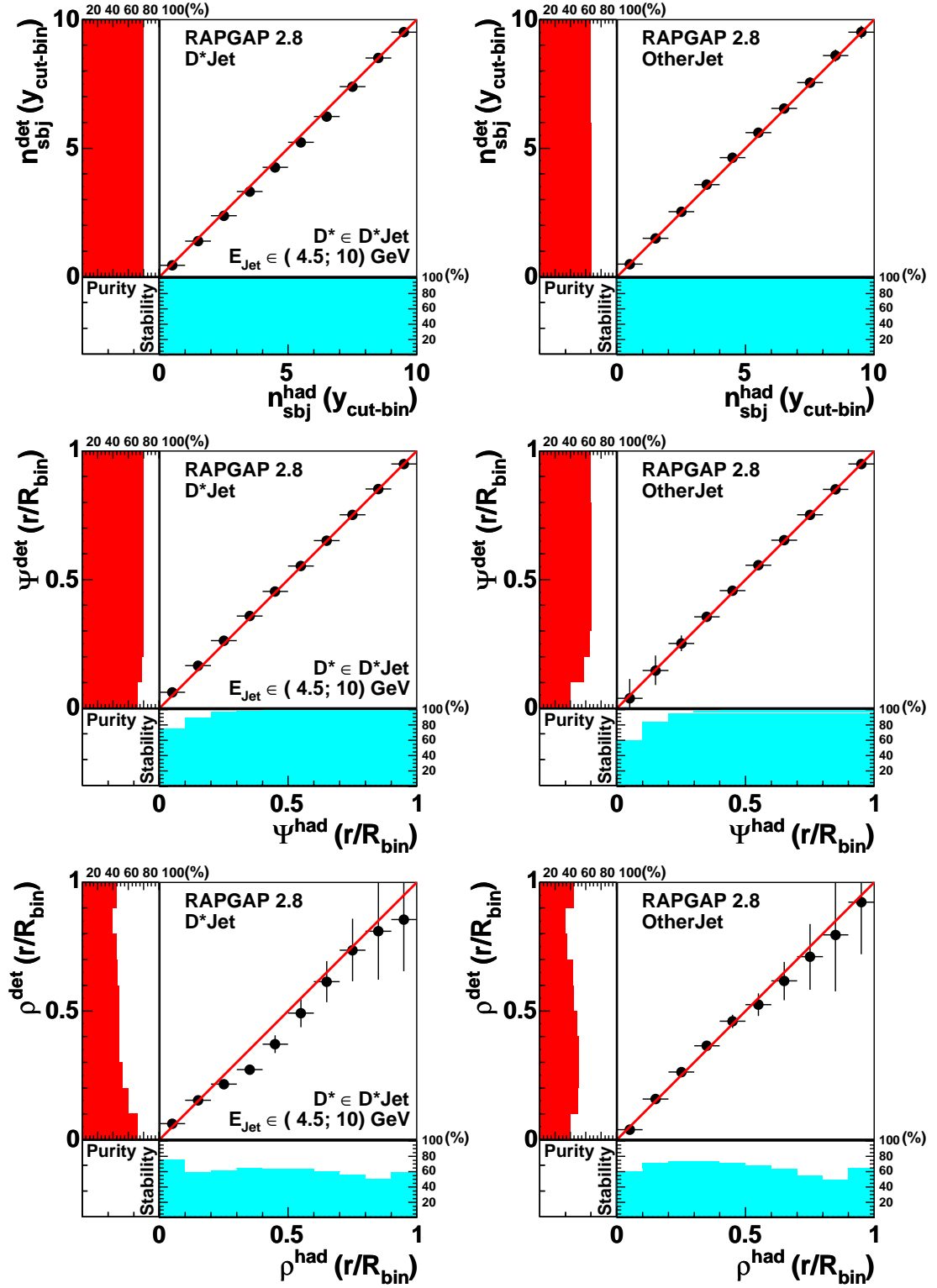


Figure H.27: The purity and the stability of the jet shape observables using for the D^* Jet definition: $D^* \in D^*$ Jet in $E_{\text{Jet}} \in (4.5; 10)$ GeV bin.

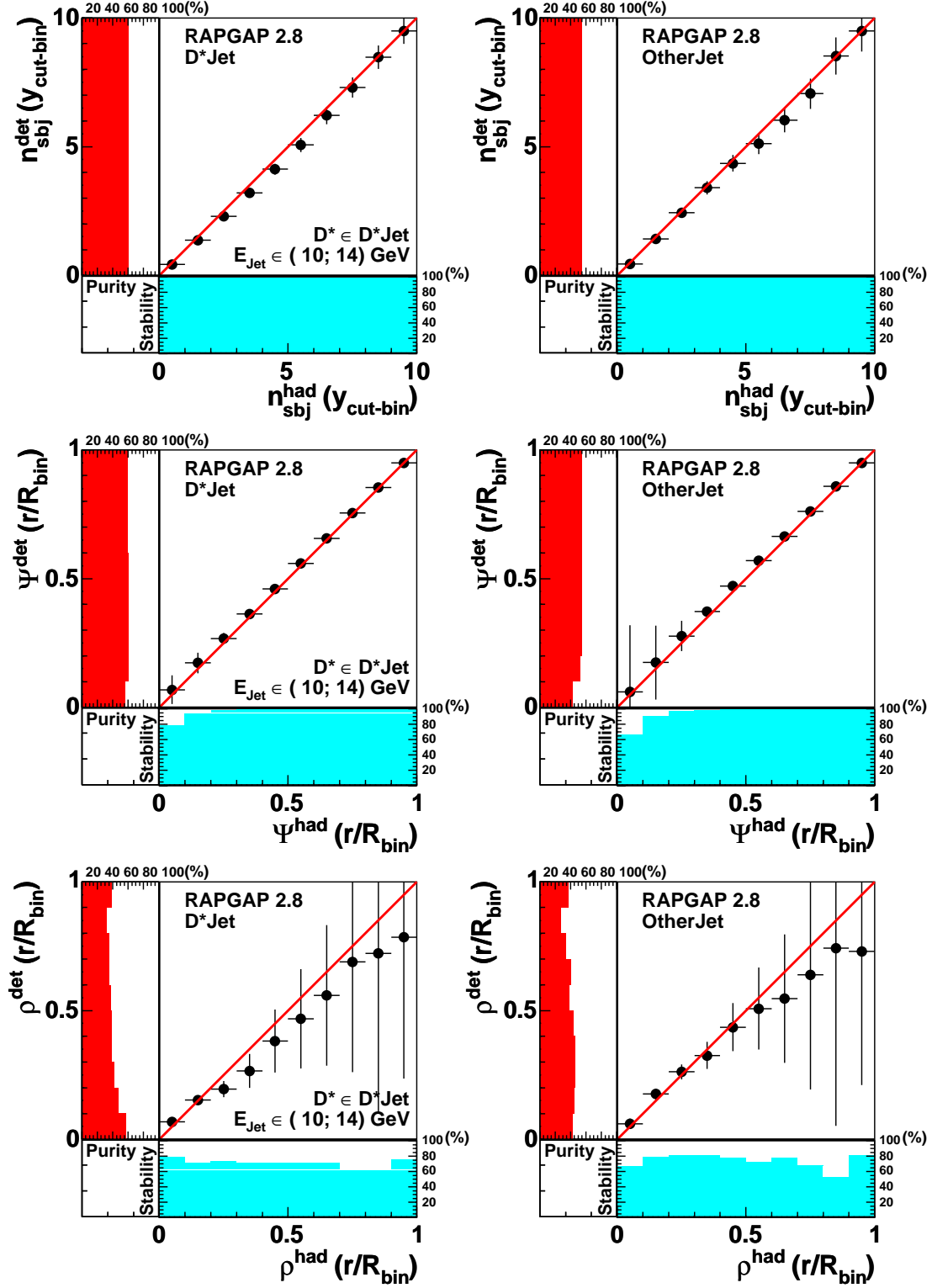


Figure H.28: The purity and the stability of the jet shape observables using for the D^* Jet definition: $D^* \in D^*$ Jet in $E_{\text{Jet}} \in (10; 14)$ GeV bin.

Acknowledgment

My first thoughts go to my Professor from faculty Ionel Lazanu who introduced me in the High Energy Physics area. I would like to express my gratitude to Carsten Niebuhr and Professor Beate Naroska who offered me the possibility to work on my Ph.D. study in the H1 collaboration at DESY.

I would like to thank Günter Grindhammer who advised and supervised my work starting with the Summer Student Project and finishing with my Ph.D. work. Special thanks go to Hannes Jung who help me in understanding and working with various Monte Carlo models.

Many thanks to all colleagues from DESY and MPIM who made the time spend with them such a nice experience. I would also like to thank all the people who read the thesis and helped me getting preliminary for my results.

Finally I would like to thank my family and Renate Wilke for their support and understanding. A more than special thanks will always go for Isa who was on my side during this time.

Bibliography

- [1] S.L.Glashow, Nucl.Phys.22(1961),579;
S.Weinberg, Phys.Rev.Lett.19(1967),1264.
- [2] H1 Collaboration, C.Adloff *et al.*, Eur.Phys.J.C19(2001),289.
- [3] M.Gell-Mann, Phys.Rev.92(1953)833;
K.Nishijima and T.Nakano, Prog.Theor.Phys.10(1953)581.
- [4] M.Gell-Mann, Phys.Lett.8(1964)214;
C.Zweig, CERN Report No.8182/TH401,1964.
- [5] J.D.Bjorken and S.L.Glashow, Phys.Lett.11(1964),255.
- [6] J.J.Aubert *et al.*, Phys.Rev.Lett.33(1974)1404;
J.E.Augustin *et al.*, Phys.Rev.Lett.33(1974)1406.
- [7] "HERA, A Proposal for a Large Electron Proton Colliding Beam
Facility at DESY", DESY HERA 81-10 (1981).
- [8] G.Engelmann and R.Rückl, Phys.Lett.B201(1988)369.
- [9] E.A.Kuraev, L.N.Lipatov and V.S.Fadin, Sov.Phys.JETP 45(1977)199;
I.I.Balitsky and L.N.Lipatov, Sov.J.Nucl.Phys.28(1978)822.
- [10] M.Ciafaloni, Nucl.Phys.B296(1988)49;
S.Catani, F.Fiorani and G.Marchesini, Phys.Lett.B234(1990)339.
- [11] G.Altarelli and G.Parisi, Nucl.Phys.B126(1977)298.
- [12] E.Laenen *et al.*, Nucl.Phys.B392(1993)162;
B.W.Harris and J.Smith, Nucl.Phys.B452(1995)109;
- [13] J.Smith and W.L.van Neerven, Nucl.Phys.B374(1992)36;
J.Smith and W.K.Tung, NIKHEF-H-93-20.
- [14] S.Bethke, hep-ex/9812026.
- [15] S.Peterson *et al.*, Phys.Rev.D27(1983)105.
- [16] V.G.Kartvelishvili *et al.*, Phys.Lett.B78(1978)615.
- [17] B.Andersson *et al.*, Phys.Rep.97(1983)31;
T.Sjöstrand, Nucl.Phys.B248(1984)469.
- [18] G.Hanson *et al.*, Phys.Rev.Lett.35(1975)1609.

- [19] G.Sterman and S.Weinberg, Phys.Rev.Lett.39(1997)1436.
- [20] JADE Collaboration, W.Bartel *et al.*, Z.Phys.C33(1986)23.
- [21] S.Catani, Y.Dokshitzer and B.Webber, Phys.Lett.B285(1992)291;
S.D.Ellis and D.E.Soper, Phys.Rev.D48(1993)3160.
- [22] OPAL Collaboration, G.Alexander *et al.*, Z.Phys.C69(1996)543.
- [23] R.K.Ellis, W.J.Stirling and B.R.Webber, QCD and Collider Physics,
Cambridge University Press,1996.
- [24] J.D.Jackson, Classical Electrodynamics,
Third Edition, John Wiley & Sons, Inc.,1999.
- [25] Yu.L.Dokshitzer, V.A.Khoze and S.I.Troian, J.Phys.G17(1991)1602.
- [26] H.Jung, Comp.Phys.Commun.,86(1995)147.
- [27] T.Sjöstrand, Comp.Phys.Commun.,82(1994)74.
- [28] G.Marchesini *et al.*, Comp.Phys.Commun.,67(1992)465.
- [29] G.A.Schuler and H.Speisberger, Proc.Workshop
"Physics at HERA",V3(1992)1419.
- [30] CTEQ Collaboration, H.L.Lai *et al.*, Eur.Phys.J.,C12(2000)375.
- [31] H.Plochow-Besch, Comp.Phys.Commun.,75(1993)396.
- [32] A.Kwiatkowski *et al.*, Comp.Phys.Commun.,69(1992)155.
- [33] R.Brun *et al.*, CERN-DD/EE-84-1(1997).
- [34] H1 Collaboration, A.Aktas *et al.*, Nucl.Instrum.Meth.A501(2001)49.
- [35] H1 Collaboration, H1 06/92-226.
- [36] H1 Collaboration, DESY PRC 99-01(1999).
- [37] H1 Collaboration, I.Abt *et al.*, Nucl.Instrum.Meth.A386(1997)348.
- [38] H1 Collaboration, H1 06/94-366.
- [39] H1 Collaboration, I.Abt *et al.*, Nucl.Instrum.Meth.A386(1997)310.
- [40] D.E.Groom *et al.*, Eur.Phys.J.C15(2000)1.
- [41] H1 Collaboration, W.Braunschweig *et al.*, Nucl.Instrum.Meth.A265(1988)419;
H1 Collaboration, W.Braunschweig *et al.*, Nucl.Instrum.Meth.A275(1989)246;
H1 Collaboration, W.Braunschweig *et al.*, DESY 89-022(1989);
H1 Calorimeter Group, B.Andrieu *et al.*, Nucl.Instrum.Meth.A336(1993)499;
H1 Calorimeter Group, B.Andrieu *et al.*, Nucl.Instrum.Meth.A350(1994)57.
- [42] H1 SpaCal Group, R.-D.Appuhn *et al.*, Nucl.Instrum.Meth.A386(1997)397.
- [43] H1 SpaCal Group, T.Nicholls *et al.*, Nucl.Instrum.Meth.A374(1996)149.

- [44] V.Karimäki, HU-SEFT-1991-10(1991).
- [45] www.desy.de/~perieanu
- [46] E.Eidelman *et al.*, Phys.Lett.B592(2004)1.
- [47] L.Gladilin, hep-ex/9912064(1999).
- [48] G.Feldmann *et al.*, Phy.Rev.Lett.38(1977)1313.
- [49] J.Gassner, A Measurement of D-Meson Production at HERA by Decay Vertex Identification, Diss.ETHZ No.14774(2002).
- [50] C.Wissing, Diploma thesis, Univ.Dortmund(1998).
- [51] J.Steinhardt, Ph.D. thesis, Univ.Hamburg(1999).
- [52] H1 Collaboration, C. Adloff *et al.*, Nucl.Phys.B545(1999)21.
- [53] H1 Collaboration, internal report, H1 01/05-616.
- [54] B.Reisert, Ph.D. thesis, (LMU)MPI-PhE/2000-26.
- [55] DELPHI Collaboration, P.Abreu *et al.*, Phys.Lett.B479(2000)118;
M. Battaglia, R.Orava and L.Salmi, DELPHI 2004-037 CONF 712.
- [56] M.Milite, Ph.D. thesis, Univ.Hamburg(2001), DESY-THESIS-2001-050.
- [57] S.V.Chekanov, Phys.Lett.B484(2000)51.
- [58] W.Ochs, private communications.
- [59] S.Mandelstam, Phys.Rev.112(1958)1344.